Study the oxidation behavior and residual stresses of AISI 430 alloy in air with water vapor

Ning Li

NNT : 2016SACLS075

THESE DE DOCTORAT
DE
L'UNIVERSITE PARIS-SACLAY
PRÉPARÉE À
L'UNIVERSITE PARIS-SUD

ECOLE DOCTORALE N°571

Sciences chimiques : molécules, matériaux, instrumentation et biosystèmes

Spécialité de doctorat: Chimie

Par

M. Ning LI

Etude du comportement à l'oxydation et des contraintes résiduelles lors de l'oxydation sous air humide de l'alliage AISI 430

Thèse présentée et soutenue à Orsay, le 4 avril 2016

Composition du Jury:

M. Frédérico GARRIDO	Professeur, Université Paris-Sud	Président
M. Manuel FRANCOIS	Professeur, Université Technologique de Troyes	Rapporteur
M. Chedly BRAHAM	Maître de Conférences HDR, Arts et Métiers ParisTech	Rapporteur
Mme Laure MARTINELLI	Ingénieur de Recherche HDR, CEA Saclay	Examinatrice
Mme Judith MONNIER	Maître de Conférences, Université Paris-Est Créteil	Examinatrice
M. Vincent JI	Professeur, Université Paris-Sud	Directeur de thèse

Acknowledgements

Foremost, I would like to thank my supervisor prof. Vincent Ji for providing me the opportunity to finish my PHD thesis at University Paris-Sud. I benefit a lot from his diligence, support and friendship.

I would like to express my appreciation to my thesis committee members, Prof. Frédérico GARRIDO, Prof. Manuel FRANCOIS, Dr. Chedly BRAHAM, Dr. Laure MARTINELLI and Dr. Judith MONNIER, for their attention, suggestions and comments.

I would like to thank Dr. Nathalie Prud'homme for her guidance and many good discussions. I would also like to express my appreciation to Mr. Patrick Ribot for sample preparation and SEM analysis, to Mr. Jérémy Forté for assistance in XRD analysis, to Dr. Diana Dragoe for XPS analysis. Many thanks go to my colleagues and friends who helped me during these three years. Their names are not given here, but their encouragements and friendships are invaluable and unforgettable.

I am deeply grateful to my parents, my elder brother and my wife for their support, understanding and love. For them, all endeavors become more worthwhile.

Finally, I would like to thank China Scholarship Council (CSC) for the financial support for my PHD thesis.

Table of Contents

List of Tables

List of Figures

List of Abbreviations

SOFC	Solid oxide fuel cell
TEC	Thermal expansion coefficient
PBR	Pilling-Bedworth ratio
ASR	Area specific resistance
TGA	Thermogravimetric analysis
SEM-FEG	Scanning electron microscope with field emission gun
EDX	Energy-dispersive X-ray spectroscopy
XRD	X-ray diffraction
SIMS	Secondary ion mass spectroscopy
XPS	X-ray photoelectron spectroscopy
AFM	Atomic force microscope

Summary

When an alloy is placed in an atmosphere containing oxygen at high temperature, the formation of oxide scale may take place. The oxidation resistance of the alloy is a very important criterion for selecting alloys to be used at high temperature. And it has been found that the oxidation behavior of alloys in atmosphere containing water vapor is different from that in dry air or oxygen. Moreover, in the oxide scale systematically accompanied the development of growth stresses during isothermal oxidation and of thermal stresses during cooling, which also limit the durability of oxide scale and the lifetime of the alloy.

The purpose of this work is to investigate the influence of water vapor on oxidation behavior of AISI 430 stainless steel at high temperature, which is expected to be used as interconnectors in the planar solid oxide fuel cells (SOFCs). The oxidation experiments have been performed in air with different absolute humidity (2%-10%) at 700 ℃, 800 ℃ and 900 ℃ by thermal gravimetric analysis (TGA) system. The oxide surface morphology, cross-section microstructure and the chemical composition of the oxide scale were studied after oxidation by FEG-SEM and EDX. The residual stresses distributions in the oxide scale were determined at room temperature by XRD method after oxidation, and the growth stresses were measured by in-situ deflection method during oxidation.

It has been found that the oxidation kinetic, surface morphology and diffusion mechanism of AISI 430 stainless steel in dry air are changed with the introduction of water vapor. The water vapor can also influence the residual stresses levels in the oxide scale. In the presence of water vapor, breakaway oxidation was observed at 900 ℃, and two possible mechanisms were given to explain this.

CHAPTER 1 Introduction

1.1 Background

The source of energy problem in our daily life has become increasingly important over the last decades. Traditional energy technologies cannot meet the continually growing needs of the human beings. Solid oxide fuel cells (SOFCs) are electrochemical generation, which can convert the chemical energy in fuels into power. It has been widely investigated and developed in recent years as a new power generation. Furthermore, compared with other traditional devices, the SOFC has higher efficiency and without harmful emissions. For the above advantages, SOFC is supposed to be used in the automobile industry.

However，the high operating temperature limits the material selection for components of SOFC, such as interconnector. The interconnector is a very significant part of the SOFC. It acts as electrical connection between a cathode of one cell to the anode of the other, and as a barrier physically separates the oxidizing and reducing gases. Lowering of the SOFCs operating temperature from 1000˚C to about 800˚C in recent years allows the use of metallic alloys in place of ceramics as interconnects. Cr_2O_3-forming Fe-Cr stainless steels are commonly used in SOFCs because they have obvious advantages, such as excellent electrical conductivity, adequate chemical and thermal stability, appropriate thermal expansion coefficient with other parts of SOFC and low cost.

Because of these reasons, oxidation of Fe-Cr stainless steels has drawn lots of attentions in recent years. Intensive studies on oxidation behaviors of Fe-Cr stainless steels in dry air have been done in the past decades, and numerous papers have been published on this field by

various researchers. Water vapor, however, exists in all stages of oxidation in reality and is the product of the SOFC. And at high temperature, most alloys tend to react with the oxidant in the atmosphere to form an oxide scale. Stresses can be generated during the scale growth and may affect the diffusion of ions leading to different oxidation kinetics. Thus, the motivation of our research is to understand the effect of concentration of humidity (vary from 2% to 10%) on oxidation behavior of Fe-Cr stainless steels at different temperature (from 700 ℃ to 900 ℃), and as well as the stresses impact on the oxide scale growth.

1.2 Research objectives

This study will mainly focus on the effect of water vapor on oxidation behavior of AISI 430 stainless steel at high temperature. The objective of this study will consist of three parts.

For the first part, a mechanism to explain the water vapor effects on the oxidation behavior of AISI 430 stainless steel has been proposed based on experiment and on theoretical study. The oxidation behavior of Fe-Cr stainless steels under dry air has been studied for many years, but for the mechanism of Fe-Cr stainless steels oxidation with water vapor, no consistent conclusion has been got and is still a contentious question. Accordingly, study the influence of water vapor on Fe-Cr stainless steel oxidation behavior at high temperature has great importance.

The second part is to determine and analyses the evolution of internal stress (growth stress, thermal stress and residual stress) levels in the oxide scale formed during the oxidation (growth stress) and during cooling after oxidation (thermal stress). It has been known that the internal stress levels in the oxide scale are also closely related to oxidation kinetic and the microstructure, but very few studies were focused on residual stress after oxidation in

atmosphere with water vapor. In this work, we try to investigate the development trend of internal stress in the oxide scale and to gain deeper understanding of the relationship between the residual stresses and the oxidation kinetics.

Last but not least, the third part is to find out the reasons of the damage of the oxide scale in atmosphere containing water vapor. Many experimental results have found that the breakaway oxidation happened with the introduction of water vapor, and a chromium evaporation mechanism has been proposed to explain this. But residual stress generation in the oxide scale may have effects on crackling, buckling and even spalling of the scale, which leads to accelerate the degradation of alloys. Thus, in this study we also want to find out if the residual stresses in the oxide scale relates to the breakaway oxidation.

1.3 Organization of this dissertation

This dissertation is consisted of seven chapters.

In chapter 1 the background of this study is given firstly, and then the objectives of this research work and the organization of this thesis are presented.

Chapter 2 will be divided into two parts. In the first part, we will introduce the principle of SOFC, the basic theory for growth of oxides and the generation of internal stresses. After that in the second part, we will provide a thorough review of the relevant works that have been done before on oxidation behaviors of Fe-Cr stainless steels in environment with and without water vapor at high temperature.

Chapter 3 is devoted to the description of the experimental facilities and the various techniques

used in our study, such as the identification of the oxides formed on the substrate surface by grazing incidence X-ray diffraction (GIXRD), the observation of the surface morphology and microstructure of the layers by FEG-SEM/EDX, SIMS and XPS, the determination of residual stresses by XRD method and the determination of growth stresses by in-situ deflection method.

Chapter 4 to chapter 6 is the majority of this dissertation. Chapter 4 mainly focuses on the oxidation behavior of AISI 430 alloy in air with different absolute humidity. The oxidation mechanism of Fe-17Cr stainless steel in dry air will be studied. And the effects of humidity, oxidation temperature and duration will also be discussed in detail.

Chapter 5 presents the residual stress levels in the oxide layers after oxidation in air with different absolute humidity determined by XRD and the growth stress levels determined by in-situ deflection method. The evolution trend of the growth stress during oxidation and thermal stress in the oxide layers will be given. The effect of water vapor on residual stress levels will also be discussed.

In chapter 6, we will discuss the relationship between the oxidation kinetic and the residual stress levels in the oxide layers. Two different mechanisms will be given to explain the oxide scale damage with the introduction of different concentration of absolute humidity in the oxidation atmosphere.

In the end, the dissertation will be concluded with Chapter 7 which gives general conclusions of this study. And to better complete the study in this field, future works are also proposed.

CHAPTER 2 Literature Review

2.1 Introduction to solid oxide fuel cell

The basic principle of fuel cell was firstly proposed by lawyer and scientist William Grove in 1839 [1, 2]. At the end of nineteenth century, with decade's development, Solid Oxide fuel cell (SOFC) has become increasingly attractive as a promising technology for clean power generation due to its higher efficiency and lower harmful emissions over other traditional energy-conversion technologies[1, 3].

2.1.1 Working principle of SOFC

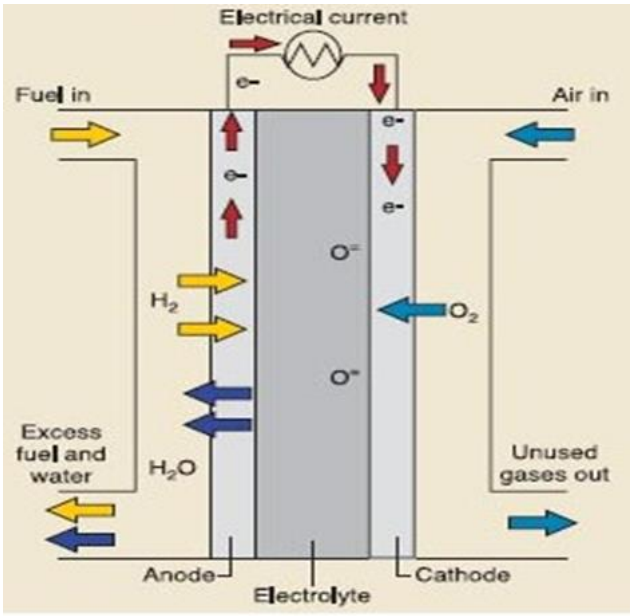

Figure 2.1 Schematic diagram of the principle of SOFC [2]

The schematic diagram of the principle of SOFC is given in Figure 2.1 [2]. A ceramic electrolyte which is capable of conducting negatively charged oxygen from the cathode to the anode is used. At the cathode side, air is provided as oxidant gas, and at the anode side fuel is provided. The oxygen atoms are reduced into oxygen ions at the cathode side. These ions can

diffuse to the anode through the ceramic electrolyte. And at the anode, these oxygen ions electrochemically oxidize the fuel and give off electrons. The basic reactions in the SOFC are given as [1]:

Cathode side: $O_2(g) + 4e^- \rightarrow 2O^{2-}$ (2-1)

Anode side: $2H_2(g) + 2O^{2-} \rightarrow 2H_2O(g) + 4e^-$ (2-2)

Total reaction: $2H_2(g) + O_2(g) \rightarrow 2H_2O(g)$ (2-3)

2.1.2 Materials for interconnector

A single unit of SOFC could only generate 0.7-0.8V open circuit potential [4]. To get sufficient voltage, SOFC needs to operate as an array of units, with interconnectors joining the neighboring units. The schematic of planar type SOFC basic units is shown in Figure 2.2. Meanwhile, interconnector also acts as physical barrier to separate the oxidizing and reducing gases.

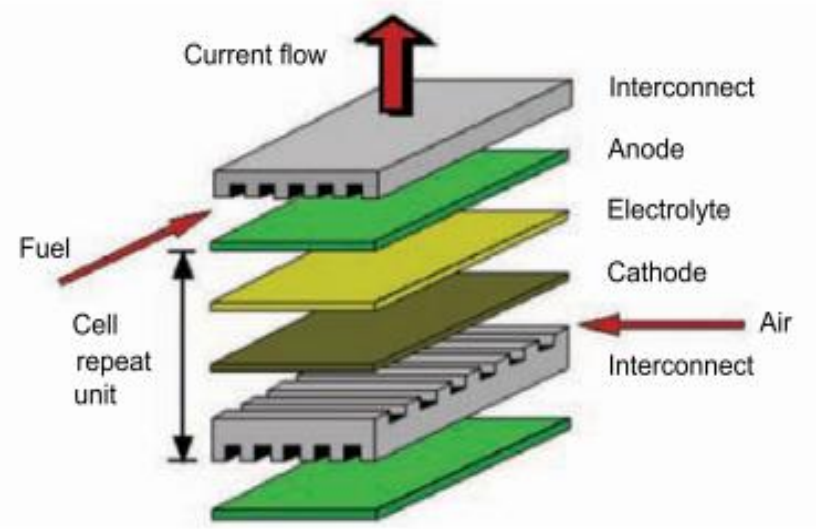

Figure 2.2 Schematic of planar type SOFC basic units [5]

Interconnector is a vital element for the functioning and reliability of SOFC, and some design

requirements for it are [2, 6, 7]:

- ✧ Excellent electrical conductivity
- ✧ High temperature oxidation and reduction resistance
- ✧ Good thermal conductivity
- ✧ Similar thermal expansion coefficient (TEC) with those of electrodes and electrolyte
- ✧ High mechanical strength
- ✧ Non reactivity with its adjoining components
- ✧ Low cost and easy to fabricate

For high temperature application (1000 ℃), the traditional material used for interconnector is ceramic obtained from lanthanum-chromium oxides doped with strontium ($(La,Sr)CrO_3$) [3, 4]. This material exhibits good corrosion resistance and high electrical conductivity in the operation atmosphere. On the other hand, the disadvantages of this material are evident: no machinability and low flexibility of complex shapes, poor tolerance of sudden temperature changes and expensive.

With the reduction of operation temperature from 1000 ℃ to 800 ℃, metallic materials are proposed to be used as alternative for the ceramic interconnector [8, 9]. As we all know, an oxide scale forms at high temperature in oxidizing environment, the ideal candidate should be Cr_2O_3, Al_2O_3 or SiO_2 forming alloys which have good high temperature oxidation resistance. At the same time, the oxide scale formed on the surface should also have good electric conductivity. Considering the insulating nature of Al_2O_3 and SiO_2, therefore, chromia forming alloys are the most promising interconnector candidates. Recently, great efforts have been devoted to apply iron-based chromia forming alloy as interconnectors, because of its

considerably lower fabrication cost compared with Cr based alloys.

2.2 High temperature oxidation of alloys

At high temperature, almost all metals are not thermodynamically stable in air or in atmosphere where oxygen exists, and a solid oxide scale will form on the surface. Oxidation resistance is a very important requirement for alloys service at high temperature. Therefore, the oxidation kinetics is an essential knowledge for using high temperature alloys.

2.2.1 Thermodynamics of alloy oxidation

If an oxidation reaction can occur or not at high temperature between an alloy and the surrounding atmosphere is a significant question. The answer can be found by the second law of thermodynamic. In atmosphere that both pressure and temperature are constant, the second law can be written as [10]:

$$\Delta G = \Delta H - T\Delta S \qquad (2\text{-}4)$$

in which ΔG is the variation of Gibbs free energy, ΔH is the variation of enthalpy, ΔS is the variation of entropy and T is the temperature. In these cases, the second law expresses:

ΔG < 0, the reaction is thermodynamically favored

ΔG = 0, the reaction is in equilibrium

ΔG > 0, the reaction is thermodynamically impossible

For a typical oxidation reaction,

$$M + O_2 \rightarrow MO_2 \qquad (2\text{-}5)$$

in which M stands for metal, the ΔG is expressed as :

$$\Delta G = \Delta G^{o} + RT\ln\left(\frac{\alpha_{MO_2}}{\alpha_M p_{O_2}}\right) \qquad (2\text{-}6)$$

in which ΔG^{o} is the standard Gibbs free energy, T is temperature, R is the gas constant and α_i is the i specie activity, which describe the deviation from the standard state for the given specie and can be expressed as:

$$\alpha_i = \frac{p_i}{p_i^{o}} \qquad (2\text{-}7)$$

in which p_i either the vapor pressure over a condensed species or the partial pressure of a gaseous species and p_i^{o} is the same quantity corresponding to the standard state of i.

In the case of the reaction is in equilibrium ($\Delta G=0$), the Equation (2-6) reduce to Equation (2-8),

$$\Delta G^{o} = -RT\ln\left(\frac{\alpha_{MO_2}}{\alpha_M p_{O_2}}\right) \qquad (2\text{-}8)$$

The term in brackets is called the equilibrium constant of the reaction. If taking the activities of pure solid as unity, the Equation (2-8) can be simplified to:

$$p_{O_2}^{M/MO_2} = \exp\frac{-\Delta G^{o}}{RT} \qquad (2\text{-}9)$$

With Equation (2-9), we can calculate the oxide dissociation pressure. The $p_{O_2}^{M/MO_2}$ can be derived from the Ellingham diagram (Figure 2.3) by drawing a straight line from the point O through the free energy line at the oxidation temperature and reading the value from its intersection with the p_{O_2} line at the right side. With this diagram, the stability of the different oxide can be compared. The lower position of the line in the diagram indicates the more stable the oxide is.

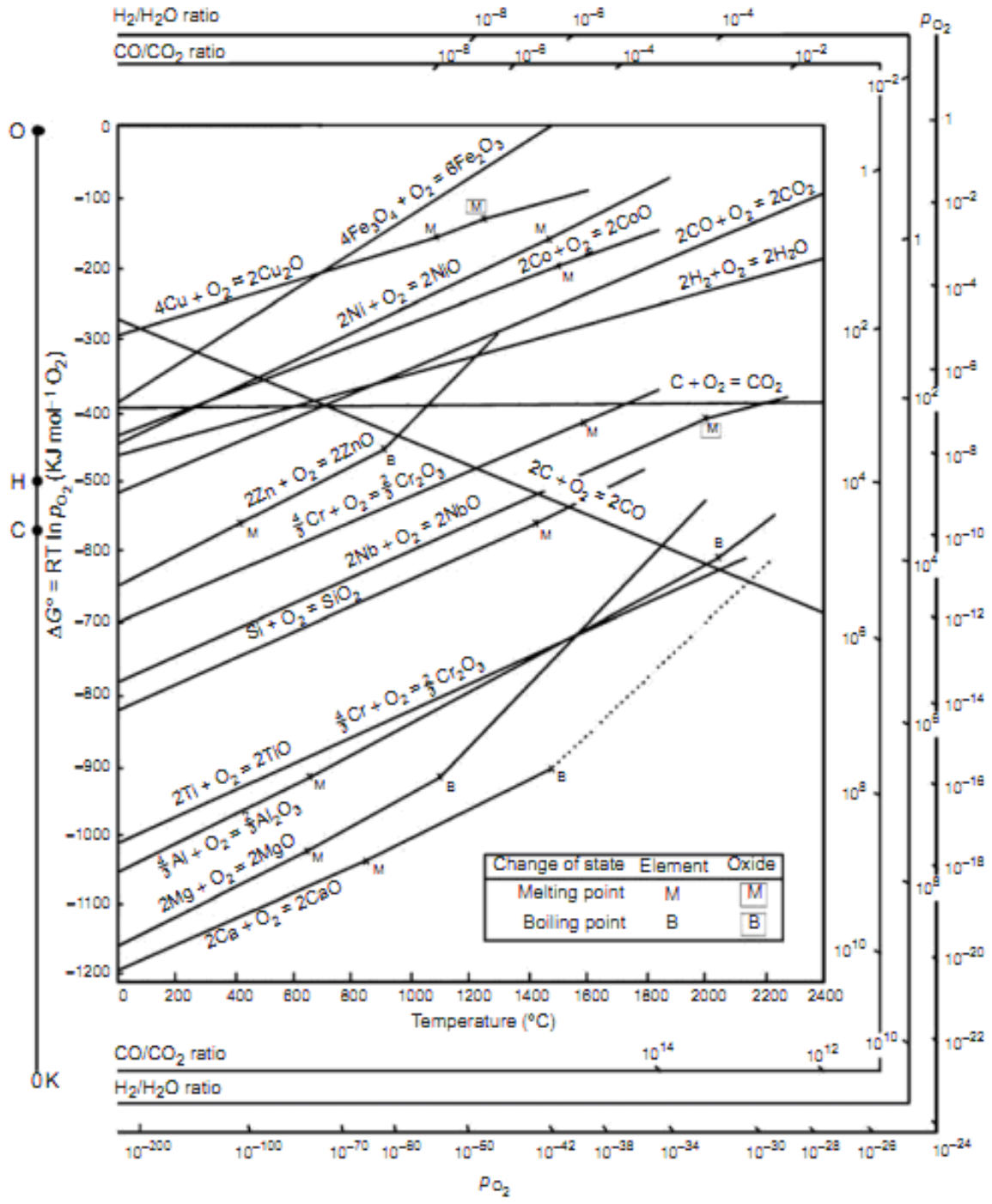

Figure 2.3 Ellingham diagram of oxide stability at different oxygen pressure and temperature [10]

2.2.2 Oxidation kinetics

The Ellingham diagram gives thermodynamically favorable conditions under which the metal

can be oxidized. When an initial oxide scale is formed, which can separate the alloy and the gas, and then the reaction is mainly controlled by the diffusion of ions through the oxide scale. And the activity gradient (or chemical potential) is the driving force of the diffusion. It has been explained by the classical Wagner's theory. It is supposed that a thermodynamic equilibrium is built at the alloy/oxide interface and at the oxygen/oxide surface as demonstrated in Figure 2.4.

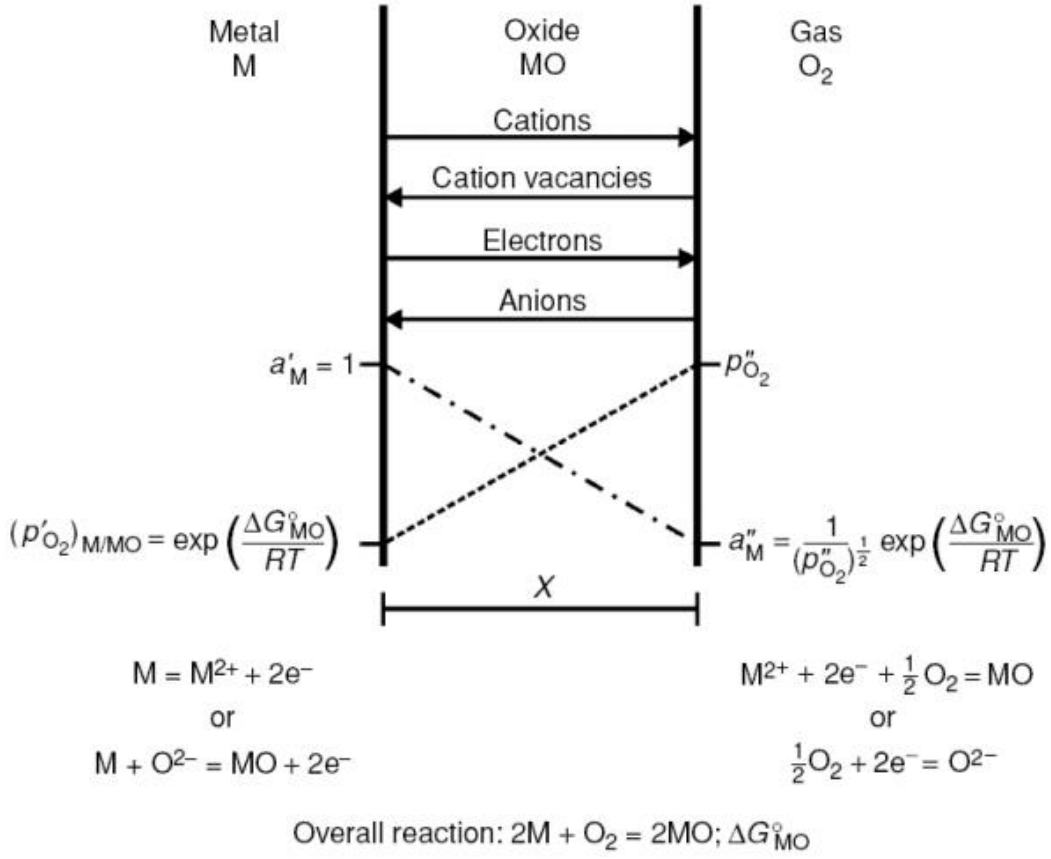

Figure 2.4. Schematic diagram of scale formation according to Wagner's model [11]

For a dense oxide scale, the scaling rate is controlled by the diffusion of ions through the growing scale. Therefore, the outward flux of cation, $j_{M^{2+}}$, is equal but in opposite direction to the inward cation defect flux j_{V_M}. Thus, the $j_{M^{2+}}$ can be given as:

$$j_{M^{2+}} = -j_{V_M} = D_{V_M} \frac{C''_{V_M} - C'_{V_M}}{x} \qquad (2\text{-}10)$$

in which x is the thickness of the oxide scale, D_{V_M} is the diffusion coefficient of cation vacancies, and $C_{V_M}^{"}$ and $C_{V_M}^{\prime}$ are the vacancy concentrations at the scale/gas and scale/metal interfaces, respectively. Since there is thermodynamic equilibrium at the two interfaces, the value $(C_{V_M}^{"} - C_{V_M}^{\prime})$ is constant and can get Equation (2-11),

$$j_{M^{2+}} = \frac{1}{V_{OX}}\frac{dx}{dt} = D_{V_M}\frac{C_{V_M}^{"} - C_{V_M}^{\prime}}{x} \qquad (2\text{-}11)$$

in which the V_{OX} is the molar volume of the oxide. Therefore, the oxide scaling rate can be given as:

$$\frac{dx}{dt} = \frac{k^{\prime}}{x} \text{ in which } k^{\prime} = D_{V_M}V_{OX}(C_{V_M}^{"} - C_{V_M}^{\prime}) \qquad (2\text{-}12)$$

Setting x=0 at t=0, we can obtain the following Equation:

$$x^2 = 2k^{\prime}t \qquad (2\text{-}13)$$

which is commonly known as the parabolic rate law.

2.2.3 Rates of oxidation

It is necessary to know that the parabolic rate law assumed highly idealistic conditions. While in some cases, deviations from the parabolic rate might be observed during oxidation of alloys, such as linear rate, logarithmic and inverse logarithmic rate. Figure 2.5 schematically presents different oxidation rates.

(1) Parabolic rate law

As we discussed in the section 2.2.2, if a protective and continuous oxide scale forms, the oxidation is mainly controlled by the diffusion of ions through the scale. With the thickening of the scale, the diffusion distance increases, thus the oxidation rate slows down.

(2) Linear rate law

If the oxide scale is not protective, then the diffusion of ions through the scale is not the rate limiting and the chemical reaction or the diffusion through the gas phase might be the determining factor. In this case, the oxide scale thickness is independent of the oxidation rate which will not slow down with the thickening of the scale. The oxidation rate may remain constant with time, a linear law is obtained:

$$x = k_l \cdot t \qquad (2\text{-}14)$$

in which x is the oxide scale thickness and k_l is the linear rate constant.

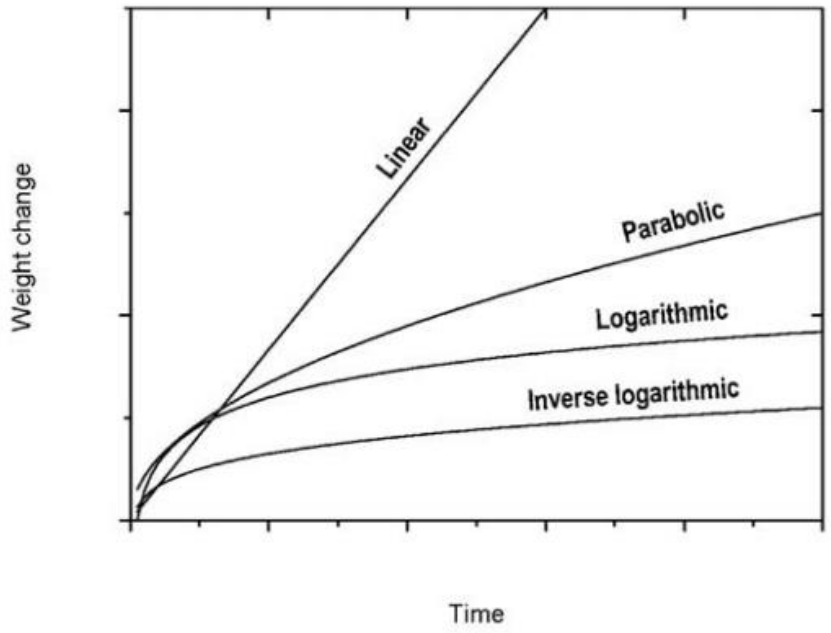

Figure 2.5 Different oxidation rates observed during the oxidation of metals [12]

(3) Logarithmic rate law

When metals are oxidized under low temperature, the initial oxide formation is rapid and followed by a very low rate of oxidation. The oxidation rate conforms to logarithmic rate law and can be given by:

$$x = k_{log} \log(a \cdot t + c) \quad (\text{Direct log law}) \qquad (2\text{-}15)$$

$$1/x = b - k_i \log t \quad (\text{Inverse log law}) \qquad (2\text{-}16)$$

in which a, b, c, k_{log} and k_i are constants.

2.3 Internal stresses in the oxide scale

During the formation of an oxide scale at high temperature, it always involves the development of internal stresses in it. These stresses have important effects on species diffusion rate and oxidation kinetics, and may also lead to buckling, crack and even spall of the oxide scale. Therefore, the internal stresses are closely related with the lifetime of the oxide scale.

2.3.1 Introduction to the residual stress

Internal stress usually generated during materials manufacturing and processing due to plastic deformations, thermal mismatch and phase transformations. The state of internal stress depends not only on the processes it has undergone, but also on the material properties in the environment. In many cases, the internal stresses themselves are not life-limiting factor. But combined with external load, these internal stresses may have a great effect on performance and lifetime. Therefore, analyzing the state of internal stresses into the materials has great technological importance.

Commonly, according to the length scale of the self-balancing, the internal stresses can be classified as three types, they are: Type I, Type II, and Type III. The Type I often categorized as macrostress or residual stress, and Type II and Type III as microstress [13].

Type I residual stress is a kind of self-balancing macroscopic internal stress existing in the absence of any external loads which develops within a considerable fraction of the sample. These residual stresses result from macroscopic misfits, such as plastic deformation and heat

treatment. This type of stress is considered to be continuous across grain and phase boundaries, as shown in Figure 2.6 (a).

Type II internal stress describes the deviation from the macroscopic residual stress level of an individual grain, as shown in Figure 2.6 (b). This low-level type of stress is discontinuous from grain to grain. They are typically a consequence of the anisotropy of each grain for single phase materials, and different properties of the different phases for polycrystalline materials.

Type III internal stress describes the deviation from average internal stress level of a special grain. Crystalline defects, with a scale shorter than the grain scale (shown in Figure 2.6 (c)), can result in this kind of stress.

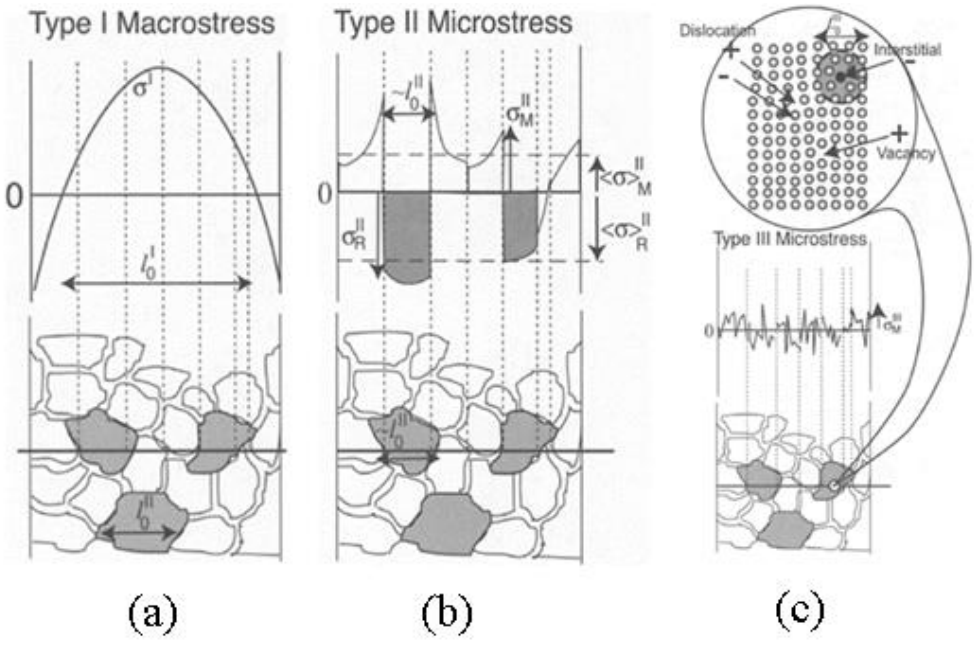

Figure 2.6 Definition of different type residual stresses in single phase material: (a) Type I, (b) Type II and (c) Type III [13]

From an engineering view, the type I internal stresses are the most important, and the type II

and type III are of interest in materials science studies. In the case of a substrate/scale system, due to the growth of an oxide scale on a metal substrate (growth stress) and the cooling after the oxidation (thermal stress), the internal macroscopic stresses (residual stress) can be generated in the scale and in the substrate. In our work, only the type I will be studied.

2.3.2 Stresses in the oxide scale

Depending on their origins, residual stresses in the oxide scale can be separated into two parts: growth stresses generated during isothermal oxidation and thermal stresses generated during cooling.

2.3.2.1 Thermal Stresses

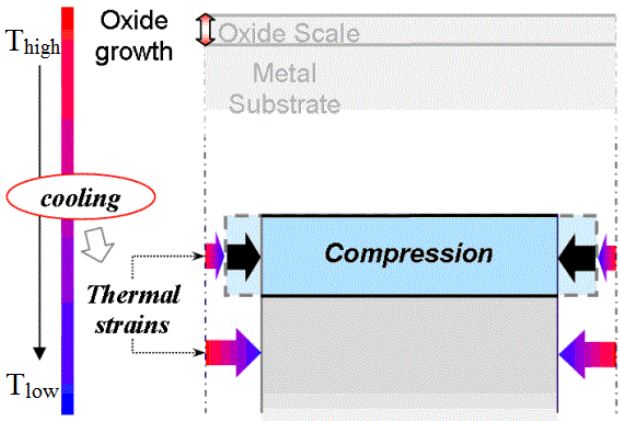

Figure 2.7 Schematic illustration of thermal strain in the oxide scale during cooling [14]

Thermal stresses will be generated during cooling the sample from the oxidation temperature to the room temperature due to the thermal expansion coefficients mismatch of the metal α_m and oxide α_{ox}. In most cases, the value of α_{ox} is smaller than that of α_m, so that the smaller retractions of the oxide scale during the cooling. Therefore, the substrate experiences a tensile stain and the oxide scale a corresponding compressive strain, as shown in Figure 2.7. For the system of an oxide on both the bottom and the top of the substrate, if they are perfectly

bonded, ignoring the thickness of the scale which is very thin compared with the substrate and assuming that between the oxide and metal there is no Poisson ratio difference, the in-plane stresses in oxide scale can be expressed as [10]:

$$\sigma_{ox} = \frac{-E_{ox}(\alpha_{ox}-\alpha_m)\Delta T}{1-\upsilon} \qquad (2\text{-}17)$$

in which E is the Young's modulus, υ is the Poisson's ratio, α_{ox} and α_m are the thermal expansion coefficients of the scale and the substrate, respectively, and ΔT is the temperature difference between the oxidation temperature and the room temperature. Using this equation, in-plane thermal stresses in oxide scale generated during the cooling can be calculated. Depending on the thermal expansion coefficient mismatch of the metal and the oxide, the value can be several gigapascals, and the thermal stresses are largely thought as the main driving force for mechanical failure. Therefore, while designing and selecting the alloy, it is important to consider the thermal expansion coefficient difference of the metal and the oxide formed on it during the oxidation.

2.3.2.2 Growth Stresses

During the oxidation, with the formation of oxide and scale growth, stresses are also generated. Although in most cases the thermal stresses are considered to be the main reason for oxide scale failure, the growth stresses might also play a very important role in some special cases. J. Mougin et al [15] have proved that the growth stresses generated in chromia layer during high temperature oxidation of Fe-18Cr-TiNb provide the major part of the residual stresses, and the effects of thermal stresses are rather small. Numerous publications have focused on the growth stress over the last decades [15-39], several consensus have been reached about the origins of this type of stresses for the alloy/oxide system:

(1) Pilling-Bedworth ratio

Pilling and Bedworth may have been the first to explain the origin of growth stresses. They proposed that the difference between the specific volume of the oxide and the substrate would generate growth stresses. The parameter related to this mechanism is the Pilling-Bedworth ratio (PBR) [19]:

$$\mathrm{PBR} = \frac{V_{ox}}{V_m} \qquad (2\text{-}18)$$

in which V_{ox} and V_m are molar volume of oxide and metal, respectively. According to this theory, an isotropic growth strain is induced:

$$\varepsilon_v = \left[(\mathrm{PBR})^{1/3} - 1\right] \qquad (2\text{-}19)$$

If the PBR is smaller than unity the stresses in the oxide layer are tensile, and if bigger than unity the stresses are compressive. When the formation of new oxide is controlled by inward diffusion of anions, PBR should be an important origin of stresses [19], because this strain just occurs at the oxide/metal interface. But, if the formation of oxides is controlled by the outward diffusion of cations, this mechanism cannot explain the phenomena that generation of growth stresses in it. For chromia which is formed due to the inward diffusion of anion, the PBR is equal to 2.07 [19].

(2) Epitaxial stresses

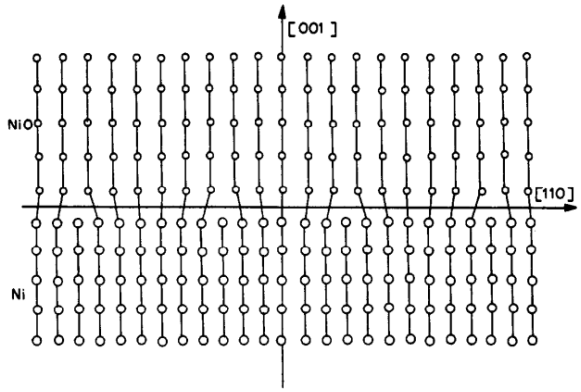

Figure 2.8 Schematic of epitaxy relationship for Ni/NiO system [17]

The formation of an oxide scale on a substrate will induce an incompatibility between the two crystalline lattices, which will result in a strain to accommodate the mismatch [29]. The stresses are either tensile or compressive depending on the epitaxial relationship. Pieraggi and Rapp [17] proposed an illustrative schematic applied to the Ni/NiO system. However, the epitaxy is an interface phenomenon, thus this mechanism would only generate significant stresses for the thin oxide scale located mainly at interface.

(3) Compositional change in the oxide scale or substrate

Compositional change in the oxide or substrate maybe another source of growth stresses generated during the oxidation. Dissolution of oxygen in the substrate, either as internal oxide particle or in solid solution, can engender significant stresses, especially for the metals which have high oxygen solubility such as Nb, Ta and Zr [10]. Compositional change in the scale can also result in stress development. Yearian et al. [40] have already found that compressive stresses were generated with the oxide change from $(Cr,Fe)_2O_3$ to $(Cr,Fe)_3O_4$.

(4) Oxide formation inside the scale

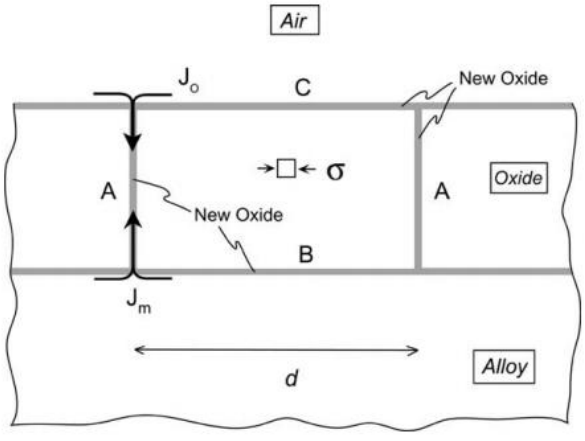

Figure 2.9 Possible locations of new oxide formed as a result of the inward flux of oxygen and the outward flux of metal ions [25]

Rhines and Wolf [16] proposed a conceptual model for the growth stresses in the oxide scale.

The model suggests that the growth stresses are only engendered by the formation of oxides along grain boundaries lying perpendicular to the interface, point A in Figure 2.9, because of the counter diffusion of oxygen and metal ions. If the inward diffusion of anions leads to the formation of new oxides at point B or the outward diffusion of cations leads to the formation of new oxides at point C, just the oxide scale thickens and no lateral strains would be generated. Although the Rhines-Wolf model doesn't consider diffusion mechanism and defect mechanism, it still represents a powerful idea.

(5) Influence of vacancies generated during oxidation

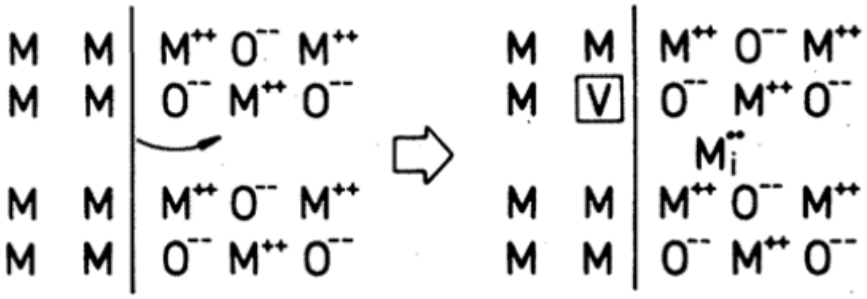

(a) Vacancy generation at oxide/alloy interface

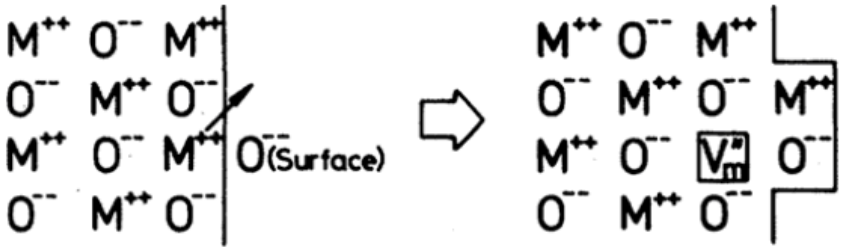

(b) Vacancy generation at oxide/gas surface

Figure 2.10 Schematic illustration of the reaction for vacancy generation during high temperature oxidation [41]

For cationic diffusion controlled oxidation, A. Atkinson [41] proposed that vacancy formed during the oxidation could generated stains, as shown in Figure 2.10. During high temperature oxidation, vacancies may form at the oxide/gas surface and oxide/alloy interface. For Fe-Cr

alloy, it has been proved that vacancies could form at the oxide/alloy interface [42]. Strains would be generated from vacancy-dislocation interactions [43]. For most cases, with the accumulating of vacancies, voids would form at the oxide/alloy interface. This vacancies' generation/annihilation mechanism is suggested to be the origin of the creep process in the oxide/alloy system that relieve growth stresses several hours after the oxidation has started [44].

2.3.3 Relaxation of residual stresses

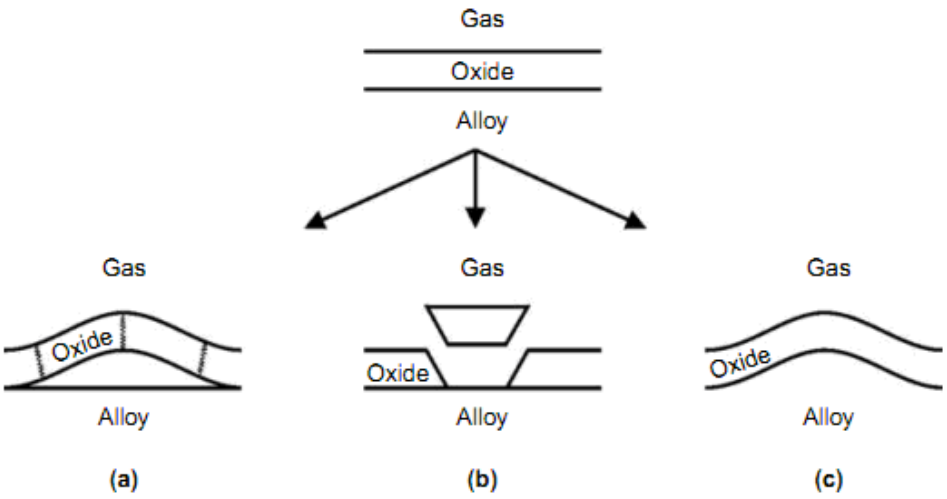

Figure 2.11 Schematic diagram of relaxation of stresses in the oxide scale. (a) Buckling of the oxide; (b) shear cracking of the oxide and (c) plastic deformation of the oxide scale and the substrate [10]

The relaxation of residual stresses may take place either during the oxidation or during heating-cooling sequences by many processes. Depending on the different mechanical properties of the oxide and the metal, different mechanisms of stress relaxation might occur [10], as shown in Figure 2.11.

The spalling of a protective oxide scale undergoing compressive stresses will occur if the elastic energy stored within the intact scale is bigger than the fracture resistance, G_c, of the

interface. The criterion for the spallation of a protective oxide scale then can be given as [10]:

$$\frac{(1-\upsilon)\sigma^2 h}{E} > G_c \qquad (2\text{-}20)$$

in which σ is the bi-axial residual stress in the oxide scale, E is the elastic modulus, υ is the Poisson ratio and h is the thickness of the oxide scale. This criterion is a necessary but not sufficient condition, an oxide scale tends to spall if the scale has a big residual stress, a big scale thickness and small interface strength. Two possible ways have been proposed: buckling of the oxide and shear cracking of the oxide.

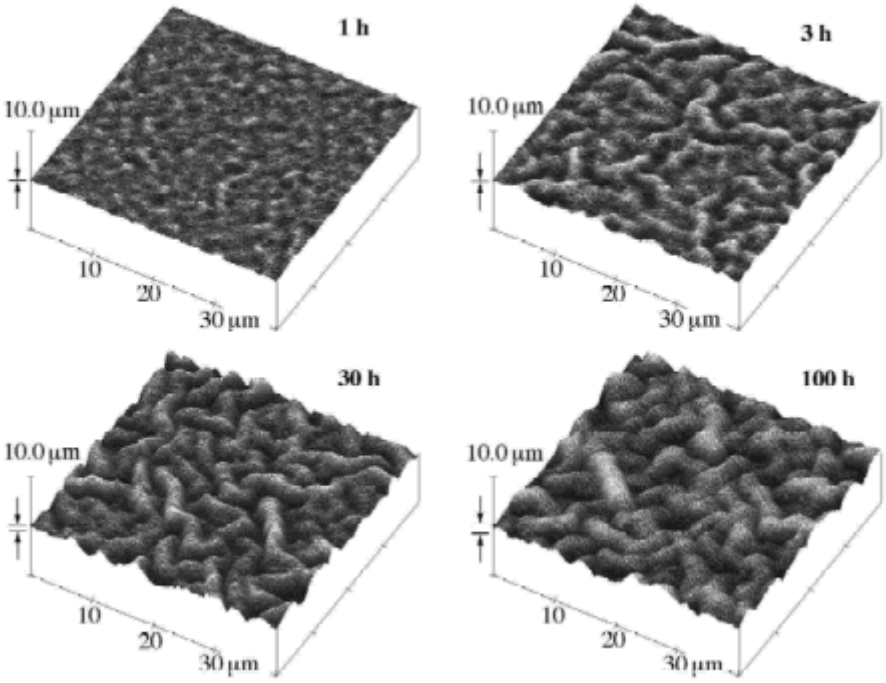

Figure 2.12 The formation of buckling on the Fe-Cr-Al alloy as a function of oxidation duration at 1000 ℃ [23]

From a resistance to failure view, buckling of the oxide (as shown in Figure 2.11 (a)) might take place when the oxide/substrate interface is weaker than the oxide scale. Buckling mainly occurs in the thin scale, and may not be feasible for the thick scale. V.K. Tolpygo et al [23, 45] observed the evolution of buckling on Fe-Cr-Al alloy surface during oxidation (show in

Figure 2.12), and they thought that is the consequence of the relaxation of residual stresses in Al_2O_3 scale.

If the oxide/substrate interface strength is high, relaxation of the residual stress is not likely to happen by buckling, and shear cracking of the oxide scale might take place, leading to spallation by a wedge mechanism as shown in Figure 2.11 (b). Both buckling and shear cracking of the oxide scale are the main failure mechanism for chromia scales formed at high temperature.

In some cases, if the Gc is high and the alloy is relatively weak, the relaxation of residual stress might perform by deformation of the oxide scale and substrate at the same time, as shown in Figure 2.11 (c).

2.3.4 Residual stress in chromia-forming alloys

Some research works have been done in recent years to determine the residual stress in oxide scale formed on Cr_2O_3 forming alloys. For Ni-Cr alloy, the residual stress is compressive and varies between -1GPa and -3.3GPa. A range of -1.2GPa to 1.7GPa was reported by B.R. Barnard [46] for Cr_2O_3 oxide scale on 230 alloy (60%Ni, 23%Cr, 14%W, 1%Fe and 1%Mo). J. Xiao [47] has found that the residual stress varies from 1.2GPa to 1.8GPa in chromia layer on Inconel 600 alloy and the level of residual stress in the oxide scale can be influenced by introduction of water vapor in the oxidation atmosphere. At same oxidation temperature, the more water vapor added in, the greater the residual stress in the oxide scale. Residual stress values of -2GPa to 3.5GPa was observed in the oxide scale formed on Ni30Cr alloy [48]. The level of residual stress in the oxide scale depends on the thickness of substrate, oxidation temperature and oxidation duration. The residual stress in the chromia scale formed on NiCr alloy is mainly thermal stress generated during cooling, and the growth stress generated

during oxidation is ignorable.

For Fe-Cr alloy, in-situ Raman spectroscopy experiments have been performed by J. Mougin et al [15] on Fe-18Cr alloy oxidized at 750 ℃ to determine the growth stress and thermal stress in chromia scale. It showed that the growth stress in the scale was near -2GPa and the thermal stress was -0.2GPa. The growth stress is almost ten times bigger than the thermal stress, as shown in Figure 2.13. Galerie et al [49] studied the influence of water vapor on Fe-18Cr alloy and found that oxide residual stress is greater when formed in H_2O.

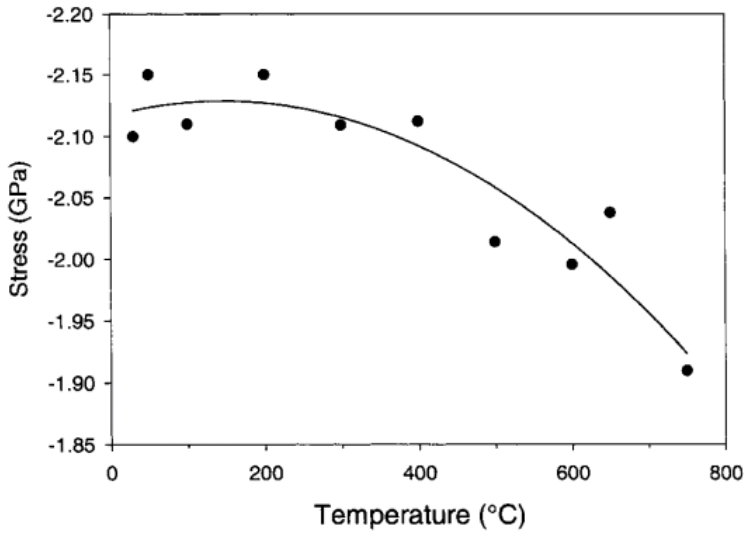

Figure 2.13 Evolution of the residual stress in chromia layer during cooling of Fe-18Cr alloy oxidized at 750 ℃ for 3h [15]

2.4 Oxidation behavior of Fe-Cr stainless steels

The oxidation behavior of chromia forming alloys has been the subject of many publications [50-56]. Figure 2.14 gives two oxidation mechanisms for chromia forming alloys: outward diffusion of Cr ions and inward diffusion of oxygen ions. And the outward diffusion of cations is more important, as shown in Figure 2.14(a). Cr vacancies are formed, by reaction (2-21), in

alloy near the oxide/alloy interface. These vacancies are filled by the outward diffusion of Cr ions in the alloy.

$$[4V_{Cr}''' + 6V_O^{\cdot\cdot}]_{surface} + 3O_2 = 6O_O^X + 4V_{Cr}''' + 12h^{\cdot} \qquad (2\text{-}21)$$

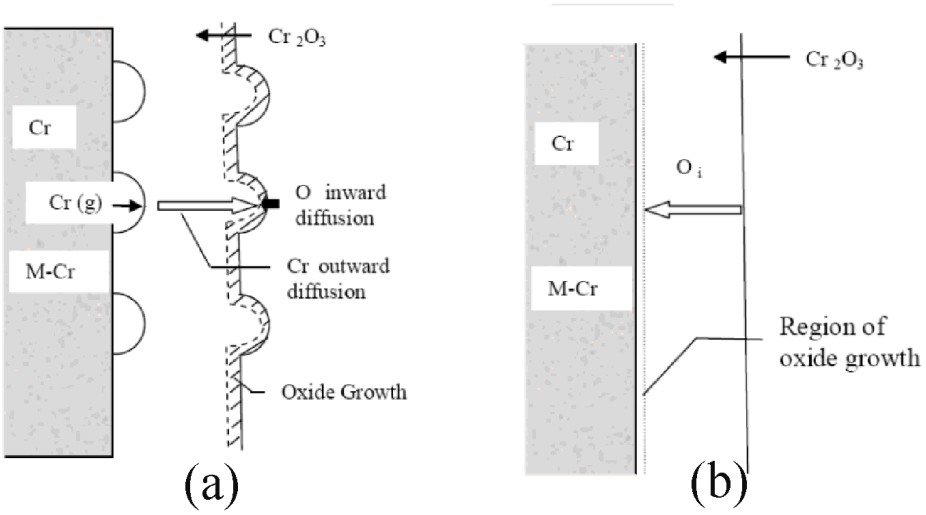

Figure 2.14 Schematic of the chromia-forming alloy oxidation mechanism [57]

Another mechanism is the inward diffusion of oxygen ions, as shown in Figure 2.14(b). Oxygen interstitials are formed at the oxide scale surface and diffuse into the oxide/scale interface always through grain boundaries. These interstitials can react with Cr ions from the alloy by reaction (2-22).

$$[4V_{Cr}''' + 6V_O^{\cdot\cdot}]_{surface} + 4Cr_{metal} + 6O_i'' + 12h^{\cdot} = 6O_O^X + 4Cr_{Cr}^X \quad (2\text{-}22)$$

For Fe-Cr alloys, reviews were given by Wood et al [58, 59]. The conventional knowledge is that there is a minimum Cr concentration in the alloy to form a protective chromia layer on the substrate. To form and maintain a continuous external oxide scale, two criteria need to be satisfied. Firstly, to avoid internal oxidation, the concentration of Cr in the steel must high enough, as given below [60]:

$$N_{Cr}^{(1)} > \left[\frac{\pi g^*}{3} N_O^{(S)} \frac{D_O V_m}{D_{Fe-Cr} V_{CrO_{1.5}}}\right]^{\frac{1}{2}} \qquad (2\text{-}23)$$

in which , $N_{Cr}^{(1)}$: minimum Cr concentration (1)

$N_O^{(S)}$: oxygen solubility in the alloy

D_O: diffusivity of oxygen in the alloy

$D_{Fe\text{-}Cr}$: alloy interdiffusion coefficient

V: molar volume

g*: factor

If the internal oxides are Cr_2O_3, then the g* is about 0.3 [61]. In this case only oxidation of Cr is considered. In the case that both Cr and Fe can be oxidized, the minimum concentration increased due to the increase of transient oxide [62].

For the second criterion, after the formation of a continuous external scale, the supply of Cr must be rapid enough to make up the consumption by oxide formation. The second criterion can be given by the equation:

$$N_{Cr}^{(2)} = \frac{V_m}{V_{CrO_{1.5}}} \left(\frac{\pi k_p}{2D_{Fe-Cr}}\right)^{\frac{1}{2}} \qquad (2\text{-}24)$$

in which, $N_{Cr}^{(2)}$: minimum Cr concentration (1)

k_p: parabolic rate constant for the formation of the oxide

Based on these two criteria, 9-10 wt% Cr is needed to form a protective chromia oxide layer on ferritic alloys at temperature below 900 ℃. Fe-Cr ferritic alloys with different Cr concentration oxidation experiment has been done [60], it is found that a continuous chromia scale was formed on the Fe-Cr alloy with 13.5% Cr after oxidation in air for 96h at 650 ℃. This value is a little larger than the calculated one because of Fe transition oxidation. At low Cr concentration, both iron oxides and chromium oxides form on the alloy. Y. Ikeda and K. Nii [51] revealed that cracks are generated during the oxidation of Fe-Cr alloys. For the low Cr concentration alloys (≤10%wt), the cracks are filled up with iron oxides and the scale is

not protective. While for Fe-20Cr alloy, the cracks are readily healed and a protective continuous scale formed.

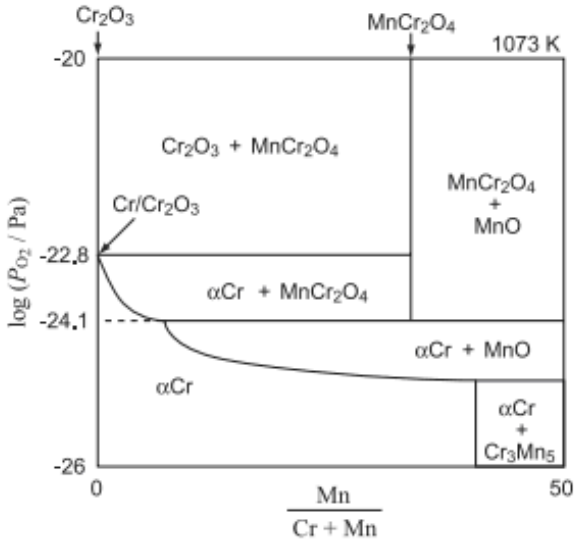

Figure 2.15 Schematic equilibrium oxygen pressures-composition diagram of Cr-Mn-O system [63]

Addition small amounts of manganese in Fe-Cr stainless steel can influence the oxidation behavior, because the free formation energy of MnO is smaller than that of Cr_2O_3. The effects of Mn on the oxidation behavior of Fe-Cr stainless steels at high temperature have been studied [64-67]. It has been found that the formation of an outer spinel type oxide is due to Mn ions can diffuse faster than other ions [68, 69]. Figure 2.15 displays schematic equilibrium oxygen pressure-composition diagram of Cr-Mn-O system at 1073 K [63], which thermodynamically indicates that the formation of $MnCr_2O_4$ spinel on the substrate no matter how little the Mn concentration in the alloy when the partial pressure of oxygen is sufficient. This spinel type oxide has adverse effects on the oxidation resistance because the formation of this non-protective spinel oxide can increase the oxidation rate [64]. At the same time, the favorable effects are that the spinel can improve the electrical conductivity of the oxide scale and suppress the evaporation of chromia. B. Hua et al [66] studied the early stage oxidation

behavior of 430 alloy with different Mn concentration (0-3 wt%) in air at 750 ℃ , and showed that the oxidation rate and area specific resistance (ASR, Ω cm^2) increased with the increase of Mn concentration in the alloy.

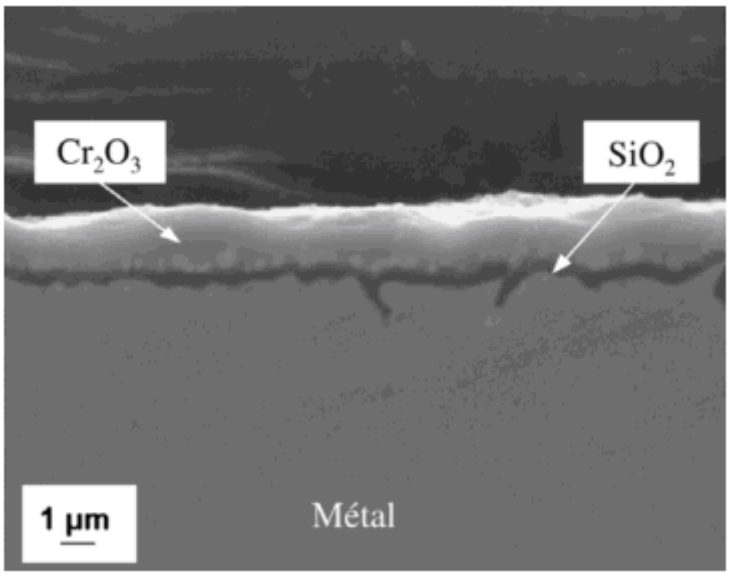

Figure 2.16 Cross section of Fe-15%Cr-0.5%Si after oxidation at 950 ℃ for 8 h [70]

Small additions of Si can also play a significant role on oxidation behavior of Fe-Cr stainless steel at high temperature. A silica layer at the alloy/scale interface has been found by several authors [70-74], as shown in Figure 2.16. And this oxide layer was thought to be a diffusion barrier favoring the formation of outer chromia layer. M. P. Brady et al [72] studied the oxidation behavior of 430 ferritic stainless steel and Fe-20Cr at 700 ℃ and 800 ℃. They found that lower weight gains for 430 than Fe-20Cr are resulted from the formation of inner SiO_2 layer by the 430.

2.5 Effect of water vapor on oxidation behavior of alloys

Water vapor exists in almost all the circumstances in which alloys are used at high temperature, but it was a “forgotten” problem as called by Kofstad [75] until the 1990s. Some

studies of effects on oxidation behavior of alloys have been done in recent years [72, 76-103]. A variety of results have been found, and it has been found that the oxidation behavior of alloys in atmosphere containing water vapor is different from that in dry air or oxygen. Generally, for the Fe-Cr alloys, with the introduction of water vapor in the oxidation circumstance, the oxidation rates will increase. Besides enhancing the oxidation rate, the water vapor has also been found to promote the protective oxide scale damaged in the form of breakaway oxidation which indicates the formation of non-protective scale. The mechanisms of the water vapor effects are still not fully understood. To explain the influence of water vapor, different models have been suggested in recent years, they are:

- Dissociation mechanism
- Volatilization of $Fe(OH)_2$
- Formation of microcracks and microchannels
- Entrance of H_2O into the oxide scale
- Volatilization of $CrO_2(OH)_2$

2.5.1 Dissociation mechanism

Fujii and Meussner [76] proposed a dissociation mechanism, and is illustrated in Figure 2.17. This mechanism was based on the oxidation study of Fe-(5-25%)Cr alloy in Ar with 10% water vapor at 700-1100 ℃. Some metal ions generated at the interfaces (2) and (4), and then diffuse to the interface (1), where water vapor is adsorbed. Wustite, adsorbed hydrogen and defects in the oxide generate in the subsequent reactions. Most of the hydrogen is thought to desorb, but some of them will inevitably dissolve in the oxide.

$$PH_2O_{(1)} > PH_2O_{(2)} > PH_2O_{(3)}$$

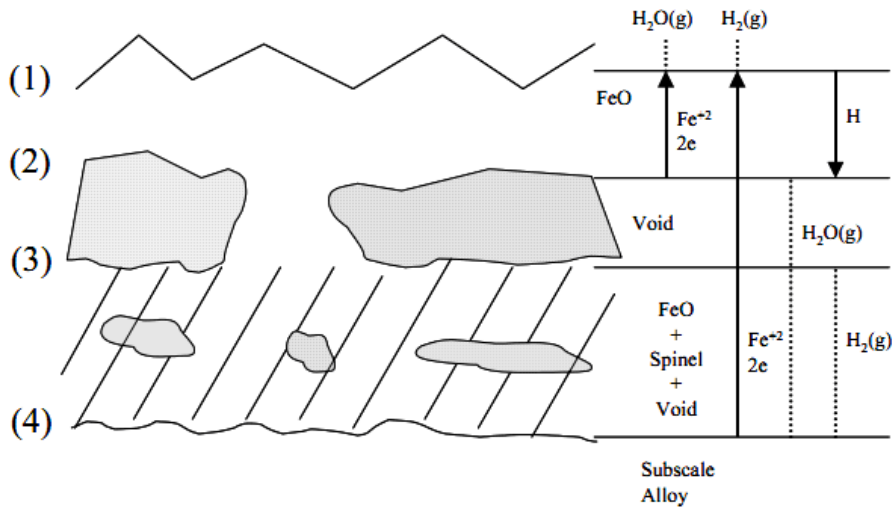

Figure 2.17 Dissociation mechanism proposed by Fujii and Meussner [76]

At the outer interface, (1), the reactions are proposed to be as follows:

$$H_2O_{(g)} \rightleftarrows H_2O_{(ads)} \quad (2\text{-}25)$$

$$H_2O_{(ads)} + Fe^{2+} + 2e^- \rightleftarrows FeO + Fe_{vac} + 2\oplus + H_{2(ads)} \quad (2\text{-}26)$$

$$H_{2(ads)} \rightleftarrows H_{2(g)} \quad (2\text{-}27)$$

$$H_{2(ads)} \rightleftarrows 2H^*_{(ox)} \quad (2\text{-}28)$$

in which Fe_{vac} is a vacant iron ion site, $\oplus$ is an electron defect and H* is the hydrogen dissolved in the oxide.

At the inner interface, (2), the iron oxide is thought to dissociate and an oxide ion appears as adsorbed species. The permeating hydrogen permits these adsorbed species to react to form the carrier gas for oxygen transport in the void.

$$FeO + Fe_{vac} + 2\oplus \rightleftarrows Fe^{2+} + O^{2-} \quad (2\text{-}29)$$

$$2H^*_{(ox)} \rightleftarrows H_{2(ads)} \quad (2\text{-}30)$$

$$H_{2(ads)} \rightleftarrows H_{2(gas)} \quad (2\text{-}31)$$

$$H_{2(ads)} + O^{2-}_{(ads)} \longrightarrow H_2O_{(g)} + 2e^- \quad (2\text{-}32)$$

Succeeding wustite layers of the outer scale are generated in this atmosphere by the reaction as defined for the interfaces (1) and (2). Thus, reactions similar to those at interface (1) also happen at interface (3). Within the inner scale, the composition of the spinel phase also has some small changes,

$$FeCr_2O_4 + 4FeO \longrightarrow 2Fe_2CrO_4 + Fe^{2+} + 2e^- \quad (2\text{-}33)$$

2.5.2 Volatilization of $Fe(OH)_2$

Surman and Castle [104] suggested a mechanism based on the volatilization of $Fe(OH)_2$ to explain the acceleration oxidation of steel in atmosphere containing water vapor. There are three possible rate-determining steps during the oxidation:

a) The outward diffusion of iron ions from the scale/alloy interface to the gas/scale surface;
b) The inward diffusion of oxygen ions from the gas/scale surface to the scale/alloy interface;
c) Vapor-phase diffusion of $Fe(OH)_2$ from the scale/alloy interface to the gas/scale interface.

They assumed the following reaction at each interface:

At scale/alloy interface,

$$Fe_{(s)} + 2H_2O_{(g)} \rightarrow Fe(OH)_{2(g)} + H_{2(g)} \quad (2\text{-}34)$$

$$3Fe_{(s)} + 4H_2O_{(g)} \rightarrow Fe_3O_{4(s)} + 4H_{2(g)} \quad (2\text{-}35)$$

At gas/scale surfae,

$$Fe(OH)_{2(g)} \rightarrow Fe_3O_{4(s)} + 2H_2O_{(g)} + H_{2(g)} \qquad (2\text{-}36)$$

2.5.3 Formation of microcracks and microchannels

Based on the study that Fe-15Cr oxidized in oxygen with different concentration of water vapor at 900-1000 ℃, Shen Jianian [105] proposed a mechanism to explain the occurrence of breakaway oxidation. During the oxidation, void and microcracks can be generated in the scale by outward diffusion of chromium. Moreover, due to the deformation of the oxide scale, microchannels are formed. These microcracks and microchannels allow H_2O molecules to transport to the alloy/oxide interface and to react with the alloy. Since the Cr depleted at the alloy surface, formation of Fe_2O_3 takes place and H_2 is released:

$$3H_2O_{(g)} + 2Fe_{(s)} = Fe_2O_{3(s)} + 3H_{2(g)} \qquad (2\text{-}37)$$

The released H_2 can react with the Cr_2O_3 as shown in reaction below. Once the protective oxide scale is destroyed, rapid oxidation ensues.

$$3H_{2(g)} + Cr_2O_{3(s)} = 2Cr_{(s)} + 3H_2O_{(g)} \qquad (2\text{-}38)$$

In the reaction (2-38), more H_2O is generated and can accelerate the reaction (2-37). Meanwhile, formation of $FeCr_2O_4$ due to the reaction of Fe_2O_3 with Cr:

$$Fe_2O_{3(s)} + 4Cr_{(s)} + 5H_2O_{(g)} = 2FeCr_2O_{4(s)} + 5H_{2(g)} \qquad (2\text{-}39)$$

2.5.4 Entrance of H_2O into the oxide scale

J. Ehlers et al [83] studied 9%Cr ferritic steel at 650 ℃ in N_2-O_2-H_2O gas for 100h, and proposed an entrance of H_2O molecule into the oxide scale mechanism. They assumed that

H_2O molecule can enter the inside of oxide scale and achieve gas-oxide equilibrium. The lower oxygen potential inside the oxide scale can generate higher partial pressures of $Fe(OH)_2$ than scale/gas surface by the reactions:

$$Fe_3O_{4(s)} + 3H_2O_{(g)} = 3Fe(OH)_{2(g)} + \frac{1}{2}O_{2(g)} \qquad (2\text{-}40)$$

$$Fe_2O_{3(s)} + 2H_2O_{(g)} = 2Fe(OH)_{2(g)} + \frac{1}{2}O_{2(g)} \qquad (2\text{-}41)$$

The outward diffusion of OH^- will take place due to the $pFe(OH)_2$ gradient, as can be seen in Figure 2.18. At high oxygen pressures, the volatilizable $Fe(OH)_2$ is unstable and deposits as Fe_2O_3. They also suggested that the breakaway oxidation is not controlled by the level of water vapor, but the ratio H_2O/O_2 ratio in the atmosphere.

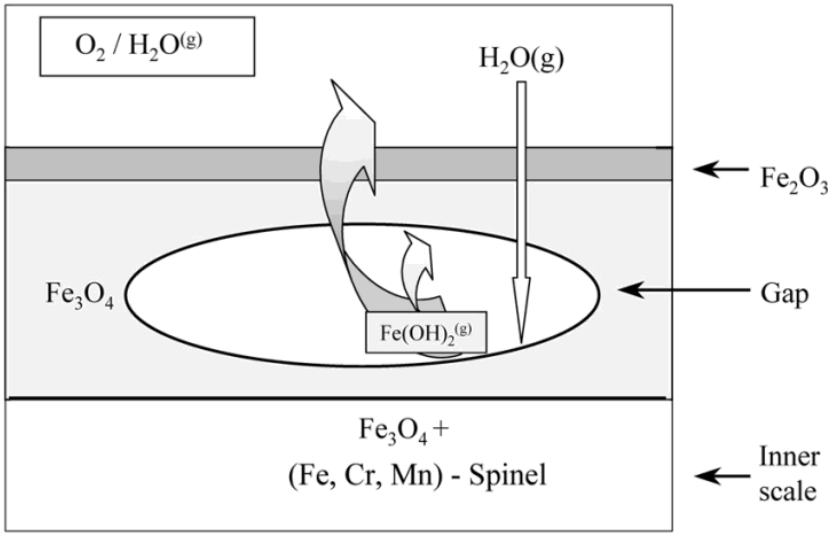

Figure 2.18 Schematic illustration of gas phase transport within the scale mechanism [83]

2.5.5 Volatilization of $CrO_2(OH)_2$

Cr-containing species evaporation is an important high temperature corrosion effect. At high temperature, CrO_3, $CrO_2(OH)$ and $CrO_2(OH)_2$ are the major volatile species in circumstance

containing water vapor. The evaporation reactions are given as below:

$$2Cr_2O_{3(s)} + 3O_{2(g)} = 4CrO_{3(g)} \quad (2\text{-}42)$$

$$Cr_2O_{3(s)} + H_2O_{(g)} + O_{2(g)} = 2CrO_2(OH)_{(g)} \quad (2\text{-}43)$$

$$Cr_2O_{3(s)} + 2H_2O_{(g)} + \frac{3}{2}O_{2(g)} = 2CrO_2(OH)_{(g)} \quad (2\text{-}44)$$

However, CrO_3 is not stable in the atmosphere containing water vapor, because it can react with H_2O to form $CrO_2(OH)_2$. For $CrO_2(OH)$, this specie was proved to be much less stable than the $CrO_2(OH)_2$ [106]. Based on the oxidation experiment of 304 steel in the presence of water vapor and oxygen, Asteman et al [79, 107, 108] found that Cr is indeed vaporized during high temperature oxidation in the presence of water vapor and concluded that the specie is $CrO_2(OH)_2$. In recent years, lots of works [84, 87, 109-112] have been done to study the Cr-containing species evaporation effect on oxidation and found that the kinetic of evaporation is accelerated by the increase of gas flow velocity and the water vapor pressure.

2.6 Summary

In this chapter, we have introduced the principle of SOFC and the material requirement for the interconnector. The basic knowledge of high temperature oxidation of alloy is given in detail, such as the oxidation kinetics and the oxide formation mechanism. Different origins of the residual stress in the oxide scale generated during the isothermal oxidation and the cooling are discussed. A summary of oxidation behavior of Fe-Cr stainless steel is presented, and the high temperature oxidation mechanism of alloy in atmosphere containing water vapor proposed by different researchers are outlined.

According to the literature review, the chromia forming stainless steel is considered to be used

as interconnector for SOFC. Although lots of work have been done to learn the influence of water vapor on oxidation at high temperature in recent years, no consistent conclusion has formed until now. The residual stresses in the oxide scale are closely related to oxidation kinetics and the microstructure, it may also relate to the failure of the scale. Therefore, our study will mainly focus on oxidation behavior of Fe-Cr stainless steel and the residual stress level in oxide scale formed during the oxidation.

2.7 References

[1]. J. Larminie, A. Dicks, Fuel Cell Systems Explained 2nd ed., John Wiley & Sons Ltd, England, 2003.

[2]. J. Wu, X. Liu, Recent Development of SOFC Metallic Interconnect, J. Mater. Sci. Technol. 26 (2010) 293-305.

[3]. J.W. Fergus, Lanthanum chromite-based materials for solid oxide fuel cell interconnects, Solid State Ionics 171 (2004) 1-15.

[4]. T. Brylewski, M. Nanko, T. Maruyama, K. Przybylski, Application of Fe–16Cr ferritic alloy to interconnector for a solid oxide fuel cell, Solid State Ionics 143 (2001) 131-150.

[5]. S. Kakaç, A. Pramuanjaroenkij, X.Y. Zhou, A review of numerical modeling of solid oxide fuel cells, Int. J. Hydrogen. Energ 32 (2007) 761-786.

[6]. W.Z. Zhu, S.C. Deevi, Development of interconnect materials for solid oxide fuel cells, Mater. Sci. Eng. A 348 (2003) 227-243.

[7]. S. Fontana, R. Amendola, S. Chevalier, P. Piccardo, G. Caboche, M. Viviani, R. Molins, M. Sennour, Metallic interconnects for SOFC: Characterisation of corrosion resistance and conductivity evaluation at operating temperature of differently coated alloys, J. Power Sources 171 (2007) 652-662.

[8]. I. Antepara, I. Villarreal, L.M. Rodr ́guez-Mart ́nez, N. Lecanda, U. Castro, A. Laresgoiti, Evaluation of ferritic steels for use as interconnects and porous metal supports in IT-SOFCs, J. Power Sources 151 (2005) 103-107.

[9]. S. Geng, J. Zhu, Promising alloys for intermediate-temperature solid oxide fuel cell interconnect application, J. Power Sources 160 (2006) 1009-1016.

[10]. N. Birks, G.H. Meier, F.S. Pettit, Introduction to the high-temperature oxidation of metals, in, Cambridge University, UK, 2006.

[11]. L. Ge, Chromium Evaporation of Metallic Component Materials in Solid Oxide Fuel Cell (SOFC) (Doctoral Dissertation), in, University of Connecticut, 2014.

[12]. P.J. Bellina, High-temperature Oxidation of Bulk RuAl Alloy (Doctoral Dissertation), in, Universitat Stuttgart, 2006.

[13]. M.T. Hutchings, P.J. Withers, T.M. Holden, T. Lorentzen, Introduction to the characterization of residual stress by neutron diffraction, Taylor & Francis Group, U.S, 2005.

[14]. A. Saillard, Modeling and Simulation of Stress-induced Non-uniform Oxide Scale Growth During High-temperature Oxidation of Metallic Alloys (Doctoral Dissertation), in, Georgia Institute of Technology, 2010.

[15]. J. Mougin, A. Galerie, M. Dupeux, N. Rosman, G. Lucazeau, A.M. Huntz, L. Antoni, In-situ determination of growth and thermal stresses in chromia scales formed on a ferritic stainless steel, Materials and Corrosion 53 (2002) 486-490.

[16]. F.N. Rhines, J.S. Wolf, The role of oxide microstructure and growth stresses in the high-temperature scaling of nickel, Metall. Trans. 1 (1970) 1701-1710.

[17]. B. Pieraggi, R.A. Rapp, Stress generation and vacancy annihilation during scale growth limited by cation-vacancy diffusion, Acta Metallurgica 36 (1988) 1281-1289.

[18]. A.M. Huntz, C. Liu, M. Kornmeier, J.L. Lebrun, The determination of stresses during oxidation of Ni: in situ measurements by XRD at high temperature, Corros. Sci. 35 (1993) 989-997.

[19]. A.M. Huntz, Stresses in NiO, Cr_2O_3 and Al_2O_3 oxide scales, Mater. Sci. Eng. A 201 (1995) 211-228.

[20]. S.J. Bull, Modeling of residual stress in oxide scales, Oxid. Met. 49 (1998) 1-17.

[21]. V.K. Tolpygo, D.R. Clarke, Determination of the growth stress and strain in α-Al2O3 scales during the oxidation of Fe-22Cr-4.8Al-0.3Y alloy, Oxid. Met. 49 (1998) 187-212.

[22]. J. Mougin, N.l. Rosman, G. Lucazeau, A. Galerie, In situ Raman monitoring of chromium oxide scale growth for stress determination, Journal of Raman Spectroscopy 32 (2001) 739-744.

[23]. D.R. Clarke, Stress generation during high-temperature oxidation of metallic alloys, Curr. Opin. Solid State Mater. Sci. 6 (2002) 237-244.

[24]. S. Chevalier, C. Valot, G. Bonnet, J.C. Colson, J.P. Larpin, The reactive element effect on thermally grown chromia scale residual stress, Mater. Sci. Eng. A 343 (2003) 257-264.

[25]. D.R. Clarke, The lateral growth strain accompanying the formation of a thermally grown oxide, Acta Mater. 51 (2003) 1393-1407.

[26]. P.R. Guduru, E. Chason, L.B. Freund, Mechanics of compressive stress evolution during thin film growth, Journal of the Mechanics and Physics of Solids 51 (2003) 2127-2148.

[27]. R. Krishnamurthy, D.J. Srolovitz, Stress distributions in growing oxide films, Acta Mater. 51 (2003) 2171-2190.

[28]. A.M. Limarga, D.S. Wilkinson, G.C. Weatherly, Modeling of oxidation-induced growth stresses, Scripta Mater. 50 (2004) 1475-1479.

[29]. B. Panicaud, J.L. Grosseau-Poussard, J.F. Dinhut, On the growth strain origin and stress evolution prediction during oxidation of metals, Appl. Surf. Sci. 252 (2006) 5700-5713.

[30]. B. Panicaud, J.L. Grosseau-Poussard, P. Girault, J.F. Dinhut, D. Thiaudi ère, Comparison of growth stress measurements with modelling in thin iron oxide films, Appl. Surf. Sci. 252 (2006) 8414-8420.

[31]. A.M. Huntz, P.Y. Hou, R. Molins, Study by deflection of the influence of alloy composition on the development of stresses during alumina scale growth, Mater. Sci. Eng. A 485 (2008) 99-107.

[32]. H. Zhou, J. Qu, M. Cherkaoui, Stress–oxidation interaction in selective oxidation of Cr–Fe alloys, Mechanics of Materials 42 (2010) 63-71.

[33]. J.L. Ruan, Y. Pei, D. Fang, Residual stress analysis in the oxide scale/metal substrate system due to oxidation growth strain and creep deformation, Acta Mechanica 223 (2012)

2597-2607.

[34]. H.-M. Tung, J.F. Stubbins, Incipient oxidation kinetics and residual stress of the oxide scale grown on Haynes 230 at high temperatures, Mater. Sci. Eng. A 538 (2012) 1-6.

[35]. H.-M. Tung, J.F. Stubbins, Incipient oxidation kinetics of alloy 617 and residual stress of the oxide scale formed in air at temperatures between 850 and 1000 ℃, Journal of Nuclear Materials 424 (2012) 23-28.

[36]. J.K. Odusote, L.A. Cornish, L.H. Chown, R.M. Erasmus, Determination of residual stress in alumina scale by photostimulated Cr3+ luminescence piezospectroscopy, Corros. Sci. 70 (2013) 276-284.

[37]. D.M. Lipkin, D.R. Clarke, Measurement of the stress in oxide scales formed by oxidation of alumina-forming alloys, Oxid. Met. 45 (1996) 267-280.

[38]. D.J. Srolovitz, T.A. Ramanarayanan, An elastic analysis of growth stresses during oxidation, Oxid. Met. 22 (1984) 133-146.

[39]. E. Schumann, C. Sarioglu, J.R. Blachere, F.S. Pettit, G.H. Meier, High-Temperature Stress Measurements During the Oxidation of NiAl, Oxid. Met. 53 (2000) 259-272.

[40]. H.J. Yearian, E.C. Randell, T.A. Longo, The structure of oxide scales on chromium steels, NACE International 12 (1956) 11.

[41]. A. Atkinson, Transport processes during the growth of oxide films at elevated temperature, Rev. Mod. Phys. 57 (1985) 437-470.

[42]. V.R. Howes, Observations of the metal oxide interface for a Fe-Cr alloy, Corros. Sci. 8 (1968) 221-224.

[43]. V.R. Howes, The early growth of oxide on a Fe-Cr alloy, Corros. Sci. 7 (1967) 735-746.

[44]. Z. Suo, D.V. Kubair, A.G. Evans, D.R. Clarke, V.K. Tolpygo, Stresses induced in alloys by selective oxidation, Acta Mater. 51 (2003) 959-974.

[45]. V.K. Tolpygo, D.R. Clarke, Wrinkling of α-alumina films grown by thermal oxidation—I. Quantitative studies on single crystals of Fe–Cr–Al alloy, Acta Mater. 46 (1998) 5153-5166.

[46]. B.R. Barnard, T.R. Watkins, P.K. Liaw, An Evaluation of the Use of X-ray Residual Stress Determination as a Means of Characterizing Oxidation Damage of Nickel-Based, Cr2O3-Forming Superalloys Subjected to Various Oxidizing Conditions, Oxid. Met. 74 (2010) 305-318.

[47]. J. Xiao, N. Prud'homme, N. Li, V. Ji, Influence of humidity on high temperature oxidation of Inconel 600 alloy: Oxide layers and residual stress study, Appl. Surf. Sci. 284 (2013) 446-452.

[48]. M. Kemdehoundja, J.F. Dinhut, J.L. Grosseau-Poussard, M. Jeannin, High temperature oxidation of Ni70Cr30 alloy: Determination of oxidation kinetics and stress evolution in chromia layers by Raman spectroscopy, Mater. Sci. Eng. A 435-436 (2006) 666-671.

[49]. A. Galerie, F. Toscan, M. Dupeux, J. Mougin, G. Lucazeau, C. Valot, A.M. Huntz, L. Antoni, Stress and adhesion of chromia-rich scales on ferritic stainless steels in relation

with spallation, Materials Research 7 (2004) 81-88.

[50]. M. Hajduga, J. Kučera, Primary stage of Fe-Cr-C alloy oxidation at 1100 ℃, Oxid. Met. 29 (1988) 121-133.

[51]. Y. Ikeda, K. Nii, Microcrack generation and its healing in the oxide scale formed on Fe-Cr alloys, Oxid. Met. 12 (1978) 487-502.

[52]. K. Kuroda, P.A. Labun, G. Welsch, T.E. Mitchell, Oxide-formation characteristics in the early stages of oxidation of Fe and Fe-Cr alloys, Oxid. Met. 19 (1983) 117-127.

[53]. I.G. Crouch, J.C. Scully, Selective oxidation of Fe-Cr alloys, Oxid. Met. 15 (1981) 101-135.

[54]. D.L. Douglass, F. Rizzo-Assuncao, The oxidation of Fe-19.6Cr-15.1Mn stainless steel, Oxid. Met. 29 (1988) 271-287.

[55]. S. Suzuki, T. Kosaka, H. Inoue, M. Isshiki, Y. Waseda, Effect of the surface segregation of chromium on oxidation of high-purity Fe Cr alloys at room temperature, Appl. Surf. Sci. 103 (1996) 495-502.

[56]. I. Saeki, T. Saito, R. Furuichi, H. Konno, T. Nakamura, K. Mabuchi, M. Itoh, Growth process of protective oxides formed on type 304 and 430 stainless steels at 1273 k, Corros. Sci. 40 (1998) 1295-1302.

[57]. Y. Zhao, Oxidation Behavior of Ferritic Alloys as Interconnect of Solid Oxide Fuel Cell (SOFC) (Doctoral Dissertation) in, Auburn University, 2012.

[58]. G.C. Wood, The oxidation of iron-chromium alloys and stainless steels at high temperatures, Corros. Sci. 2 (1962) 173-196.

[59]. G.C. Wood, T. Hodgkiess, D.P. Whittle, A comparison of the scaling behaviour of pure iron-chromium and nickel-chromium alloys in oxygen, Corros. Sci. 6 (1966) 129-147.

[60]. G.H. Meier, K. Jung, N. Mu, N.M. Yanar, F.S. Pettit, J. Pirón Abellán, T. Olszewski, L. Nieto Hierro, W.J. Quadakkers, G.R. Holcomb, Effect of Alloy Composition and Exposure Conditions on the Selective Oxidation Behavior of Ferritic Fe–Cr and Fe–Cr–X Alloys, Oxid. Met. 74 (2010) 319-340.

[61]. R.A. Rapp, The transition from internal to external oxidation and the formation of interruption bands in silver-indium alloys, Acta Metallurgica 9 (1961) 730-741.

[62]. F. GESMUNDO, F. VIANI, Transition from internal to external oxidation for binary alloys in the presence of an outer scale, Springer, Heidelberg, ALLEMAGNE, 1986.

[63]. H. Kurokawa, Oxidation behavior of Fe–16Cr alloy interconnect for SOFC under hydrogen potential gradient, Solid State Ionics 168 (2004) 13-21.

[64]. A.L. Marasco, D.J. Young, The oxidation of Iron-Chromium-Manganese alloys at 900 ℃, Oxid. Met. 36 (1991) 157-174.

[65]. I. Saeki, H. Konno, R. Furuichi, Initial oxidation of type 430 stainless steels with 0.09–0.9 Mn in O2-N2 atmosphere at 1273 K, Corros. Sci. 38 (1996) 1595-1612.

[66]. B. Hua, Y. Kong, W. Zhang, J. Pu, B. Chi, L. Jian, The effect of Mn on the oxidation behavior and electrical conductivity of Fe–17Cr alloys in solid oxide fuel cell cathode

atmosphere, J. Power Sources 196 (2011) 7627-7638.

[67]. D.E. Alman, P.D. Jablonski, Effect of minor elements and a Ce surface treatment on the oxidation behavior of an Fe–22Cr–0.5Mn (Crofer 22 APU) ferritic stainless steel, Int. J. Hydrogen. Energ 32 (2007) 3743-3753.

[68]. P.A. Tempest, R.K. Wild, Thickness measurements of spinel and chromia layers in stainless steel oxide scales by X-ray diffractometry, Oxid. Met. 17 (1982) 345-357.

[69]. P.A. Tempest, R.K. Wild, Formation and growth of spinel and Cr_2O_3 oxides on 20% Cr-25% Ni-Nb stainless steel in CO_2 environments, Oxid. Met. 23 (1985) 207-235.

[70]. Y. Wouters, G. Bamba, A. Galerie, M. Mermoux, J.P. Petit, Oxygen and Water Vapour Oxidation of 15Cr Ferritic Stainless Steels with Different Silicon Contents, Materials Science Forum 461-464 (2004) 839-848.

[71]. H.E. Evans, D.A. Hilton, R.A. Holm, S.J. Webster, Influence of silicon additions on the oxidation resistance of a stainless steel, Oxid. Met. 19 (1983) 1-18.

[72]. M.P. Brady, J.R. Keiser, K.L. More, M. Fayek, L.R. Walker, R.A. Peascoe-Meisner, L.M. Anovitz, D.J. Wesolowski, D.R. Cole, Comparison of Short-Term Oxidation Behavior of Model and Commercial Chromia-Forming Ferritic Stainless Steels in Dry and Wet Air, Oxid. Met. 78 (2012) 1-16.

[73]. G.C. Wood, J.A. Richardson, M.G. Hobby, J. Boustead, The identification of thin healing layers at the base of oxide scales on FeCr base alloys, Corros. Sci. 9 (1969) 659-671.

[74]. C. Lowell, Cyclic and isothermal oxidation behavior on some Ni-Cr alloys, Oxid. Met. 7 (1973) 95-115.

[75]. P. Kofstad, High temperature corrosion, Elsevier, Essex, England, 1988.

[76]. C.T. Fujii, R.A. Meussner, The mechanism of the high-temperature oxidation of iron-chromium alloys in water vapor J. Electrochem. Soc. 111 (1964) 1215-1221.

[77]. A. Galerie, Y. Wouters, M. Caillet, The Kinetic Behaviour of Metals in Water Vapour at High Temperatures: Can General Rules Be Proposed?, Materials Science Forum 369-372 (2001) 231-238.

[78]. L. Mikkelsen, S. Linderoth, High temperature oxidation of Fe–Cr alloy in O2–H2–H2O atmospheres; microstructure and kinetics, Mater. Sci. Eng. A 361 (2003) 198-212.

[79]. H. Asteman, J.E. Svensson, L.G. Johansson, Effect of Water-Vapor-Induced Cr Vaporization on the Oxidation of Austenitic Stainless Steels at 700 and 900 ℃, J. Electrochem. Soc. 151 (2004) B141.

[80]. D. Laverde, T. Gómez-Acebo, F. Castro, Continuous and cyclic oxidation of T91 ferritic steel under steam, Corros. Sci. 46 (2004) 613-631.

[81]. Z. Yang, G. Xia, P. Singh, J.W. Stevenson, Effects of water vapor on oxidation behavior of ferritic stainless steels under solid oxide fuel cell interconnect exposure conditions, Solid State Ionics 176 (2005) 1495-1503.

[82]. S.-Y. Cheng, S.-L. Kuan, W.-T. Tsai, Effect of water vapor on annealing scale formation

on 316 SS, Corros. Sci. 48 (2006) 634-649.

[83]. J. Ehlers, D.J. Young, E.J. Smaardijk, A.K. Tyagi, H.J. Penkalla, L. Singheiser, W.J. Quadakkers, Enhanced oxidation of the 9%Cr steel P91 in water vapour containing environments, Corros. Sci. 48 (2006) 3428-3454.

[84]. D.J. Young, B.A. Pint, Chromium volatilization rates from Cr_2O_3 scales into flowing gases containing water vapor, Oxid. Met. 66 (2006) 137-153.

[85]. G. Bamba, Y. Wouters, A. Galerie, G. Borchardt, S. Shimada, O. Heintz, S. Chevalier, Inverse growth transport in thermal chromia scales on Fe–15Cr steels in oxygen and in water vapour and its effect on scale adhesion, Scripta Mater. 57 (2007) 671-674.

[86]. H. Götlind, F. Liu, J.E. Svensson, M. Halvarsson, L.G. Johansson, The Effect of Water Vapor on the Initial Stages of Oxidation of the FeCrAl Alloy Kanthal AF at 900 ℃, Oxid. Met. 67 (2007) 251-266.

[87]. M. Stanislowski, E. Wessel, K. Hilpert, T. Markus, L. Singheiser, Chromium Vaporization from High-Temperature Alloys, J. Electrochem. Soc. 154 (2007) A295.

[88]. N.K. Othman, N. Othman, J. Zhang, D.J. Young, Effects of water vapour on isothermal oxidation of chromia-forming alloys in Ar/O2 and Ar/H2 atmospheres, Corros. Sci. 51 (2009) 3039-3049.

[89]. N.K. Othman, J. Zhang, D.J. Young, Temperature and water vapour effects on the cyclic oxidation behaviour of Fe–Cr alloys, Corros. Sci. 52 (2010) 2827-2836.

[90]. B. Pujilaksono, T. Jonsson, M. Halvarsson, J.-E. Svensson, L.-G. Johansson, Oxidation of iron at 400–600 ℃ in dry and wet O2, Corros. Sci. 52 (2010) 1560-1569.

[91]. L. Xing, Y. Zheng, L. Cui, M. Sun, M. Shao, G. Lu, Influence of water vapor on the oxidation behavior of aluminized coatings under low oxygen partial pressure, Corros. Sci. 53 (2011) 3978-3982.

[92]. H. Li, J. Zhang, D.J. Young, Oxidation of Fe–Si, Fe–Al and Fe–Si–Al alloys in CO2–H2O gas at 800 ℃, Corros. Sci. 54 (2012) 127-138.

[93]. L. Liu, Z.G. Yang, C. Zhang, M. Ueda, K. Kawamura, T. Maruyama, Effect of water vapour on the oxidation of Fe–13Cr–5Ni martensitic alloy at 973K, Corros. Sci. 60 (2012) 90-97.

[94]. A. Srisrual, S. Coindeau, A. Galerie, J.P. Petit, Y. Wouters, Identification by photoelectrochemistry of oxide phases grown during the initial stages of thermal oxidation of AISI 441 ferritic stainless steel in air or in water vapour, Corros. Sci. 51 (2009) 562-568.

[95]. C.W. Tuck, M. Odgers, K. Sachs, The oxidation of iron at 950 ℃ in oxygen/water vapour mixtures, Corros. Sci. 9 (1969) 271-285.

[96]. I. Kvernes, M. Oliveira, P. Kofstad, High temperature oxidation of Fe-13Cr-xAl alloys in air H_2O vapour mixtures, Corros. Sci. 17 (1977) 237-252.

[97]. H.E. Evans, A.T. Donaldson, T.C. Gilmour, Mechanisms of Breakaway Oxidation and Application to a Chromia-Forming Steel, Oxid. Met. 52 (1999) 379-402.

[98]. S. Chevalier, J. Favergeon, French Activity on High Temperature Corrosion in Water Vapor Trans Tech Publications Ltd, Switzerland 2014.

[99]. A. Zeller, F. Dettenwanger, M. Schütze, Influence of water vapour on the oxidation behaviour of titanium aluminides, Intermetallics. 10 (2002) 59-72.

[100]. J.R. Regina, J.N. DuPont, A.R. Marder, The Effect of Water Vapor on Passive-Layer Stability and Corrosion Behavior of Fe–Al–Cr Base Alloys, Oxid. Met. 61 (2004) 69-90.

[101]. R. Peraldi, B.A. Pint, Effect of Cr and Ni Contents on the Oxidation Behavior of Ferritic and Austenitic Model Alloys in Air with Water Vapor, Oxid. Met. 61 (2004) 463-483.

[102]. A. Yamauchi, K. Kurokawa, H. Takahashi, Evaporation of Cr_2O_3 in Atmospheres Containing H_2O, Oxid. Met. 59 (2003) 517-527.

[103]. D. Kim, C. Jang, W. Ryu, Oxidation Characteristics and Oxide Layer Evolution of Alloy 617 and Haynes 230 at 900 ℃ and 1100 ℃, Oxid. Met. 71 (2009) 271-293.

[104]. P.L. Surman, J.E. Castle, Gas phase transport in the oxidation of Fe and steel, Corros. Sci. 9 (1969) 771-777.

[105]. S. Jianian, Z. Longjiang, L. Tiefan, High-temperature oxidation of Fe-Cr alloys in wet oxygen, Oxid. Met. 48 (1997) 347-356.

[106]. Ø. Espelid, K.J. Børve, V.R. Jensen, Structure and Thermodynamics of Gaseous Oxides, Hydroxides, and Mixed Oxohydroxides of Chromium: CrOm(OH)n(m,n= 0−2) and CrO3. A Computational Study, The Journal of Physical Chemistry A 102 (1998) 10414-10423.

[107]. H. Asteman, J.E. Svensson, L.G. Johansson, Evidence for Chromium Evaporation Influencing the Oxidation of 304L: The Effect of Temperature and Flow Rate, Oxid. Met. 57 (2002) 193-216.

[108]. H. Asteman, J.E. Svensson, L.G. Johansson, Oxidation of 310 steel in H2O/O2 mixtures at 600 ℃: the effect of water-vapour-enhanced chromium evaporation, Corros. Sci. 44 (2002) 2635-2649.

[109]. G.R. Holcomb, Calculation of Reactive-evaporation Rates of Chromia, Oxid. Met. 69 (2008) 163-180.

[110]. P.J. Meschter, E.J. Opila, N.S. Jacobson, Water Vapor–Mediated Volatilization of High-Temperature Materials, Annual Review of Materials Research 43 (2013) 559-588.

[111]. R. Sachitanand, M. Sattari, J.-E. Svensson, J. Froitzheim, Evaluation of the oxidation and Cr evaporation properties of selected FeCr alloys used as SOFC interconnects, Int. J. Hydrogen. Energ 38 (2013) 15328-15334.

[112]. H. Taimatsu, Kinetic Analysis of High-Temperature Oxidation of Metals Accompanied by Scale Volatilization, J. Electrochem. Soc. 146 (1999) 3686.

CHAPTER 3 Experimental

In this chapter, we will present the studied material, sample surfaces preparation method, different techniques and experimental apparatus used in this study, such as thermogravimetric analysis (TGA), the scanning electron microscope with field emission gun (SEM-FEG), the X-ray diffraction (XRD), the secondary ion mass spectroscopy (SIMS), X-ray photoelectron spectroscopy (XPS), atomic force microscope (AFM), and the stress analysis techniques by X-ray diffraction and by in-situ deflection.

The used experimental conditions (oxidation temperature, duration, percentage of humidity and flow rate) will be given in details.

3.1 Material and specimen preparation

The AISI 430 ferritic stainless steel used in this study was supplied by PX Precimet SA as sheets with a thickness of 1.5mm, and the chemical composition is given in Table 3.1. It has a relatively homogeneous microstructure and the average grain size is about 20-30 μm.

Table 3.1 Chemical composition of AISI 430 stainless steel (weight %)

Fe	Cr	Mn	Si	P	S	C
Bal.	16-18	< 1.00	< 1.00	< 0.04	< 0.03	< 0.08

All high temperature oxidation experiments were carried out on surface polished samples. Before oxidation, the samples were cut into a dimension of 10mm x 10mm x 1mm by cutting machine ESCIL-ESC 250 GTL, and a 0.8 mm hole was drilled near an edge of the samples to hang them by Platinum cricket for the thermal gravimetric analysis (TGA). The sensibility of the caliper gauge used to measure the dimension of the sample is 0.02mm. All 6 surfaces of

the samples were ground to 1200-grit by SiC paper and polished by silicon solution. Then the samples were ultrasonically washed by ethanol and dried by compressed nitrogen. Each sample dimensions were measured by a digital caliper. The purpose of all these steps is to have the same initial surface state to make comparisons between different samples after oxidation.

3.2 Thermogravimetric analysis

Thermogravimetric analysis (TGA) is a device that could continuously measure the mass gain of the sample as a function of oxidation duration at a given temperature by an automatic recording balance. With this analysis, many details come to light that are concealed by other analyses. For example, as shown in Figure 3.1, sudden weight loss indicates spalling of some oxides layer during the oxidation; slow reduction in oxidation rate is due to the oxide scale separated from the scale/metal interface; small increase in the rate of weight gain indicates cracking of the oxide scale. The correct explanation of weight change curve requires patience but is worthwhile.

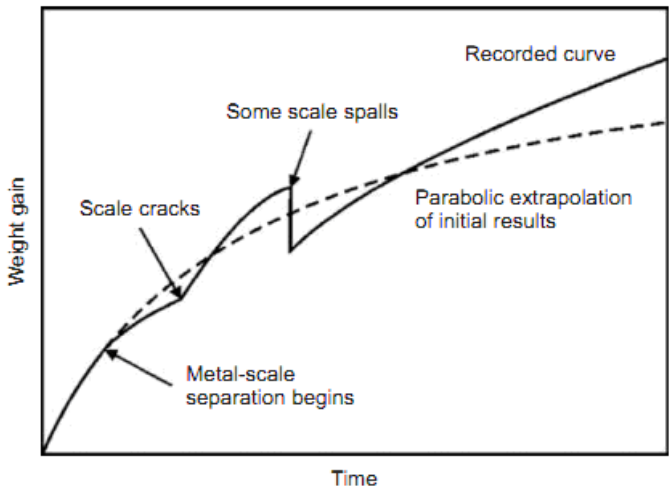

Figure 3.1 Possible feature that would be revealed by TGA [10]

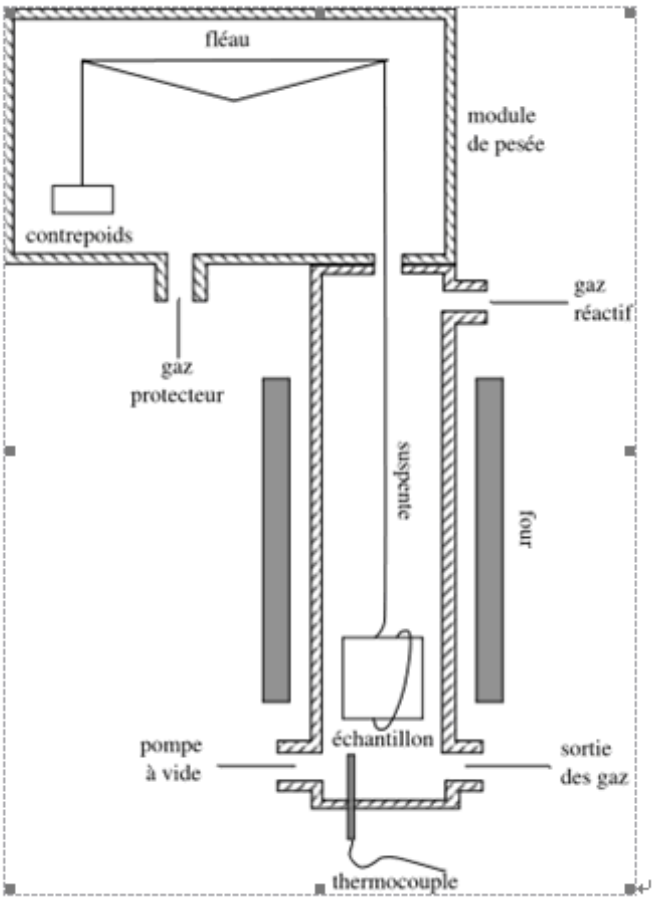

Figure 3.2 Schematic of TGA used in this study [113]

In order to measure the weight change of samples during the oxidation, SETARAM TGA 92-16.18 was used to perform the oxidation experiments (see Figure 3.2) in this study, and the precision of TGA analysis is more than 10^{-6} g. Our oxidation experiments were performed at 700℃, 800℃ and 900℃ under artificial air (O_2=20%, N_2=80%, H_2O＜3ppm, CO_2＜1ppm,CO＜1ppm, total CnHm＜100ppm) with different absolute humidity (0-10%) for more than 96 hours. The regulation of absolute humidity is realized by using a vapor generator (SETARAM D/WETSYS-2F) and the sensibility of regulation is about 1.5% in relative humidity. For ensuring the reliability of the experiments, every oxidation conditions have been conducted at least 2 times and the results were reproducible. A total of 160 samples were used in this study.

3.3 X-ray diffraction (XRD) phase analysis

To identify the oxide phases formed on the AISI 430 alloy during the oxidation, XRD analysis was carried out on PANALYTICAL X'PERT MRD PRO. This is a high resolution system, and a phase in the sample can be detected if its volume percentage is bigger than 1%. The XRD studies were performed using Cu-Kα (λ=0.154 nm) radiation under 45kV and 40mA. The diffraction patterns were obtained in the 2θ range of 20-120 °with a step size of 0.01 °and 5 sec/step. Comparing the peak matching with standard JCPDS, the oxide phases formed on the substrate can be identified. To obtain sufficient peak intensity for the relatively thin oxide layer, 0.5 ° and 2 ° Grazing Incidence X-ray diffraction (GIXRD) was performed, and the penetration depth are 0.3μm and 1μm, relatively.

3.4 Scanning electron microscopy (SEM)

The field emission scanning electron microscope (FEG-SEM) is a technique that is capable of producing high resolution image of sample surface. Scanning the sample's surface with a beam of electrons will generate some signals due to electron-sample interactions. These signals contain some important information of the surface, such as morphology and chemical composition. Generally, SEM imaging was also accompanied by the use of energy dispersive X-ray spectroscopy (EDX) and EDX elemental map. EDX elemental map creates an elemental image of the conventional SEM image. A region where an element is abundant will correspond to a bright area in the EDX elemental map and vice versa. This creates a distribution of the main elements throughout the oxide layer but can also be used by zooming on a special feature and determining its chemical composition.

In our study, the surface morphology images were obtained by using FEG-SEM (ZEISS SUPRA 55VP) with EDX. After surface observation, the samples for cross-section analysis

were embedded in epoxy resin and polished to 1μm. The EDX analysis is performed to analyze the chemical characterization of the oxides. For most elements, the sensitivity of the EDX analysis is of the order of 1000 ppm. EDX elemental map of the oxide scale has also been taken.

3.5 Atomic force microscope (AFM)

The atomic force microscope is one kind of high resolution technique to get surface image and other information from the sample. The advantage of this technique is that it can give images from any kind of samples. The schematic of principle of AFM is given in Figure 3.3. A sharp tip is in close contact with the sample surface. When the tip scans over the surface, the tip-surface distance can be recorded. Thus, the surface topography can be obtained.

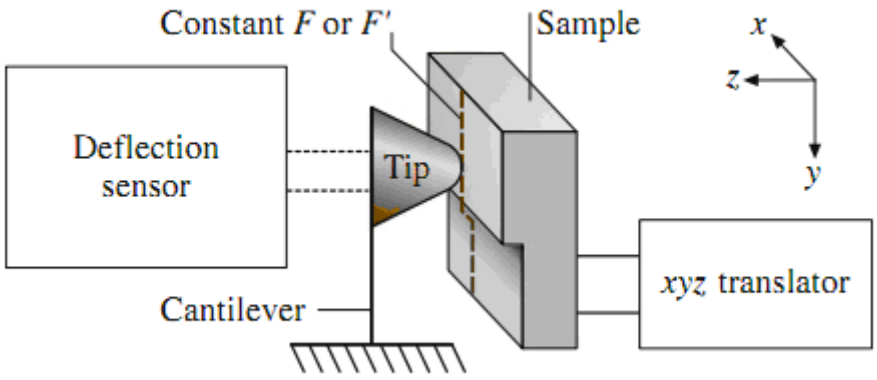

Figure 3.3 Principle of operation of the AFM [114]

In this study, the surface topography of the oxidized samples was measured by AFM (Dimension Icon, Bruker Corporation, Germany) in the tapping mode at the Northwest Institute for Non-ferrous Metal Research in China.

3.6 Oxidation with $^{18}O_2$

An oxidation furnace (see Figure 3.4) which is capable of heating to 1400 ° and has an $^{18}O_2$

recovery system in particular is available for $^{18}O_2$ oxidation experiment at SP2M/ICMMO. For better understanding the oxidation mechanism of AISI 430 in air, one- and two-stage oxidation experiments were carried out at 700 ℃, 800 ℃ and 900 ℃. The samples were first oxidized under synthetic air ($^{16}O_2$) for 6 hours to obtain an oxide scale. Then the oxidized samples were placed in the oxidation furnace for a second oxidation under pure $^{18}O_2$ for 3 hour. With the use of SIMS technique, the atomic diffusion characteristic of oxygen can be studied because the SIMS can make difference between ions diffusion profile of ^{16}O and ^{18}O as a function of surface depth.

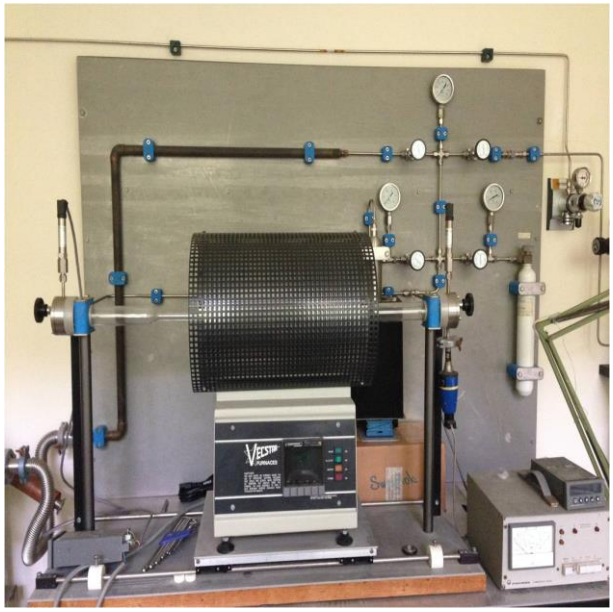

Figure 3.4 Image of oxidation furnace with $^{18}O_2$ in SP2M/ICMMO

3.7 Secondary Ion Mass Spectrometry (SIMS)

SIMS analysis is a destructive surface analytic technique. In this analysis, the surface is bombarded with a primary ion beam, and secondary ions can be ejected from the surface. With a mass spectrometer, these secondary ions are extracted and analyzed to identify the elemental and composition of the surface. Generally, the depth of this analysis is about a few μm. The schematic of SIMS principle is given in Figure 3.5. Depth information of the sample

can be provided by continuous detection of the secondary ions by SIMS. SIMS is not quantitative analysis, and there is no simple a priori relationship between concentration of a given mass and peak intensity.

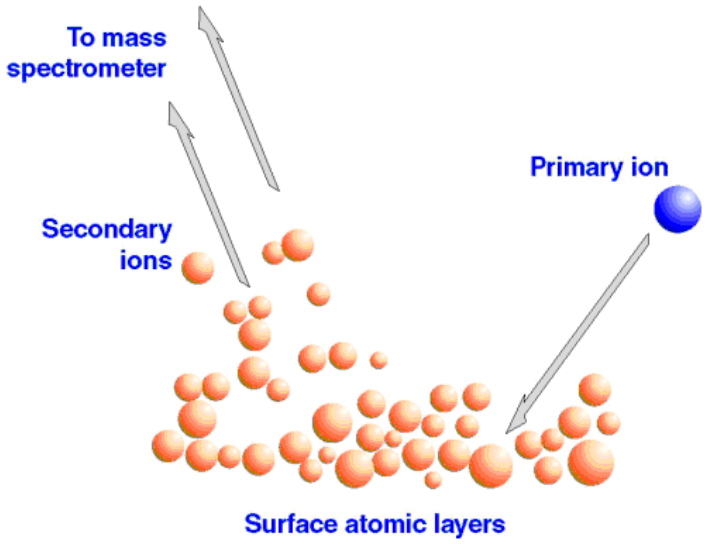

Figure 3.5 Schematic of principle of SIMS [115]

In this study, the SIMS analyses were conducted with a Cameca IMS 4F SIMS instrument at the GEMAC laboratory of the University Versailles. The samples after one-stage in $^{16}O_2$ and two-stage oxidation in $^{18}O_2$ were sputtered using a cesium primary ion beam accelerated at 15 KeV. The scanned area was 150μm×150μm, and the diameter of analyzed zone was 33μm. The profile of the atomic distribution of ^{18}O as a function of depth has been obtained for the samples oxidized with $^{18}O_2$. The sensibility of the ion detection is about 0.1ppm [115].

3.8 X-ray photoelectron spectroscopy (XPS)

X-Ray Photoelectron Spectroscopy (XPS) is a broadly used surface analysis technique used to determine the chemical information of the sample surface, such as elemental composition, chemical state and electronic state of the elements within a material.

The operating principle of XPS is the photoelectric effect which occurs when an electron is emitted from the outer 1-10 nm of the analyzed surface after being exposed to a photon whose energy exceeds a critical value. When incident X-ray hits the surface, the energy of incident photons (hν) can transfer to surface electrons. If the energy of the photons are bigger than the binding energy of the electrons and the electrons have enough energy to overcome the work function (Φ) of the solid, they can leave the solid (Figure 3.6).

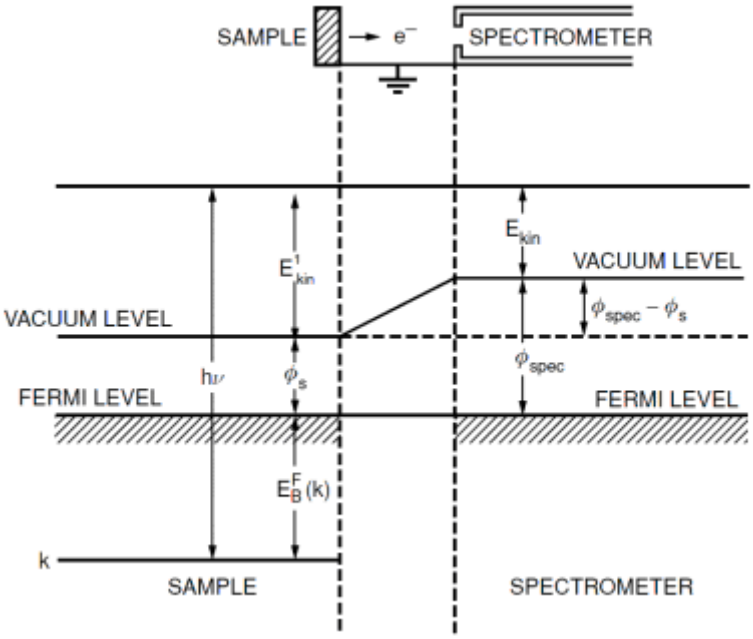

Figure 3.6 Schematic representation of the photoemission [116]

Due to the emission of the electron, the inner shell of the atom (A) is ionized. The energy conservation requires:

$$E(A) + h\nu = E(A^*) + E_{kin} + \Phi \qquad (3\text{-}1)$$

$$E_{kin} = h\nu - [E(A^*) - E(A)] - \Phi = h\upsilon - E_B - \Phi \qquad (3\text{-}2)$$

in which E_B is the binding energy relative to the Fermi level E_F and E_{kin} is the kinetic energy of the photoelectron (relative to the vacuum level E_V). The photoelectron spectrum is given by the kinetic energy distribution of the photoelectron measured with an electron analyzer. For

known photon energy (hν) the binding energy can be determinate for all core electrons with $E_B < h\nu - \Phi$, see Equation (3-2). The disadvantage of XPS is that it cannot be used to detect hydrogen and helium in the sample.

To get the distribution of OH^- as a function of oxide scale depth in this study, XPS analysis was carried out with a K-ALPHA spectrometer from ThermoFisher, equipped with a monochromatic X-ray Source (AlKα, 1486.6 eV). The depth profile was performed by etching the samples with a scanning with 1 keV argon-ion beam on a 1 x 2 mm^2 area (Figure 3.7）. Etching and data acquisition were done sequentially. All samples studied as a part of this study were determined to contain small amounts of adventitious C. The binding energies were determined with respect to the C-(C,H) component of the C 1s peak of carbon fixed at 284.8 eV. The spectra were acquired using the Avantage software by manufacturer. XPSpeak4.1 peak fitting software was used to analyze the data. The detection limit of this method is about 1 at%.

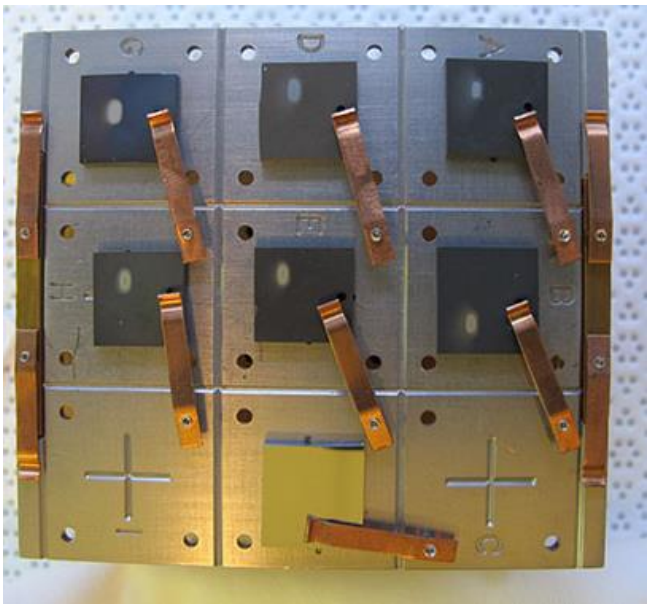

Figure 3.7 Image of samples after XPS etching

3.9 Determination of residual stresses

Over the last few decades, attempts have been made to determine residual stress in the oxide scale, and the measurement techniques can be divided into X-ray diffraction method, Raman spectroscopy and mechanical methods.

3.9.1 By XRD method

The most accurate technique to determine the residual stresses is the one that can directly measure the strain in the oxide lattice. The strain in the oxide layer can be measured by X-Ray diffraction, which is a non-destructive technology to determine the residual stresses in the surface of samples. As we all known, the elastic deformation of a sample will change the inter-planar spacing from it unstressed value d_0. The changes of d could lead to a shift in the diffraction pattern. The inter-planar spacing of the diffraction planes can be obtained by Bragg's law:

$$2d_{hkl} \cdot \sin\theta = n\lambda \qquad (3\text{-}3)$$

in which n: a positive integer

λ: wavelength

d_{hkl}: the inter- planar spacing of planes (hkl)

θ: the scattering angle.

Once the inter-planar spacing, d, is obtained from the position of the diffraction peak for a given plane, the strain expressed as:

$$\varepsilon = \frac{d-d_0}{d_0} = \frac{\sin\theta_0}{\sin\theta} - 1 = -\cot\theta_0 \times \Delta\theta \qquad (3\text{-}4)$$

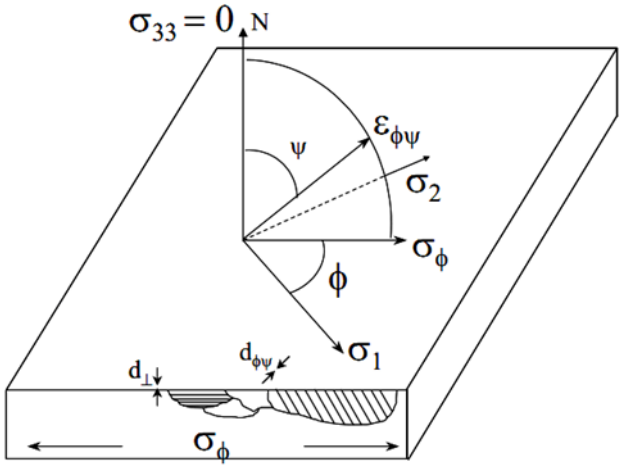

Figure 3.8 Schematic showing diffraction planes parallel to the surface and at an angle ϕΨ

By changing the tilt of the sample within the diffractometer, measurements of planes at an angle ψ can be made (see Figure 3.8) and the strains along that direction can be calculated using

$$\varepsilon_{\Psi} = \frac{d_{\phi\Psi} - d_0}{d_0} \qquad (3\text{-}5)$$

Assuming a state of plane stress exists (σz=0) and the stresses are biaxial, then the ratio of the transverse to longitudinal strains is Poisson's ratio, ν;

$$\varepsilon_x = \varepsilon_y = -\upsilon\varepsilon_z = \frac{-\upsilon\sigma_y}{E} \qquad (3\text{-}6)$$

If we assume that at the surface of the material σ_z=0, then

$$\varepsilon_z = -\upsilon(\varepsilon_x + \varepsilon_y) = \frac{-\upsilon}{E}(\sigma_x + \sigma_y) \qquad (3\text{-}7)$$

Thus combining equation (3-4) and (3-7)

$$\frac{d - d_0}{d_0} = \frac{-\upsilon}{E}(\sigma_x + \sigma_y) \qquad (3\text{-}8)$$

Equation (3-8) applies to a general case, where only the sum of the principal stresses can be obtained, and the precise value of d_0 is still required. We wish to determine stress acting in

some direction in the surface σ_ϕ. Elasticity theory for isotropic solid shows that the strain along an inclined line is

$$\varepsilon_{\phi\Psi} = \frac{1+\upsilon}{E}(\sigma_1 cos^2\phi + \sigma_2 sin^2\phi)sin^2\Psi - \frac{\upsilon}{E}(\sigma_1 + \sigma_2) \qquad (3\text{-}9)$$

If we consider the strains in terms of inter-planar spacing, and use the strains to evaluate the stresses, then it can be shown that

$$\sigma_\phi = \frac{E}{(1+\upsilon)sin^2\Psi}\left(\frac{d_\Psi - d_n}{d_n}\right) \qquad (3\text{-}10)$$

This equation allows us to calculate the stress in any chosen direction from the inter-planar spacing determined from two measurements, made in a plane normal to the surface and containing the direction of the stress to be measured.

The most commonly used method for stresses determination is the $sin^2\psi$ method. A number of XRD measurements are made at different Psi angle. The inter-planar spacing or 2-theta peak position is measured and plotted as a curve. The stress then can be calculated from such a plot by calculating the gradient of the line and with basic knowledge of the elastic properties of the materials.

Many metallic samples strongly absorb X-rays, and the depth of penetration is governed by the linear absorption coefficient of the material for the radiation. Therefore, the majority of the diffracted beam originates from the outer surface of the samples, the X-ray penetration is extremely shallow (<10 μm in metallic alloys).

In this study, European standard NF EN 15305 (version of April 2009) [117] has been applied to measure the residual stresses levels in different oxide layers and in the alloy. There are two requirements for selecting the diffraction condition: the Bragg angle should be as high as

possible to ensure the accuracy of peak shifting measurement and must have sufficient intensity to have good statistic of diffraction peak definition. In our experiments, a high resolution configuration XRD system (Panalytical X'Pert MRD Pro) was used, whatever the relative low of 2θ, the determined peak position error is smaller than 0.005 ° in 2θ. For each selected plane family, more than 13 peaks with different Psi angles (varying from -60 ° to 60 °) are recorded. The calculation of the residual stress was performed via X'Pert Stress software. The precision for stress determination is about 30 MPa under our experimental conditions.

3.9.2 By deflection method

Thin rectangular samples are usually used for deflection method, and the length of sample is far greater than its width and thickness. A protective layer needs to be prepared on one surface before experiment. The other surface will generate a bend during the oxidation and a corresponding deflection which can be recorded. This method allows us to determine in situ growth stresses during the oxidation. The relation between the stress and the deflection can be given as:

$$\sigma_f = D\frac{E_m}{1-\nu_m^2}\frac{e_m^2}{3e_f L^2} \qquad (3\text{-}11)$$

in which L is the length of the sample, E is the Young's modulus, ν is the Poisson's ratio and e is the thickness. The subscript m and f represent the metal and oxide scale, respectively. This method is just suitable for qualitative and semi-quantitative analysis.

The in situ stresses were determined by deflection method. The deflection apparatus (Figure3.9) is composed of a high temperature furnace and a CCD camera coupled to a computer [31, 118, 119]. There is a hole in the front side of the furnace to observe the sample which is attached to an alumina rod by a screw inside the furnace. There is also a hole at the right side of the furnace to improve the brightness inside the furnace if the light intensity is

not sufficient.

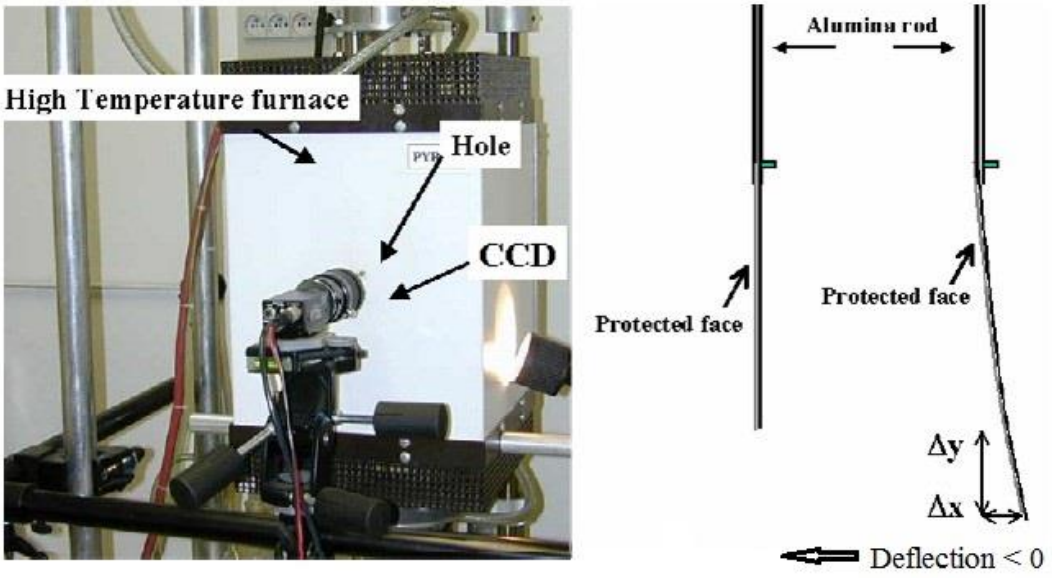

Figure 3.9 Deflection apparatus and principle

All of the AISI 430 samples used in this study were cut to a 45 mm×10 mm ×0.2 mm blade, and oxidized in air at 920℃ for 6 hours followed by furnace cooling. A protective Cr_2O_3 oxide scale was formed on both sides of the samples. For curvature experiment, one of the main faces of the samples was carefully polished mechanically, while keeping the other main face as a protective scale against further oxidation. The asymmetrical sample is then introduced in the furnace for a second oxidation. After this operation, the images collected by the camera are available on the computer, and the tip of the sample was been measured by ImageJ software. With these measurements of curvature (Δx) and elongation (Δy), we can calculate the growth stress by the Equation (3-11). The precision of curvature measurement is more than 5μm and the corresponding error for growth stress determination is less than 50 MPa.

3.10 References

[10]. N. Birks, G.H. Meier, F.S. Pettit, Introduction to the high-temperature oxidation of metals, in, Cambridge University, UK, 2006.

[31]. A.M. Huntz, P.Y. Hou, R. Molins, Study by deflection of the influence of alloy composition on the development of stresses during alumina scale growth, Mater. Sci. Eng. A 485 (2008) 99-107.

[113]. J. Xiao, Etude du comportement et de contraintes résiduelles de l'Inconel 600 oxydé sous air humide (Doctoral Dissertation), in, Université Paris-Sud, 2014.

[114]. G. Binnig, C.F. Quate, C. Gerber, Atomic Force Microscope, Phys. Rev. Lett. 56 (1986) 930-933.

[115]. P. Bertrand, W. Lu-Tao, Time-of-Flight Secondary Ion Mass Spectrometry (ToF-SIMS), in: D. Benoit, J.-F. Bresse, L. Van't dack, H. Werner, J. Wernisch (Eds.) Microbeam and Nanobeam Analysis, Springer Vienna, 1996 pp. 167-182.

[116]. J. Andrade, X-ray Photoelectron Spectroscopy (XPS), in: J. Andrade (Ed.) Surface and Interfacial Aspects of Biomedical Polymers, Springer US, 1985 pp. 105-195.

[117]. Test Method for Residual Stresses Analysis by X-ray diffraction, in: European Standard no NF15305, 2009.

[118]. A.M. Huntz, P.Y. Hou, R. Molins, Study by deflection of the oxygen pressure influence on the phase transformation in alumina thin films formed by oxidation of Fe3Al, Mater. Sci. Eng. A 467 (2007) 59-70.

[119]. A.M. Huntz, L. Maréchal, B. Lesage, R. Molins, Thermal expansion coefficient of alumina films developed by oxidation of a FeCrAl alloy determined by a deflection technique, Appl. Surf. Sci. 252 (2006) 7781-7787.

CHAPTER 4 The Study of the Oxidation Behavior of AISI 430 Stainless Steel

As we discussed in chapter 2, SOFC is a promising electrochemical energy conversion device, and chromia forming Fe-Cr stainless steel is proposed to be used as interconnector for it in recent years. Water vapor, one of the products of SOFC, has adverse effect on the oxidation resistance at high temperature. Some works have been done, and several possible mechanisms have been proposed by different researchers to explain the effect of water vapor on high temperature oxidation behavior of alloy. Till now, however, there is no consistent conclusion about this problem. In this chapter, we want to study the effect of water vapor on oxidation behavior of AISI 430 stainless steel at 700℃, 800℃ and 900℃ with different absolute humidity (from 0% to 10%). The oxidation experiments were carried out in ICMMO/SP2M. The oxidation kinetics was studied, and surface morphology and cross section were observed.

4.1 Oxidation of AISI 430 stainless steel in dry air

To better understand how water vapor influences the oxidation behavior of AISI 430 stainless steel, the oxidation mechanism of this alloy in dry air has been studied firstly.

4.1.1 Oxidation kinetics

Figure 4.1 shows the mass gain curves as a function of isothermal oxidation duration at 700^{o}C, 800^{o}C and 900^{o}C in dry air for 96h. Also shown is the total gain after oxidation for 96 hours, the weight gain after oxidation are 0.0426 mg/cm^2, 0.2204 mg/cm^2, and 0.8929 mg/cm^2 for 700^{o}C, 800^{o}C and 900^{o}C, respectively. The weight gain increases rapidly at 900℃, and slowly at 700℃ and 800℃. With the increasing of the oxidation temperature from 700℃ to 900℃,

the oxidation rates increase obviously.

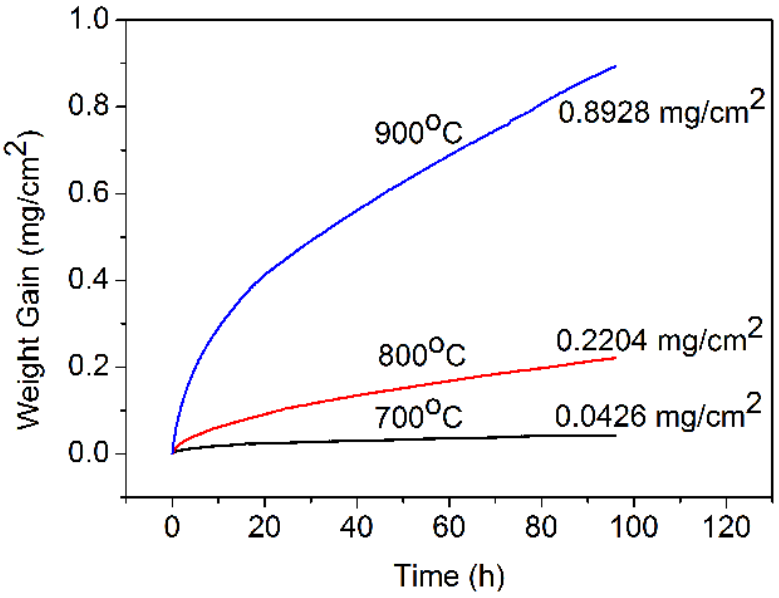

Figure 4.1 Weight gain curves of AISI 430 steel during exposure in dry air for 96h at 700°C, 800°C and 900°C

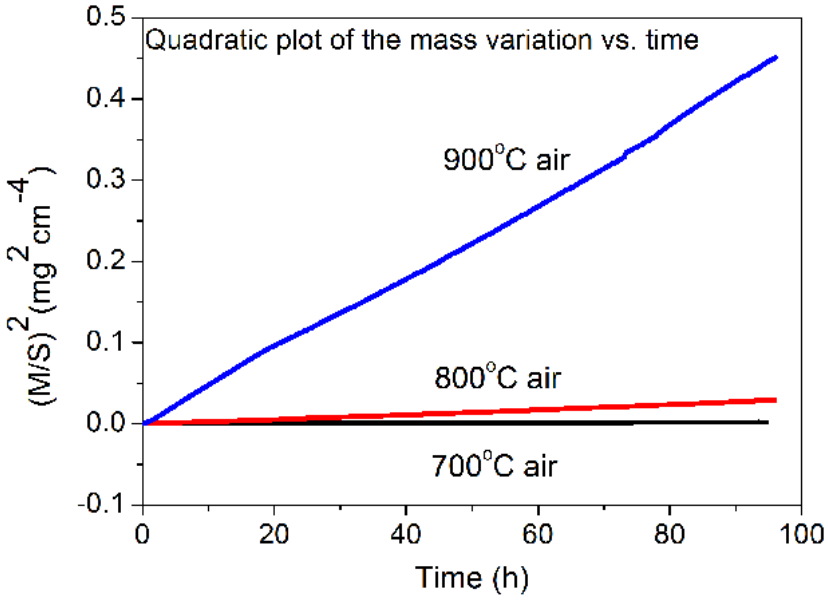

Figure 4.2 Quadratic plot of the mass variation as a function of oxidation time during exposure in dry air at 700°C, 800°C and 900°C

Figure 4.2 is quadratic plot of the mass variation as a function of oxidation time after oxidation in dry air. It is clear that all the three curves are linear, indicating that the oxidation rates obey a parabolic law at all studied temperatures [10]:

$$(\Delta M/S)^2 = k_p t \qquad (4\text{-}1)$$

where ΔM is the weight change, S is the surface area of the sample, k_p is the parabolic rate constant and t is the oxidation time. The parabolic rate constants calculated from the kinetic curves are listed in Table 4.1. According to Wagner's theory, a parabolic oxidation rate indicates the formation of a protective scale acting as a diffusion barrier and the oxidation kinetics is controlled by ions diffusion through the oxide scale [75]. The increasing thickness of oxide scale leads to an increasing transport distance for the reactants, thus smaller driving force for the diffusion of species. Therefore, as the oxidation duration increases, the oxidation rate decreases.

Table 4.1 Parabolic rate constants calculated for the samples after oxidation in dry air

Temperature	k_p ($g^2cm^{-4}s^{-1}$)
700°C	5.251×10^{-15}
800°C	1.4055×10^{-13}
900°C	2.3064×10^{-12}

The parabolic rate constant k_p can be related to the activation energy Q by Arrhenius equation

$$k_p = k_0 \exp(\frac{-Q}{RT}) \qquad (4\text{-}2)$$

where k_o is the pre-exponential factor, R is the universal gas constant and T is absolute temperature. The activation energy Q can be evaluated by taking logarithm for both sides of Equation (4-2):

$$\ln k_p = \ln k_0 - \frac{Q}{R}\left(\frac{1}{T}\right) \qquad (4\text{-}3)$$

The evolution of k_p with the oxidation temperatures can be plotted in an Arrhenius graph using to determine the oxidation activation energy. Figure 4.3 shows a linear relationship between log k_p and 1/T at different oxidation temperature, and the activation energy is 279.9 kJ/mol which is comparable to that obtained by M. Palcut et al for the formation of Cr_2O_3. [120].

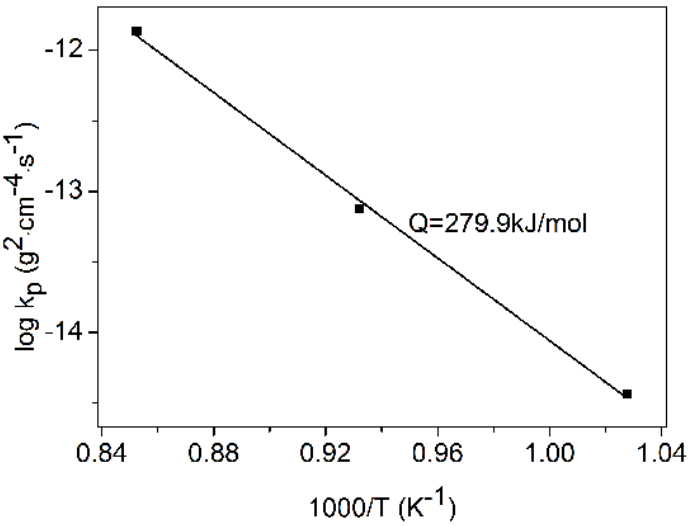

Figure 4.3 Log k_p of AISI 430 as a function of (1000/T) at 700°C, 800°C and 900°C in dry air

4.1.2 Structure of the oxide scale

The scale composition was studied at room temperature by XRD after oxidized at 700 ℃, 800 ℃ and 900 ℃. Figure 4.4 shows the XRD pattern of AISI 430 stainless steel oxidized in dry air for 96h at 900°C, which indicates the formation of Cr_2O_3 (JCPDS 38-1479) and spinel-type $Mn_{1.5}Cr_{1.5}O_4$ (JCPDS 33-0892) on the alloy surface. Since the oxide scale is very thin, the oxides peak intensities are relatively low. In order to get higher intensities, 0.5 ° and 2 ° grazing incidence XRD were performed. Figure 4.5 shows diffraction patterns obtained by 2 ° incidence angle XRD for the oxide formed on AISI 430 alloy in dry air at 700 ℃, 800 ℃ and 900 ℃ for 96h. It is clear that the oxide scales are mainly composed of the same peaks after oxidized at various temperatures: Cr_2O_3, $Mn_{1.5}Cr_{1.5}O_4$ and substrate peaks. Although the

oxidation kinetic at these temperatures is different, the composition of the oxide scales is similar. Since the thickness of the oxide scale increases with the increasing of the oxidation temperature, the intensity of oxides peaks are different. The higher intensity of substrate at 700 ℃ is due to the oxide scale formed at that temperature is thinner than that formed at 800 ℃ and 900 ℃.

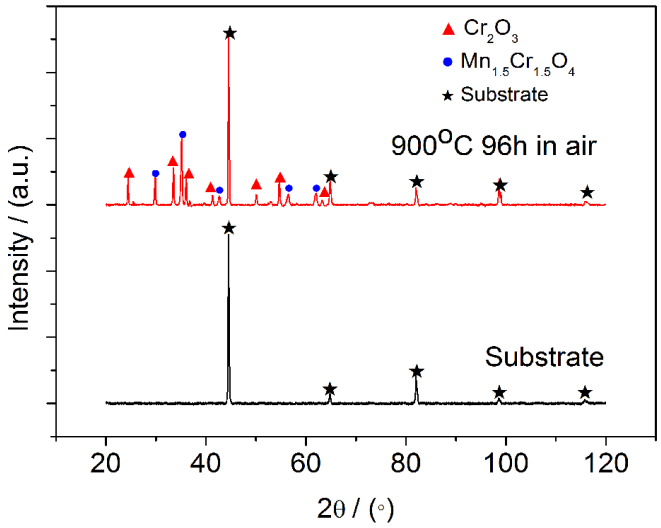

Figure 4.4 XRD patterns of AISI 430 before and after oxidation at 900 ℃ in dry air for 96h

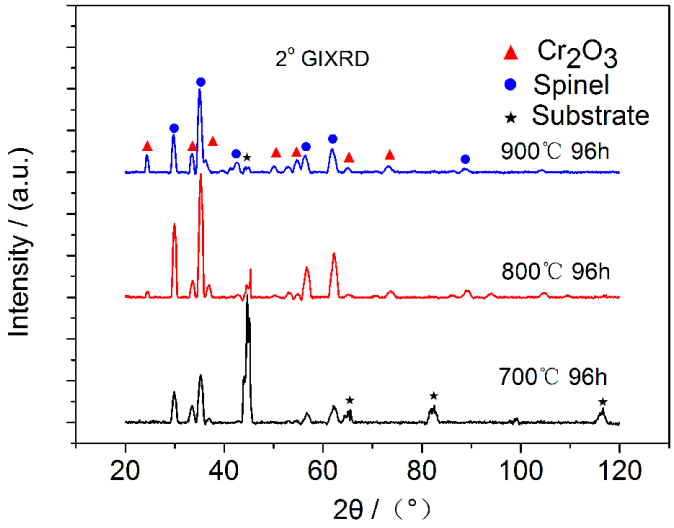

Figure 4.5 2 ℃GIXRD patterns of AISI 430 alloy after oxidation at 700 °, 800 ℃ and 900 ℃ in dry air for 96h

Figure 4.6 are the room temperature 2 °GIXRD patterns of the AISI 430 alloy oxidized in dry

air up to 96h at 700 °, 800 ℃ and 900 ℃, in which the diffraction patterns as a function of oxidation duration can be found. At 700 ℃ (Figure 4.6 (a)), only Cr_2O_3 type oxide formed within first 1h of oxidation, $Mn_{1.5}Cr_{1.5}O_4$ spinel oxide appeared in the oxide scale after 6h oxidation. With increasing of the oxidation temperature, the incubation time for the formation of spinel type oxide is shortened. Spinel type oxide was detected in the oxide scale after 0.5h and 1h oxidation at 800 ℃ and 900 ℃, respectively. As oxidation time prolonged, the oxides peaks intensities increased and the substrate intensities decreased at all of these three oxidation temperatures.

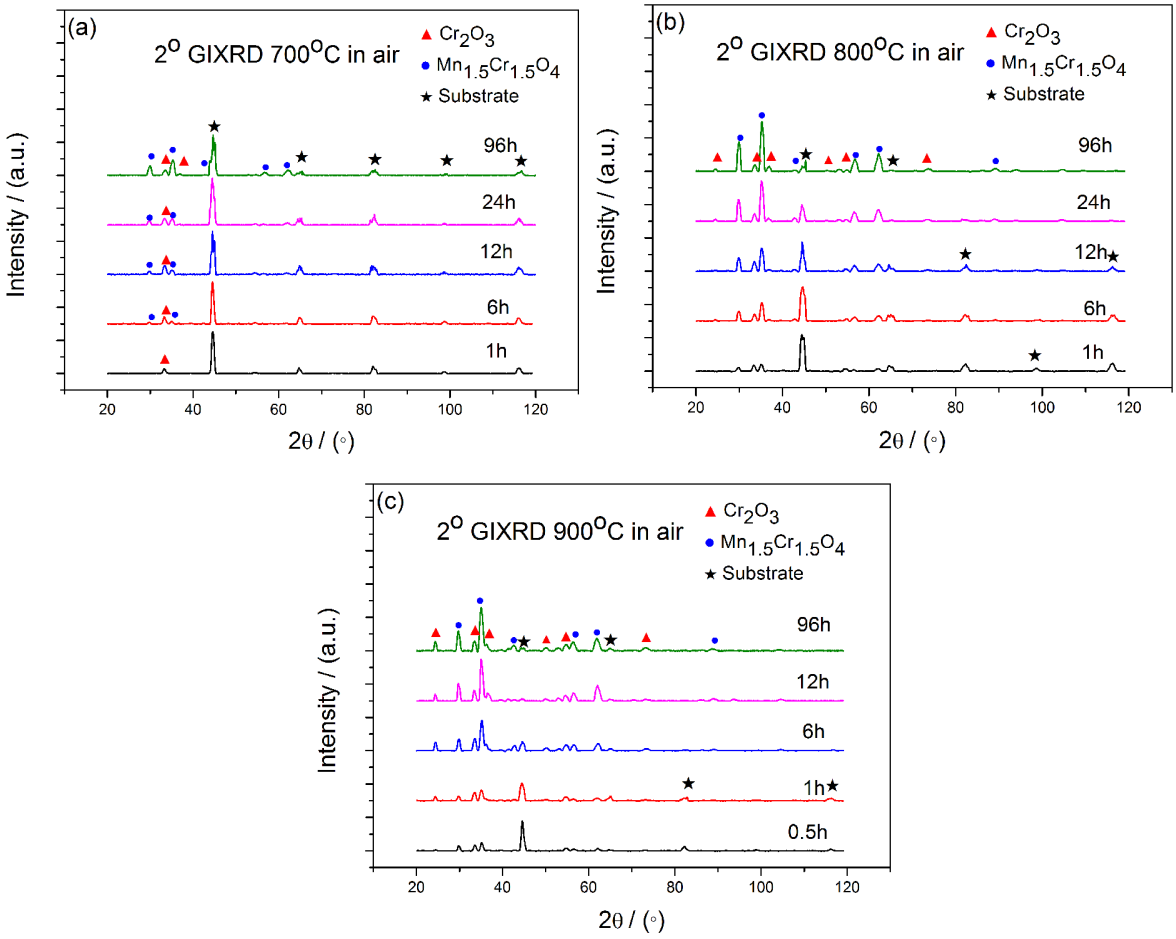

Figure 4.6 2 °GIXRD patterns of the AISI 430 alloy oxidized in dry air up to 96h at: (a) 700 ℃; (b) 800 ℃; (c) 900 ℃

Figure 4.7 shows room temperature 0.5°, 2° GIXRD and normal XRD pattern of AISI 430

after 48h oxidation at 900°C. In the 0.5° pattern, only spinel type oxide was detected. Along with this, Cr_2O_3 was detected in 2° and normal pattern, so we can assume that the spinel type oxide may be in the outer part of the oxide scale and the Cr_2O_3 is in the inner part of the scale. And there are no obvious texture effects, because all XRD intensities correspond to theoretical proportions.

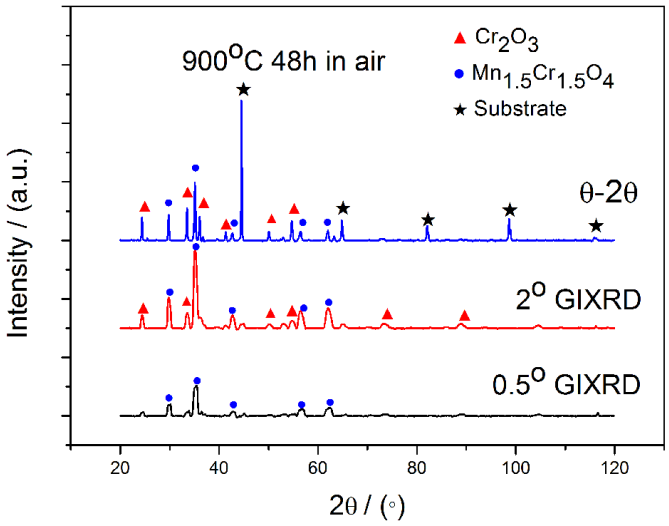

Figure 4.7 0.5 °, 2 °and normal XRD pattern of AISI 430 alloy after 48h oxidation in dry air at 900 ℃

4.1.3 Surface morphology of the oxide scale

Figure 4.8 displays the surface morphology of the oxide scale formed on the AISI 430 substrate after oxidation in dry air at 700 ℃, 800 ℃ and 900 ℃ for 12h. With the EDX analyses, we observed that the oxide scale is mainly consisted of Cr, Mn and oxygen, and little Fe was also detected. After oxidation at 700 ℃ for 12h, as shown in Figure 4.8 (a) and (b), some small octahedral grains formed on the surface, especially at the initial grain boundaries of the substrate. After oxidation at 800°C for 12h, as given in Figure 4.8 (c) and (d), there are bigger octahedral grains on the surface than that at 700°C. Figure 4.8 (e) and (f) show that the surface was nearly covered by the grains after oxidation at 900°C for 12h, and

the grains are nearly three times bigger than that formed at 700°C and 800°C. According to the XRD analysis and the crystal structure of spinel, it can be suggested that the octahedral grains are $Mn_{1.5}Cr_{1.5}O_4$ spinel phase.

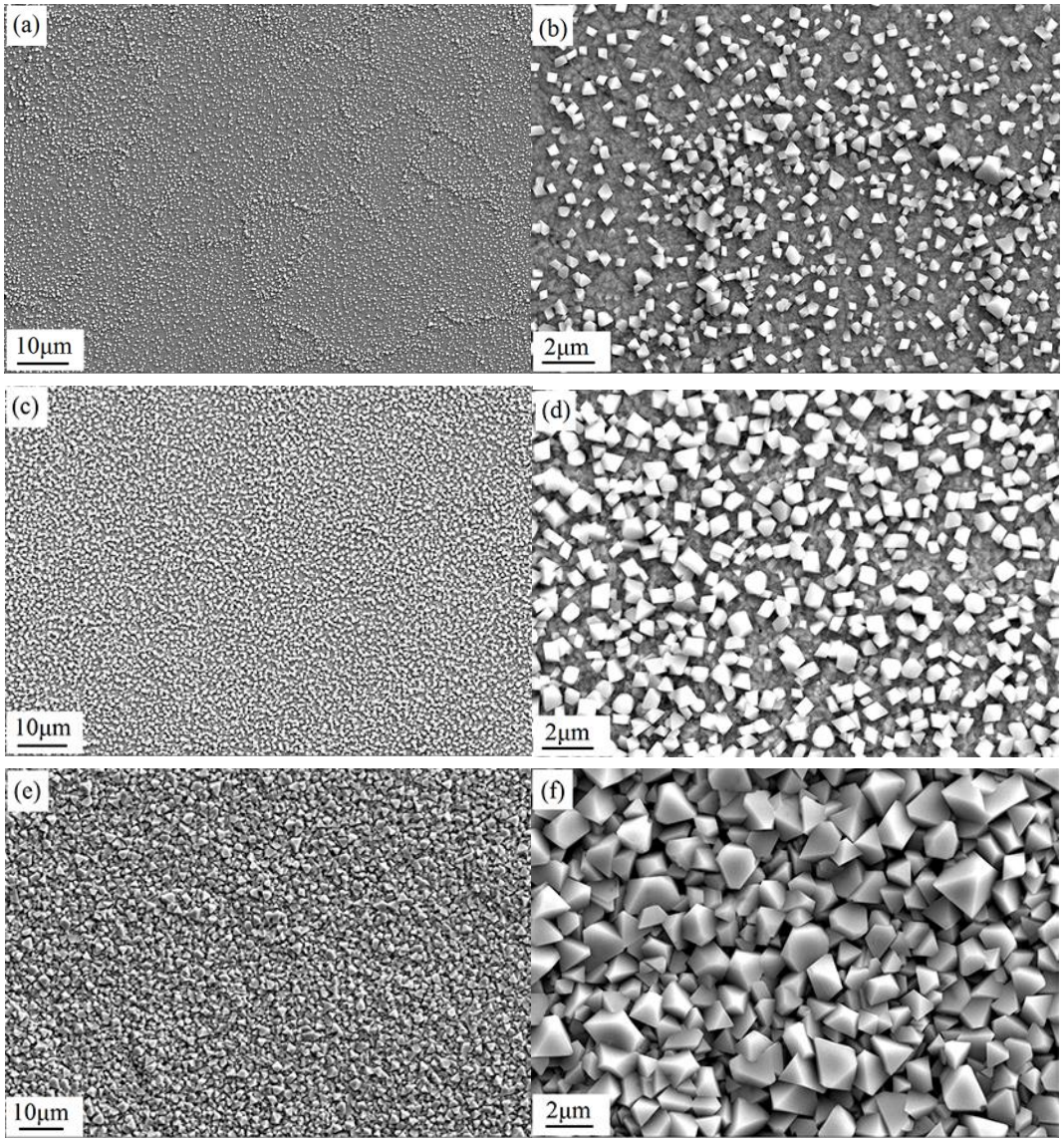

Figure 4.8 Surface morphology of oxide scale on the AISI 430 substrate after oxidation in dry for 12h at: 700 ℃ (a, b), 800 ℃ (c, d) and 900 ℃ (e, f)

At 700 ℃, more spinel oxides at the grain boundaries might relate with the formation of new oxides along alloy grain boundaries. The compositions of grain and gain boundary are compared by EDX analysis. 10 random points are measured and the atomic ratio of Mn to

(Cr+Mn) is given in Figure 4.9. It is clear that the Mn concentration at the grain boundaries is higher than that in grain. It can be explained by the faster diffusion rate of Mn ions along the grain boundary than that in the bulk [66, 121, 122].

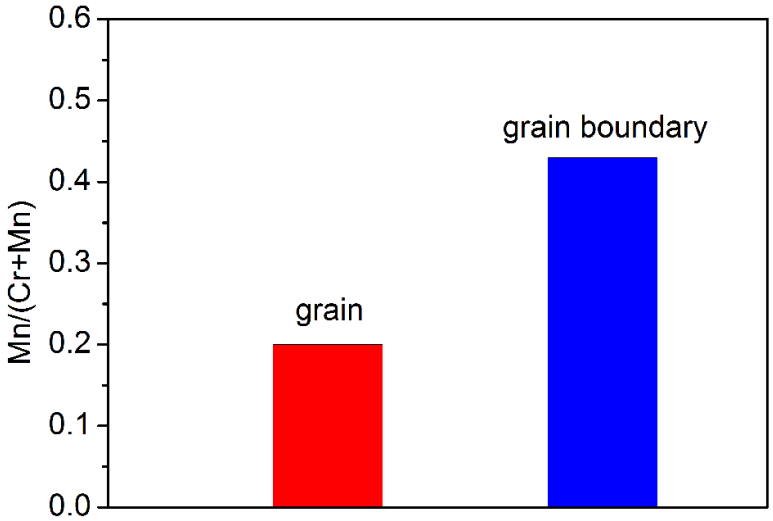

Figure 4.9 Atomic ratio of Mn to Cr+Mn at grain and grain boundary after 12h oxidation in dry air at 700 ℃

After oxidation in dry air for 24h at 900 ℃, the element distributions across the scale were displayed in Figure 4.10. It is clear that an irregular, dense and adherent oxide scale was formed on the substrate, and the thickness was something like 2 μm. The oxide thickness can be estimated from the weight gain during the oxidation. Assuming a dense and pure chromia scale formed, and the thickness of the scale, X, can be calculated by:

$$x = \frac{W_o M_{Cr_2O_3}}{3 M_o \rho_{Cr_2O_3}} \qquad (4\text{-}4)$$

in which W_o is total weight of O in the scale, M_o is atomic weigh of oxygen, $M_{Cr_2O_3}$ is the molecular weight of Cr_2O_3, and ρ is the density of chromia (5.21g/cm^3). Taking weight gain from Figure 4.1, the calculated X=2.08 μm, in good agreement with that in Figure 4.10. The EDX elemental mapping indicates inhomogeneous accumulation of Cr in the oxide scale, a

gradient of Mn concentration richer in outer part of the scale, and discontinuous distribution of Si at the scale/substrate interface. A very thin layer of iron was also found in the top of the surface.

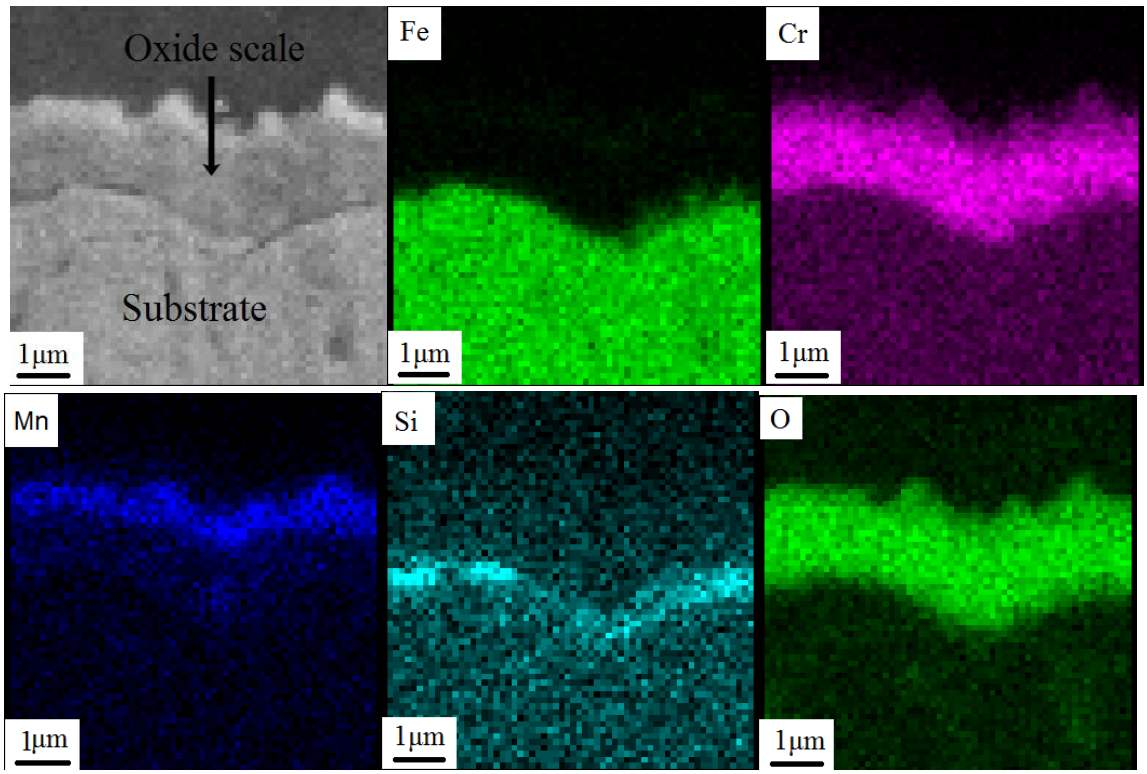

Figure 4.10 SEM image and corresponding EDX elemental mapping of the cross section of the AISI 430 oxidized in dry air at 900 ℃ for 24h

Observation of the cross section after oxidation at 900°C for 48h by FEG-SEM is given in Figure 4.11, and it shows clearly that the oxide scale consisted of two layers. With the EDX data and XRD analysis, we can conclude that the outer layer is $Mn_{1.5}Cr_{1.5}O_4$ (with little Fe incorporation) and the inner layer is Cr_2O_3. Moreover, formation of thin and discontinuous SiO_2 was also observed at the scale/substrate interface. Isolated voids were found at the scale/substrate interface, which may be result from outward diffusion of ions.

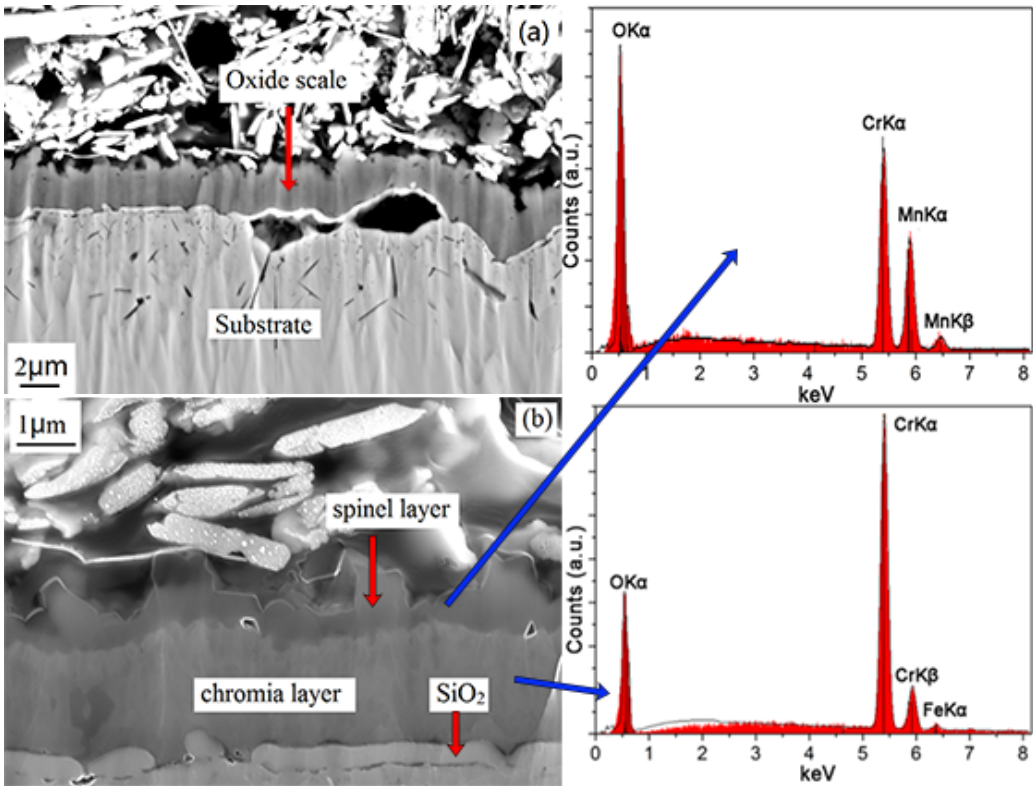

Figure 4.11 Cross section of the AISI 430 alloy oxidized in dry air at 900 ℃ for 48h and the corresponding EDX analysis

4.1.4 SIMS analysis

The principle of the two-stage oxidation experiments is: the alloy is oxidized first in air and then in an atmosphere enriched with isotope ^{18}O. When ^{18}O isotope is used in the second stage, the distribution of it as a function of scale depth can be obtained, from which we can infer the oxide scale growth mechanism. Figure 4.12 shows the typical profiles of the ^{18}O tracer after two-stage oxidation and the corresponding growth mechanisms [123-125].

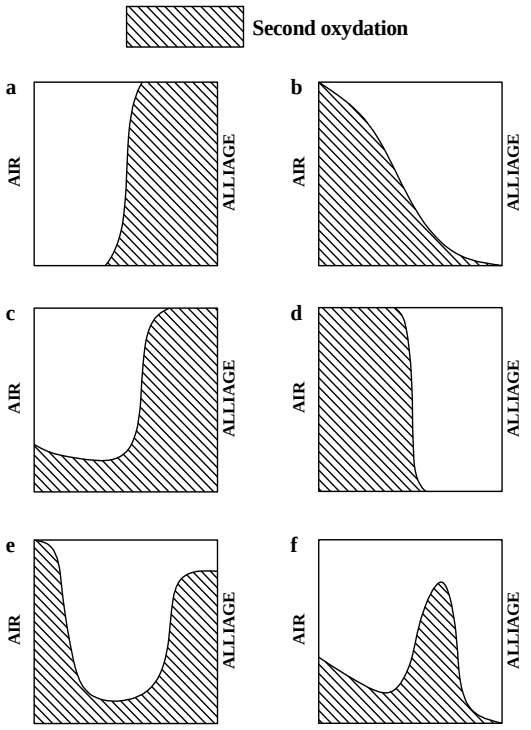

Figure 4.12 Schematic illustration of the relationship between the depth profiles of the ^{18}O tracer and the growth mechanism during the two-stage oxidation experiment [123-125]: (a) oxygen inward through cracks; (b) oxygen inward through lattice; (c) oxygen inward through grain boundary; (d) metal outward; (e) metal outward and oxygen inward through different paths; (f) metal outward and oxygen inward through the same paths

Figure 4.13 shows the diffusion profiles of isotope oxygen $^{18}O_2$ in the oxide scale after two-stage oxidation at 700 ℃, 800 ℃ and 900 ℃. It is true that the thickness of oxide scales is different after oxidation at different temperature, but the diffusion profiles are nearly the same. This indicates that the oxidation mechanism is similar at all these three temperatures. It is clear that separated isotopic profiles were got after two-stage oxidation, with ^{18}O at the outer part of the scale and ^{16}O at the inner part. The concentration of ^{18}O is nearly 6 times larger than that of ^{16}O at the surface, which suggests that the oxidation is mainly controlled by the outward diffusion of metallic cations.

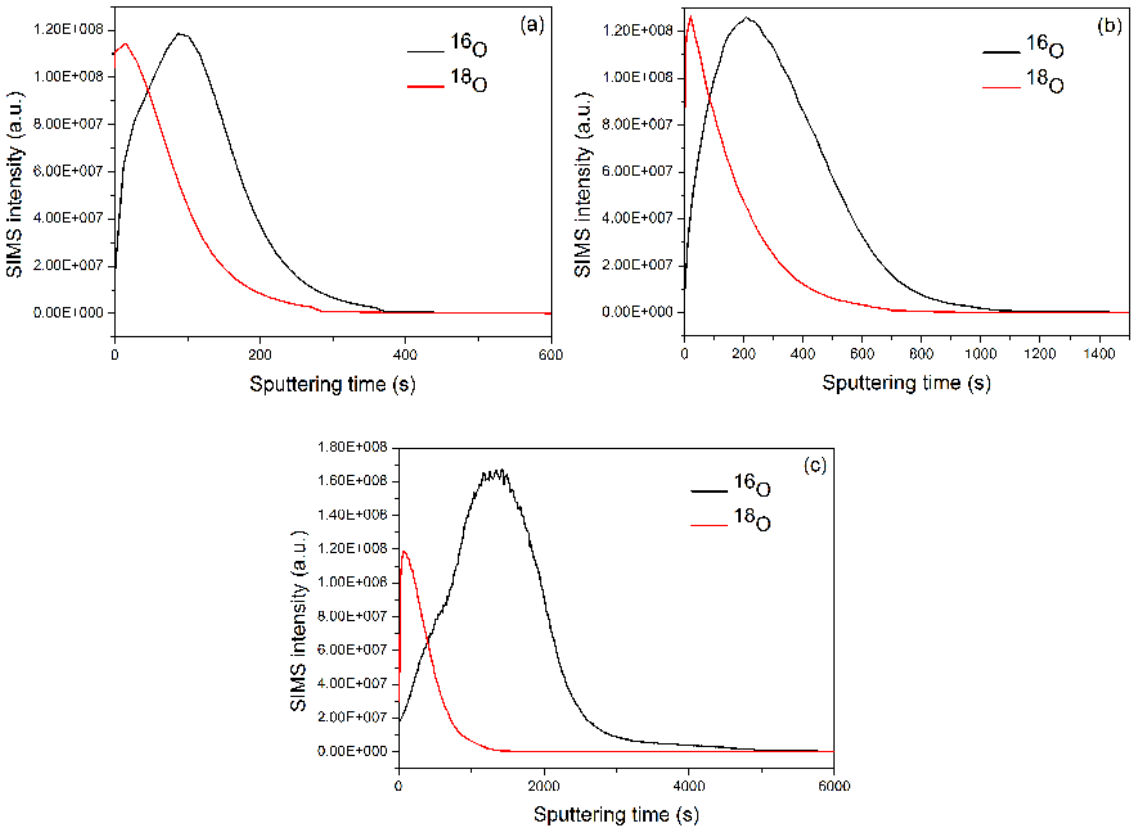

Figure 4.13 The diffusion profiles of isotope oxygen $^{18}O_2$ in the oxide scale after two-stage oxidation at 700 ℃, 800 ℃ and 900 ℃

4.1.5 Discussion

The results obtained in this work indicate that a protective oxide scale is formed at all three oxidation temperatures under dry air. The scale consists of an outer $Mn_{1.5}Cr_{1.5}O_4$ spinel layer (with little Fe incorporation) and an inner Cr_2O_3 layer, and a discontinuous SiO_2 layer oxide was also found at the scale/substrate interface. This is because the oxidation procedure was followed by three steps. Figure 4.14schematically illustrates the steps of the oxidation in dry air.

At the step 1, the oxidation is mainly controlled by the outward diffusion of Cr^{3+} because of selective oxidation, and a thin protective Cr_2O_3 oxide layer is formed rapidly.

After that at step 2, the oxidation is mainly controlled by the outward diffusion of Mn^{3+} which result into the formation of an outer spinel layer, this occurs as the Mn ion diffuses faster than Cr^{3+} via Cr^{3+} lattice in Cr_2O_3 [9]. Wild [126] has proved that Mn ions diffuses two orders of magnitude faster than Cr ions. In the meantime, this can also explain that the relative high GIXRD intensity of $Mn_{1.5}Cr_{1.5}O_4$ peaks occurs due to the presence of the $Mn_{1.5}Cr_{1.5}O_4$ phase in outer part of the scale instead of the higher proportion in the scale.

Meanwhile, silica is formed at the scale/substrate interface. Some authors [71, 127] also found that SiO_2 precipitates at the scale/substrate interface because of the high oxygen affinity of silicon. Although, too much amount of silicon in alloy has detrimental effect on mechanical properties, its addition can improve the alloy oxidation resistance. Once a silica interlayer formed between the outer oxide scale and the substrate, the oxidation process is controlled by chromium ions diffusion through this silica layer [71]. It has been found that too much amount of silicon can lead to spallation at the silica/chromia interface [128]. Silica has a much lower thermal expansion coefficient than the substrate and chromia, therefore, has adverse effect on scale adhesion. Normally, silicon is added no more than 1 wt%.

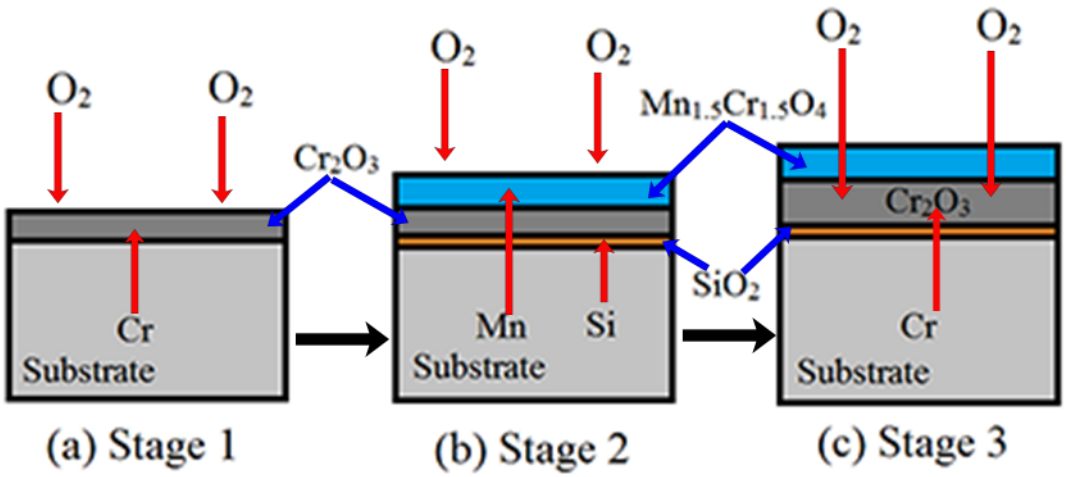

Figure 4.14 Schematic illustration of oxidation stage of AISI 430 alloy in air

The percentage composition of Mn and Si in the alloy is small, that's why at step 3 the oxidation is controlled by the diffusion of Cr^{3+} again. At this step, the oxygen transports through the spinel layer to the chromia layer and the Cr ions diffuse to the same layer; both of them react with each other, which make the Cr_2O_3 layer thicker.

In this study, the activation energy for AISI 430 alloy is 279.9kJ/mol, and the activation energy of Cr diffusion in Cr_2O_3 is 280kJ/mol [120]. Therefore, it can be suggested that the oxidation of AISI 430 alloy under dry air is mainly controlled by the outward diffusion of Cr in the oxide scale, consistent with the SIMS results after two-stage oxidation. This outward diffusion mechanism has been claimed as main mechanism by all authors for the chromia forming alloys [85, 129]. With the outward diffusion of ions, Cr vacancies are formed in alloy near the scale/substrate interface, by reaction

$$[4V_{Cr}''' + 6V_O^{\cdot\cdot}]_{surface} + 3O_2 = 6O_O^X + 4V_{Cr}''' + 12h^{\cdot} \qquad (4\text{-}5)$$

These vacancies are filled by the outward diffusion of Cr in the alloy. The coarsening of vacancies can lead to formation of voids. It is in agreement with the result that some voids are formed at the scale/substrate interface (Figure 4.11). Void formation can accelerate the oxidation rate by dissociative transport through it [130], and lead to detachment of the oxide scale, which is very important to the electric conductivity.

4.2 Oxidation of AISI 430 stainless steel in air with different absolute humidity

After understanding the oxidation mechanism of AISI 430 alloy in dry air, in this section the oxidation behavior of this alloy in air with different absolute humidity will be studied, to clarify the influence of water vapor on it.

4.2.1 Oxidation kinetics

Figure 4.15 shows the weight change of the AISI 430 alloy after oxidation in atmosphere with different absolute humidity (AH) at 700 ℃, 800 ℃. It has been mentioned that a protective oxide scale was formed in air without water vapor because the oxidation rate obeyed the parabolic law. With the introduction of water vapor into the oxidation atmosphere, the weight change curves show the same trend as it in dry air, indicating the oxidation rates also obey the parabolic law at 700 ° (Figure 4.15 a) and 800 ℃ (Figure 4.15 b). The weight gain decreases with the increase of water vapor. Anyway, the oxide scale formed is still protective at 700 ℃ and 800 ℃. The parabolic rate constants calculated from the kinetic curves are listed in Table 4.2 and Table 4.3 . The fluctuation of weight gain curves is due to the influence of the flow of water vapor. The more water vapor added in, the more obvious the fluctuation, especially at 700 ℃. So, we will just focus on the main evaluation trend.

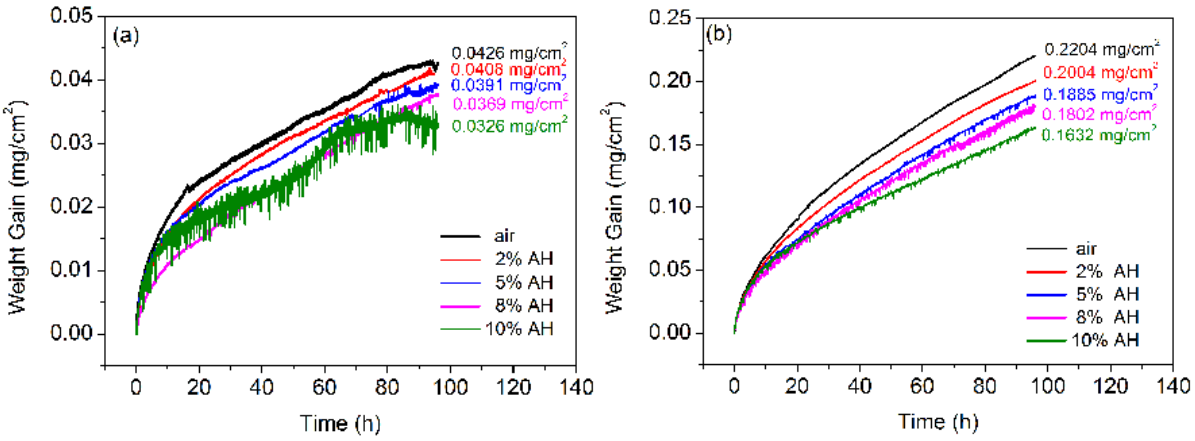

Figure 4.15 Weight gain curves of AISI 430 steel during exposure in air with different absolute humidity (AH) at 700 ℃ for 96h (a), at 800 ℃ for 96h (b)

Table 4.2 Parabolic rate constants calculated for the samples after 96h oxidation in air with different absolute humidity at 700 ℃

700 ℃	Air	2% AH	5% AH	8% AH	10% AH
k_p ($g^2cm^{-4}s^{-1}$)	5.127×10^{-15}	4.817×10^{-15}	4.291×10^{-15}	4.183×10^{-15}	3.528×10^{-15}

Table 4.3 Parabolic rate constants calculated for the samples after 96h oxidation in air with different absolute humidity at 800 ℃

800 ℃	Air	2% AH	5% AH	8% AH	10% AH
k_p ($g^2cm^{-4}s^{-1}$)	1.416×10^{-13}	1.187×10^{-13}	1.046×10^{-13}	9.423×10^{-14}	7.402×10^{-14}

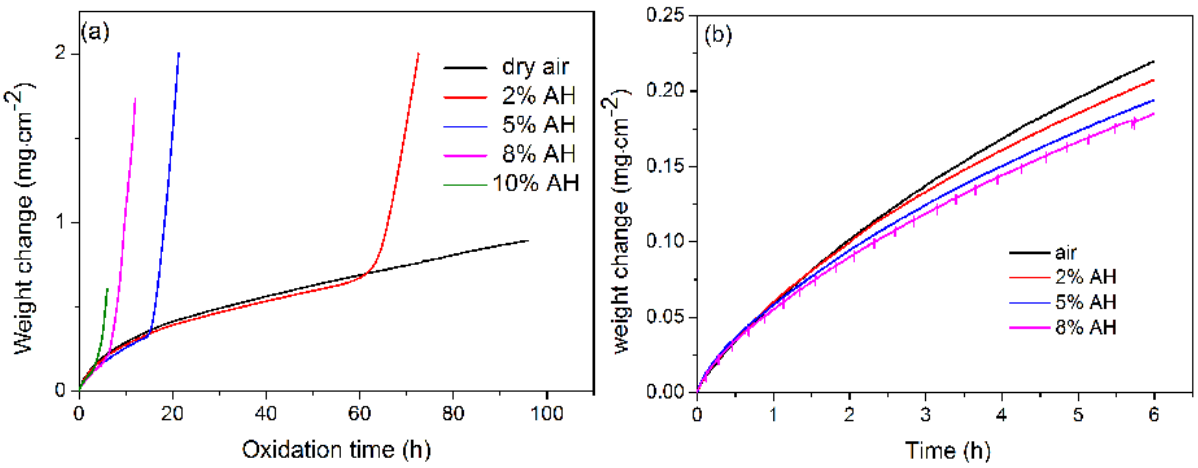

Figure 4.16 Weight gain curves of AISI 430 steel during exposure in air with different absolute humidity (AH) at 900 ℃ for 96h (a) and at 900 ℃ for 6h (b)

Figure 4.16 shows the weight change of the AISI 430 alloy after oxidation in atmosphere with different absolute humidity (AH) at 900 ℃. However, a significant increase of the weight gain occurred with the introduction of the water vapor at 900 ℃, which indicates a catastrophic breakaway oxidation, as shown in Figure 4.16 a. The breakaway oxidation is very sensitive to the water vapor. A slight increase in humidity causes the breakaway oxidation took place more rapidly. With 2%, 5%, 8% and 10% absolute humidity, the breakaway oxidation happened at about 60h, 16h, 7h and 3h respectively. But before breakaway oxidation occurred, as shown in Figure 4.16 b, weight change curves also followed the parabolic kinetics, and the weight gain decreased with the increase of the absolute humidity, same as that at 700 ℃ and

800 ℃. The parabolic rate constants calculated from the kinetic curves before the occurrence of breakaway oxidation are given in Table 4.4.

Table 4.4 Parabolic rate constants calculated for the samples after 6h oxidation in air with different absolute humidity at 900 ℃

900 ℃	Air	2% AH	5% AH	8% AH
k_p ($g^2cm^{-4}s^{-1}$)	2.367×10^{-12}	2.100×10^{-12}	1.826×10^{-12}	1.676×10^{-12}

4.2.2 Structure of the oxide scale

Figure 4.17 gives the 2 º GIXRD patterns after oxidation in air with different humidity at 700 ℃, 800 ℃ for 96h and at 900 ℃ for 6h. It is clear that the oxide scales are mainly consisted of Cr_2O_3 and $Mn_{1.5}Cr_{1.5}O_4$ whatever the oxidation atmospheres at 700 ℃ (Figure 4.17 a) and 800 ℃ (Figure 4.17 b), indicating that the water vapor doesn't affect the scale composition before the breakaway oxidation happens. The intensity of substrate peaks is larger in the atmosphere containing water vapor because the oxide scales formed during the oxidation are thinner than in the dry air. This is in accordance with the TGA result. XRD results obtained under air with different absolute humidity at 900 ℃ after oxidation for 6h (before breakaway oxidation happens), as shown in Figure 4.17 c, are similar to that obtained under dry air.

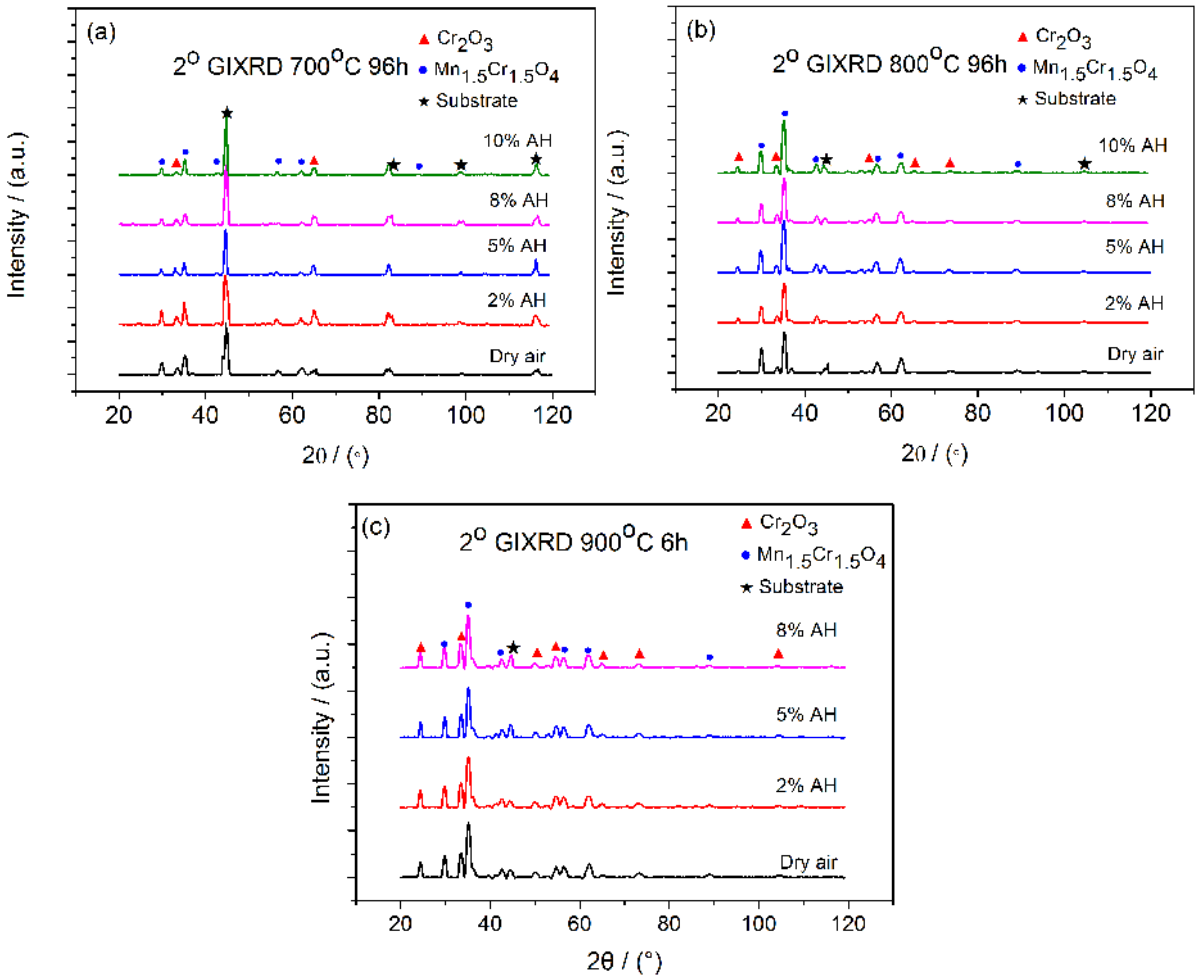

Figure 4.17 2 °GIXRD pattern of AISI 430 after oxidation in air with different absolute humidity (AH) at 700 ℃ for 96h (a), at 800 ℃ for 96h (b), at 900 ℃ for 6h (c)

Figure 4.18 displays the 2 °GIXRD pattern of AISI 430 stainless steel after oxidation in dry air and in air with 5% absolute humidity at 900 ℃ for 96h. With the occurrence of breakaway oxidation, however, Fe_2O_3 (JCPDS 33-0664) and $(Fe_{0.6}Cr_{0.4})_2O_3$ (JCPDS 34-0412) are also obtained on the surface besides Cr_2O_3 and $Mn_{1.5}Cr_{1.5}O_4$. And $(Fe_{0.6}Cr_{0.4})_2O_3$ might be a solid solution of Fe_2O_3 and Cr_2O_3. The disappearance of the substrate peaks for the sample oxidized in atmosphere with water vapor is due to the thicker oxide scale formed during the breakaway oxidation than that formed in dry air.

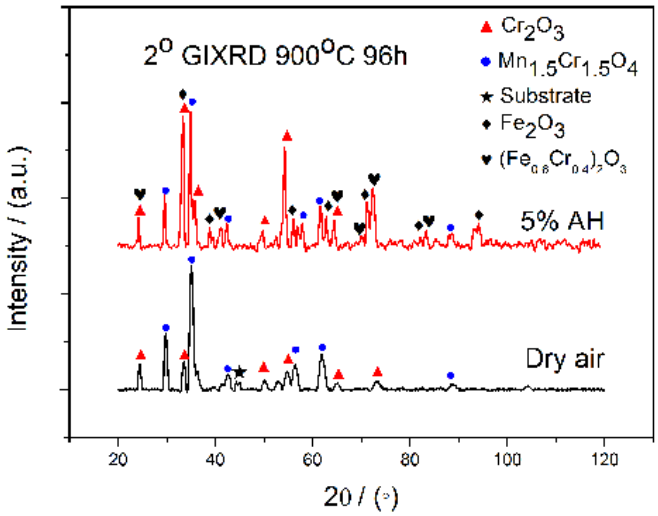

Figure 4.18 2 °GIXRD pattern of AISI 430 after oxidation in dry air and in air with 5% absolute humidity (AH) at 900 ℃ for 96h

4.2.3 Surface morphology of the oxide scale

SEM surface morphology after oxidation in dry air and in air with 5% absolute humidity at 700 ℃ and 800 ℃ for 96 hours is given in Figure 4.19 and Figure 4.20. No spallation is observed on the surface for all the samples after oxidation. At 700 ℃, big octahedral (points 1 and 3) and small polycrystalline grains (points 2 and 4) were formed on the surface. The EDX results of the points 1 to 4 are shown in Table 3. The atomic ratio of O, Cr and Mn indicates that the octahedral grains are spinel type oxide and the polycrystalline grains are Cr_2O_3 oxide. At 800 ℃, whatever the oxidation atmosphere, the octahedral grains (point 5) nearly covered the surface. It is also clear to see that the growth rate is greatly increased by the increasing of the oxidation temperature as more octahedral grains are formed on the surface oxidized at 800 ℃. At both 700 ℃ and 800 ℃, the only difference is that the octahedral grains formed in the atmospheres with and without water vapor are not the same. All the grains formed in dry air are regular octahedral. While in the atmosphere with 5% absolute humidity, some irregular shaped grains formed on the surface (point 6). This phenomenon is more obvious at 800 ℃. Nevertheless, the composition of the oxide is not greatly modified by the introduction of

water vapor, as shown in Table 4.5.

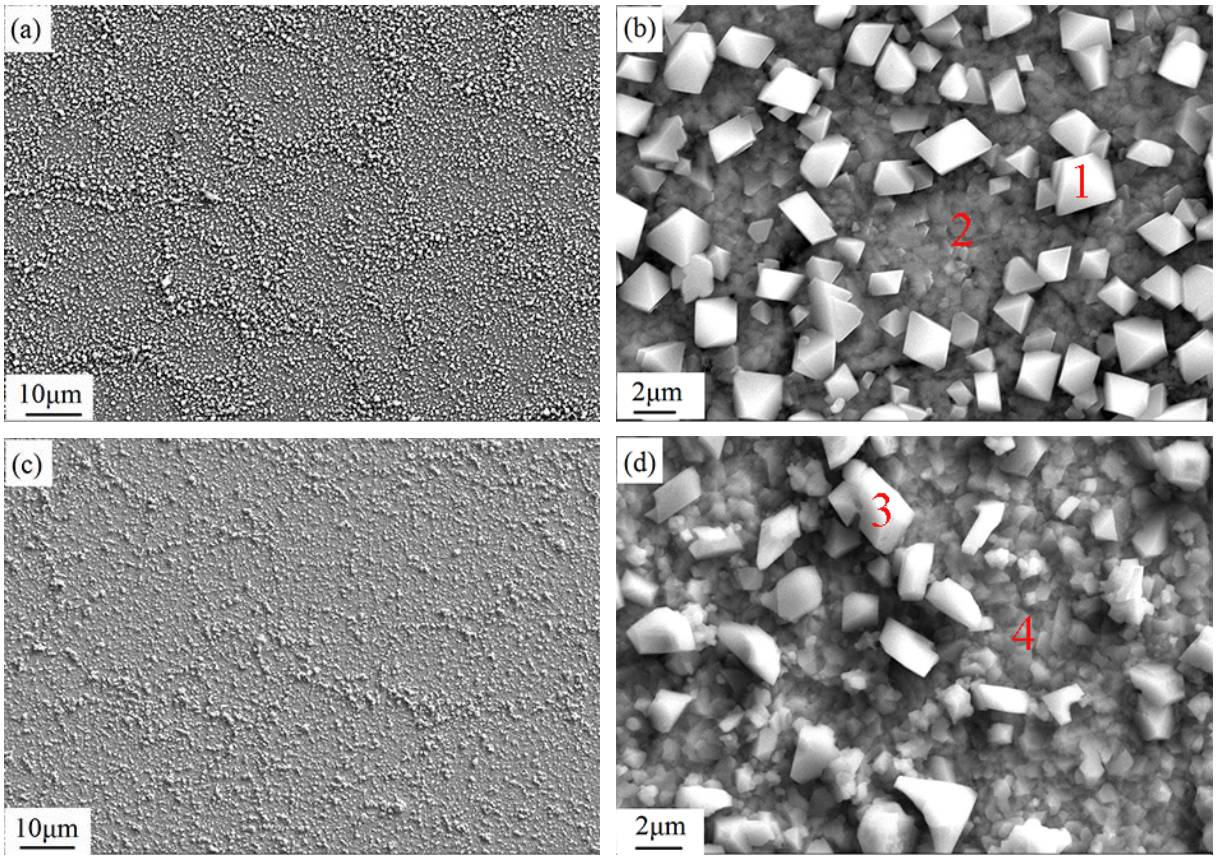

Figure 4.19 SEM surface morphology of oxide scale on the substrate after oxidation at 700 ℃ for 96h in dry air (a, b); in air with 5% AH (c, d)

Table 4.5 The EDX analysis results from locations 1 to 6 shown in Figure 4.19 and Figure 4.20 (atomic %)

Point	O	Fe	Mn	Cr
1	49.1	1.67	22.36	26.87
2	54.84	3.08	8.43	33.65
3	49.37	1.83	21.19	27.61
4	52.32	3.30	9.16	35.22
5	52.09	0.89	22.63	24.39
6	51.52	1.21	22.96	24.31

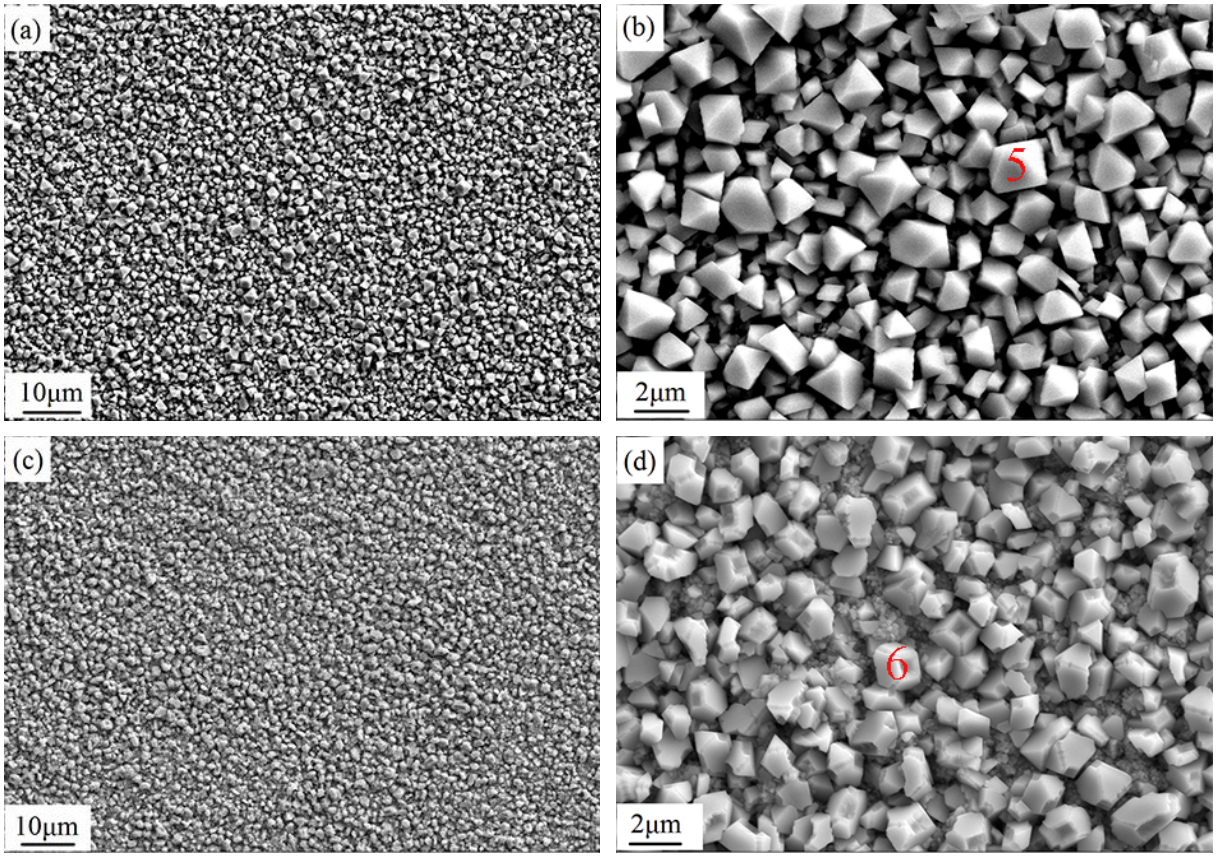

Figure 4.20 SEM surface morphology of oxide scale on the substrate after oxidation at 800 ℃ for 96h in dry air (a, b); in air with 5% AH (c, d)

SEM surface morphology after oxidation in dry air and in air with 5% absolute humidity for 6h (before the occurrence of breakaway oxidation) is given in Figure 4.21. It can be found that the surface morphologies after oxidation in air with and without water vapor are nearly the same, and no spallation was observed on the surface.

Figure 4.22 presents the digital photographs of the AISI 430 stainless steel after oxidation with 2% (Figure 4.22 a) and 5% (Figure 4.22 b) absolute humidity at 900 ℃ for 96h. It is shown that the sample edges are thicker than the center, and some nodules formed on the surface, indicating that the breakaway oxidation preferentially occurred at these parts of the sample. For the 2% absolute humidity, the nodules are formed randomly on the entire surface, but for the 5% absolute humidity, the nodules are mainly occurred near the upstream edge of

the sample (the flow direction of the water vapor is from the bottom of the TGA to the top).

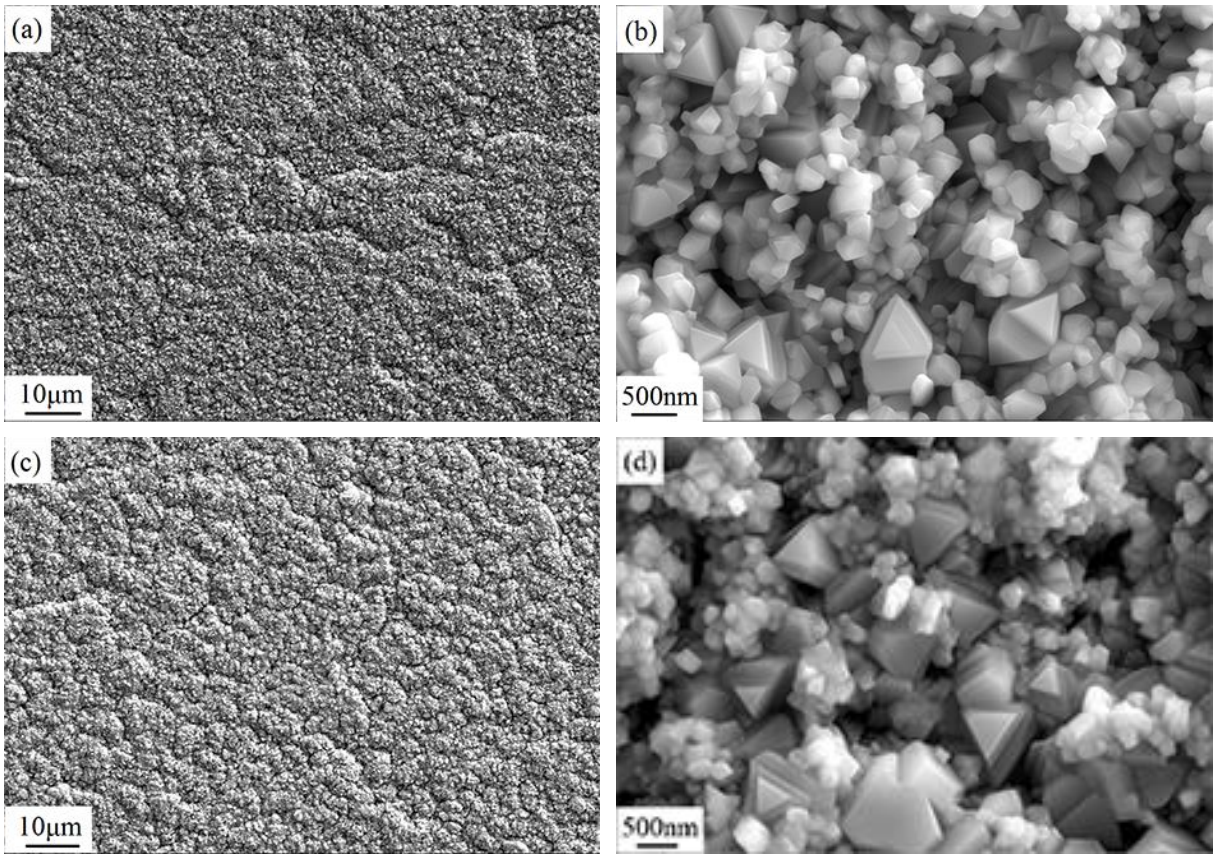

Figure 4.21 SEM surface morphology of oxide scale on the substrate after oxidation at 900 ℃ for 6h in dry air (a, b); in air with 5% AH (c, d)

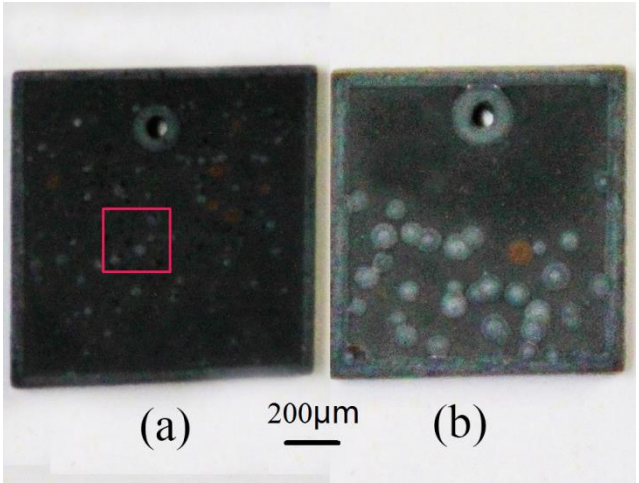

Figure 4.22 Digital photograph of the AISI 430 alloy after oxidation 96h at 900 ℃ in air with 2% AH (a), and in air with 5%AH (b)

Figure 4.23 displays the surface morphology of the framed area in the Figure 4.22. The atomic ratio O:Fe of point A analyzed by EDX is approximately 3:2, indicating that these nodules are Fe_2O_3. Once the Fe_2O_3 formed, the oxidation kinetic doesn't follow the parabolic kinetic because the protective oxide scale is damaged.

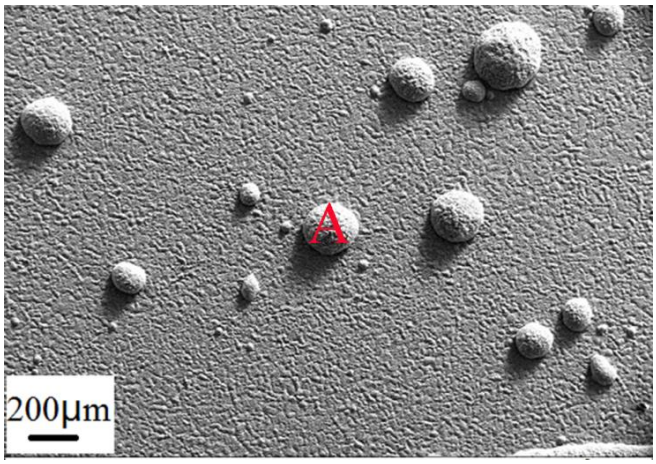

Figure 4.23 SEM surface morphology of the framed area in Figure 4.22 (a)

Observation of the cross section after oxidation in air with 5% absolute humidity at 800°C and 900°C by SEM is given in Figure 4.24. It is clearly that, same as that formed in dry air, the oxide scale is consists of two layers: an outer $Mn_{1.5}Cr_{1.5}O_4$ layer and an inner Cr_2O_3 layer. Meanwhile, discontinuous SiO_2 and isolated voids are also observed at the scale/substrate interface. At 900°C (Figure 4.24 a, b), the Cr_2O_3 layer is in dominant (1.5μm of thickness), and the spinel layer is nearly continuous at external surface. At 800°C (Figure 4.24 c, d), the Cr_2O_3 layer is about 300nm of thickness, and some big spinel grains are formed on the surface. These spinel grains are still in isolated state, and easy to fall off during the polishing of the cross section. Several dropped spinel grains are found, as shown in Figure 4.24 c.

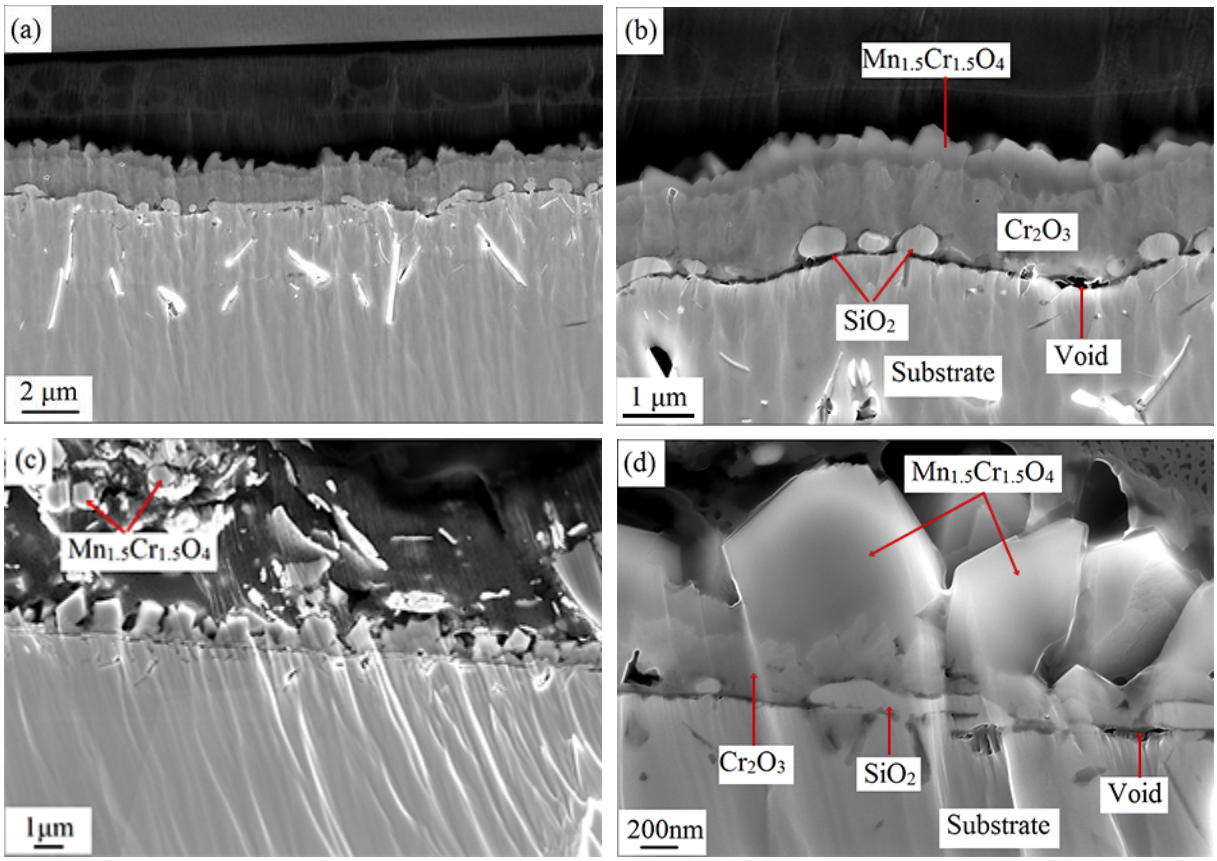

Figure 4.24 Cross section of the AISI 430 alloy oxidized in air with 5% absolute humidity at 900 ℃ for 12h (a, b) and at 800 ℃ for 48h (c, d)

Figure 4.25 displays the SEM image and corresponding EDX elemental mapping of the cross section of the AISI 430 stainless steel oxidized in air with 2% absolute humidity at 900 ℃ for 24h. It is nearly the same as that observed in dry air at 900 ℃ for 24h: thin Fe layer in the top of the surface, accumulation of Cr in the oxide scale, a gradient of Mn concentration richer in outer part of the scale, and discontinuous Si layer at the scale/substrate interface.

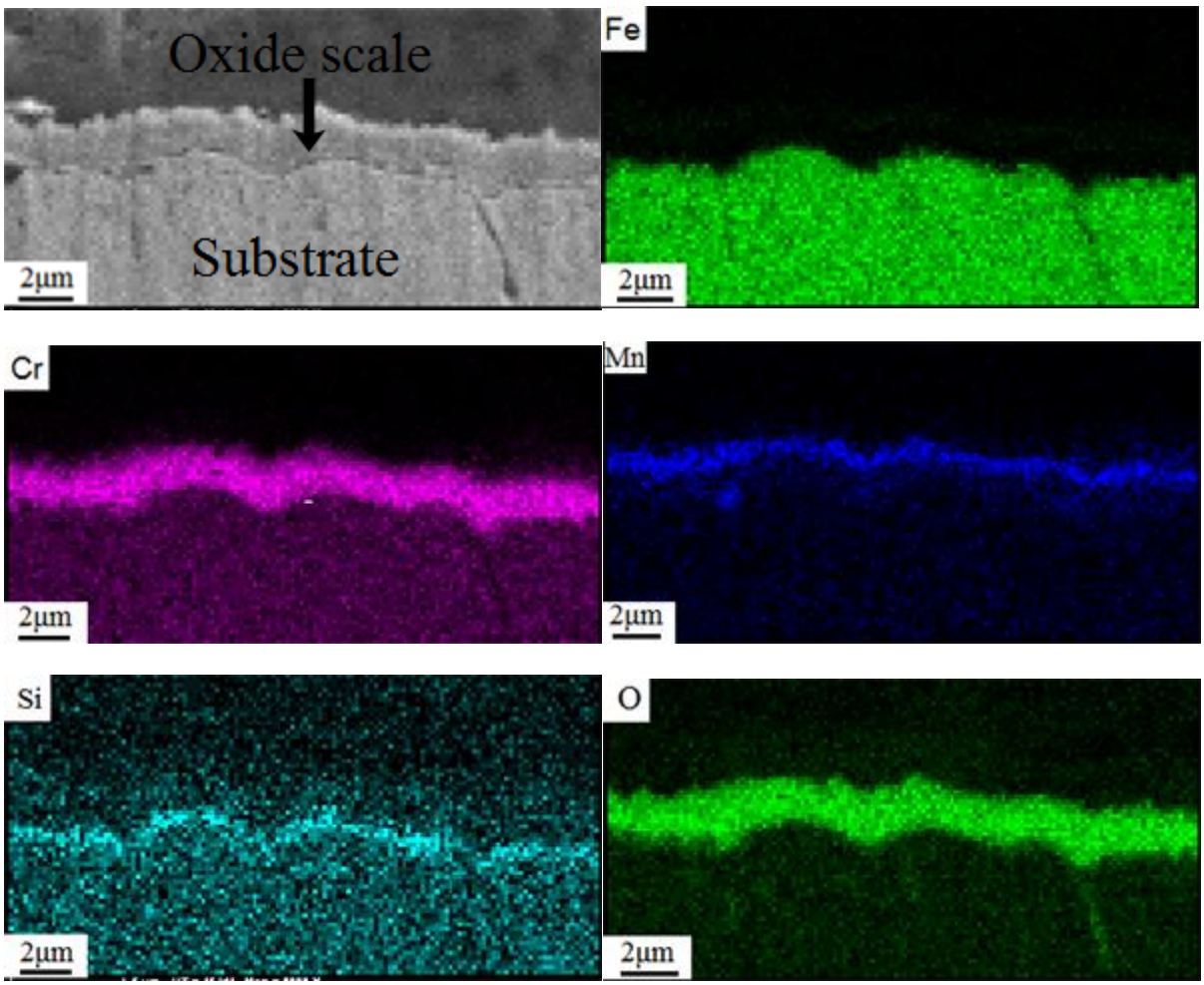

Figure 4.25 SEM image and corresponding EDX elemental mapping of the cross section of the AISI 430 alloy oxidized in air with 2% absolute humidity at 900 ℃ for 24h

4.2.4 XPS analysis

XPS analyses have been done for samples after 12h oxidation in dry and in air with 5% absolute humidity at 700 ℃, 800 ℃ and 900 ℃. To ensure that the samples free from the possible contamination, the samples were placed in the XPS analysis chamber as soon as the oxidation finished. A typical XPS spectrum obtained from the AISI 430 alloy oxidized in dry air at 900 ℃ is illustrated in Figure 4.26, obvious oxygen (O1s), chromium (Cr2p), manganese (Mn2p) and small iron (Fe2p) peaks are observed.

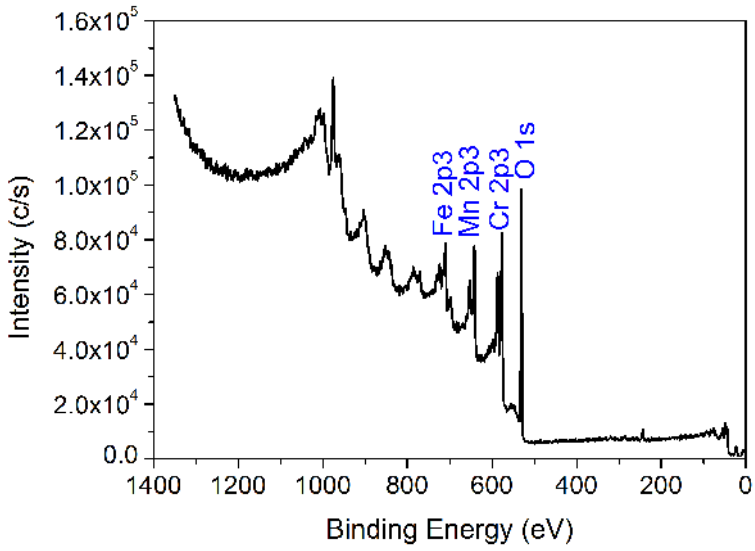

Figure 4.26 XPS survey spectrum of a sample oxidized in dry air at 900 ℃ for 12h

Figure 4.27 shows the XPS depth profiles of the oxide scales formed on AISI 430 alloy after oxidation in air and in air with 5% absolute humidity for 12h at different temperature. These profiles can give information about the composition of the scales. If the element concentration is higher than that in the substrate, it is considered as a scale/substrate interface. After oxidation for 12h at 700 ℃, chromium oxide is dominant in the scale and manganese is also detected at the surface. At the early stage of etching, the oxide scale is enriched in Mn obviously. The presence of Mn would be due to the formation of $Mn_{1.5}Cr_{1.5}O_4$ at the surface. With increasing etch depth, the relative concentration of Mn decreases whereas the Cr concentration increases, indicating the formation of a second layer oxide scale. This is in agreement with the results we have got from the section 4.1. As the oxidation temperature increases, the oxide scale becomes more and more thick and the two layers structure becomes obviously. Generally the elements distributions in the oxide scale are nearly the same after oxidation in dry air and in air with 5% absolute humidity.

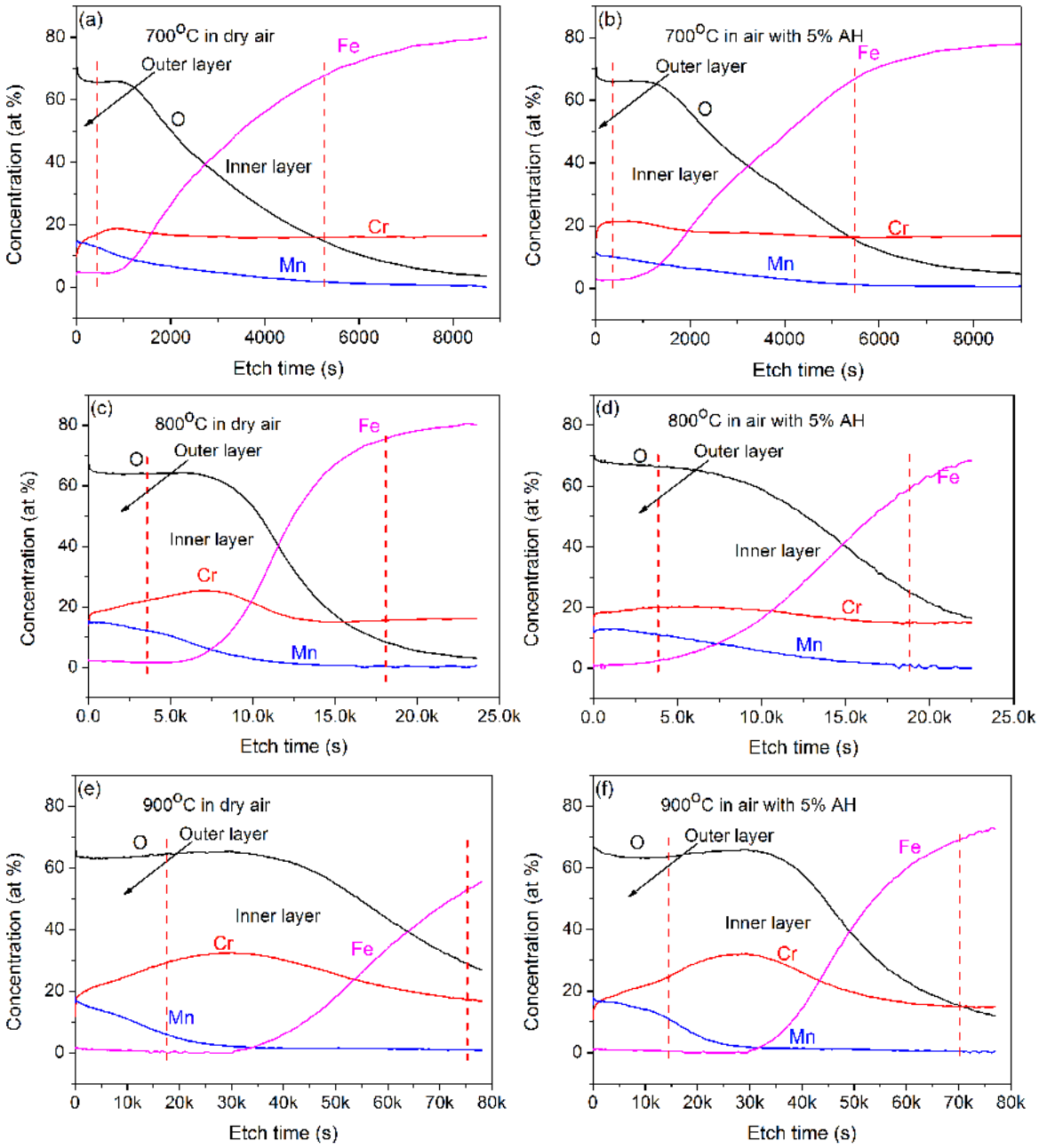

Figure 4.27 The XPS profiles of the oxide scale formed on AISI 430 alloy after oxidation in dry air and in air with 5% AH at different temperature

Figure 4.28 shows the Cr $2p_{1/2}$ and $2p_{3/2}$ transitions after different etching times for the sample oxidized in dry air for 12h at 900 ℃, which will be used to fit different peaks based on their binding energies shown in Table 4.6. With etching, the oxides component intensities decreased and only the metallic component remained at last. For Cr $2p_{3/2}$, $Mn_{1.5}Cr_{1.5}O_4$, Cr_2O_3, CrO_3, $Cr(OH)_3$ four oxide peaks and a metallic peak are used for fitting. The Mn and O data

are performed similarly. MnO and $Mn_{1.5}Cr_{1.5}O_4$ two peaks were used for Mn fitting, O^{2-} and OH^- were used for O fitting.

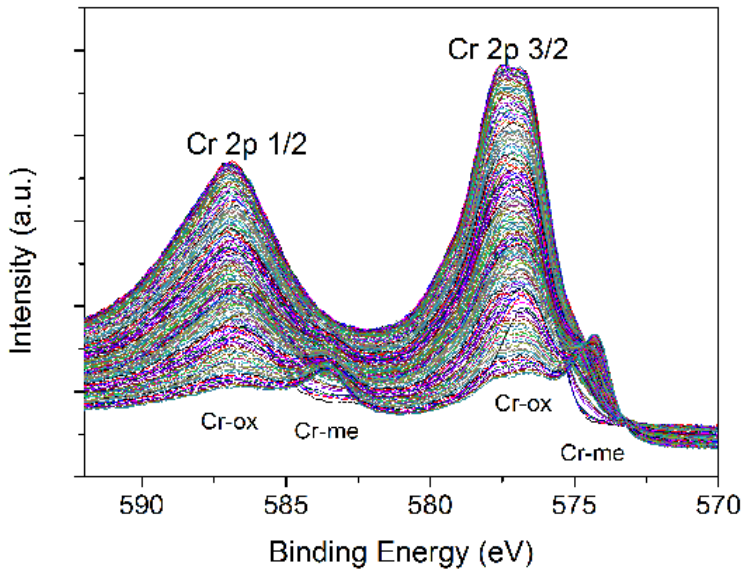

Figure 4.28 Set of high-resolution XPS spectra of Cr 2p after different etching times for the sample oxidized in air for 12h at 900 ℃. The top spectrum is from the surface before etching, and the spectra below are with increasing depth from the surface

Table 4.6 Binding energy of reference spectra

Element	Peak	Binding energy (eV)	Reference
Cr $2p_{3/2}$	Cr	574.1	[131]
	Cr_2O_3	576.4	[131]
	$Mn_{1.5}Cr_{1.5}O_4$	575.8	[132]
	$Cr(OH)_3$	577.3	[133, 134]
	CrO_3	578.6	[134, 135]
Mn $2p_{3/2}$	MnO	640.3	[132]
	$Mn_{1.5}Cr_{1.5}O_4$	642.1	[132]
O 1s	O^{2-}	530.1	[131]
	OH^-	531.7	[131]

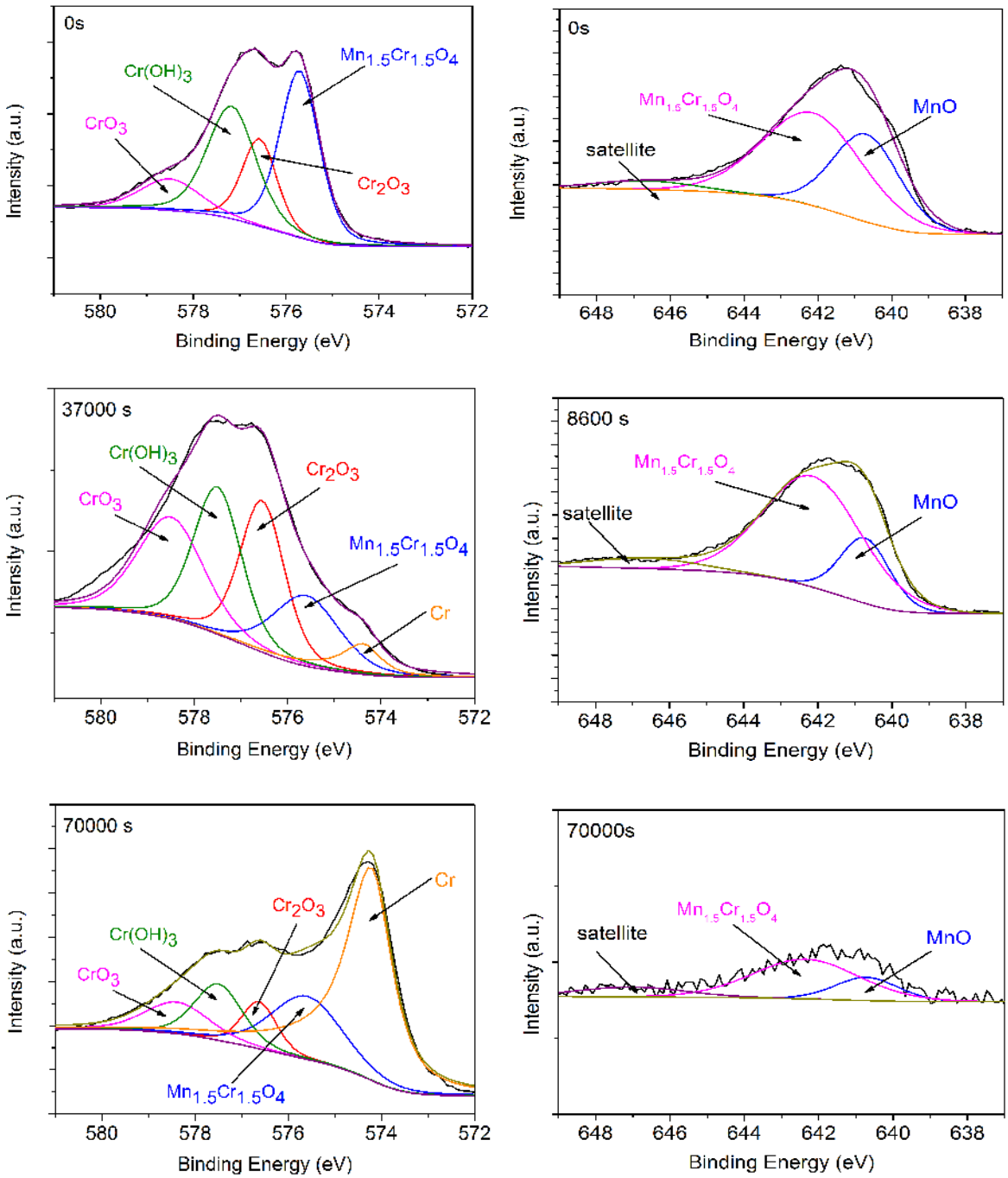

Figure 4.29 The detailed XPS spectra of Cr $2p_{3/2}$ and Mn $2p_{3/2}$ peaks collected from oxide scale formed after 12h oxidation in dry air at 900 ℃

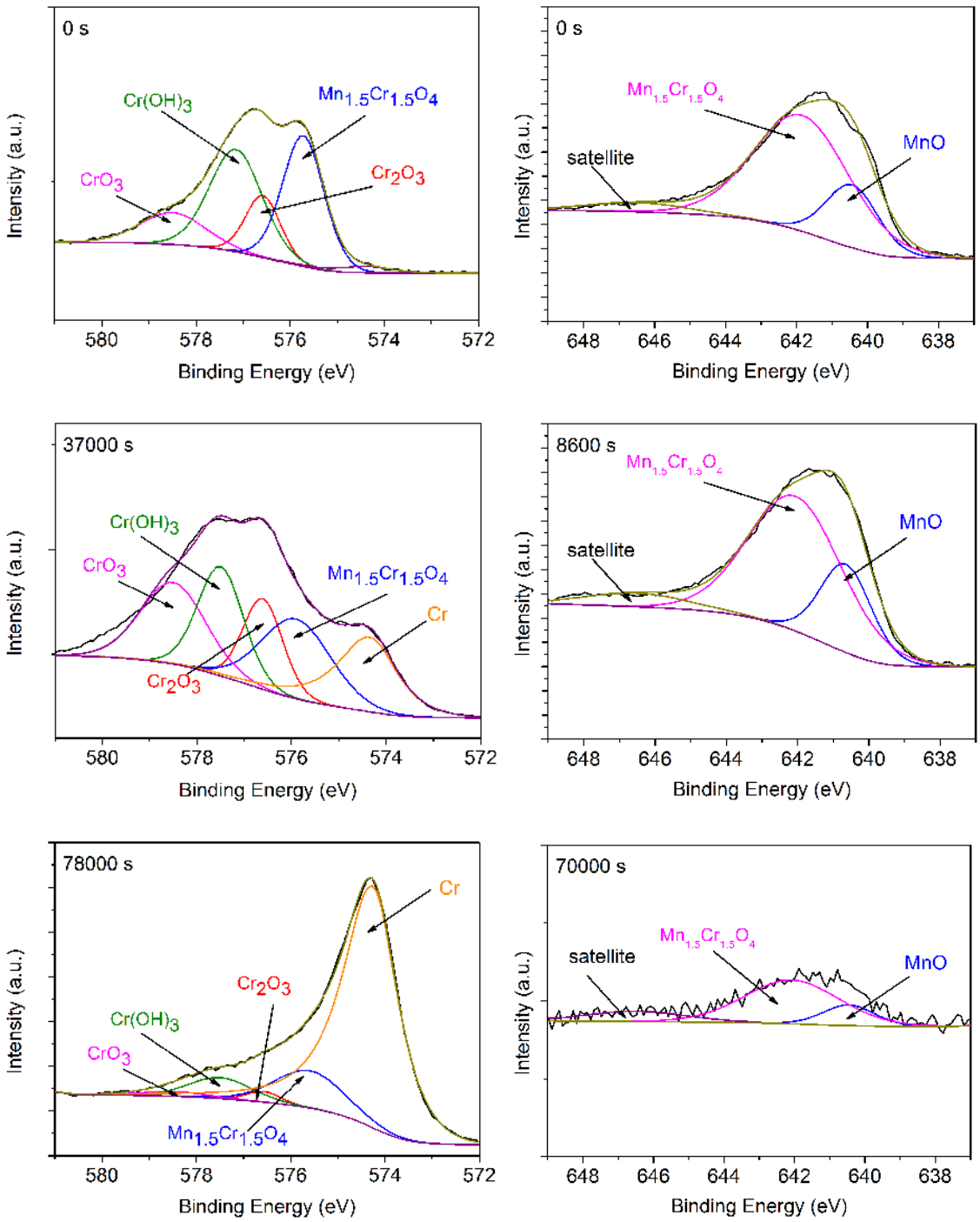

Figure 4.30 The detailed XPS spectra of Cr $2p_{3/2}$ and Mn $2p_{3/2}$ peaks collected from oxide scale formed after 12h oxidation in air with 5% absolute humidity at 900 ℃

Figure 4.29 and Figure 4.30 show the detailed XPS spectra of Cr $2p_{3/2}$ and Mn $2p_{3/2}$ peaks collected from oxide scale formed after 12h oxidation in dry air and in air with 5% absolute humidity. In general, the composition and the distribution of the oxide are similar after

oxidation in air and in air with water vapor. For Cr, the main peak of Cr $2p_{3/2}$ can be separated into four possible peaks correspond to $Mn_{1.5}Cr_{1.5}O_4$, Cr_2O_3, CrO_3 and $Cr(OH)_3$. No metallic Cr peak was observed at the surface. With etching for 37000s, the $Mn_{1.5}Cr_{1.5}O_4$ peak intensity decreased, $Cr(OH)_3$ and Cr_2O_3 peak intensity increased, indicating that there is a $Mn_{1.5}Cr_{1.5}O_4$ top layer. As the etching time increases to 78000s, the oxide peaks decreased their intensities and the metallic Cr peak increased.

Three peaks were detected at the surface for Mn. According to their energy, it can be found that the first peak is MnO, the second is $Mn_{1.5}Cr_{1.5}O_4$ spinel and the last one corresponds to a satellite [132]. With increasing etching time to 8600s, the spinel peak is dominant in the scale. As the etching time increases to 70000s, the Mn spectra intensity is very small.

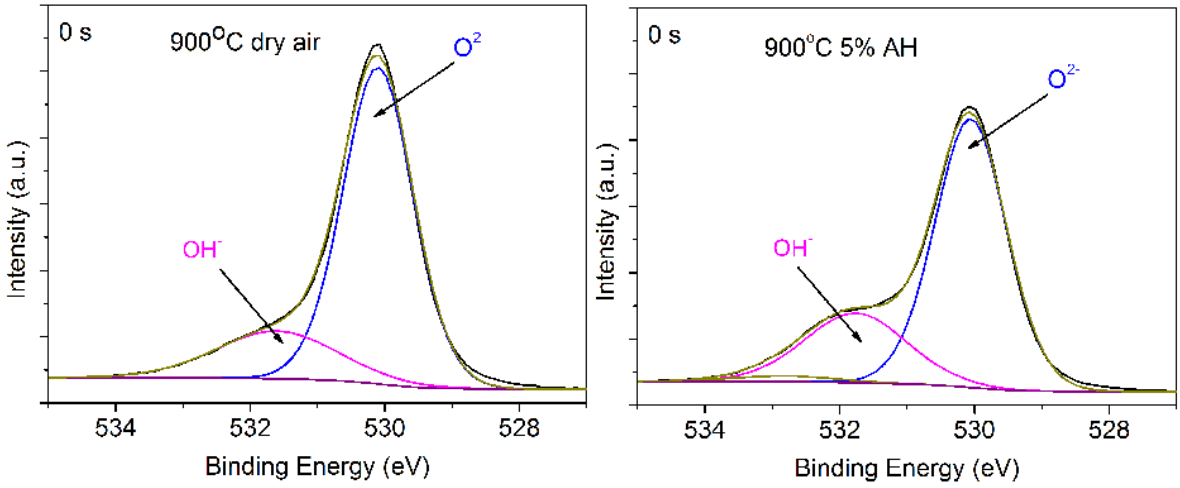

Figure 4.31 The detailed XPS spectra of O 1s peaks collected from oxide scale formed after 12h oxidation in dry air and in air with 5% absolute humidity at 900 ℃

Figure 4.31 displays the detailed XPS spectra of O 1s peaks collected from oxide scale formed after 12h oxidation in dry air and in air with 5% absolute humidity at 900 ℃. The O 1s spectra can be separated into two peaks, which are attributed to O^{2-} in oxide species and OH^- in hydroxide species. It is clear that the intensities of the OH^- in 5% absolute humidity are higher

than that in dry air. For the O^{2-}, however, is just the opposite, the intensities of it are smaller in 5% absolute humidity. This suggests that a larger proportion of hydroxides were formed on the surface of the sample after oxidized in atmosphere containing water vapor.

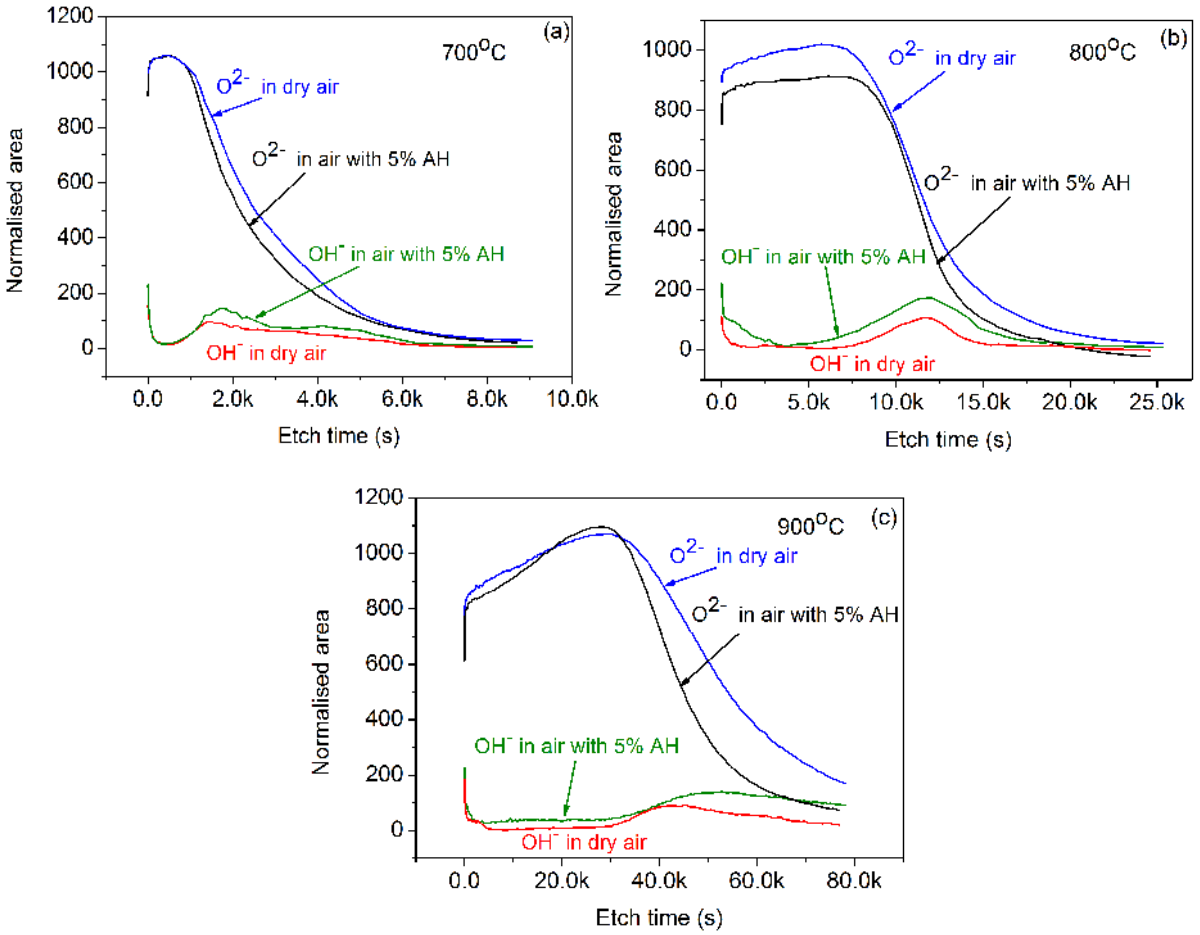

Figure 4.32 The XPS depth profiles of O^{2-} and OH^- for AISI 430 alloy after oxidized in dry air and in air with 5% AH at different temperature

To understand the hydroxides distribution as a function of the oxide scale thickness, the XPS depth profiles of O^{2-} and OH^- for AISI 430 alloy after oxidized in dry air and in air with 5% absolute humidity at different temperature are given in Figure 4.32. The OH^- observed after a short time of abrasion is due to the absorption of it on the surface of the sample. It is clear that the XPS profiles are not identical at the same temperature with the introduction of water vapor. More hydroxides exist in the oxide scale formed in the atmosphere containing water vapor

than that formed in dry air. It is true that the increase of OH^- is not significant, but it might have great influence on oxidation behavior.

4.2.5 Discussion

4.2.5.1 Oxidation kinetic

In this study, the weight gain decreased with the introduction of water vapor at 700 ℃, 800 ℃ and at 900 ℃ before the occurrence of breakaway oxidation, the higher the absolute humidity, the smaller the weight gain (Figure 4.15 and Figure 4.16 b). This is opposite to the results observed by some researchers [83, 132]. J. Ehlers et al [83]proved that the presence of water can accelerate the oxidation rate. A.M. Huntz et al [132] thought that the oxidation rate of Fe-Cr alloy shows no obvious dependence on oxidation atmosphere. But our experiment result is consistent with other studies of oxidation of stainless steels in atmosphere containing water vapor [89, 136]. According to H. Asteman et al. [79, 107, 108] this is the result of evaporation of chromium oxide hydroxide in atmosphere containing water vapor through the reaction (4-6). And this explanation has been demonstrated by other researchers [87, 109-111].

$$\frac{1}{2}Cr_2O_3(s) + \frac{3}{4}O_2(g) + H_2O(g) = CrO_2(OH)_2(g) \qquad (4\text{-}6)$$

So in the presence of water vapor, the total weight gain is composed of two parts, can be given as below:

$$W_{total} = W_{oxidation} + W_{evaporation} \qquad (4\text{-}7)$$

The oxidation weight gain curve is the result of combination of two processes, on the one hand the oxidation induced a mass increase, and on the other hand the evaporation of chromium species leaded to a mass decrease. The $W_{oxidation}$ is obtained by TGA analysis and the weight

evaporation ($W_{evaporation}$) can be calculated from gas transport theory in the viscous flow regime, and is given as [84]:

$$W_{evaporation} = J_{Cr}t = \frac{k_m}{RT}P_{CrO_2(OH)_2}t \quad (4\text{-}8)$$

where J_{Cr} is molar flux of Cr containing specie, R is the thermodynamic constant, T is the absolute temperature, t is the oxidation duration, k_m is the mass-transfer coefficient and is given by:

$$k_m = 0.664\left(\frac{D^4}{\upsilon}\right)^{1/6}\left(\frac{v}{L}\right)^{1/2} \quad (4\text{-}9)$$

where D is gas diffusion coefficient, υ is the kinematic viscosity, v is the bulk-gas linear velocity and L is the sample length. And for the Eq. (1), the equilibrium partial pressure of $CrO_2(OH)_2$ can be given as:

$$P_{CrO_2(OH)_2} = K_1 P_{O_2}^{3/4} P_{H_2O} \quad (4\text{-}10)$$

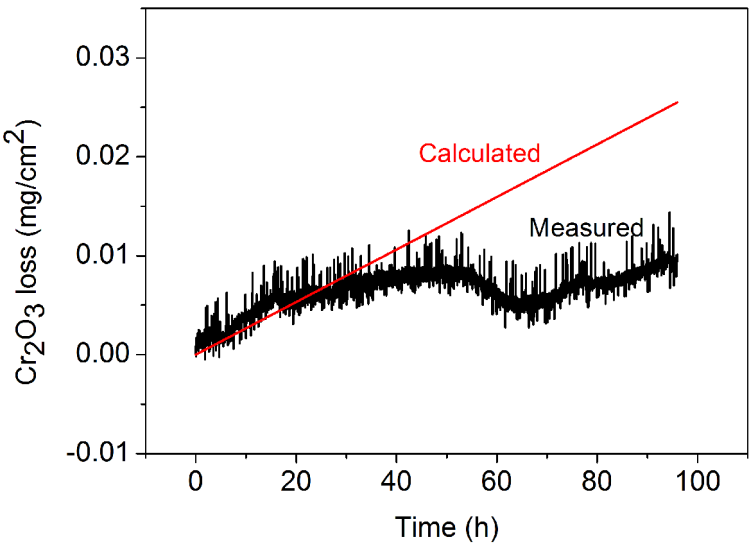

Figure 4.33 Comparison of the calculated and measured Cr_2O_3 loss due to evaporation from AISI 430 alloy oxidized in air with 10% absolute humidity at 700 ℃

The calculated parameters were given in Table 4.7. With these parameters, the weight loss due to $CrO_2(OH)_2$ evaporation can be calculated. Every mg of $CrO_2(OH)_2$ evaporation from the oxide scale leads to an equivalent loss of 0.64 mg of Cr_2O_3. The comparison of the calculated and measured weight loss due to evaporation at 700 ℃ is given in Figure 4.33. The measured value is the weight gain difference between the samples oxidized in air and in air with 10% absolute humidity. It is clear that the agreement is very good in first 25h，while after that the measured value is smaller than the calculated one. This may attribute to the formation of an outer $Mn_{1.5}Cr_{1.5}O_4$ spinel layer, for this spinel layer can suppress the evaporation of $CrO_2(OH)_2$ [66, 137]. With the increase of oxidation duration, the spinel layer thickness increased, thus the weight loss due to evaporation decreased. Therefore, the thickness of spinel layer can affect the evaporation rate and indirectly the thickness of protective chromia layer.

Figure 4.34 shows the corrected mass change curves of AISI 430 stainless steel during exposure in air with different absolute humidity. It is clear that the corrected weight gain in atmosphere containing different absolute humidity is nearly the same as the weight gain in dry air at 800 ℃, it indicates that the evaporation of $CrO_2(OH)_2$ is the main reason for weight loss. However, at 700 ℃ and 900 ℃, there is a difference between the corrected weight gains in different humidity and the weight gain in dry air. Considering the small weight gain at 700 ℃ compared to that at 800 ℃, the difference at 700 ℃ can be ignored. In addition, breakaway oxidation happened with the introduction of water vapor into the oxidation atmosphere at 900 ℃, the corrected weight gain given in Figure 4.34 c is just 6h, might too short to reflect the real situation.

A comparison of uncorrected (Figure 4.15 and Figure 4.16) and corrected (Figure 4.34) weight change curves indicates that evaporation of $CrO_2(OH)_2$ has a significant influence on weight

change. Using the TGA experimental data to estimate the oxidation kinetic could lead to misunderstanding in the circumstance where evaporation of $CrO_2(OH)_2$ takes place.

The evaporation calculation has ignored the influence of CrO_3, which is important at above 1000 ℃, E.J. Opila et al [138] have proved that $p_{CrO_3}/p_{CrO_2(OH)_2} < 0.01$ in Ar-20O_2-5H_2O at 950 ℃, justified the assumption made in this study.

Table 4.7 Parameters for chromium evaporation as $CrO_2(OH)_2$ in air with different humidity

T (℃)	Absolute humidity	k_m (cm/s)	$P_{CrO_2(OH)_2}$(atm)	J_{Cr} (g/cm^{2}s)
700	2	0.2323	6.7579×10^{-8}	2.2904×10^{-11}
	5	0.2325	1.6895×10^{-7}	5.7287×10^{-11}
	8	0.2326	2.7031×10^{-7}	9.1704×10^{-11}
	10	0.2327	3.3790×10^{-7}	1.1467×10^{-10}
800	2	0.2500	1.2515×10^{-7}	4.1393×10^{-11}
	5	0.2502	3.1288×10^{-7}	1.0353×10^{-10}
	8	0.2503	5.0062×10^{-7}	1.6573×10^{-10}
	10	0.2504	6.2577×10^{-7}	2.0723×10^{-10}
900	2	0.2712	2.0866×10^{-7}	6.8484×10^{-11}
	5	0.2714	5.2166×10^{-7}	1.7710×10^{-10}
	8	0.2715	8.345×10^{-7}	2.7420×10^{-9}
	10	0.2716	1.0433×10^{-6}	3.4286×10^{-9}

With the presence of water vapor, the occurrence of breakaway oxidation is related to the oxidation temperature, duration and atmosphere. With different absolute humidity, the breakaway oxidation happens at different parts of simples, as shown in Figure 4.22, indicating that the reasons of breakaway are not the same. The breakaway oxidation was also observed in the studies other authors [79, 82, 107].The details of breakaway oxidation will be discussed in Chapter 6.

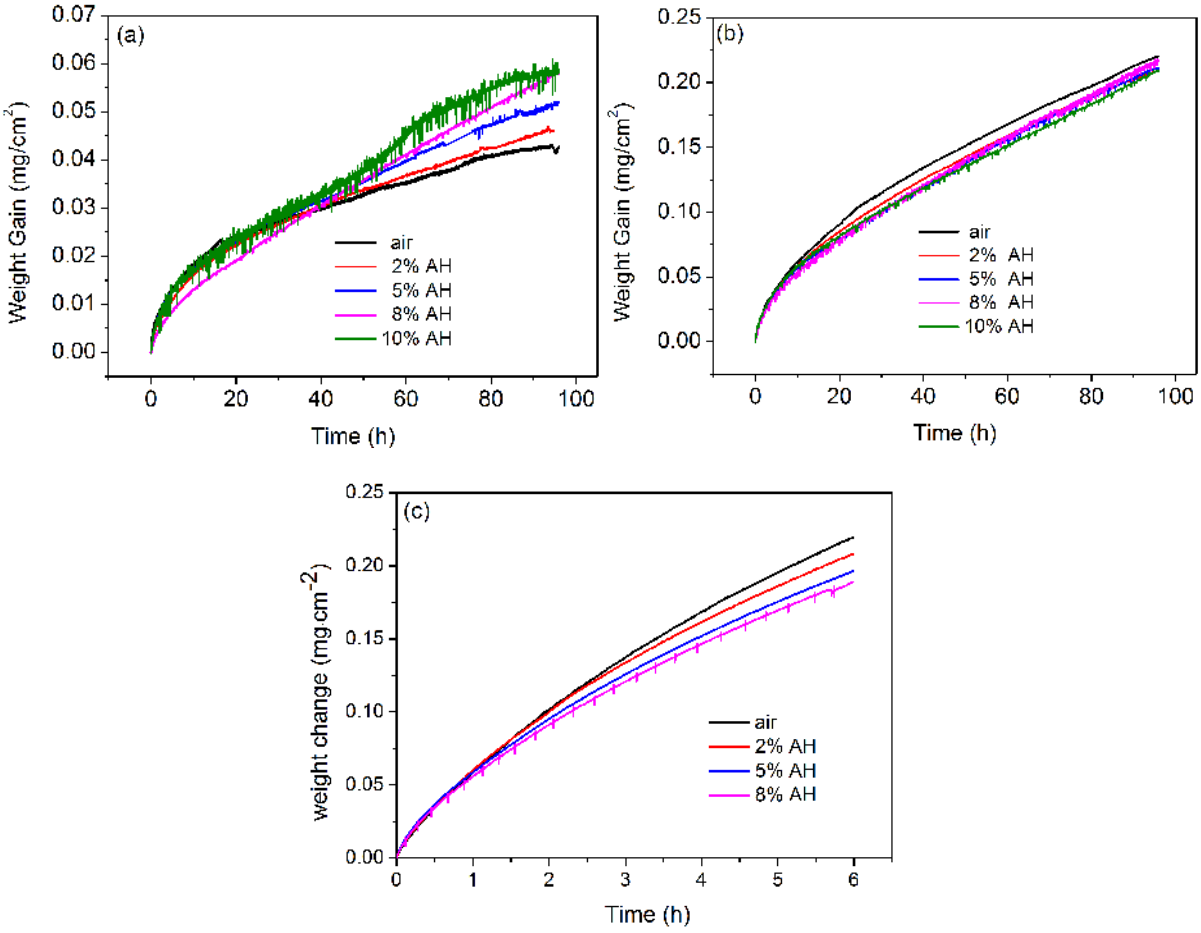

Figure 4.34 Corrected weight change curves of AISI 430 stainless steel during exposure in air with different absolute humidity (AH) at 700 ℃ for 96h (a), at 800 ℃ for 96h (b) and at 900 ℃ for 6h (c)

4.2.5.2 Composition and structure

X-ray diffraction and SEM/EDX analysis indicate that the oxide scales formed under different oxidation atmosphere had similar composition and structure: an outer $Mn_{1.5}Cr_{1.5}O_4$ spinel layer (with little Fe incorporation), an inner Cr_2O_3 and a discontinuous SiO_2 at the scale/substrate interface.

But the $Mn_{1.5}Cr_{1.5}O_4$ grains formed in the atmospheres with and without water vapor are not the same. All the grains formed in air are regular octahedral. While in the atmosphere with water vapor, some irregular shaped grains formed on the surface. This is because the H_2O molecules took part in the formation of $Mn_{1.5}Cr_{1.5}O_4$ grains at the surface. Then the irregular shaped grains are formed due to the volatilization of these molecules from the grains.

4.2.5.3 Growth mechanism

With the XPS analysis, we found that $Cr(OH)_3$ was formed in the oxide scale. According to Junbo Huang et al [139], this is due to the nucleation and growth of $Cr(OH)_3$ prefer on the Cr^{3+} enrichment surface by Reaction (4-11). And the $Cr(OH)_3$ can converted into Cr_2O_3 by Reaction (4-12).

$$Cr^{3+} + 3OH^- \rightarrow Cr(OH)_3 \qquad (4\text{-}11)$$

$$Cr(OH)_3 + Cr + 3OH^- \rightarrow Cr_2O_3 + 3H_2O + 3e^- \qquad (4\text{-}12)$$

In the section 4.1, we have definitely demonstrated that the formation of oxide scale is controlled by the outward diffusion of metal ions in dry air. The SIMS analysis of ^{16}O and ^{18}O has also been done by G. Bamba et al [85], they found that the oxidation of Fe-15Cr is predominated by inward transport of OH^- in atmosphere containing water vapor, and the adhesion of scale is improved. In this work, more hydroxides were found in the oxide scale

formed with the introduction of water vapor, but the increase is not significant. It is unconvincing to get the conclusion that the oxidation is controlled by the inward diffusion of OH^-. Based on the above analysis, an oxidation mechanism of AISI 430 stainless steel in atmosphere containing water vapor is proposed. Figure 4.35 displays the schematic diagram of the growth mechanism of the oxide scale, the oxidation is still controlled by the outward diffusion of metal ions. The only difference between the oxidation in dry air and in air with water vapor is that more amount of OH^- inward transport through the oxide scale.

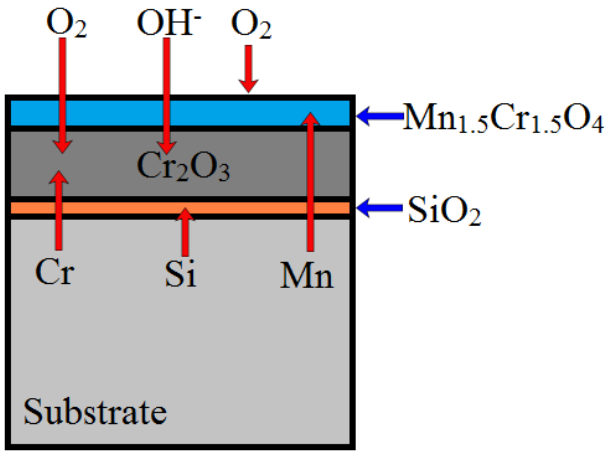

Figure 4.35 Schematic diagram of the growth mechanism of oxide scale on AISI 430 alloy at high temperature in atmosphere containing water vapor

4.3 Conclusion

The oxidation behavior of AISI 430 stainless steel was studied at 700 ℃, 800 ℃ and 900 ℃ in air with different absolute humidity (0-10%). The oxidation kinetics, surface morphology, oxide composition and growth mechanism were discussed in this chapter.

A parabolic kinetics was observed at all temperatures in dry air. It showed the formation of

$Mn_{1.5}Cr_{1.5}O_4$ spinel layer and protective Cr_2O_3 layer. A discontinuous SiO_2 layer at the scale/substrate was also observed. The relatively high intensities of spinel peaks are not due to the high proportion of this phase in the oxide scale but to the formation of it in the outer part of the scale. The concentration of SiO_2 is small due to it is determined by the amount of Si in the alloy. The oxidation mechanism in dry air is present and the oxidation is mainly controlled by the outward diffusion of metal ions.

Table 4.8 Comparison of the oxidation behavior of AISI 430 stainless steel in dry air and in air with water vapor

	In dry air	With water vapor
Oxidation kinetic	Oxidation kinetic followed the parabolic law at 700 ℃, 800 ℃ and 900 ℃	1) Breakaway oxidation took place at 900 ℃ 2) Before the occurrence of the breakaway oxidation, the weight gain decreased with the increasing of absolute humidity and also followed the parabolic law
Surface morphology	Spinel grains formed on the surface were regular	Some irregular shaped spinel grains formed on the surface
Diffusion mechanism	Controlled by the outward diffusion of Cr ions	More OH^- ions inward transport through the oxide scale

With the introduction of water vapor in the oxidation atmosphere, the oxidation behaviors were not the same at different temperature. At 700 ℃ and 800 ℃, this alloy exhibits a good oxidation resistance due to the fact that whatever the composition of oxidation atmosphere, the oxide scale is protective. The breakaway oxidation took place at 900 ℃ with the introduction of water vapor. The breakaway oxidation is related to the oxidation temperature, duration and oxidation atmosphere. Before the occurrence of breakaway oxidation, the weight gain decreased with the increase of water vapor due to evaporation of $CrO_2(OH)_2$, and the outer spinel layer can suppress the evaporation. The oxide growth on AISI 430 stainless steel

in atmosphere containing water vapor is not identical as that in dry air. In the presence of water vapor, the oxidation is still controlled by the outward diffusion of metal ions; in addition, more amount of OH^- inward transport through the scale. The comparison of the oxidation behavior in dry air and in air with water vapor is given in Table 4.8.

4.4 References

[9]. S. Geng, J. Zhu, Promising alloys for intermediate-temperature solid oxide fuel cell interconnect application, J. Power Sources 160 (2006) 1009-1016.

[10]. N. Birks, G.H. Meier, F.S. Pettit, Introduction to the high-temperature oxidation of metals, in, Cambridge University, UK, 2006.

[66]. B. Hua, Y. Kong, W. Zhang, J. Pu, B. Chi, L. Jian, The effect of Mn on the oxidation behavior and electrical conductivity of Fe–17Cr alloys in solid oxide fuel cell cathode atmosphere, J. Power Sources 196 (2011) 7627-7638.

[71]. H.E. Evans, D.A. Hilton, R.A. Holm, S.J. Webster, Influence of silicon additions on the oxidation resistance of a stainless steel, Oxid. Met. 19 (1983) 1-18.

[75]. P. Kofstad, High temperature corrosion, Elsevier, Essex, England, 1988.

[79]. H. Asteman, J.E. Svensson, L.G. Johansson, Effect of Water-Vapor-Induced Cr Vaporization on the Oxidation of Austenitic Stainless Steels at 700 and 900℃, J. Electrochem. Soc. 151 (2004) B141.

[82]. S.-Y. Cheng, S.-L. Kuan, W.-T. Tsai, Effect of water vapor on annealing scale formation on 316 SS, Corros. Sci. 48 (2006) 634-649.

[83]. J. Ehlers, D.J. Young, E.J. Smaardijk, A.K. Tyagi, H.J. Penkalla, L. Singheiser, W.J. Quadakkers, Enhanced oxidation of the 9%Cr steel P91 in water vapour containing environments, Corros. Sci. 48 (2006) 3428-3454.

[84]. D.J. Young, B.A. Pint, Chromium volatilization rates from Cr_2O_3 scales into flowing gases containing water vapor, Oxid. Met. 66 (2006) 137-153.

[85]. G. Bamba, Y. Wouters, A. Galerie, G. Borchardt, S. Shimada, O. Heintz, S. Chevalier, Inverse growth transport in thermal chromia scales on Fe–15Cr steels in oxygen and in water vapour and its effect on scale adhesion, Scripta Mater. 57 (2007) 671-674.

[87]. M. Stanislowski, E. Wessel, K. Hilpert, T. Markus, L. Singheiser, Chromium Vaporization from High-Temperature Alloys, J. Electrochem. Soc. 154 (2007) A295.

[89]. N.K. Othman, J. Zhang, D.J. Young, Temperature and water vapour effects on the cyclic oxidation behaviour of Fe–Cr alloys, Corros. Sci. 52 (2010) 2827-2836.

[107]. H. Asteman, J.E. Svensson, L.G. Johansson, Evidence for Chromium Evaporation Influencing the Oxidation of 304L: The Effect of Temperature and Flow Rate, Oxid. Met. 57 (2002) 193-216.

[108]. H. Asteman, J.E. Svensson, L.G. Johansson, Oxidation of 310 steel in H2O/O2 mixtures at 600 ℃: the effect of water-vapour-enhanced chromium evaporation, Corros. Sci. 44 (2002) 2635-2649.

[109]. G.R. Holcomb, Calculation of Reactive-evaporation Rates of Chromia, Oxid. Met. 69 (2008) 163-180.

[110]. P.J. Meschter, E.J. Opila, N.S. Jacobson, Water Vapor–Mediated Volatilization of

High-Temperature Materials, Annual Review of Materials Research 43 (2013) 559-588.

[111]. R. Sachitanand, M. Sattari, J.-E. Svensson, J. Froitzheim, Evaluation of the oxidation and Cr evaporation properties of selected FeCr alloys used as SOFC interconnects, Int. J. Hydrogen. Energ 38 (2013) 15328-15334.

[120]. M. Palcut, L. Mikkelsen, K. Neufeld, M. Chen, R. Knibbe, P.V. Hendriksen, Corrosion stability of ferritic stainless steels for solid oxide electrolyser cell interconnects, Corros. Sci. 52 (2010) 3309-3320.

[121]. H.V. Atkinson, Evolution of grain structure in nickel oxide scales, Oxid. Met. 28 (1987) 353-389.

[122]. P. Kofstad, K.P. Lillerud, Chromium transport through Cr_2O_3 scales I. On lattice diffusion of chromium, Oxid. Met. 17 (1982) 177-194.

[123]. J. Jedlinski, G. Borchardt, On the oxidation mechanism of alumina formers, Oxid. Met. 36 (1991) 317-337.

[124]. S.N. Basu, J.W. Halloran, Tracer isotope distribution in growing oxide scales, Oxid. Met. 27 (1987) 143-155.

[125]. B.A. Pint, J.R. Martin, L.W. Hobbs, 18O/SIMS characterization of the growth mechanism of doped and undoped α-Al2O3, Oxid. Met. 39 (1993) 167-195.

[126]. R.K. Wild, High temperature oxidation of austenitic stainless steel in low oxygen pressure, Corros. Sci. 17 (1977) 87-104.

[127]. M. Landkof, A.V. Levy, D.H. Boone, R. Gray, E. Yaniv, The Effect of Surface Additives on the Oxidation of Chromia-Forming Alloys, Corrosion 41 (1985) 344-357.

[128]. F.H. Stott, G.C. Wood, J. Stringer, The influence of alloying elements on the development and maintenance of protective scales, Oxid. Met. 44 (1995) 113-145.

[129]. M. Skeldon, J.M. Calvert, D.G. Lees, An Investigation of the Growth-Mechanism of Cr2O3 on Pure Chromium in 1 Atm Oxygen at 950C, Oxid. Met. 28 (1987) 109-125.

[130]. D.W. Yun, H.S. Seo, J.H. Jun, J.M. Lee, K.Y. Kim, Molybdenum effect on oxidation resistance and electric conduction of ferritic stainless steel for SOFC interconnect, Int. J. Hydrogen. Energ 37 (2012) 10328-10336.

[131]. R.-H. Jung, H. Tsuchiya, S. Fujimoto, XPS characterization of passive films formed on Type 304 stainless steel in humid atmosphere, Corros. Sci. 58 (2012) 62-68.

[132]. A.M. Huntz, A. Reckmann, C. Haut, C. Sévérac, M. Herbst, F.C.T. Resende, A.C.S. Sabioni, Oxidation of AISI 304 and AISI 439 stainless steels, Mater. Sci. Eng. A 447 (2007) 266-276.

[133]. J. Xu, X. Wu, E.-H. Han, The evolution of electrochemical behaviour and oxide film properties of 304 stainless steel in high temperature aqueous environment, Electrochim. Acta 71 (2012) 219-226.

[134]. X. Cheng, Z. Feng, C. Li, C. Dong, X. Li, Investigation of oxide film formation on 316L stainless steel in high-temperature aqueous environments, Electrochim. Acta 56 (2011) 5860-5865.

[135]. Č. Donik, A. Kocijan, J.T. Grant, M. Jenko, A. Drenik, B. Pihlar, XPS study of duplex stainless steel oxidized by oxygen atoms, Corros. Sci. 51 (2009) 827-832.

[136]. X. Peng, J. Yan, Y. Zhou, F. Wang, Effect of grain refinement on the resistance of 304 stainless steel to breakaway oxidation in wet air, Acta Mater. 53 (2005) 5079-5088.

[137]. B. Hua, J. Pu, F. Lu, J. Zhang, B. Chi, L. Jian, Development of a Fe–Cr alloy for interconnect application in intermediate temperature solid oxide fuel cells, J. Power Sources 195 (2010) 2782-2788.

[138]. E.J. Opila, D.L. Myers, N.S. Jacobson, I.M.B. Nielsen, D.F. Johnson, J.K. Olminsky, M.D. Allendorf, Theoretical and Experimental Investigation of the Thermochemistry of CrO2(OH)2(g), The Journal of Physical Chemistry A 111 (2007) 1971-1980.

[139]. J. Huang, X. Wu, E.-H. Han, Electrochemical properties and growth mechanism of passive films on Alloy 690 in high-temperature alkaline environments, Corros. Sci. 52 (2010) 3444-3452.

CHAPTER 5 The Study of the Residual Stresses in the Oxide Scale

The exposure of a metallic alloy in an oxidizing atmosphere at high temperature would result in the formation of an oxide scale on the surface of the alloy. If the scale is protective, then the oxidation will be controlled by the ions diffusion through the scale. The growth of the oxide is accompanied by stresses, which can influence in return the oxidation kinetic and structure of the oxide scale. The residual stresses in the oxide scale mainly come from two parts: growth stresses generated during the oxidation and thermal stresses generated during the cooling. The generation of thermal stresses is due to the mismatch of the thermal expansion of the oxide scale and the alloy, which has been well studied. While, the origins of the growth stresses are still unclear. Some works have been done to study this stresses and it has been found that the generation of growth stresses in the oxide scale is related to the oxide growth mechanism. The possible origins of the growth stresses have been given in Chapter 2.

In the Chapter 4, we have found that the oxidation mechanisms in dry air and in air with water vapor are not identical. Therefore, the evolution of residual stresses in the oxide scale might be different. To study the influence of water vapor on residual stresses, in this chapter, XRD method will be used at room temperature to determine the residual stresses experimentally in the oxide layers formed on AISI 430 alloy after oxidation in air with different absolute humidity at 700 ℃, 800 ℃ and 900 ℃. Evolution of growth stresses in the oxide scale will be determined by deflection method in dry air and in air with 5% absolute humidity.

5.1 Conditions and parameters for determining residual stresses

The determination of residual stresses in the oxide scale can be conducted by the classic $\sin^2\psi$ method according to the European Standard EN 15305 (version of April 2009) [117]. In this study, as we mentioned before, the oxide scale is mainly composed of an inner Cr_2O_3 layer and an outer $Mn_{1.5}Cr_{1.5}O_4$ layer. It is true that SiO_2 layer was also found at the scale/substrate interface, but it very thin and discontinuous. Therefore, for the oxide, we just focus on the residual stresses in the Cr_2O_3 layer and $Mn_{1.5}Cr_{1.5}O_4$ layer in this study. At the same time, the residual stresses in the substrate will also be determined.

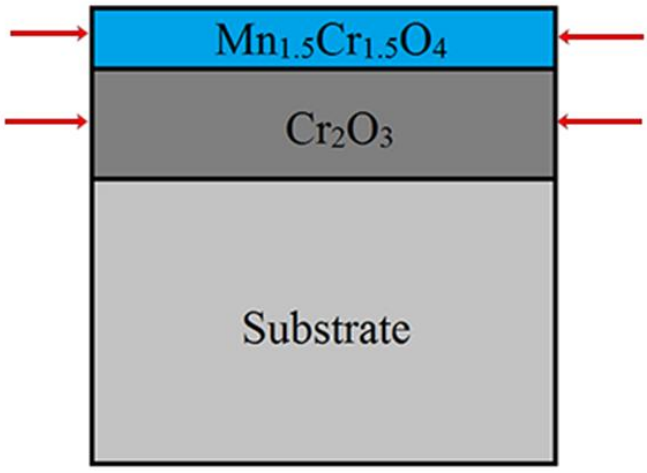

Figure 5.1 Schematic of the oxide layers studied by residual stresses analysis

In order to get sufficient intensity, the {104}, {311} and {110} peaks are selected respectively for Cr_2O_3, $Mn_{1.5}Cr_{1.5}O_4$ and substrate to determine the residual stress level (shown in Figure 5.2), and more than 13 peaks with different ψ (-60 ° to +60 °) were recorded. Each step of 2θ scanning is 0.04 °, and lasts for 15s per step. The details of the operation parameters for determining residual stresses by XRD method is given in Table 5.1.

Table 5.1 Operation parameters for determining residual stresses by XRD method

Analyzed zone	2mm x 2mm		
ψ angle amplitude	[-60 °; 60 °]		
Number of ψ angle	13		
diffraction angle 2θ	33.6 ° for $\{104\}_{Cr2O3}$, 35.1 ° for $\{311\}_{Mn1.5Cr1.5O4}$, 44.6 ° for $\{110\}_{substrate}$		
2θ angle interval	[32.2 °-35 °]	[33.7 °-36.5 °]	[43.2 °-46 °]
2θ step	0.04		
Acquisition time	15s/step		
Peak position error	0.005^{o}		

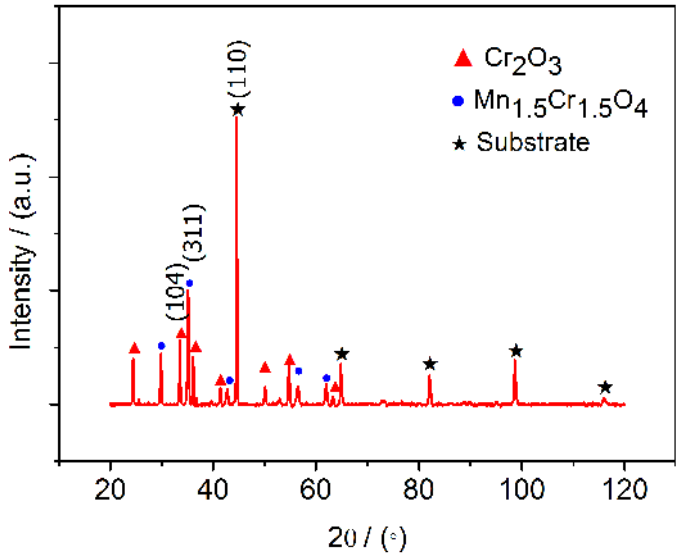

Figure 5.2 Peaks selected for residual stresses analysis from XRD pattern after oxidation in dry air for 96h

The Poisson's ratio, Young's modulus and thermal expansion coefficients used for the residual stresses calculation are given in Table 5.2. For oxide phases, the elastic anisotropy factor has been fixed to be one because of the lack of information in bibliography. Since all XRD intensities correspond to theoretical proportions, there are no obvious texture effects. The slopes of the d-spacing vs. f ($\sin^2\psi$) plots of sample after oxidation in dry air for 96h at 900 ℃,

used to determine stresses, are shown in Figure 5.3. The precision of stress determination is smaller than 30 MPa.

Table 5.2 Young's modulus, Poisson's ratio and thermal expansion coefficients used in calculation

	Young's modulus (GPa)	Poisson's ratio	TEC (k^{-1})
Cr_2O_3	280 [19]	0.29 [47]	$9.6x10^{-6}$ [9]
$Mn_{1.5}Cr_{1.5}O_4$	250 [140]	0.27 [140]	$7.5x10^{-6}$ [9]
Substrate	220 [141]	0.28 [141]	$12.6x10^{-6}$[66]

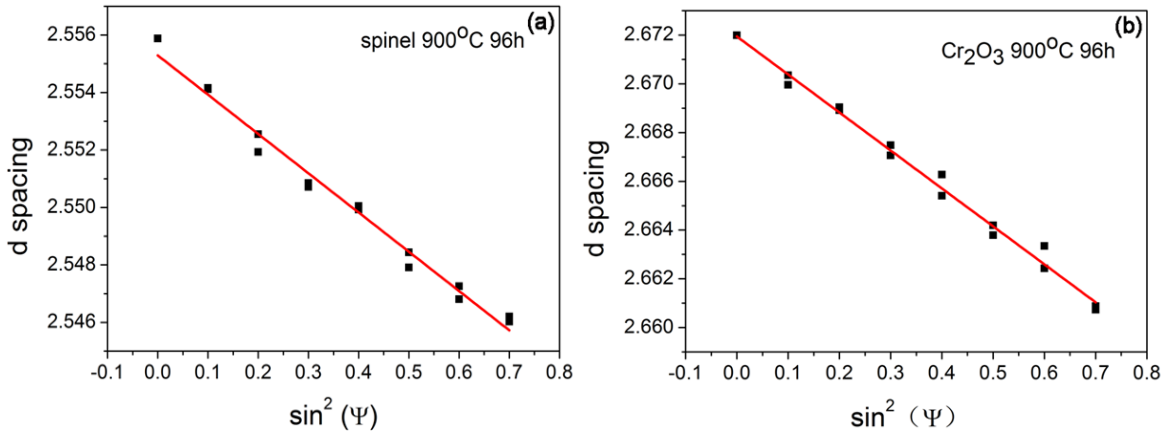

Figure 5.3 The d vs. f ($\sin^2\psi$) plot of oxide layers after oxidation in dry air for 96h at 900 ℃

5.2 Residual stresses in the oxide layers determined by XRD method

5.2.1 Residual stresses after oxidation in dry air

It is known that the residual stresses determined by XRD method at room temperature is composed of thermal stresses, growth stresses and chemical stresses.

$$\sigma_{\text{residual}} = \sigma_{\text{growth}} + \sigma_{\text{thermal}} + \sigma_{chemical} \qquad (5\text{-}1)$$

The chemical stresses are coming from the diffusion of ions during the isothermal oxidation, and are very small compared to the growth stresses and thermal stresses. In this study, the chemical stresses are ignored.

$$\sigma_{residual} = \sigma_{growth} + \sigma_{thermal} \quad (5\text{-}2)$$

Table 5.3 Thermal stresses at room temperature in the oxide layers calculated from Equation (5-4)

Temperature	Cr_2O_3 (MPa)	$Mn_{1.5}Cr_{1.5}O_4$ (MPa)
700 ℃	-800	-485
800 ℃	-915	-555
900 ℃	-1035	-630

For the elastic thermal stresses in the oxide scale, it can be calculated through the theoretical equation [34, 142]:

$$\sigma_{thermal} = \frac{\frac{E_o}{1-\nu_o}(\alpha_o-\alpha_m)}{1+\frac{e_o E_o}{e_m E_m}(\frac{1-\nu_m}{1-\nu_o})}\Delta T \quad (5\text{-}3)$$

Considering the relative thicknesses of the oxide scale and metal and assuming that the oxide layers and the substrate are remain elastic (no plasticity, no creep, no cracking and no spalling) during the whole cooling from oxidation temperature to room temperature, the equation (5-3) can be simplified as:

$$\sigma_{thermal} = \frac{E_o(\alpha_o-\alpha_m)}{1-\nu_o}\Delta T \quad (5\text{-}4)$$

where ν is the Poisson's ratio, E is the Young's modulus, e is the thickness, α is the thermal expansion coefficients and ΔT is the temperature difference of the oxidation temperature and room temperature, and the subscript m and o represent metal and oxide, respectively. The

calculated thermal stresses in the two layers at different oxidation temperature are given in Table 5.3.

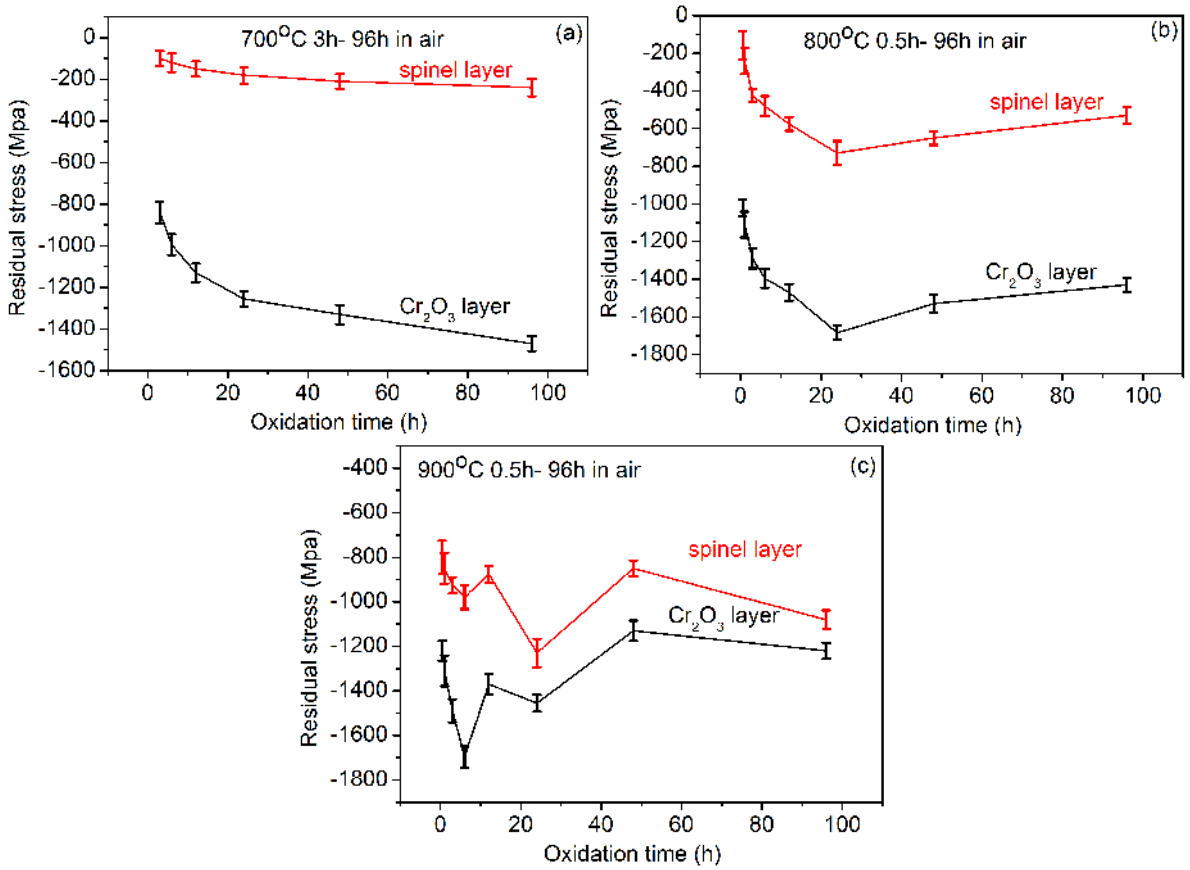

Figure 5.4 Residual stresses in the oxide layers after oxidation in dry air at (a) 700 ℃, (b) 800 ℃ and (c) 900 ℃

The in-plane residual stresses levels in oxide layers after oxidation at 700˚C, 800˚C and 900˚C are shown in Figure 5.4, indicating that the residual stresses are compressive. And as the time went by, the changing trends of the residual stresses in the two oxide layers are similar at all oxidation temperature, this may due to the good adherence between the two oxide layers. Thus, there is an accommodation problem between the stress levels of the chromia layer and the spinel layer. For this system composed of two oxide layers and one substrate, the residual stresses in the each layer could be expressed as Equation (5-5). Since the thermal expansion coefficient of the spinel is smaller than that of the chromia, the

retractions of these two layers are different during the cooling, as shown in Figure 5.5. Therefore, the stresses in the spinel layer can be affected by the stresses in the chromia layer. But it is unclear that if these two layers can influence each other during the isothermal oxidation stage.

$$\sigma_{residual} = \sigma_{growth} + \sigma_{thermal} + \sigma_{accommodation} \quad (5\text{-}5)$$

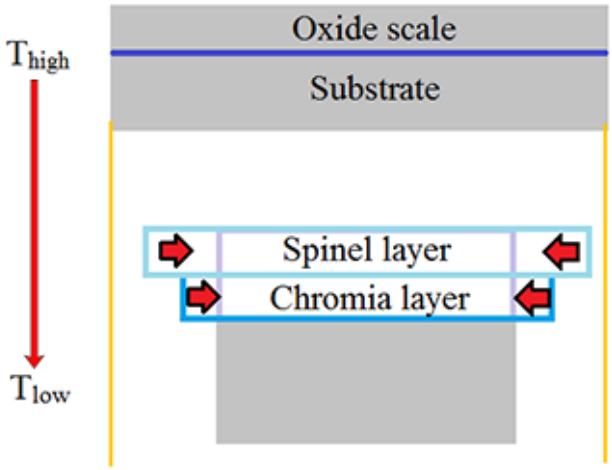

Figure 5.5 Schematic illustration of thermal strain in the two layers during cooling

For its protective property, more attentions are paid on Cr_2O_3 layer in our study. At the beginning of the oxidation, the stresses increase very fast at all temperatures. At 700 ℃, the residual stresses levels in this layer increase with the increasing of oxidation duration. At 800 ℃, stresses values increase at the first 24 hours and followed by an obvious decrease from 24h to 96h. At 900 ℃, the evolution of stresses in chromia layer is more complicated. The stresses increase at 0-6h, 12-24h and 48-96h, and decrease at 6-12 h and 24-48h. According to Equation (5-4), the thermal stress level does not depend on the oxidation duration or on the scale thickness but only on the temperature variation, as shown in Table 5.3. So the fluctuation of the stresses values at the same oxidation temperature indicates the competition of stresses generation and relaxation during oxidation [28].

Stresses relief is not observed at 700 ℃, but is observed at 800 ℃ and 900 ℃. Stresses are relaxed after 24h for 800 ℃ and after 6h for 900 ℃. What is more, a second stresses relief occurs from 24h to 48h at 900 ℃. This indicates that the stresses relaxation is related to the thickness of the oxide layer, and this can explain that why no stresses relief was observed at 700 ℃. The thickness of the chromia layer formed at 700 ℃ is not thick enough to relax. The elastic strain energy stored in the scale per unit area is $(1-\upsilon)\ \sigma^2\ h\ /\ E$, and the criterion for spallation failure is given in Equation [10]:

$$\frac{(1-\upsilon)\sigma^2 h}{E} > G_c \qquad (5\text{-}6)$$

where E and ν are the elastic modulus and Poisson's ratio of the scale, h is the scale thickness, σ is the equal biaxial residual stresses in the scale and G_c is fracture resistance of the interface. But no spallation is found in the oxide surface morphology in present experiments. If G_c is high, the compressive stresses can be accommodated by simultaneous deformation of the scale and alloy without spallation. In this study, this simultaneous deformation has been observed in the cross section of AISI 430 alloy after oxidation in dry air for 96h (Figure 4.11).

Figure 5.6 Surface morphology of the oxide scale on the AISI 430 alloy after oxidation in dry air for 96h at 900 ℃

Tolpygo et al [21] have found that the lateral dimensions of the samples increase with oxidation duration, which indicates relaxation of residual stresses during the oxidation. In this study, buckling is observed on the oxide scale after oxidation, as shown in Figure 5.6. It is believed that the generation of buckling is due to the expansion of oxide scale in the lateral direction. And this lateral expansion may be the result of formation of new oxide inside the oxide scale. Buckling is one of the ways by which the elastic strain energy in the oxide scale can be reduced. Thus，buckling is a very important way by which the residual stresses in the oxide scale can be relieved.

From 12h to 24h the residual stresses increased at 900℃, especially in the spinel layer, this is because after 12h oxidation the continuous spinel layer did not form as we mentioned before, and there was no contribution of thermal stresses to the total residual stresses, so the -875±35 MPa stresses mainly come from the growth stresses. After the formation of continuous spinel layer at 24h, the thermal stresses play a part in the total stresses, thus lead to the increase of stresses obviously. The calculated thermal stress in the spinel layer is -630 MPa, but not all the calculated stresses can appear in the total residual stresses level, because there is an accommodation problem between the two oxide layers. The good adherence between the two oxide layers arise the stresses in the Cr_2O_3 layer simultaneously. The increase of residual stresses from 48h to 96h is mainly originated from growth stresses in the duration when the Cr_2O_3 layer thickens after the stresses relaxation at 48h. All this indicates that the growth stresses generated during oxidation plays an important role in residual stresses at room temperature for AISI 430 stainless steel, and it is in contrary to the previous studies of residual stresses in Cr_2O_3 for Ni-Cr alloy [18, 19]. The thermal stress model tends to exaggerate the stress value: at high temperature some creep may occur, especially in the substrate, and the waviness of the surface will also relax part of the thermal stresses. The Rhines-Wolf model suggests that the growth stresses is generated by the formation of new oxide inside the scale due

to counter diffusion of the oxidizing component and oxygen during high temperature oxidation [16, 28, 29]. Although oxidation of AISI 430 alloy is mainly controlled by the outward diffusion of Cr and Mn, the inward diffusion of oxygen happens inevitable, thus generating the growth stresses in the oxide scale.

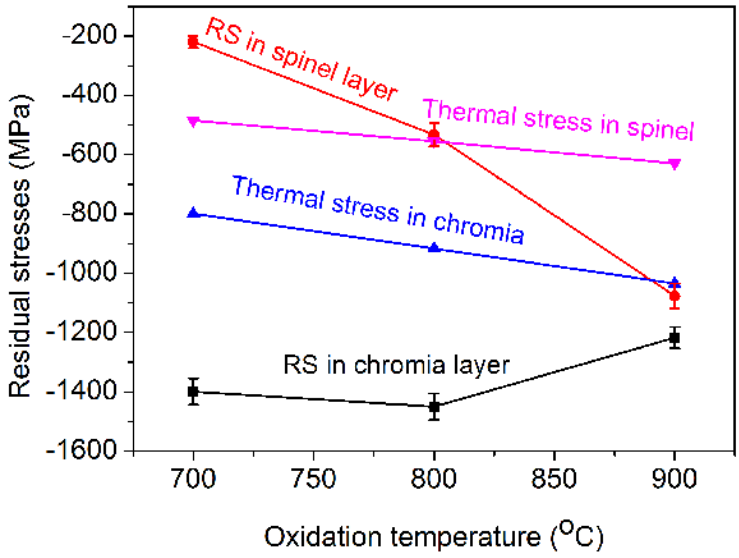

Figure 5.7 Residual stresses in oxide layers after oxidation in dry air at 700-900 ℃ for 96h

Figure 5.7 shows the effect of oxidation temperature on the residual stresses in chromia layer and in spinel layer. It can be seen that the oxidation temperature has different effect on two layers. For the chromia layer, after 96h oxidation from 700°C to 800°C, the residual stresses increased a little, this is mainly due to the increase of thermal stresses. Since the stresses relaxation happens at 900°C 48h, the stresses decreased from 800°C to 900°C. But for the spinel layer, the compressive residual stresses increased obviously, from 700°C to 800°C only the growth stresses lead to increase of stresses, because the continuous oxide layer didn't form. While from 800°C to 900°C, the stresses increase was due to the combination of growth stresses, thermal stresses and also stresses relaxation. So the influences of the temperature on residual stresses in the two layers are definitely different, especially before the formation of the continuous spinel layer. However, seldom previous theoretical and experimental studies

considered this difference, just saw the oxide layers as a whole during calculate and measure the residual stresses [143].

Table 5.4 lists the residual stresses in substrate after oxidation at 900°C. The residual stresses in the substrate are smaller than that in oxide scale. The stresses are still compressive, and there is no much difference between the residual stresses in the substrate with increasing oxidation time. It's in agreement with the result of A.M. Huntz et al. [18] on Nickel, and the author thought that was the result of internal oxidation of the substrate, but in our experiments we didn't observe internal oxidation zone. Moreover, considering the small compressive stresses still existed after the stresses relief by the undulation of the substrate, we attribute that to the good adherence of the oxide scale and the substrate. Due to the limitation of penetration of X-ray, the determined residual stresses are just from the substrate near the scale/substrate interface. Increasing the depth of penetration, tensile residual stresses would be observed to balance the stresses in the oxide scale. And the tensile stresses in the substrate that balance the compressive stresses in the scale should be close to the interface and decrease with the depth.

Table 5.4 Residual stresses in substrate after oxidation in dry air at 900°C

Condition	RS in substrate (MPa)
900°C 1h	- 85 ±10
900°C 6h	- 95 ±15
900°C 12h	- 80 ±10
900°C 24h	- 90 ±10
900°C 48h	- 95 ±15
900°C 96h	- 75 ±20

5.2.2 Residual stresses after oxidation in air with different absolute humidity

For the samples after oxidation in air with different absolute humidity, the in-plane residual stresses in the two oxide layers and in the substrate were determined by XRD method at room temperature at 700 ℃ and 800 ℃, and at 900 ℃ before the occurrence of the breakaway oxidation. The determined residual stresses in chromia layer and in spinel layer after oxidation in air with 2% absolute humidity are given in Figure 5.8. The compressive residual stresses in the two oxide layers decrease and increase simultaneously, same as that in dry air, indicating that the residual stresses in each layer can also influence each other in atmosphere with water vapor.

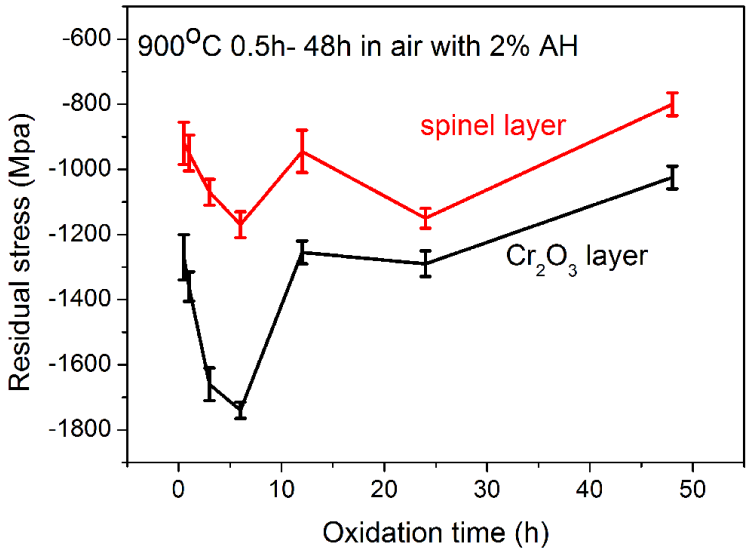

Figure 5.8 Residual stress evolution in oxide layers after oxidation in air with 2%AH

Residual stresses in protective chromia layer after oxidation in air with different absolute humidity at different temperature are given in Figure 5.9. It is clear that the concentration of water vapor in the atmosphere can affect the residual stresses levels in the chromia layer. At 700 ℃ (Figure 5.9 a), the residual stresses increase with the increase of water vapor. For 800° C (Figure 5.9 b), the higher the concentration of water vapor, the bigger the residual stresses

at first 24h and smaller the residual stress after 48h. For 900 ℃, it can be observed that at the beginning of the oxidation (first 6h), the residual stresses are higher in the presence of water vapor (Figure 5.9 c). However, from 12h to 48h the presence of water vapor cause a decrease in the residual stresses level (Figure 5.9 d). In the presence of water vapor, stresses relief was observed at 800 ℃ and 900 ℃, same as that in dry air.

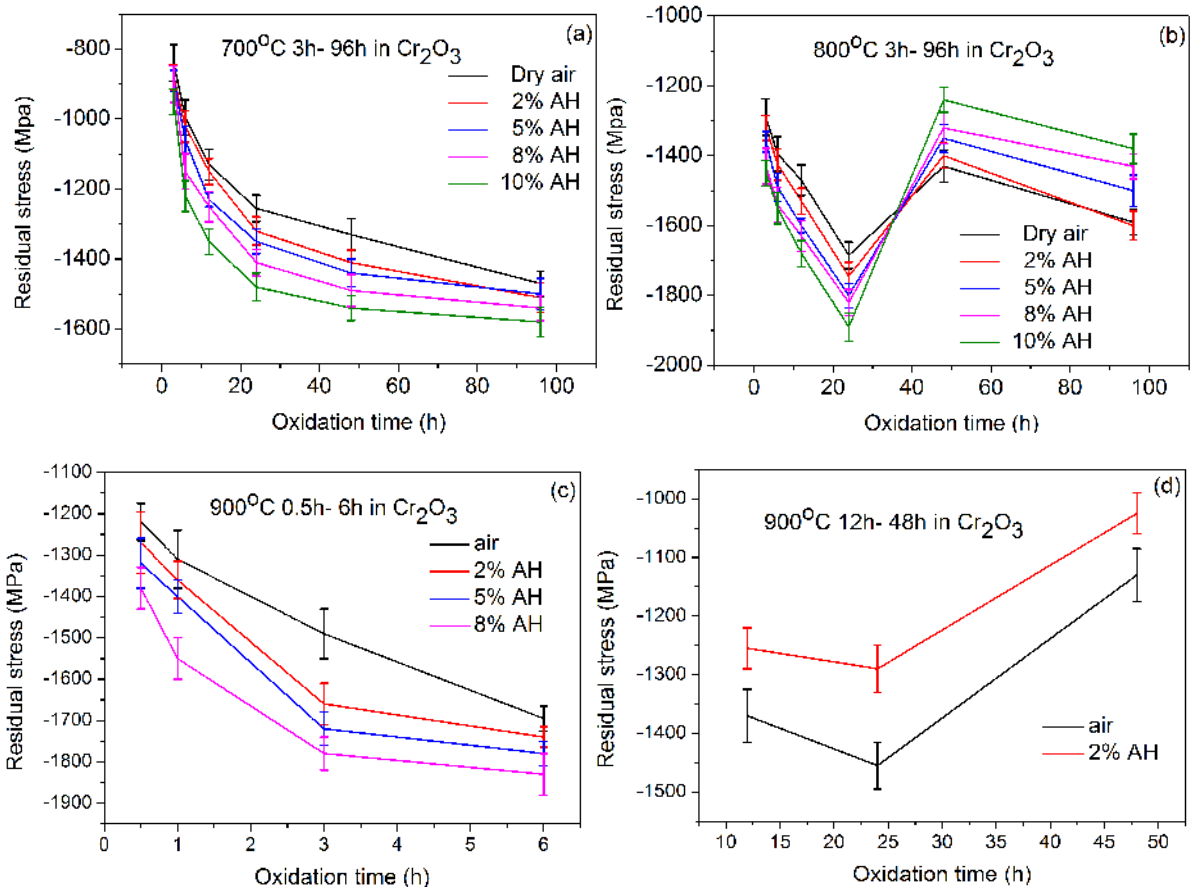

Figure 5.9 Residual stresses in chromia layer after oxidation in air with different absolute humidity (AH) at different temperature

In this study, before the occurrence of stress relief, higher the humidity, larger the compressive residual stresses level in the chromia layer. This is due to oxidation in atmosphere containing water vapor, although the oxidation is mainly controlled by the outward diffusion of ions, hydroxide ions could easily diffuse inside the grain boundaries because of their small radius [85]. In the chapter 4, we have proved that more amount of OH^-

inward transport through the oxide scale in the presence of water vapor. Therefore, more oxides formed in the oxide layer, resulting in bigger growth stresses generated during the oxidation.

While with the increase of oxidation duration, the trend is changed. After the occurrence of stresses relief, the higher the humidity, the smaller the compressive residual stresses level in the chromia layer. As we all know, the stress in the oxide layer can be relaxed by several processes, and the creep of the layer at high temperature is a very important way [21, 23]. The chromia layer formed in the water vapor atmosphere contains hydroxide defects, and these defects would increase with the water humidity, which would increase the mobility of oxygen in it and lead the creep faster. So, the higher the humidity, the more residual stresses relieved in the chromia layer during the oxidation, thus, smaller the residual stresses level.

Figure 5.10 shows the residual stresses in spinel layer after oxidation in air with different absolute humidity at different temperature, indicates that the residual stresses in this layer are increased with the introduction of water vapor in the oxidation atmosphere. At all three temperatures studied, the higher the concentration of water vapor, the bigger the level of residual stresses. The stresses relaxation is also observed in this layer, this might due to the effect of accommodation between the two oxide layers. The stresses in spinel layer decease with the deceasing of stress in the chromia layer.

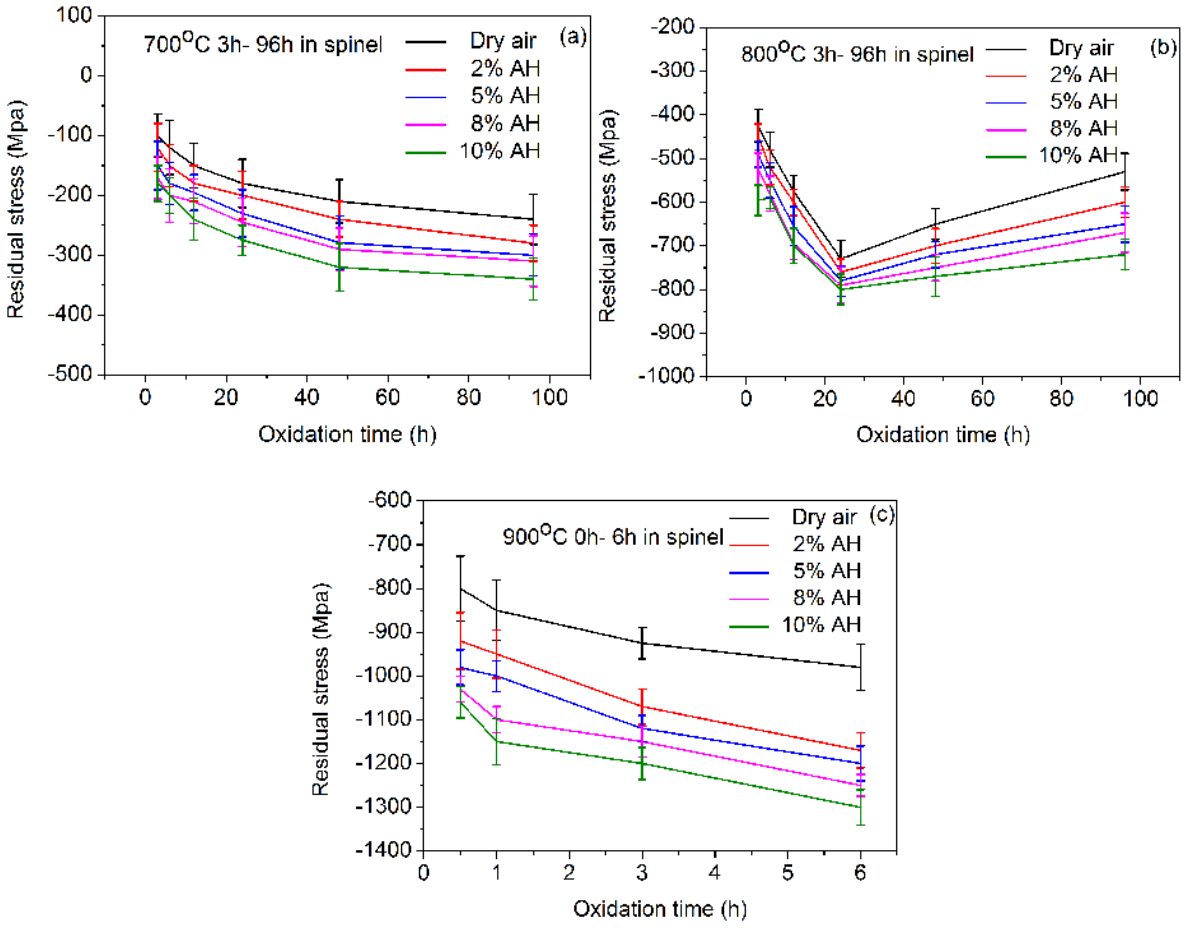

Figure 5.10 Residual stresses in spinel layer after oxidation in air with different absolute humidity (AH) at different temperatures

Table 5.5 Residual stresses in substrate after oxidation at 900 ℃ corresponding to different absolute humidity (AH) and different oxidation time

Condition	Air	2%AH	5%AH
900°C 1h	- 85 ±10	- 85 ±10	- 90 ±10
900°C 6h	- 95 ±15	- 90 ±15	- 95 ±15
900°C 12h	- 80 ±10	- 90 ±10	- 85 ±10
900°C 24h	- 75 ±20	- 85 ±10	- 85 ±10

Table 5.5 lists the residual stresses in the substrate after oxidation in air with different humidity at 900^{o}C. All the residual stresses are small and compressive, and the humidity level had no significant influence on the residual stresses in the substrate.

5.3 Growth stresses determined by deflection method

Generally, the stresses measured after cooling are "residual" stresses, it might confuse the effect of growth stresses and thermal stresses. It is well known that growth stresses generated during the isothermal oxidation can induce the deformation of sample. With this deformation, the level of growth stresses can be estimated. The so-called deflection method is one of these techniques. The deflection method, introduced in chapter 2, is used to measure in-situ growth stresses formed in the oxide scale during the oxidation. This method can measure continuously the growth stresses and the requirement for the equipment is simple. To compare with the residual stresses obtained by XRD method, the deflection experiments are carried out.

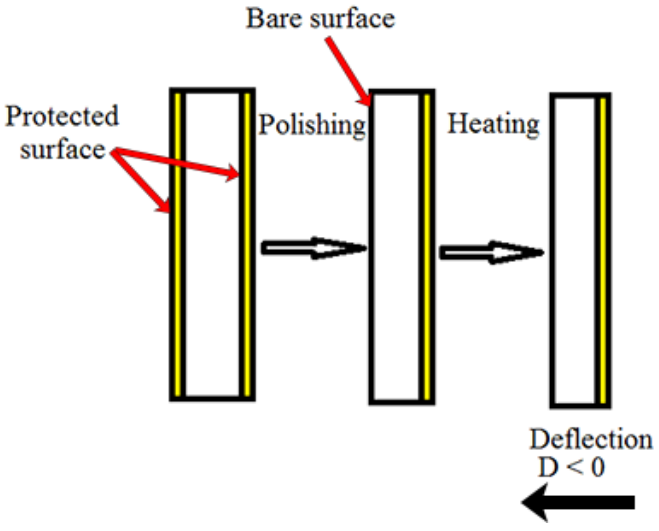

Figure 5.11 Procedure of preparing a sample for deflection experiment

For the deflection experiment, a protective scale must be prepared on one surface of the blade and the other surface is bare. In this study, all the samples were first oxidized in air at 920 ℃

for 8 hours to form a protective chromia scale, and then one of the two surfaces was polished to a bare surface. After that, the asymmetrical samples were used for deflection experiments (shown in Figure 5.11). Comparing to the bare surface, the oxidation on the protective surface is negligible, and the growth stresses generated in it should be ignored. The different stress state in the two surfaces will lead to the curvature of the sample to one direction. In this study, the curvature of the sample toward the right is regarded as positive (see sample position Figure 5.11). What kind of phenomena can lead to a curvature toward the right and the left is given as below [31, 118, 119]:

- Generation of compressive stresses on the bare side or of tensile stresses on the protected side will lead to a curvature of the sample towards the right.
- On the contrary of the phenomena mentioned above will lead to a curvature towards the left. Moreover, relaxation of compressive stresses on the bare side can also induce a curvature toward the left.

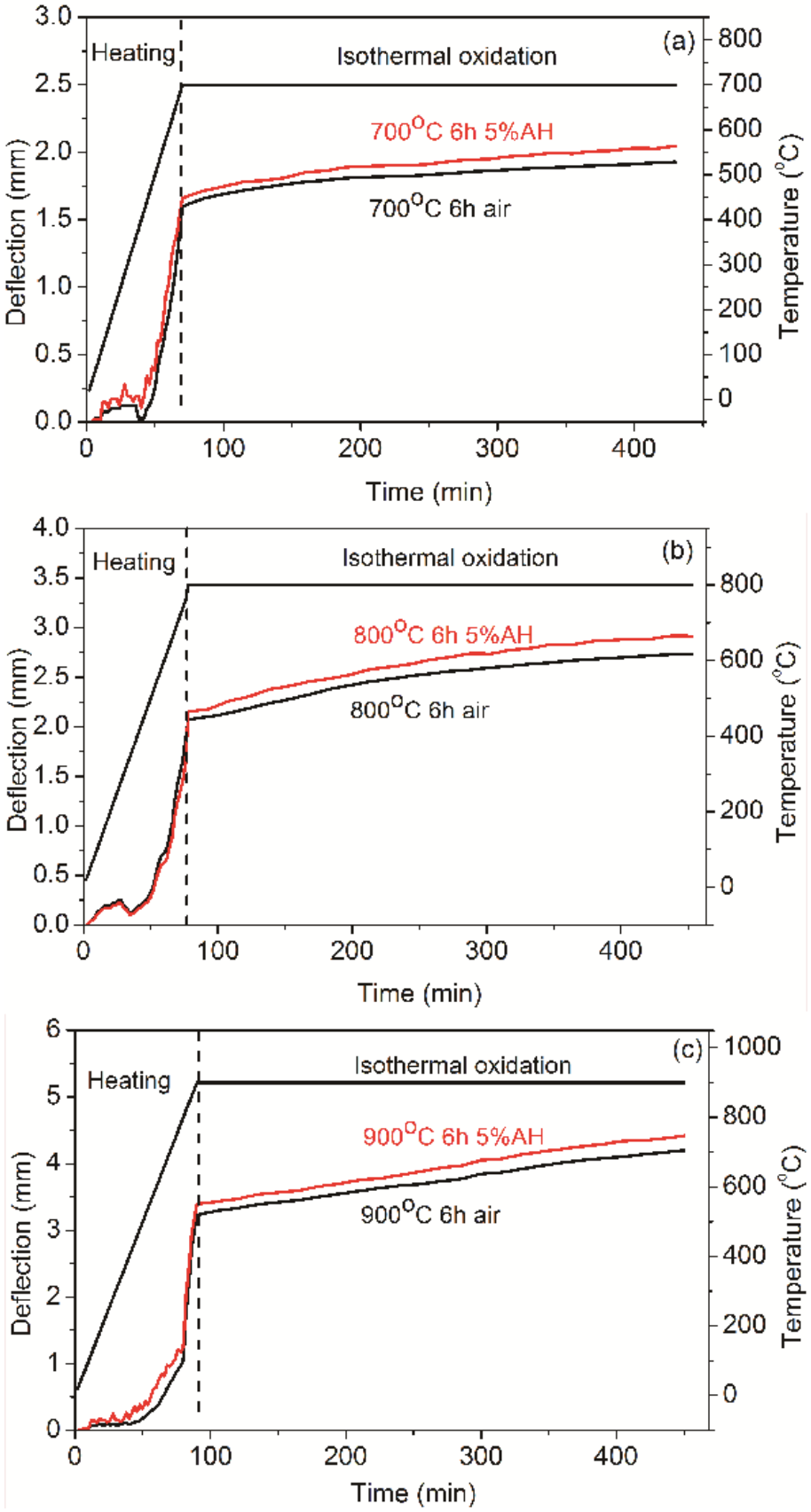

Figure 5.12 Deflection curves of AISI 430 alloy in air at 700 ℃ (a), 800 ℃ (b) and 900 ℃ (c)

Whatever the oxidation temperature and atmosphere, the deflection curves are composed of two parts: temperature rising, isothermal oxidation. Curvature generated during the temperature rising stage might mainly be due to the thermal stresses, and generated during the isothermal oxidation is obviously the result of growth stresses. The thermal expansion coefficient of alloy is bigger that of oxide scale, as shown in Table 5.2, which will result in the curvature toward right side during the temperature rise and toward left side during the cooling.

Figure 5.12 shows the deflection curves of AISI 430 alloy in dry air and in air with 5% absolute humidity at different temperature for 6 hours. At the heating stage, curvatures toward right side are observed at all temperatures. Oscillations in deflection took place at the beginning of the heating stage, and this is because the deflection curves are the result of several phenomena. Compressive stresses were generated during polishing the bare surface, and relaxation of these stresses leads to a negative deviation. A positive deflection generates due to the difference between the thermal expansion coefficient of the protective scale and the alloy. New oxides formed on the bare surface leads to a positive deflection. Therefore, the deflections at the heating stage shows in Figure 5.12 are mainly the combination of these three effects.

During the isothermal stage, the deflection trend of samples is similar at 700℃, 800℃ and 900℃. For all of them, a small positive deviation is throughout the isothermal oxidation, and the amplitude of the deviation is increased with the increasing of temperature. It has been found that relaxation of the compressive polishing stresses is finished at the end of heating [144]，and thermal stresses cannot influence the deflection during the isothermal oxidation stage. Consequently, the positive deflection during isothermal oxidation is the result of new oxides formation. Therefore, the growth stresses in the oxide scale can be calculated by the

Equation (5-7)

$$\sigma_f = D\frac{E_m}{1-v_m^2}\frac{e_m^2}{3e_f L^2} \qquad (5\text{-}7)$$

in which L is the length of the sample, E is the Young's modulus, ν is the Poisson's ratio and e is the thickness. The subscript m and f represent the metal and oxide scale, respectively. The residual stresses calculated by this equation include the growth stresses in both chromia layer and spinel layer. The growth stresses in the oxide scale after oxidation during 6h in dry air are about -750MPa, -915MPa and -1020MPa for 700℃, 800℃ and 900℃, respectively. This indicates that the growth stresses in the oxide scale is very sensitive to the oxidation temperature.

The effect of water vapor on deflection extent is obvious as shown in Figure 5.12. The positive deflection is stronger in air with 5% absolute humidity than that in dry air under all three oxidation temperatures. The growth stresses in the oxide scale after oxidation in air with 5% absolute humidity are about -800MPa, -960MPa and -1075MPa for 700℃, 800℃ and 900℃, respectively. It is clear that more growth stresses generated during the isothermal oxidation stage in atmosphere containing water vapor. This is in accordance with the results of XRD method.

For Fe-Cr alloy, J. Mougin determined the growth stress in oxide scale formed on Fe-18Cr-TiNb at 750℃ during 3h under oxygen by in-situ Raman spectroscopy, and found that the growth stress can reach -2GPa and almost ten times bigger than the thermal stress [15]. In our study, we also found that the growth stress plays an important role in the residual stress. But the growth stress in the oxide scale determined in our study, about 1GPa, is obviously smaller than that got by J. Mougin. Since the oxide scale in our research is

composed by two layers, and there is an accommodation effect between the two oxide layers. This accommodation stress might lead to smaller growth stress determined by in-situ deflection during oxidation.

For the chromia layer formed on Ni-Cr alloy, it has been reported that the growth stress, compared with thermal stress, can be ignored [19]. The in-situ deflection experiments have been done by J. Xiao for Ni-Cr alloy (Inconel 600), oxide growth stress value of -78MPa has been reported [47]. This difference between Ni-Cr alloy and Fe-Cr alloy might due to the oxidation mechanisms of these two alloys are different. The oxidation of Ni-Cr alloy is mainly controlled by the inward diffusion of oxygen ions, and new oxides formed at the scale/substrate interface [34, 35, 47]. In this case, the growth stress is result from the difference between the specific volume of the oxide and the substrate (PBR). For Fe-Cr alloy, as we mentioned, the oxidation is mainly controlled by the outward diffusion of chromium ions, and the growth stress is result from the formation of new oxide inside the oxide scale. PBR mechanism cannot be used to explain the phenomena that generation of growth stress in it. Therefore, the diffusion mechanism of ions during oxidation can affect the residual stress level in the oxide scale.

In our study, the chemical stress is ignored and the residual stress is composed by two parts: thermal stress and growth stress. Since the spinel layer is very thin, it is reasonable to assume that the stress is mainly from chromia layer. The superposition of values of thermal stress in chromia layer calculated by Equation 5-4 and growth stress determined by in-situ deflection method after oxidation at 700 ℃, 800 ℃ and 900 ℃ in dry air for 6h are -1548MPa, -1830MPa, and -2052MPa, respectively, as shown in Table 5.6. At all oxidation temperatures, the calculated values are greater than the residual stress determined by XRD method at room temperature. This mismatch partly can be explained by the fact that the uncertainty of the

thermal expansion coefficients, which are taken from other references. In addition, stress relaxation might take place more or less during the cooling, especially in the alloy. This can also result in the calculated residual stress is smaller than the measured one.

Table 5.6 Comparison of the residual stress calculated by Equation (5-2) and determined by XRD method

	$\sigma_{thermal}$ calculated MPa	σ_{growth} deflection MPa	$\sigma_{residual}$ calculated MPa	$\sigma_{residual}$ XRD MPa
700 ℃	-800	-750	-1550	-995±35
800 ℃	-920	-915	-1835	-1395±50
900 ℃	-1035	-1020	-2055	-1725±45

5.4 Conclusion

The residual stresses in the oxide scale after oxidation in air with different absolute humidity were determined by XRD method at room temperature, and growth stresses were determined by deflection method.

Compressive residual stresses are formed in both chromia and spinel layers, and small compressive residual stresses are also observed in the substrate near the scale/substrate interface. The relaxation of growth stresses was observed at 800 ℃ and 900 ℃. The competition of the stresses generation and relaxation affects the residual stresses level. The growth stresses during oxidation plays an important role in residual stresses obtained in oxide scale for AISI 430 after oxidation. The residual stresses in the oxide scale are depend on oxidation temperature, duration and diffusion mechanism.

The influences of the oxidation temperature on residual stresses levels in two oxide layers

after oxidation are different, which was unnoticed before, and the two layers can effect each other because of good adherence. For the spinel layer, the thermal stresses contribute to the residual stresses only after the formation of continuous layer.

The water vapor can influence the stresses level. Before the occurrence of stress relaxation, the compressive residual stresses are increased with the absolute humidity; after the stress relaxation, the creep of the Cr_2O_3 layer leads to the stress relief, as a result, the residual stresses level decreases with the increase of absolute humidity.

5.5 References

[9]. S. Geng, J. Zhu, Promising alloys for intermediate-temperature solid oxide fuel cell interconnect application, J. Power Sources 160 (2006) 1009-1016.

[10]. N. Birks, G.H. Meier, F.S. Pettit, Introduction to the high-temperature oxidation of metals, in, Cambridge University, UK, 2006.

[15]. J. Mougin, A. Galerie, M. Dupeux, N. Rosman, G. Lucazeau, A.M. Huntz, L. Antoni, In-situ determination of growth and thermal stresses in chromia scales formed on a ferritic stainless steel, Materials and Corrosion 53 (2002) 486-490.

[16]. F.N. Rhines, J.S. Wolf, The role of oxide microstructure and growth stresses in the high-temperature scaling of nickel, Metall. Trans. 1 (1970) 1701-1710.

[18]. A.M. Huntz, C. Liu, M. Kornmeier, J.L. Lebrun, The determination of stresses during oxidation of Ni: in situ measurements by XRD at high temperature, Corros. Sci. 35 (1993) 989-997.

[19]. A.M. Huntz, Stresses in NiO, Cr_2O_3 and Al_2O_3 oxide scales, Mater. Sci. Eng. A 201 (1995) 211-228.

[21]. V.K. Tolpygo, D.R. Clarke, Determination of the growth stress and strain in α-Al2O3 scales during the oxidation of Fe-22Cr-4.8Al-0.3Y alloy, Oxid. Met. 49 (1998) 187-212.

[23]. D.R. Clarke, Stress generation during high-temperature oxidation of metallic alloys, Curr. Opin. Solid State Mater. Sci. 6 (2002) 237-244.

[28]. A.M. Limarga, D.S. Wilkinson, G.C. Weatherly, Modeling of oxidation-induced growth stresses, Scripta Mater. 50 (2004) 1475-1479.

[29]. B. Panicaud, J.L. Grosseau-Poussard, J.F. Dinhut, On the growth strain origin and stress evolution prediction during oxidation of metals, Appl. Surf. Sci. 252 (2006) 5700-5713.

[31]. A.M. Huntz, P.Y. Hou, R. Molins, Study by deflection of the influence of alloy composition on the development of stresses during alumina scale growth, Mater. Sci. Eng. A 485 (2008) 99-107.

[34]. H.-M. Tung, J.F. Stubbins, Incipient oxidation kinetics and residual stress of the oxide scale grown on Haynes 230 at high temperatures, Mater. Sci. Eng. A 538 (2012) 1-6.

[35]. H.-M. Tung, J.F. Stubbins, Incipient oxidation kinetics of alloy 617 and residual stress of the oxide scale formed in air at temperatures between 850 and 1000 ℃, Journal of Nuclear Materials 424 (2012) 23-28.

[47]. J. Xiao, N. Prud'homme, N. Li, V. Ji, Influence of humidity on high temperature oxidation of Inconel 600 alloy: Oxide layers and residual stress study, Appl. Surf. Sci. 284 (2013) 446-452.

[66]. B. Hua, Y. Kong, W. Zhang, J. Pu, B. Chi, L. Jian, The effect of Mn on the oxidation behavior and electrical conductivity of Fe–17Cr alloys in solid oxide fuel cell cathode atmosphere, J. Power Sources 196 (2011) 7627-7638.

[85]. G. Bamba, Y. Wouters, A. Galerie, G. Borchardt, S. Shimada, O. Heintz, S. Chevalier, Inverse growth transport in thermal chromia scales on Fe–15Cr steels in oxygen and in water vapour and its effect on scale adhesion, Scripta Mater. 57 (2007) 671-674.

[117]. Test Method for Residual Stresses Analysis by X-ray diffraction, in: European Standard no NF15305, 2009.

[118]. A.M. Huntz, P.Y. Hou, R. Molins, Study by deflection of the oxygen pressure influence on the phase transformation in alumina thin films formed by oxidation of Fe3Al, Mater. Sci. Eng. A 467 (2007) 59-70.

[119]. A.M. Huntz, L. Maréchal, B. Lesage, R. Molins, Thermal expansion coefficient of alumina films developed by oxidation of a FeCrAl alloy determined by a deflection technique, Appl. Surf. Sci. 252 (2006) 7781-7787.

[140]. W.N. Liu, X. Sun, E. Stephens, M.A. Khaleel, Life prediction of coated and uncoated metallic interconnect for solid oxide fuel cell applications, J. Power Sources 189 (2009) 1044-1050.

[141]. N. Li, J. Xiao, N. Prud'homme, Z. Chen, V. Ji, Residual stresses in oxide scale formed on Fe–17Cr stainless steel, Appl. Surf. Sci. 316 (2014) 108-113.

[142]. D. Burgreen, Elements of Thermal Stress Analysis, C.P.Press, 1971.

[143]. V.R. Howes, C.N. Richardson, The initial stresses developed during high temperature oxidation of Fe-Cr alloys, Corros. Sci. 9 (1969) 385-394.

[144]. C. Liu, J.L. Lebrun, A.M. Huntz, F. Sibieude, An advanced technique for high temperature X-ray elastic constant measurement and stress determination, Hanser, Munchen, ALLEMAGNE, 1993.

CHAPTER 6 Damage of the Oxide Scale Discussion

In the chapter 4, breakaway oxidation was observed with the introduction of water vapor in the oxidation atmosphere, and it was found that it relates to the oxidation temperature, duration and oxidation conditions. Several mechanisms have been proposed by different researchers in recent years to explain the occurrence of breakaway oxidation [76, 83, 104, 105, 107]. But none of them considers the effect of residual stresses on the damage of the oxide scale. In practical applications, however, the oxide scales are stressed either by thermal stresses or by growth stresses. These stresses can also influence the oxidation behavior, such as oxidation kinetics and surface morphology. What is more, residual stresses play a significant role in alloy failure, and are useful for life prediction. In this chapter, the effects of residual stresses on oxidation behaviors will be discussed in details. And possible mechanisms will be given to explain the occurrence of breakaway oxidation at high temperature with the introduction of water vapor.

6.1 Effect of residual stresses on the oxidation behavior

It is known that stresses can affect the grain boundary diffusion and accelerate excessive vacancies at the scale/substrate interface, thus the diffusion process of cations might be changed. To explain the effect of stresses on the oxidation rate of alloy, mechanical-chemical activity is cited [145]:

$$\alpha' = \alpha \exp(\frac{\Delta pV}{RT}) \qquad (6\text{-}1)$$

where α' is mechanical-chemical activity, α is chemical activity, Δp is residual compression, V

is molar volume of metal, R is thermodynamic constant and T is absolute temperature. It is clear that the increase of a compressive residual stress in the oxide scale will lead to the increase of mechanical-chemical activity. And the increase of mechanical-chemical activity can induce an acceleration of oxide nucleation, and thus the oxidation rate is increased.

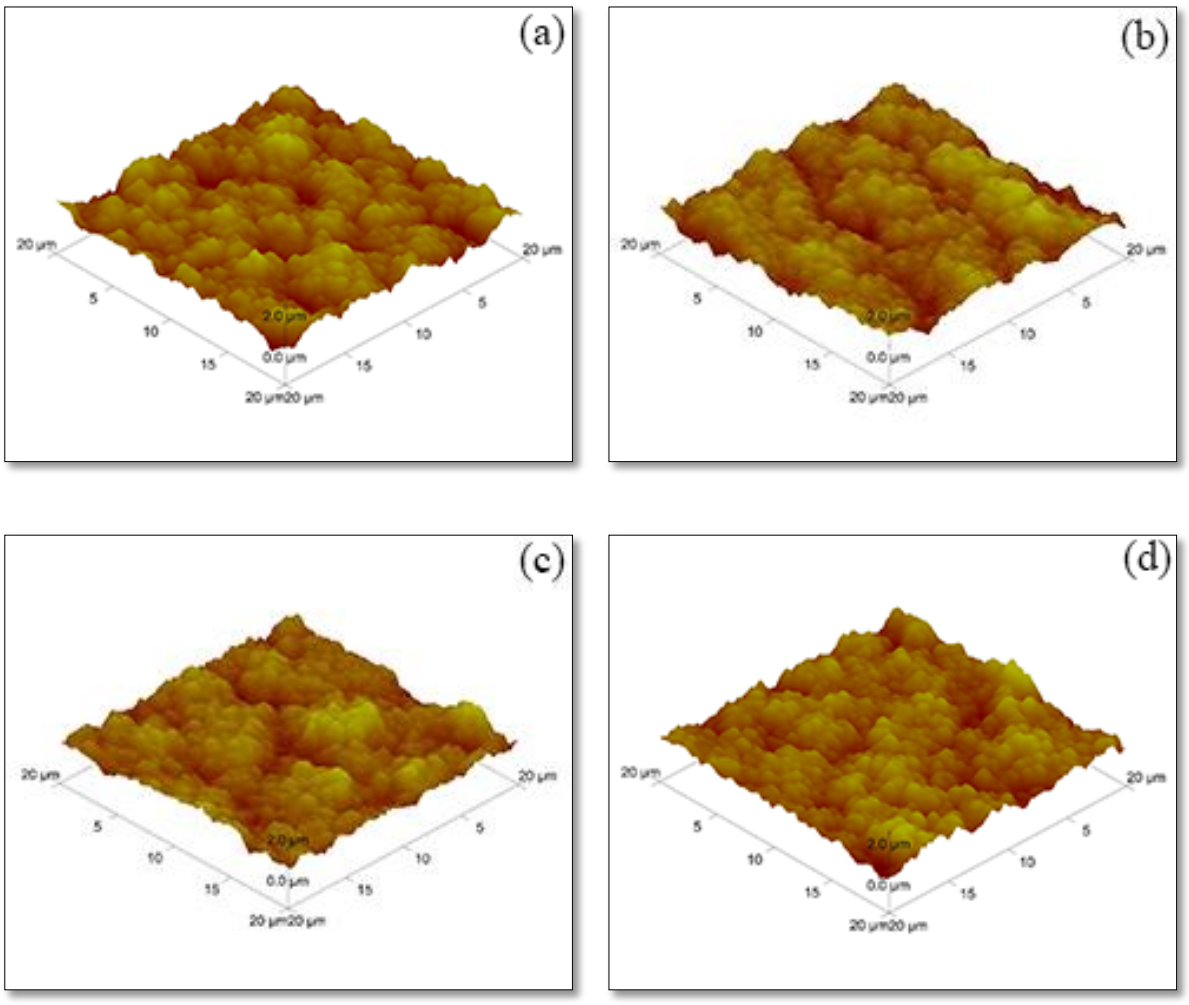

Figure 6.1 AFM surface topography of oxide scale on the substrate after oxidation in air with different humidity at 900 ℃: air (a); 2% AH (b); 5% AH (c); 8% AH (d).

For the surface morphology, V.K. Tolpygo [45] suggested that the residual stresses in the α-Al_2O_3 layer formed on Fe-Cr-Al alloy can affect the surface topography. The surface topography of the AISI 430 alloy after oxidation in air with different absolute humidity at 900 ℃ for 6 hours is given in Figure 6.1, showing that similar topography for all of the

oxidized surfaces. This indicates that the water vapor concentration has little effect on surface morphology before breakaway oxidation in this study.

6.2 Mechanism of breakaway oxidation

With the introduction of water vapor in the oxidation atmosphere at 900℃, as we have mentioned in the section 4.2, the breakaway oxidation preferentially occurred at the edge parts of the samples (Figure 6.2). This is because at these parts of the samples, there are 2 directions of diffusion and more Cr is needed to form a protective oxide layer. Thus, the breakaway oxidation occurs at the edges of the samples.

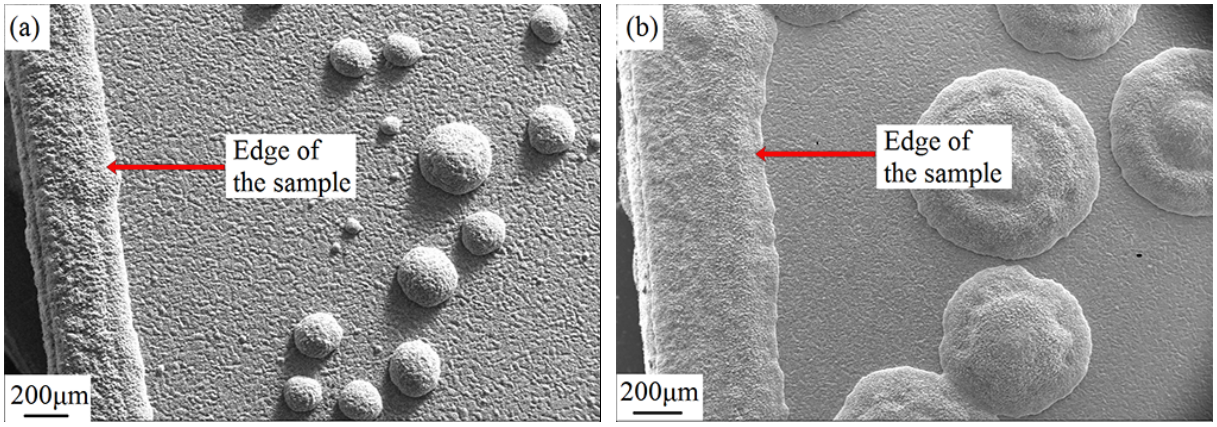

Figure 6.2 SEM micrographs of edge parts of AISI 430 alloy after oxidized in air with 2% absolute humidity (a) and with 5% absolute humidity

Meanwhile, with different levels of absolute humidity, the breakaway oxidation took place at the different parts of the samples (Figure 4.22), indicating the mechanism of breakaway oxidation might not be the same. With 2% absolute humidity, the nodules are formed randomly on the entire surface. While, with 5% absolute humidity, the nodules mainly occur near the upstream edge of the sample (the flow direction of the water vapor is from the bottom of the TGA to the top).

The calculation of weight loss due to evaporation of $CrO_2(OH)_2$ during oxidation has been done in Chapter 4. Combination of equation (4-8) and equation (4-10) shows that the weight due to evaporation would be increased with the absolute humidity, consistent with the result we have got in Figure 4.16 b. Combining equation (4-8) and (4-9), it can be seen that the weight loss due to evaporation is also related to the L, the smaller the L, the more mass transfer. This can explain that why the breakaway oxidation is easier to happen at the upstream edge of the samples. With the evaporation of Cr containing species from the oxide scale, there is not enough Cr to form protective chromia layer. The oxidation kinetic is not controlled by the diffusion of Cr ions, but the oxidation of Fe ions at these parts, and un-protective Fe_2O_3 nodules formed. So it is suggested that the evaporation of $CrO_2(OH)_2$ is the main reason for taking place of breakaway oxidation in air with more than 5% absolute humidity. This mechanism was first proposed by Asteman et al [107, 108].

But this mechanism might ignore the influence of stress in the oxide on breakaway oxidation, since we have found that the stress levels in the oxide scale are related with the mechanical-chemical activity. The decrease of compressive stress in the oxide scale could lead to a decrease of mechanical-chemical activity, thus, less oxide formed during the oxidation. It has been found in this study that the residual stress level in the chromia layer formed in the atmosphere containing water vapor are smaller than that formed in dry air after stress relaxation. Therefore, less chromia formed in atmosphere containing water vapor. So there are two reasons lead to the decrease of the weight gain with the introduction of water vapor for more than 5% absolute humidity in the oxidation atmosphere: evaporation of chromia and decreased oxide formation due to the reduction of residual stresses in the oxide layer. Therefore, the change of the stress levels in the oxide scale would also relate to the breakaway oxidation.

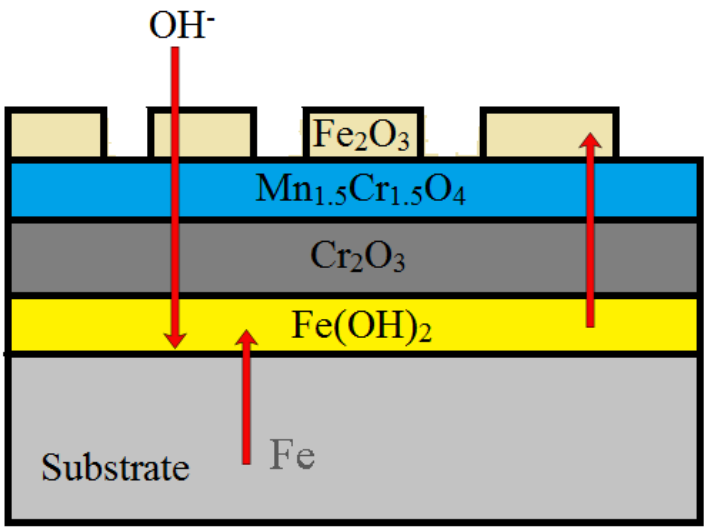

Figure 6.3 Schematic illustration of breakaway mechanism of AISI 430 alloy in air with 2% absolute humidity

But in air with 2% absolute humidity, it is not convincing that the evaporation is the main reason resulting in the breakaway oxidation, since the weight loss due to evaporation is very small under this atmosphere and the breakaway oxidation doesn't just onset at the upstream edge of the sample. Therefore, the evaporation of Cr containing species during the oxidation is negligible in the atmosphere with 2% absolute humidity. In this study, more OH^- ions diffuse inward the scale was observed in atmosphere containing water vapor. Theses OH^- ions can react with Fe ions at the scale/substrate interface to generate $Fe(OH)_2$, which would diffuse from the scale/substrate interface to the scale/gas surface and deposit as Fe_2O_3 by reaction (6-2). The schematic of the proposed breakaway mechanism is given in Figure 6.3.

$$2Fe(OH)_{2(g)} \rightarrow Fe_2O_3 + H_2O_{(g)} + H_{2(g)} \qquad (6\text{-}2)$$

In recent years, lots of oxidation experiments have been done to study the effects of water vapor on alloys [76, 83, 104, 105, 107, 146], and some researchers have observed that the occurrence of breakaway oxidation during high temperature oxidation with the introduction of water vapor. The effects of water vapor on oxidation can be classified as follows: (1) dissociation mechanism [76], (2) volatilization of $Fe(OH)_2$ [104], (3) formation of

microcracks and microchannels [105], (4) entrance of H_2O into the oxide scale [83], (5) volatilization of $CrO_2(OH)_2$ [107, 108].

Although mechanisms (1) and (2) can explain why the oxidation kinetic is increased with the introduction of the water vapor, cannot explain why the breakaway oxidation occurs. Mechanisms (3), (4) and (5) are proposed to explain the breakaway oxidation. Mechanism (3) is based on the study of Fe-15Cr at 900-1000 ℃ with different concentration of water vapor, and the author thought that H_2 forms at the scale/substrate interface and reduces Cr_2O_3 into chromium. But it is difficult to believe that the hydrogen can reduce chromia, because chromia is thermodynamically more stable than H_2O.

This mechanism (4) which proposed by J. Ehlers et al [83] was based on the oxidation of 9%Cr ferritic steel at 650 ℃ in N_2-O_2-H_2O gas for 100h. This mechanism is similar to the mechanism proposed in our study for breakaway oxidation in air with 2% AH. The only difference is that they thought the formation of $Fe(OH)_2$ is the result of inward transport of H_2O molecules, not the inward diffusion of OH^-. Considering the radii of OH^- is smaller than that of H_2O, and no microcrack and microchannel are found in the oxide scale to allow H_2O molecules to transport, it is reasonable to believe that the formation of $Fe(OH)_2$ is not result from the entrance of H_2O molecule, but inward diffusion of OH^-.

By studying the oxidation behavior of 304 steel in atmosphere containing water vapor, a volatilization of $CrO_2(OH)_2$ mechanism was suggested by Asteman et al [107, 108] to explain the breakaway oxidation. And this mechanism has been proved by different researchers in recent years [84, 87, 102]. It is true that the volatilization of $CrO_2(OH)_2$ mechanism is a powerful explanation, but it only works in atmosphere with high concentration of water vapor. For atmosphere containing low concentration of water vapor, the mass loss due to evaporation

can be ignored, and cannot explain the breakaway oxidation.

In spite of several mechanisms have been proposed to explain the breakaway oxidation by different researchers, none of them considered the influence of water vapor concentration in the environment. As several different steps during the oxidation can be affected with the introduction of water vapor, it seems that the reason for breakaway oxidation might be different in atmosphere with different concentration of water vapor. It is unreasonable to find one mechanism to interpret breakaway oxidation in all kinds of atmospheres. Comparing with the mechanisms proposed before, we considered the content of absolute humidity in the oxidation atmosphere and two different mechanisms are suggested to explain the breakaway oxidation of AISI 430 alloy. In this study, moreover, it is proved that the residual stress levels in the oxide scale are also related to the breakaway oxidation, which was not mentioned in the previous studies.

6.3 Conclusion

In this chapter, the effects of residual stresses on oxidation behavior have been discussed. A mechanical-chemical activity was cited, and found that the oxidation kinetic is closely related to the residual stresses level in the oxide scale. The residual stresses have little effect on the surface morphology. It is possible that there is a definite relation between the residual stresses and the breakaway oxidation.

Two different breakaway oxidation mechanisms were proposed. In air with more than 5% absolute humidity, evaporation of chromia and decreased oxide formation due to the reduction of residual stresses in the oxide layer lead to the occurrence of breakaway oxidation. While, in air with 2% absolute humidity, the occurrence of the breakaway oxidation is the result of

inward diffusion of OH^-, which can reacts with Fe to form $Fe(OH)_2$ at the scale/substrate interface. The evaporation of $Fe(OH)_2$ to the surface leads to the formation of Fe_2O_3.

6.4 References

[45]. V.K. Tolpygo, D.R. Clarke, Wrinkling of α-alumina films grown by thermal oxidation—I. Quantitative studies on single crystals of Fe–Cr–Al alloy, Acta Mater. 46 (1998) 5153-5166.

[76]. C.T. Fujii, R.A. Meussner, The mechanism of the high-temperature oxidation of iron-chromium alloys in water vapor J. Electrochem. Soc. 111 (1964) 1215-1221.

[83]. J. Ehlers, D.J. Young, E.J. Smaardijk, A.K. Tyagi, H.J. Penkalla, L. Singheiser, W.J. Quadakkers, Enhanced oxidation of the 9%Cr steel P91 in water vapour containing environments, Corros. Sci. 48 (2006) 3428-3454.

[84]. D.J. Young, B.A. Pint, Chromium volatilization rates from Cr_2O_3 scales into flowing gases containing water vapor, Oxid. Met. 66 (2006) 137-153.

[87]. M. Stanislowski, E. Wessel, K. Hilpert, T. Markus, L. Singheiser, Chromium Vaporization from High-Temperature Alloys, J. Electrochem. Soc. 154 (2007) A295.

[102]. A. Yamauchi, K. Kurokawa, H. Takahashi, Evaporation of Cr_2O_3 in Atmospheres Containing H_2O, Oxid. Met. 59 (2003) 517-527.

[104]. P.L. Surman, J.E. Castle, Gas phase transport in the oxidation of Fe and steel, Corros. Sci. 9 (1969) 771-777.

[105]. S. Jianian, Z. Longjiang, L. Tiefan, High-temperature oxidation of Fe-Cr alloys in wet oxygen, Oxid. Met. 48 (1997) 347-356.

[107]. H. Asteman, J.E. Svensson, L.G. Johansson, Evidence for Chromium Evaporation Influencing the Oxidation of 304L: The Effect of Temperature and Flow Rate, Oxid. Met. 57 (2002) 193-216.

[108]. H. Asteman, J.E. Svensson, L.G. Johansson, Oxidation of 310 steel in H2O/O2 mixtures at 600 ℃: the effect of water-vapour-enhanced chromium evaporation, Corros. Sci. 44 (2002) 2635-2649.

[145]. C.H. Zhou, H.T. Ma, L. Wang, Comparative study of oxidation kinetics for pure nickel oxidized under tensile and compressive stress, Corros. Sci. 52 (2010) 210-215.

[146]. E. Essuman, G.H. Meier, J. Żurek, M. Hänsel, L. Singheiser, W.J. Quadakkers, Enhanced internal oxidation as trigger for breakaway oxidation of Fe–Cr alloys in gases containing water vapor, Scripta Mater. 57 (2007) 845-848.

CHAPTER 7 Conclusions and Future Works

7.1 Conclusions

Chromia forming ferritic stainless steels seem to be promising candidates for interconnect materials in solid oxide fuel cell. Since oxidation is one of the issues for these alloy at high temperature, especially in atmosphere containing water vapor. Understanding the oxidation behavior of these alloys in atmosphere with water has great importance. In the presented study, AISI 430 alloy was used and the oxidation behavior of this alloy in air with different absolute humidity was investigated. The major outcomes of the present study are summarized as below.

A parabolic kinetics was observed after oxidation in dry air at 700 ℃, 800 ℃ and 900 ℃, and a protective oxide scale was formed. The oxide scale is consisted of an inner Cr_2O_3 layer and an outer $Mn_{1.5}Cr_{1.5}O_4$ layer (with little incorporation of Fe). A discontinuous SiO_2 layer at the scale/substrate was also observed. The oxidation of this alloy is mainly controlled by the outward diffusion of metal ions.

With the presence of water vapor in the oxidation atmosphere, the oxidation behaviors of this alloy are different at different temperature. At 700 ℃ and 800 ℃, the oxide scale formed during the oxidation is still protective and the alloy exhibits a good oxidation resistance. At 900 ℃, however, breakaway oxidation took place with the introduction of water vapor. The breakaway oxidation is related to the oxidation temperature, duration and oxidation atmosphere. The more water vapor, the earlier the breakaway oxidation happens. Before the occurrence of breakaway oxidation, the oxide the water vapor has little effect on oxides and

surface morphology, and the weight gain decreased with the increase of water vapor due to evaporation of $CrO_2(OH)_2$. The outer $Mn_{1.5}Cr_{1.5}O_4$ spinel layer can suppress the evaporation. In the presence of water vapor, the oxidation is still controlled by the outward diffusion of metal ions, just more amount of OH^- inward transport through the scale.

Compressive residual stresses were observed in both chromia and spinel layers at all temperature. The relaxation of growth stresses was observed at 800 ℃ and 900 ℃. The growth stresses generate during oxidation plays an important role in the total residual stresses determined at room temperature for AISI 430 alloy. The concentration of water vapor can affect the residual stresses levels in the oxide layers. Before the occurrence of stresses relaxation, the compressive residual stresses increase with the increase of absolute humidity; as the stresses relaxation took place, the residual stresses levels decrease with the increase of absolute humidity.

Two possible breakaway oxidation mechanisms were proposed. In air with more than 5% absolute humidity, the breakaway oxidation is the result of combination of evaporation of $CrO_2(OH)_2$ and the decrease of residual stresses in the protective chromia layer. But in air with 2% absolute humidity, OH^- ions diffuse inward the scale and react with Fe ions at the scale/substrate to generate $Fe(OH)_2$. The evaporation of $Fe(OH)_2$ to the scale/gas surface and lead to the formation of Fe_2O_3.

7.2 Future work

Based on the findings from this work, some suggestions are given to the future study.

In this study, $^{18}O_2$ isotope was used to mechanism of oxidation in dry air. To better understand the role of water vapor in oxidation of AISI 430 alloy at high temperature, $D_2{}^{18}O$ should be used with SIMS analysis.

This dissertation is mainly focused on the oxidation behavior of the alloy in dry air and in air with water vapor. Considering the complex environment in reality, the effect of hydrogen on oxidation should also be studied.

It is still unclear how $\sigma_{accommodation}$ influence the total residual stresses level in the oxide layers, more In-situ XRD experimental studies need to be done to explain the stresses accommodation problem.

Synthèse en français

Mis à part les facteurs économiques et les propriétés mécaniques, la corrosion est l'un des facteurs les plus importants dans le choix et l'utilisation d'un matériau métallique. Une couche d'oxyde se forme sur la majorité des métaux et des alliages à haute température en présence de l'oxygène. Mais sous des différents effets physiques-chimiques, tel que les flux atomiques diffusionnels, les réarrangements atomiques, la distorsion du réseau, l'apparition de phases métallurgiques, des contraintes internes peuvent être générées durant l'oxydation à haute température et après l'oxydation [1-3]. La connaissance des comportements à l'oxydation à haute température et de la génération des contraintes internes associées aux résistances des alliages Fe-Cr est importante pour les applications à haute température dans la pile à combustible SOFC (solid oxide fuel cell) comme interconneteurs.

De nombreuses recherches sur l'oxydation à haute température des alliages Fe-Cr ont été réalisées, mais la plupart d'entre elles sont seulement axées sur l'oxydation à haute température sous air sec [4-6]. Bien que dans toutes les conditions d'applications industrielles, il y a toujours la présence de vapeur de l'eau (humidité de l'air) et cette humidité peut influencer la cinétique d'oxydation à haute température de l'alliage et le niveau et la distribution des contraintes internes dans la couche d'oxyde [7, 8]. Ainsi, le présent travail se concentre essentiellement sur l'étude de la cinétique et les contraintes internes (résiduelles, thermiques et croissances) dans les couches d'oxydes lors de l'oxydation de l'alliage AISI 430 sous air synthétique ($20\%O_2+80\%N_2$) sec et sous air synthétique humide (avec différents pourcentages de vapeur d'eau) allant de 700°C à 900°C.

Dans le chapitre 1 de ce manuscrit, les objectifs de l'étude et de l'organisation du manuscrit sont présentés. Le chapitre 2 est consacré à l'étude bibliographique de mécanismes d'oxydation (sec et humide) à haute température, ainsi que les mécanismes de développement des contraintes internes dans les oxydes. Une description succincte des techniques expérimentales utilisées est donnée dans le chapitre 3. Nous décrirons, dans le chapitre 4, les

études du comportement à l'oxydation de l'alliage AISI 430 sous air synthétique sec ou humide (avec vapeur d'eau) de 700°C à 900°C. Nous présentons les résultats expérimentaux concernant la détermination des contraintes résiduelles par la diffraction des rayons-X (DRX) des échantillons oxydés ainsi que l'analyse des contraintes de croissance par la mesure de déflexion in situ dans le chapitre 5. L'interaction entre les contraintes internes et l'oxydation à haute température est discutée, et le mécanisme de la dégradation de la couche d'oxyde est proposé dans le chapitre 6. En fin, des conclusions générales sont présentées dans le chapitre 7, et des perspectives d'études expérimentales sont aussi proposées.

1 Etude du comportement à l'oxydation de l'alliage AISI 430

1.1 Comportement à l'oxydation sous air sec

L'étude des cinétiques d'oxydation est réalisée à l'aide de l'analyse thermogravimétrique (ATG). La Figure 1.1 présente la prise de masse et la prise de masse au carré en fonction du temps de maintien pour l'oxydation isotherme à différentes températures sous air sec jusqu'à 96h. Les résultats montrent que les coubes de prise de masse suivent une loi parabolique (les coubes de prise de mass au carré sont linéaires). La vitesse d'oxydation augmente en fonction de la température de 700 °C à 900 °C. Les constantes paraboliques correspondant à la vitesse d'oxydation à différentes températures sont présentées au Tableau 1.1. Selon la théorie de Wagner, la cinétique d'oxydation parabolique à haute température signifie que la vitesse d'oxydation est contrôlée essentiellement par la diffusion des ions qui migrent à travers une couche d'oxyde dense [9]. L'énergie d'activation déterminée pour la gamme de température étudiée est égale à 279,9 $kJ.mol^{-1}$, très proche de l'énergie d'activation pour la formation de la phase Cr_2O_3 (280 $kJ.mol^{-1}$) [10].

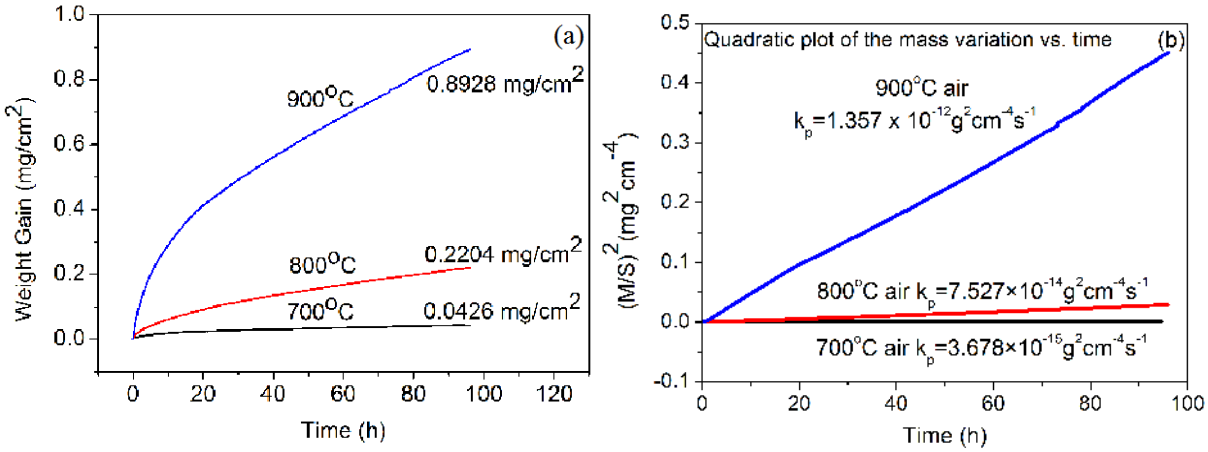

Figure 1.1 Cinétiques de l'oxydation à différentes températures (700°C, 800°C et 900°C) pour l'alliage AISI 430 oxydé pendant 96h sous air sec : la prise de masse en fonction du temps (a), la prise de masse au carré en fonction du temps (b)

Tableau 1.1 Les constantes paraboliques (kp) pour l'oxydation sous air sec à 700 ℃, 800 ℃ et 900 ℃

Température	k_p ($g^2cm^{-4}s^{-1}$)
700°C	5,127 $\times 10^{-15}$
800°C	1,416 $\times 10^{-13}$
900°C	2,367 $\times 10^{-12}$

Afin d'identifier la nature des oxydes obtenus en surface des échantillons, la diffraction des rayons X à faible incidence (Grazing incidence X-ray diffraction, GIXRD) a été réalisée. Le temps nécessaire pour obtenir un diffractogramme complet est de l'ordre de 13h. La Figure 1.2 nous montre les diffractogrammes (avec une incidence rasante de 2°) en fonction de la durée d'oxydation à différentes températures sous air sec. Dans nos conditions d'essais sous air sec et de 700 ℃ à 900 ℃, les diffractogrammes obtenus sont principalement composés de mêmes pics de diffraction: pics du substrat, pics de $Mn_{1.5}Cr_{1.5}O_4$ (JCPDS 33-0892) et pics de Cr_2O_3 (JCPDS 38-1479). Bien que la cinétique d'oxydation à 700°C, 800°C et 900°C soit un peu différente, la composition des oxydes est quasiment identique. A toutes les températures, avec l'augmentation de la durée d'oxydation, l'intensité des pics d'oxydes s'accroît.

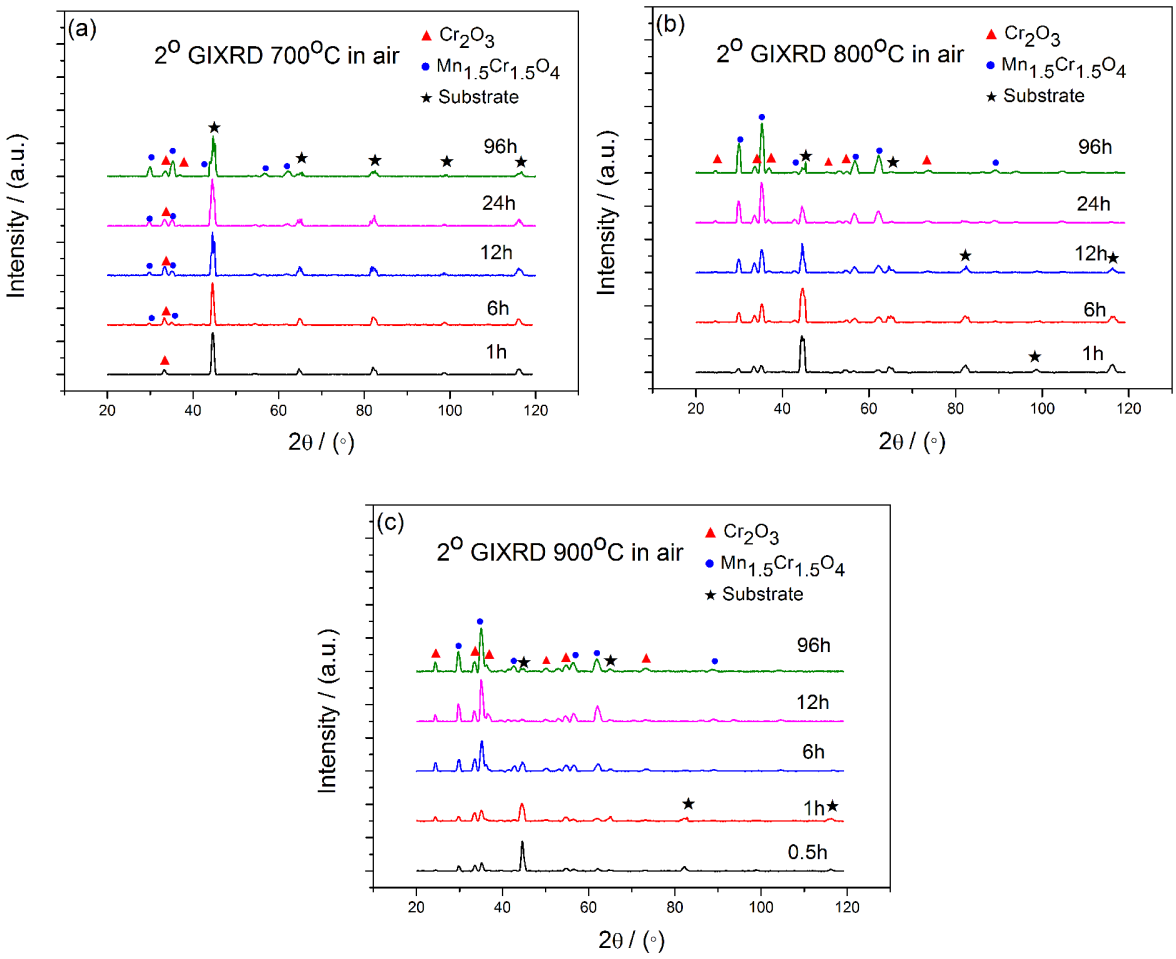

Figure 1.2 Diffractogrammes (avec une incidence rasante de 2°) de couches d'oxyde formées sur l'alliage AISI 430 avec différentes durées d'oxydation à différentes températures (700 ℃, 800 ℃ et 900 ℃) sous air sec

Les images au microscope électronique à balayage à émission de champs (Field Emission Gun Scanning Electronic Microscope, FEG-SEM) de la surface des couches d'oxyde obtenues sur l'alliage AISI 430 oxydé pendant 12h sous air sec à différentes températures (de 700 ℃ à 900 ℃) sont présentées dans la Figure 1.3. On peut constater que certains grains octaédriques sont formés sur la surface, en particulier aux joints de grains initiaux du substrat. La composition chimique des grains et aux joints de grains a été étudiée par analyse dispersive en énergie (Energy dispersive X-ray spectroscopy, EDX). Il faut noter qu'il y a plus de Mn aux joints de grains que dans la couche d'oxyde à l'intérieur des grains. Avec l'augmentation de la température, les grains octaédriques couvrent presque de la totalité de la surface.

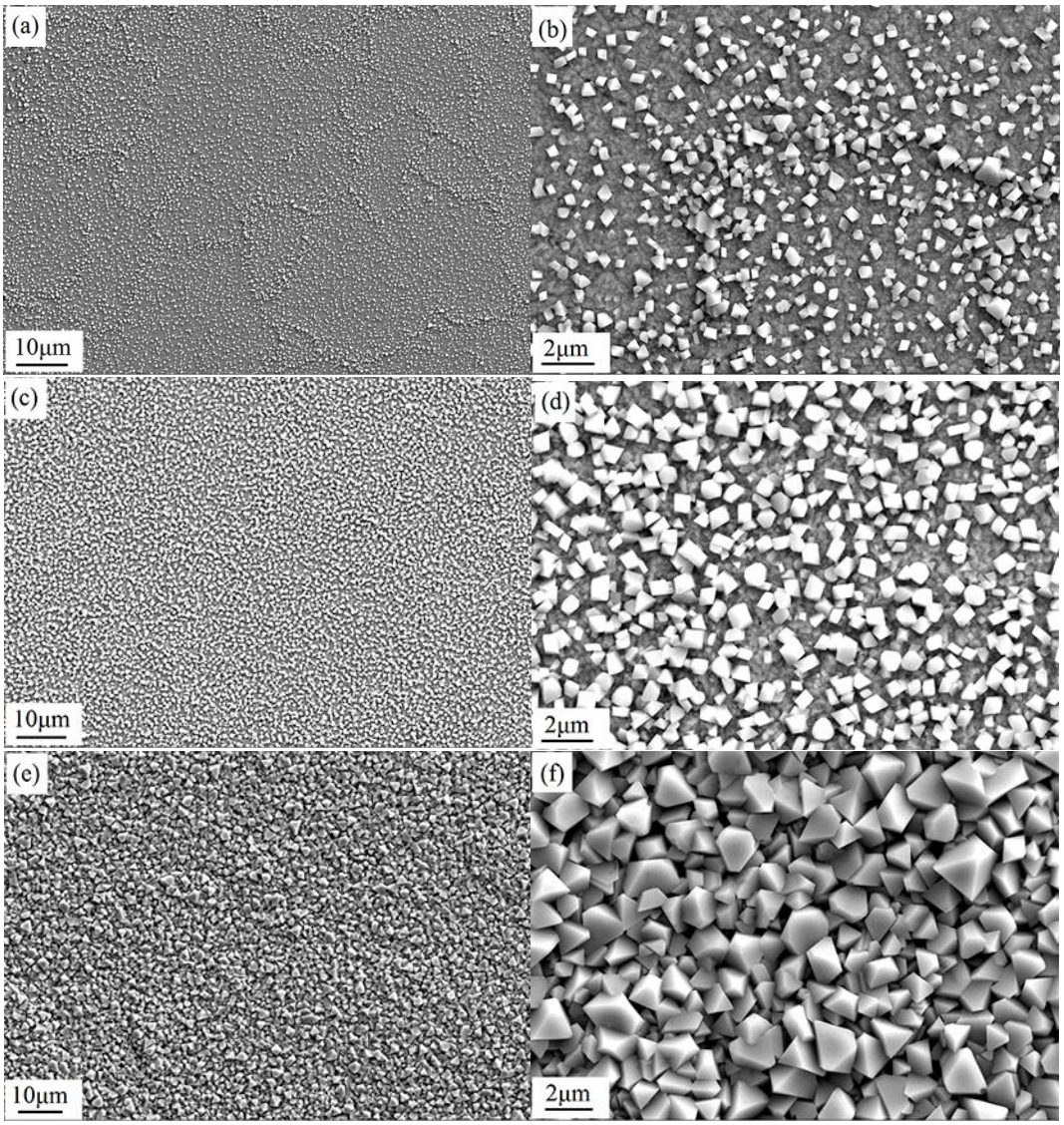

Figure 1.3 Images FEG-SEM des couches d'oxyde sur l'alliage AISI 430 oxydé après 12h d'oxydation sous air sec à 700 °C (a, b), 800 °C (c, d) and 900 °C (e, f)

La Figure 1.4 montre les images de FEG-SEM en section transverse des couches d'oxyde formées sous air sec pendant 48h sur l'alliage AISI 430 à 900°C. L'observation révèle que l'épaisseur de couches d'oxyde est d'environ 3 μm et deux couches distinctes sont formées: la couche extérieure est moins épaisse par rapport à la couche intérieure, elle est composée principalement de Mn, Cr et O (selon l'analyse par EDX), indiquant que la phase spinelle (selon l'analyse par GIXRD) se développe en une couche externe. La couche interne contient principale de Cr et O, donc on peut conclure que la couche intérieure se compose essentiellement de Cr_2O_3. En outre, la formation d'une couche discontinue de SiO_2 est détectée à l'interface oxyde/métal. La présence de nombreux pores à l'interface oxyde/métal,

témoins d'un mécanisme de croissance par le transport des ions métalliques vers l'extérieur.

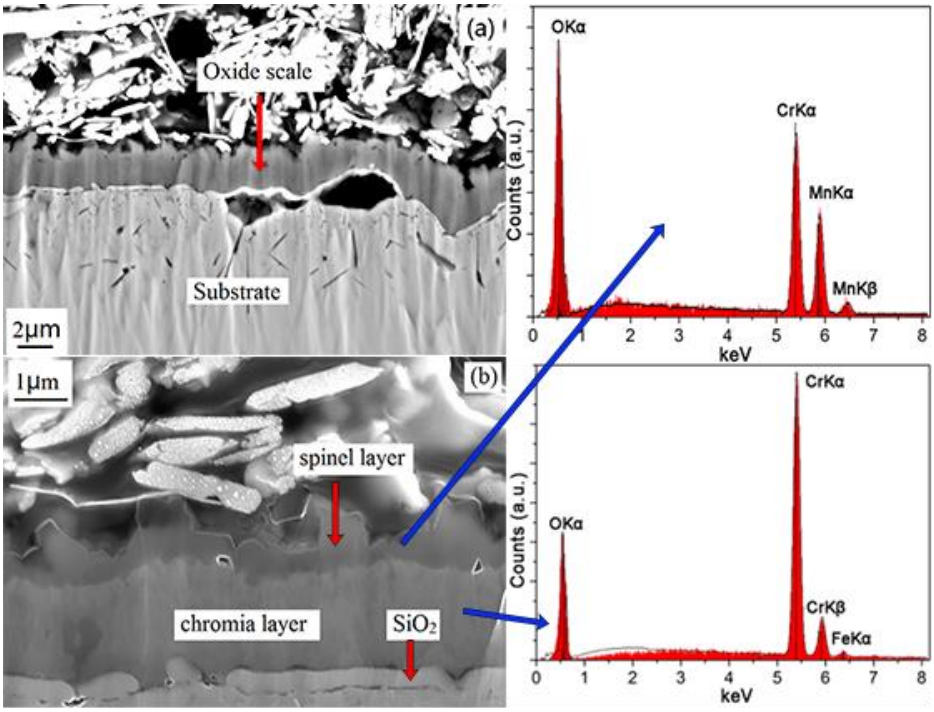

Figure 1.4 Images FEG-SEM et EDX de sections transversales sur l'alliage AISI 430 oxydé sous air sec pendant 48 h à 900 °C

Les expériences de marquages isotopiques sous $^{18}O_2$ ont été réalisées sur l'alliage AISI 430. Les conditions de marquages sont de 6 h d'oxydation sous $^{16}O_2$, suivies de 3 h d'oxydation sous $^{18}O_2$. Les profils SIMS (Secondary Ion Mass Spectrometry) de l'alliage AISI 430 oxydé en 2 étapes sont présentés dans la Figure 1.5. A toutes les températures étudiées, la surface de la couche d'oxyde formée sur l'alliage AISI 430 est riche en ^{18}O; le signal en ^{18}O diminue ensuite progressivement en fonction de la profondeur tandis que la couche s'enrichit en ^{16}O. Ceci indique que la croissance de la couche est contrôlée par le transport des ions métalliques vers l'extérieur. Ce résultat est parfaitement conforme aux théories établies jusqu'à présent dans la littérature dans le cas de la croissance d'une couche de Chromine sur l'alliage Fe-Cr par [1]

$$[4V_{Cr}''' + 6V_O^{\cdot\cdot}]_{surface} + 3O_2 = 6O_O^X + 4V_{Cr}''' + 12h^{\cdot} \qquad (1\text{-}1)$$

Par ailleurs, ce mécanisme aboutit à la génération de lacunes et la formation de pores à

l'interface oxyde/substrat, nous pouvons les observer dans la Figure 1.4

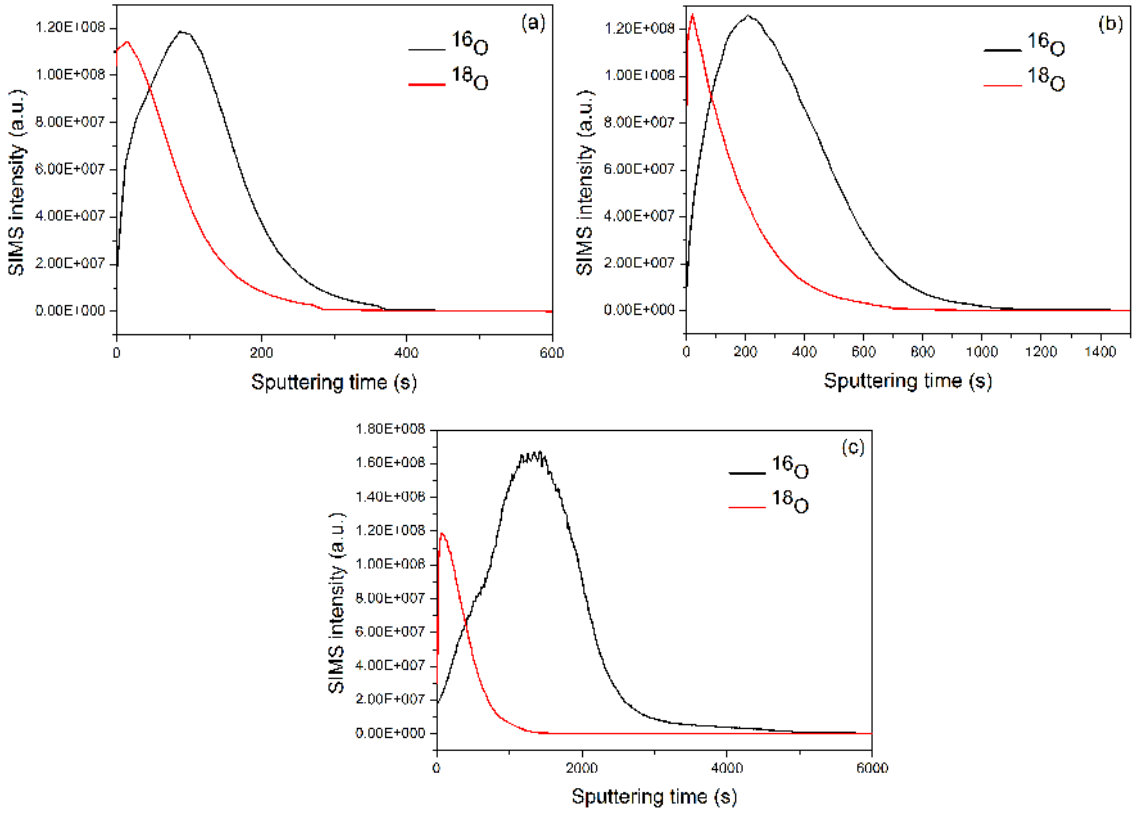

Figure 1.5 Profils SIMS dans la couche d'oxyde formée sur l'alliage AISI 430, oxydé (a)à 700 ℃ (b) à800 ℃ et (c) 900 ℃ pendant 6 h sous air sec puis 3h sous $^{18}O_2$.

Dans notre cas d'étude, l'avancement d'oxydation s'est divisé en trois étapes. Le schéma du développement de la couche d'oxyde sous air sec est présenté dans la Figure 1.6.

- A l'étape 1, l'oxydation est contrôlée par la diffusion des ions de Cr vers l'extérieur en raison de l'oxydation sélective, et une mince couche d'oxyde de Cr_2O_3 est formée rapidement et couvre la surface de l'échantillon.
- A l'étape 2, l'oxydation est contrôlée par la diffusion des ions de Mn vers l'extérieur car les ions de Mn diffusent plus rapide que les ions de Cr dans la couche de Cr_2O_3. Les couches de $Mn_{1.5}Cr_{1.5}O_4$ sont formées en surface extérieure de l'échantillon.
- A l'étape 3, l'oxydation est contrôlée par la diffusion des ions de Cr vers l'extérieur encore une fois, c'est à dire l'augmentation de l'épaisseur de la couche de Cr_2O_3 en surface interne .

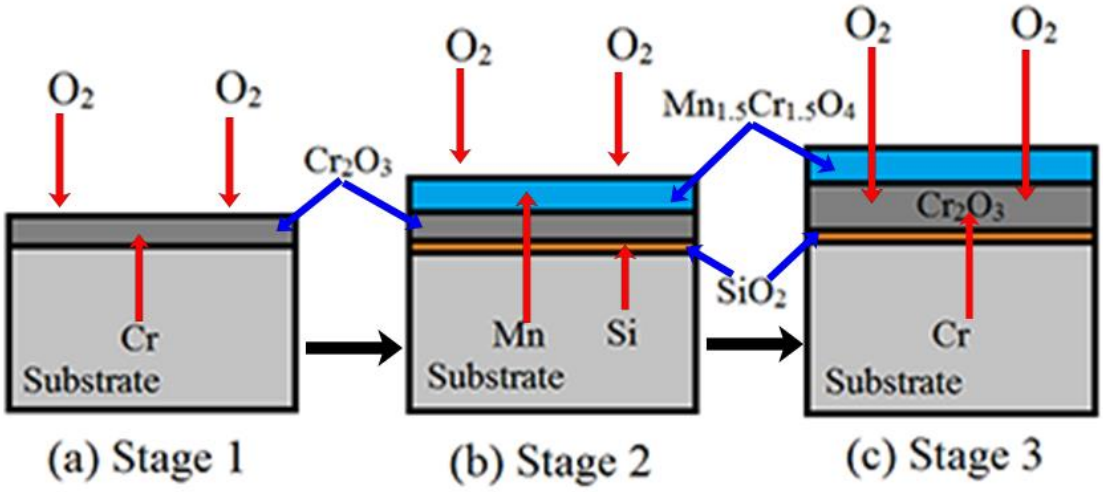

Figure 1.6 Schéma du développement de la couche d'oxyde de l'alliage AISI 430 sous air sec

1.2 Comportement à l'oxydation avec vapeur d'eau

Les essais d'oxydation sous vapeur d'eau ont été réalisés avec le branchement d'un générateur de vapeur d'eau de marque SETARAM. La Figure 1.7 montre la prise de masse en fonction du temps de l'alliage AISI 430 oxydé à différentes teneurs en vapeur d'eau. En ajoutant de la vapeur d'eau à 700°C et 800°C, les cinétiques suivent une loi d'évolution parabolique similaire, mais la prise de masse diminue par rapport à celle sans vapeur d'eau. Les constantes paraboliques correspondant à la vitesse d'oxydation à différentes température sont présentées au Tableau 1.2. A 900 ℃, on peut diviser chaque courbe en deux parties. La vitesse d'oxydation suit une loi parabolique au début. Une accélération drastique de la vitesse d'oxydation est observée à 60h, 16h, 7h et 3h avec 2%, 5%, 8% et 10% de l'humidité absolue, respectivement, c'est à dire la dégradation de la couche d'oxyde.

Tableau 1.2 Les constantes paraboliques d'oxydation à différentes teneurs en vapeur d'eau de l'alliage AISI 430 à différentes températures

k_p ($g^2cm^{-4}s^{-1}$)	Air	2% AH	5% AH	8% AH	10% AH
700 ℃ 96h	$5{,}13\times10^{-15}$	$4{,}82\times10^{-15}$	$4{,}29\times10^{-15}$	$4{,}18\times10^{-15}$	$3{,}53\times10^{-15}$
800 ℃ 96h	$1{,}42\times10^{-13}$	$1{,}19\times10^{-13}$	$1{,}05\times10^{-13}$	$9{,}42\times10^{-14}$	$7{,}40\times10^{-14}$
900 ℃ 6h	$2{,}37\times10^{-12}$	$2{,}10\times10^{-12}$	$1{,}83\times10^{-12}$	$1{,}68\times10^{-12}$	

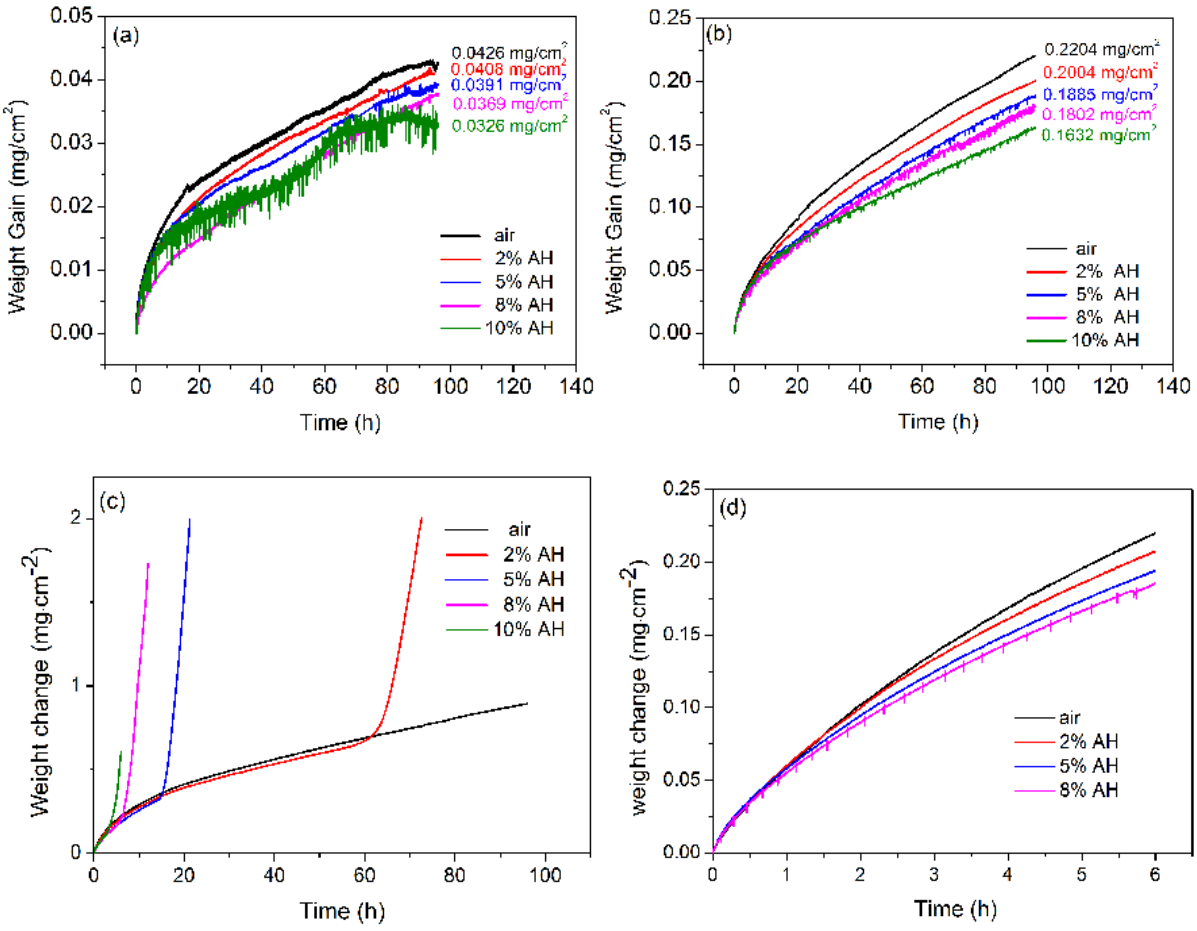

Figure 1.7 Les cinétiques d'oxydation de l'alliage AISi 430 oxydé *à différentes teneurs en vapeur d'eau* (a) 96h à 700 ℃, (b) 96h à 800 ℃, (c) 96h à 900 ℃ et (d) 6h à 900 ℃

Les phases cristallines d'oxyde obtenues sur l'alliage AISI 430 oxydé à différents température avec différentes teneurs en vapeur d'eau ont été déterminées par GIDRX avec une incidence rasante de 2 ° comme illustrent dans la Figure 1.8. La présence de vapeur d'eau n'affecte pas la nature des produits d'oxydation avant la dégradation de la couche d'oxyde, car les diffractogrammes des oxydes formés à différentes teneurs en vapeur d'eau (de 0% à 10% HA) sont presque identiques. Mais après la dégradation de la couche d'oxyde (La Figure 1.8 d), on peut aussi observer les pics de Fe_2O_3 (JCPDS 33-0664) et $(Fe_{0.6}Cr_{0.4})_2O_3$ (JCPDS 34-0412).

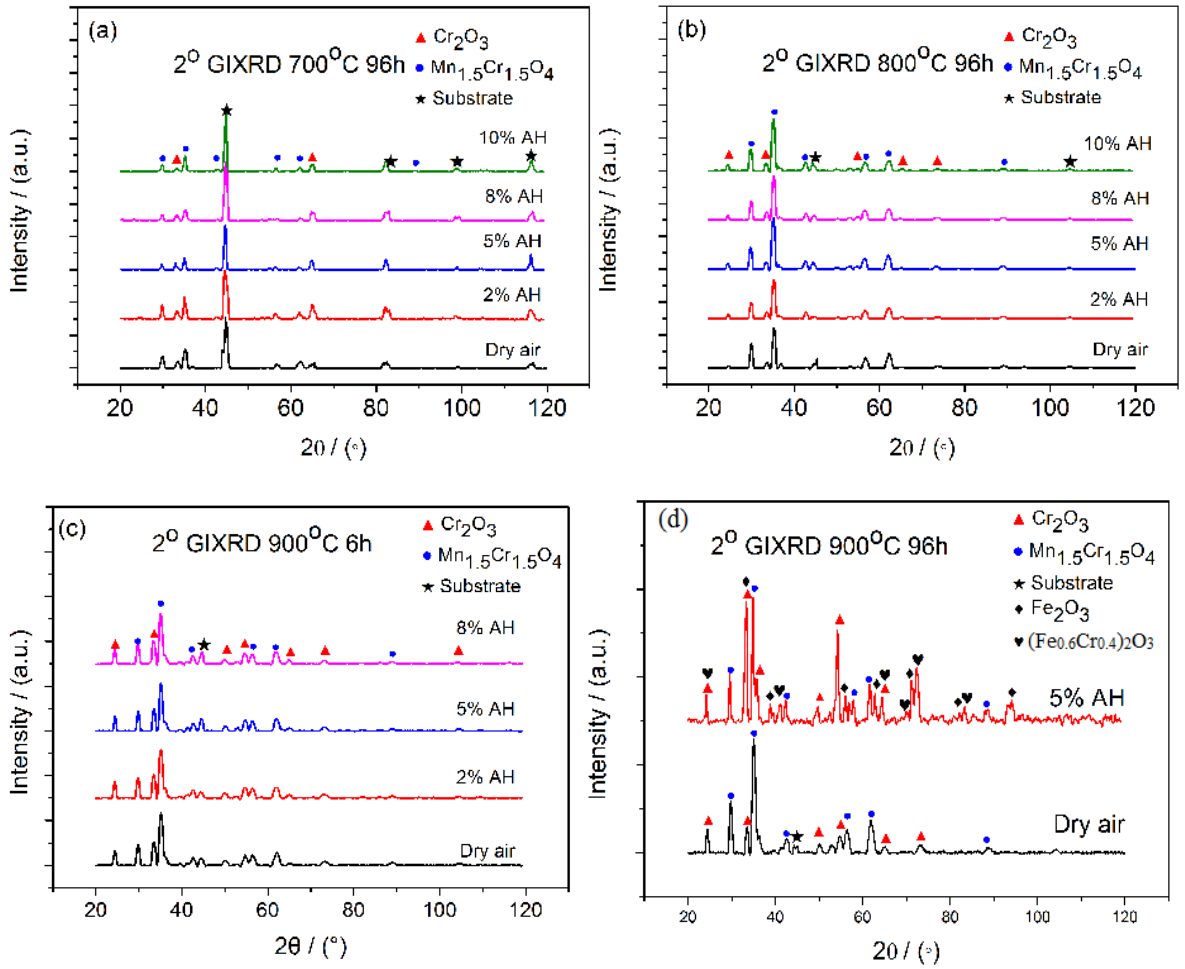

Figure 1.8 Diffractogrammes (avec une incidence rasante de 2 °) des couches d'oxydes formées sur l'alliage AISI 430 avec différentes teneurs en vapeur d'eau après d'oxydation(a) 96h à 700 °C, (b) 96h à 800 °C, (c) 6h à 900 °C et (d) 96h à 900 °C

Les images FEG-SEM de la surface des couches d'oxyde obtenues sur l'alliage AISI 430 oxydé sous air sans et avec 5% HA à 800 °C sont présentées dans la Figure 1.9. La morphologie de l'alliage AISI 430 oxydé sous air avec 5%HA est nettement différente que celle oxydée sous air sec. Tous les grains formés sous l'air sec sont réguliers. Mais avec la présence de vapeur de l'eau, des grains formés sur la surface sont irréguliers, les analyses EDX ont révélé que les grains sont riches en Mn, Cr et O, c'est une phase de l'oxyde spinelle. Cette différence s'explique simplement par la participation des molécules de H_2O à la formation de grains $Mn_{1.5}Cr_{1,5}O_4$ à haute température à la surface. Ensuite, les grains de forme irrégulière sont formés en raison de la volatilisation de ces molécules de H_2O à partir de grains après avoir refroidi en température ambiante.

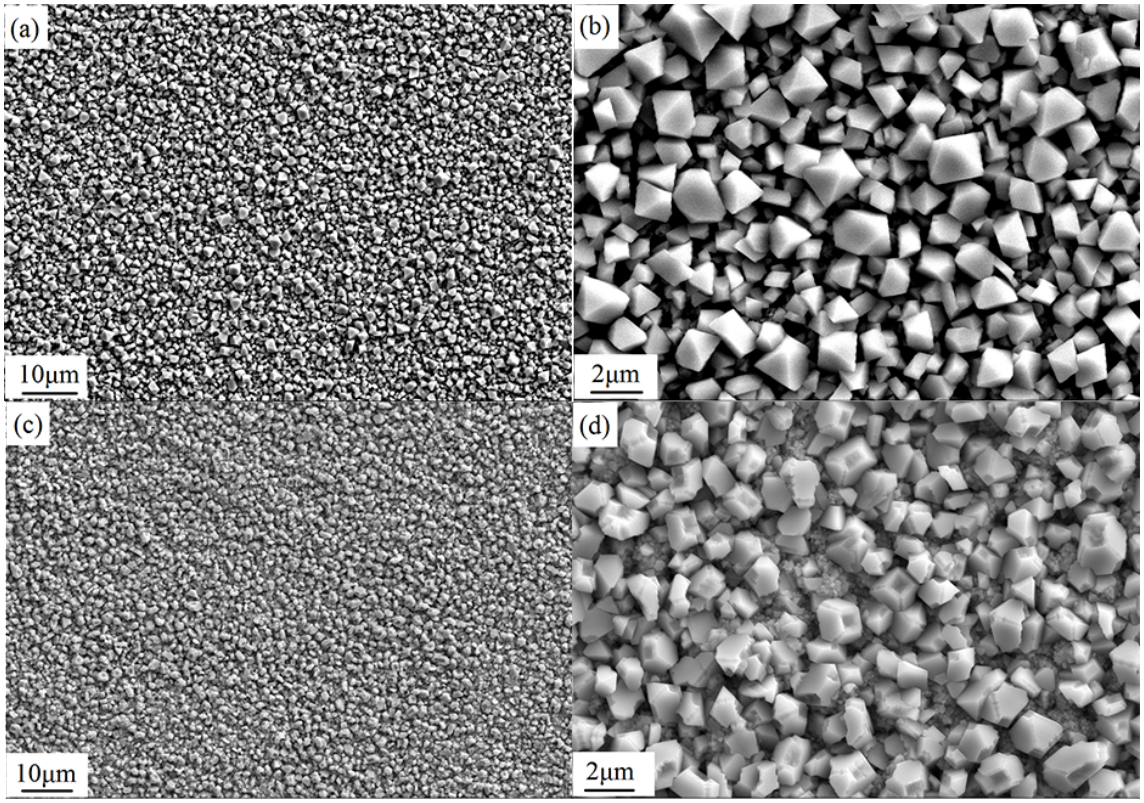

Figure 1.9 Images FEG-SEM des couches d'oxyde sur l'alliage AISI 430 oxydé après 96h à 800 ℃ (a, b) sous air sec, (c, d) sous air avec 5% l'humidité absolue

La Figure 1.10 présente les images de FEG-SEM en section transverse de la couche d'oxyde formée sur l'alliage AISI 430 à 800°C pendant 96h sous air sec et avec 5%HA. La présence de vapeur d'eau n'a pas d'influence sur la structure de l'oxyde, deux couches d'oxyde sont observées clairement.

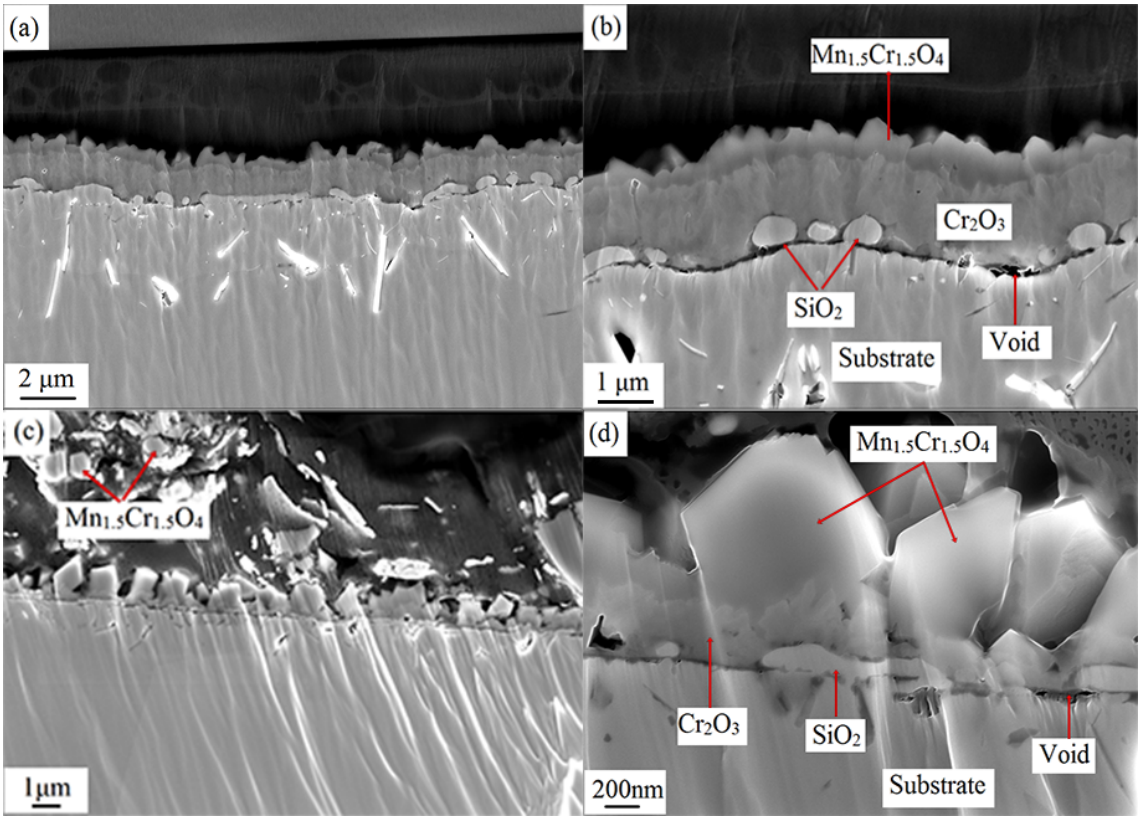

Figure 1.10 Images FEG-SEM de sections transversales sur l'alliage AISI 430 oxydé pendant 96 h à 800 °C sous air sec (a, b) et avec 5%HA (c, d)

Une série d'analyses par XPS (X-ray Photoelectron Spetrocopy) a été faite sur l'alliage AISI 430 oxydé pendant 9h à différentes températures sans et avec vapeur d'eau (5% d'humidité absolue), pour étudier la formation d'oxyde et de possible hydroxyde. Selon la Figure 1.11, sans ou avec vapeur d'eau, à la même température d'oxydation, les profils XPS ne sont pas les mêmes. Une augmentation de la quantité d'hydroxyde est observée dans l'oxyde formé en présence de vapeur d'eau. Par conséquent, le mécanisme d'oxydation sous air sans et avec vapeur de l'eau n'est pas identique. Le schéma du développement de la couche d'oxyde sous air avec vapeur d'eau est présenté dans la Figure 1.12. L'oxydation est aussi contrôlée par la diffusion des ions de Cr vers l'extérieur, mais en plus il y a des ions de hydroxyde transportés vers l'intérieur.

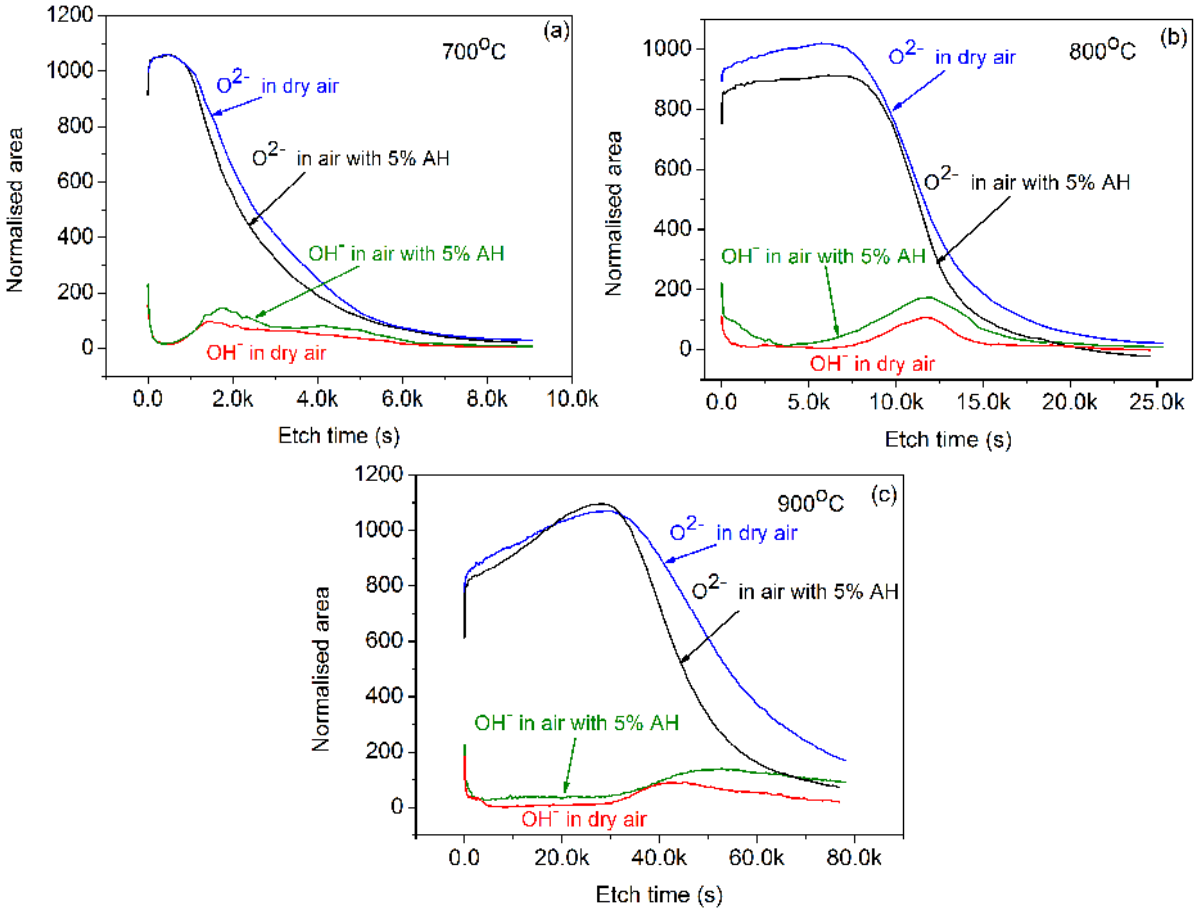

Figure 1.11 Profils XPS de –O et –OH sur l'alliage AISI 430 oxydé sous air sans et avec 5% HA pendant 9h à différentes températures (a) 700 ℃, (b) 800 ℃ et (c) 900 ℃

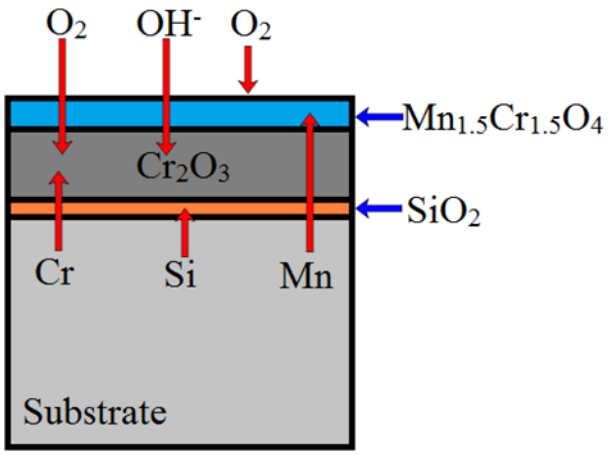

Figure 1.12 Schéma du développement des couches d'oxyde de l'alliage AISI 430 sous air avec la présence de vapeur de l'eau

1.3 Conclusion

Pour l'oxydation sous air sec, la cinétique d'oxydation de l'alliage AISI 430 suit une loi parabolique de 700 ℃ à 900 ℃ pour une durée jusqu'à 96h. L'oxyde se compose de deux couches: la couche externe est spinelle $Mn_{1.5}Cr_{1.5}O_4$ et la couche interne est Cr_2O_3. L'oxydation est contrôlée essentiellement par la diffusion des ions de Cr vers l'extérieur.

Tableau 1.3 La comparaison du comportement en oxydation de l'alliage AISI 430 sous air sec et avec vapeur de l'eau

	Air sec	Avec vapeur d'eau
Cinétique d'oxydation	Les cinétiques suivent un régime parabolique à 700 ℃, 800 ℃ and 900 ℃ jusqu'à 96h	1) La dégradation de la couche d'oxyde est observée à 60h, 16h, 7h et 3h avec 2%, 5%, 8% et 10% de l'humidité absolue à 900 ℃, respectivement. 2) Avant la dégradation de la couche, les cinétiques suivent un régime parabolique et la prise de masse diminue par rapport à celle sans vapeur d'eau
Morphologie des couches d'oxyde	Les oxydes spinelles formés sur la surface sont réguliers	Les oxydes spinelles formés sur la surface sont irréguliers
Mécanismes d'oxydation	Contrôlé par la diffusion des ions de Cr vers l'extérieur	Une augmentation de la quantité d'hydroxyde est observée dans l'oxyde

Avec l'introduction de vapeur d'eau dans l'atmosphère d'oxydation, des comportements à l'oxydation de l'alliage AISI 430 à haute température ont été affectés, particulièrement à 900 ℃, car la dégradation de la couche d'oxyde est apparue relativement tôt. Avant la

dégradation de la couche d'oxyde, la prise de masse diminue par rapport à celle sans vapeur d'eau, par contre la présence de vapeur d'eau n'affecte pas la nature des produits d'oxydation. Après la dégradation de la couche d'oxyde, les pics de Fe_2O_3 et $(Fe_{0.6}Cr_{0.4})_2O_3$ ont observés. La présence de vapeur d'eau a d'influence sur le mécanisme d'oxydation. La comparaison du comportement en oxydation de l'alliage AISI 430 sous air sec et avec vapeur de l'eau est montrée dans le Tableau 1.3.

2 Etude des contraintes résiduelles dans les couches d'oxyde

2.1 Contraintes internes dans les couches obtenues sans vapeur d'eau

Les contraintes résiduelles obtenues par la Diffraction des Rayons X (DRX) à la température ambiante sont notées comme σ_{DRX}, dans notre cas d'étude. Il y a trois sources principales de contrainte résiduelle : les contraintes de croissance (des contraintes qui sont générées pendant l'oxydation isotherme), les contraintes thermiques (des contraintes qui sont générées lors du refroidissement qui suit l'oxydation) et les contraintes chimiques (des contraintes qui sont générées par le gradient chimique et le potentiel chimique pendant l'oxydation).

$$\sigma_{\text{Résiduelles}} = \sigma_{\text{Croissance}} + \sigma_{\text{Thermique}} + \sigma_{\text{Chimie}} \qquad (2\text{-}1)$$

Les contraintes thermiques dans la couche peuvent être évaluées par l'équation suivante [2]

$$\sigma_{\text{Thermique}} = \frac{\frac{E_o}{1-\nu_o}(\alpha_o - \alpha_m)}{1+\frac{e_o E_o}{e_m E_m}\left(\frac{1-\nu_m}{1-\nu_o}\right)}\Delta T \qquad (2\text{-}2)$$

avec: E_o, E_m: module de Young respective de l'oxyde et du métal

e_o, e_m : épaisseur respective de l'oxyde et du métal

ν_o, ν_m : coefficient de Poisson respective de l'oxyde et du métal

α_o, α_m : coefficient de dilatation thermique respective de l'oxyde et du métal

En première approximation, compte tenu des épaisseurs relatives de l'oxyde et du métal et en supposant que les coefficients de dilatation sont indépendants de la température, on obtient l'expression simplifiée :

$$\sigma_{\text{Thermique}} = \frac{E_o(\alpha_o - \alpha_m)}{1-T}\Delta T \qquad (2\text{-}3)$$

Les contraintes thermiques dans les couches d'oxyde calculées par l'Equation (2-3) sont présentées dans le Tableau 2.1.

Tableau 2.1 Les contraintes thermiques dans les couches d'oxyde calculées par l'Equation (2-4)

Température	Cr_2O_3 (MPa)	$Mn_{1.5}Cr_{1.5}O_4$ (MPa)
700 ℃	-800	-485
800 ℃	-915	-555
900 ℃	-1035	-630

Les résultats d'analyses des contraintes résiduelles dans les couches formées sur de l'alliage AISI 430 après une oxydation sous air sec à différente température sont présentés dans la Figure 2.1. Nous constatons que, quelle que soit la température de l'oxydation, les contraintes résiduelles dans les couches d'oxyde sont toujours en compression. Le niveau de contraintes résiduelles augmente avec l'augmentation de la température d'oxydation. La contrainte résiduelles dans la couche de Cr_2O_3 est plus importante que celle dans la couche de spinelle $Mn_{1.5}Cr_{1.5}O_4$. A toute les températures d'oxydation, la tendance d'évolution des contraintes résiduelles dans les deux couches est similaire en fonction de la durée d'oxydation. Il y a une contrainte d'accommodation entre les deux couches qui est en relation directe avec les contraintes d'origine chimique.

$$\sigma_{\text{Résiduelle}} = \sigma_{\text{Croissance}} + \sigma_{\text{Thermique}} + \sigma_{\text{Accommodation}} \qquad (2\text{-}4)$$

Pour la couche Cr_2O_3, les contraintes résiduelles augmentent avec la durée d'oxydation à 700°C. Mais, la valeur des contraintes résiduelles augmentent d'abord, et puis diminuent en

fonction du temps d'oxydation à 800°C et 900°C. Cette allure peut être interprétée par le phénomène de relaxation se déclenchant au bout d'une certaine épaisseur de couche.

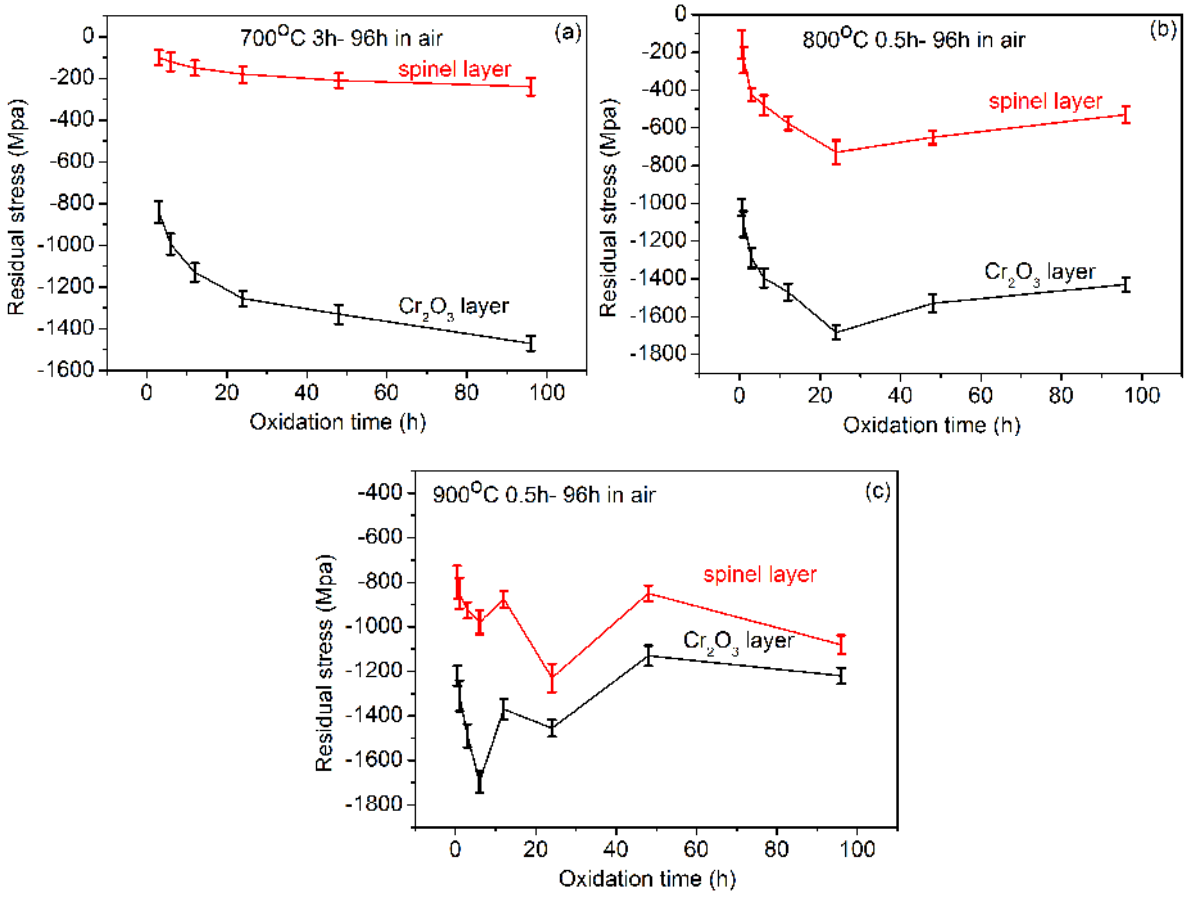

Figure 2.1 Evolution des contraintes résiduelles dans les couches formée sur de l'alliage AISI 430 après une oxydation sous air sec à (a) 700 ℃, (b) 800 ℃ et (c) 900 ℃

2.2 Contraintes résiduelles dans les couches obtenues avec vapeur d'eau à différentes températures

Le rôle de la teneur en vapeur d'eau dans l'atmosphère d'oxydation sur les contraintes résiduelles a également été étudié. Les résultats dans la couche de chromine sont présentés dans la Figure 2.2. Pour la couche de Cr_2O_3, avec la présence de vapeur d'eau, le niveau de contraintes résiduelles augmente en fonction de la teneur en vapeur d'eau dans l'atmosphère d'oxydation à 700°C, et à 800°C, 900 ℃ avant la relaxation qui se déclenche. En revanche,

après la relaxation qui se déclenche, le niveau de contraintes résiduelles diminue en fonction de la teneur en vapeur d'eau.

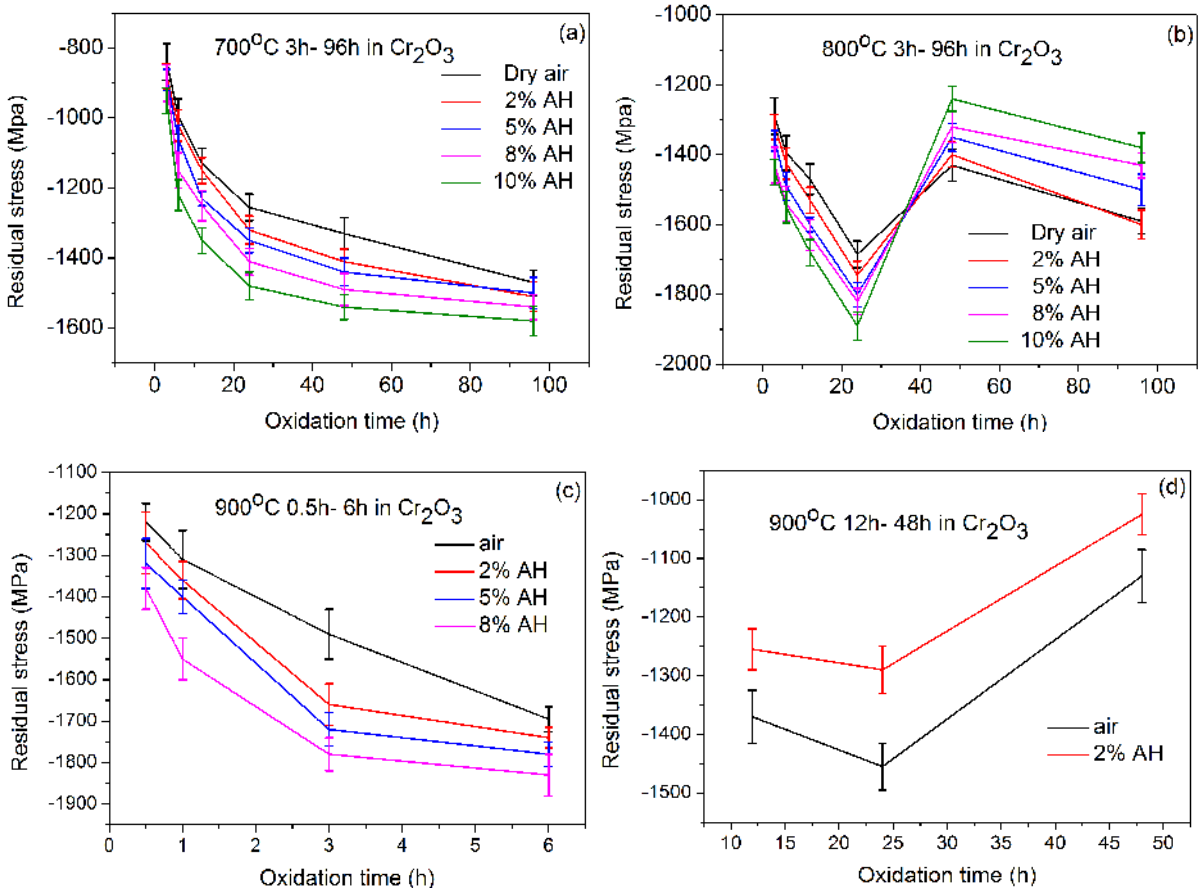

Figure 2.2 Evolution des contraintes résiduelles dans la couche de Cr_2O_3 en surface de l'alliage AISI 430 après une oxydation sous différents taux de vapeur d'eau à différents température

Les résultats des contraintes résiduelles dans la couche de spinelle sont présentés dans la Figure 2.3. La tendance de l'évolution des contraintes résiduelles dans la couche de spinelle est similaire que celle dans la couche de Chromine. La relaxation des contraintes résiduelles est aussi observée à 800 ℃ et 900 ℃ au bout d'un certain temps d'oxydation. Les niveaux de contraintes résiduelles dans la couche de spinelle $Mn_{1.5}Cr_{1.5}O_4$ augmentent en fonction de l'augmentation du taux d'humidité absolue à toutes les températures.

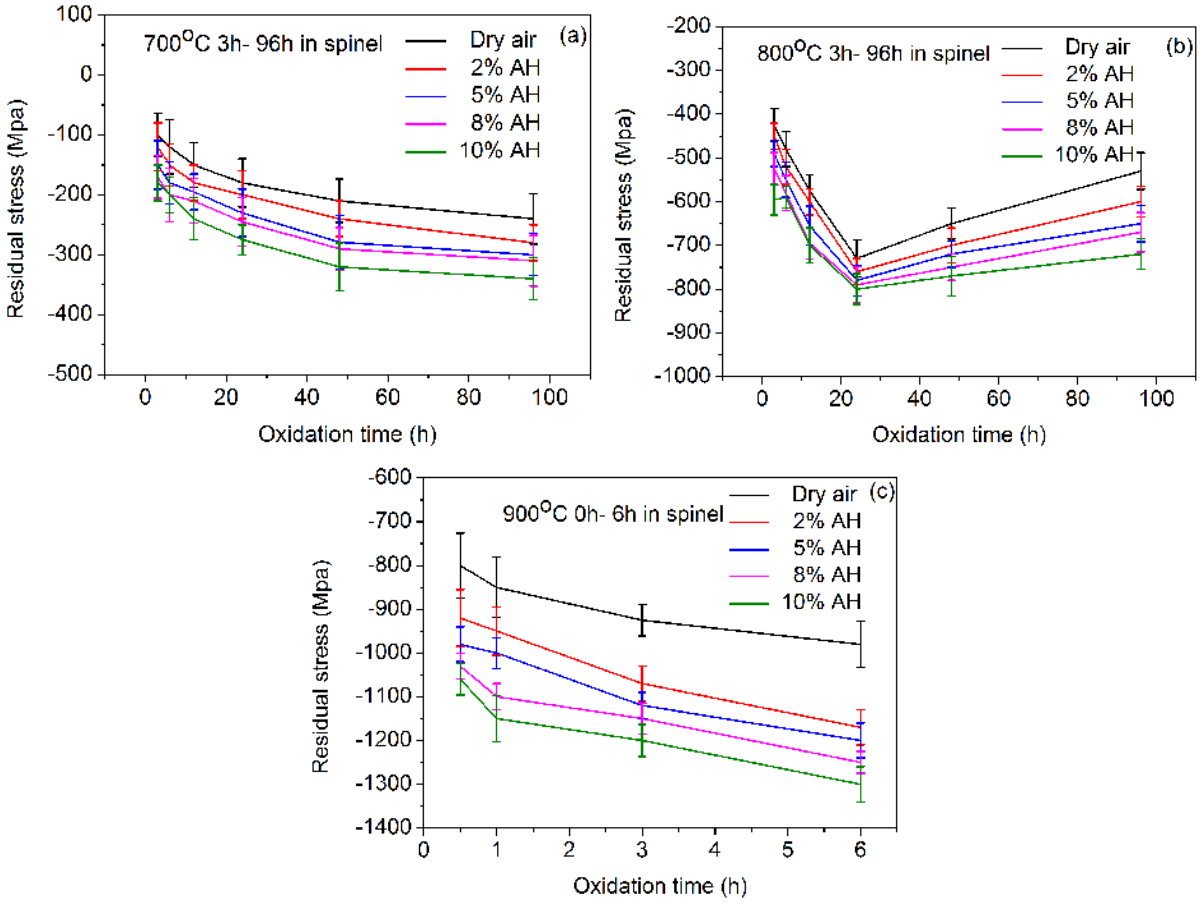

Figure 2.3 Evolution des contraintes résiduelles dans la couche de $Mn_{1.5}Cr_{1.5}O_4$ en surface de l'alliage AISI 430 après une oxydation sous différents taux de vapeur d'eau à différentes températures

2.3 Etude des contraintes de croissance par la déflexion in-situ

La méthode de déflexion est une technique bien particulière destinée pour les études de contraintes de croissance in-situ lors de l'oxydation à haute température. Les contraintes dues à la croissance des oxydes sont reliées à la déflexion D (en mm) par l'Equation 2-5.

$$\sigma_f = D\frac{E_m}{1-v_m^2}\frac{e_m^2}{3e_f L^2} \qquad (2\text{-}5)$$

où E_s et υ_s sont le module d'Young (en MPa) et le coefficient de Poisson du substrat respectivement, e_s (en mm) est l'épaisseur du substrat, e_{ox} (en mm) est l'épaisseur de l'oxyde ; L (en mm) est la longueur de l'échantillon.

La Figure 2.4 montre la courbe brute de déflexion de la lame de l'alliage AISI 430 sous air sec et sous air avec 5% d'humidité absolue à différents températures. La contrainte de croissance calculée à partir des résultats expérimentaux de déflexion inclue la contrainte de croissance de la couche de Cr_2O_3 ainsi que celle de la couche de $Mn_{1.5}Cr_{1.5}O_4$. Ce résultat montre que la contrainte de croissance est plus importante sous air qu'avec vapeur d'eau. Selon la équation (2-5), on a obtenu une contrainte de croissance sous air sec à 700 ℃, 800 ℃ et 900 ℃ et elles sont de -750 MPa, -915 MPa et -1015 MPa respectivement. Avec la présence de 5% d'humidité absolue, les contraintes de croissance à 700 ℃, 800 ℃ et 900 ℃ sont de -805 MPa, -960 MPa et -1075 MPa respectivement.

Tableau 2.2 Comparaison de la contrainte résiduelle calculée par l'équation (2-2) et déterminé par la méthode de DRX pour les échantillons oxydés sous air sec

	$\sigma_{thermique}$ calculée MPa	$\sigma_{croissance}$ déflexion MPa	$\sigma_{résiduelle}$ calculée MPa	$\sigma_{résiduelle}$ DRX MPa
700 ℃	-800	-750	-1550	-995 ±35
800 ℃	-920	-915	-1835	-1395 ±50
900 ℃	-1035	-1020	-2055	-1725 ±45

Le Tableau 2.2 présente la comparaison de la contrainte résiduelle calculée par l'équation (2-1) et déterminé par la méthode de DRX dans le cas d'une oxydation sous air sec. Les valeurs de la contrainte résiduelles déterminées par la méthode de DRX sont toujours moins importantes que celles calculées par l'équation (2-1). Cette différence peut s'expliquer partiellement par la relaxation des contraintes au cours du refroidissement, par l'incertitude des coefficients de dilatation thermique ainsi que les contraintes d'origine chimique.

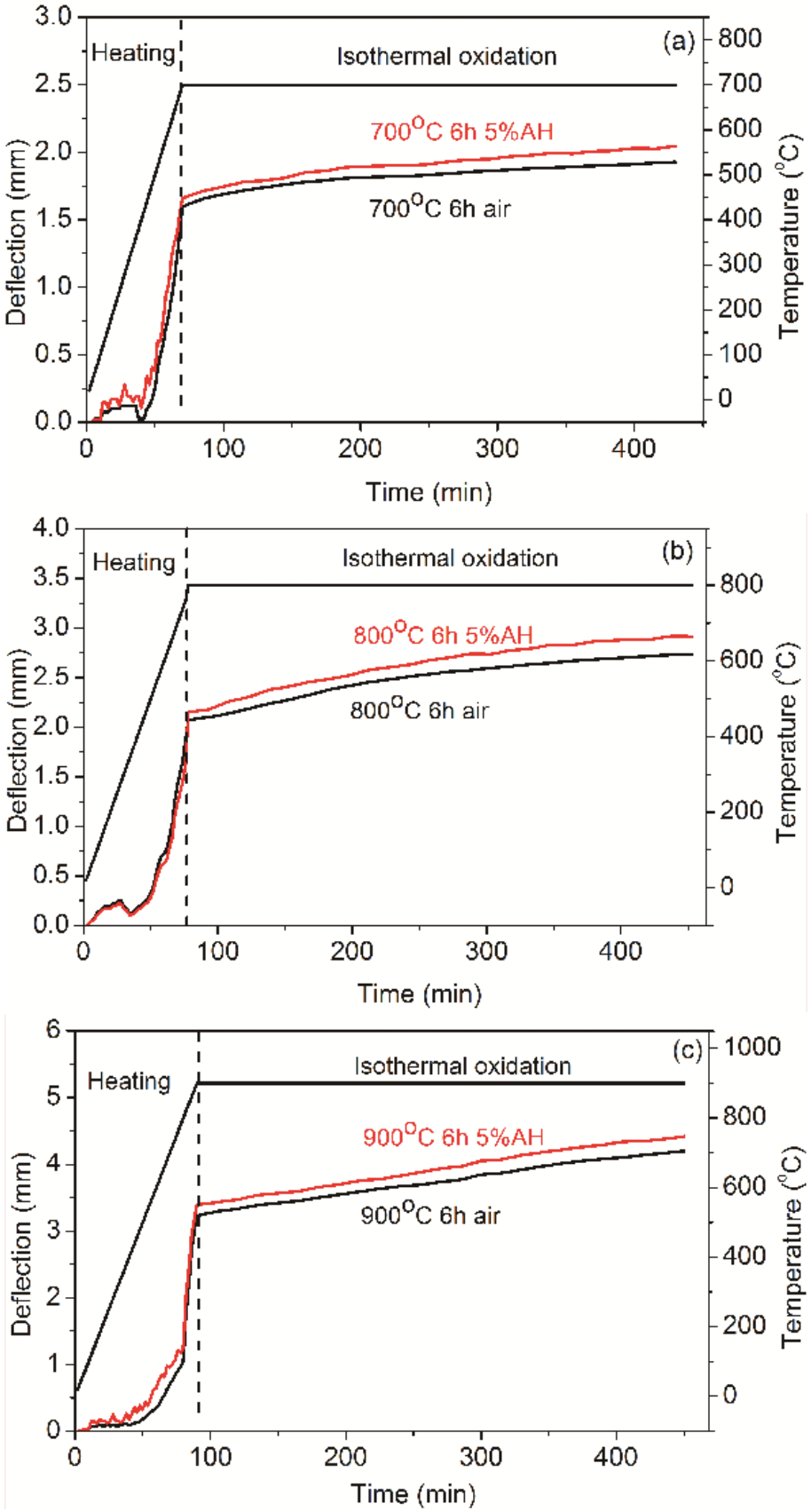

Figure 2.4 Courbe brute de déflexion de la lame de l'alliage AISI 430 sous air sec et sous air avec 5% d'humidité absolue à différentes températures

2.4 Conclusion

A partir des résultats obtenus, les remarques ainsi que les conclusions suivantes peuvent être proposées:

Après l'oxydation sous air sec ou avec vapeur d'eau, les contraintes résiduelles existant dans les deux couches sont en compression. Les contraintes résiduelles dans la couche de Cr_2O_3 sont plus importante que celle dans la couche de spinelle $Mn_{1.5}Cr_{1.5}O_4$. Il y a une contrainte d'accommodation entre les deux couches. Le phénomène de relaxation se déclenchant au bout d'une certaine épaisseur de couche.

La présence de vapeur d'eau modifie donc le niveau de contraintes résiduelles dans les deux couches de l'oxydation de l'alliage AISI 430. Avant la relaxation, le niveau de contraintes résiduelles augmente en fonction de la teneur en vapeur d'eau. Mais après la relaxation qui se déclenche, le niveau de contraintes résiduelles diminue en fonction de la teneur en vapeur d'eau. La contrainte de croissance est plus importante sous air qu'avec vapeur d'eau.

3 Dégradation de la couche d'oxyde

Comme nous l'avons déjà dit, une accélération cinétique est observée après une courte durée d'oxydation à 900°C avec la présence de vapeur d'eau, qui indique la dégradation de la couche d'oxyde. Ce phénomène est appelé <<breakaway>>. Le temps d'incubation pour la dégradation est fonction de la teneur en vapeur d'eau. Des nodules sont formés sur la surface (Figure 3.1), ce qui indique que la dégradation de la couche commence dans ces parties de l'échantillon. Deux mécanismes possibles sont proposés pour expliquer ce phénomène.

L'alliage étudié étant un chromino-formeur, on peut s'attendre à la formation d'oxyhydroxyde de chrome due à la réaction suivante

$$\frac{1}{2}Cr_2O_3(s) + \frac{3}{4}O_2(g) + H_2O(g) = CrO_2(OH)_2(g) \qquad (3\text{-}1)$$

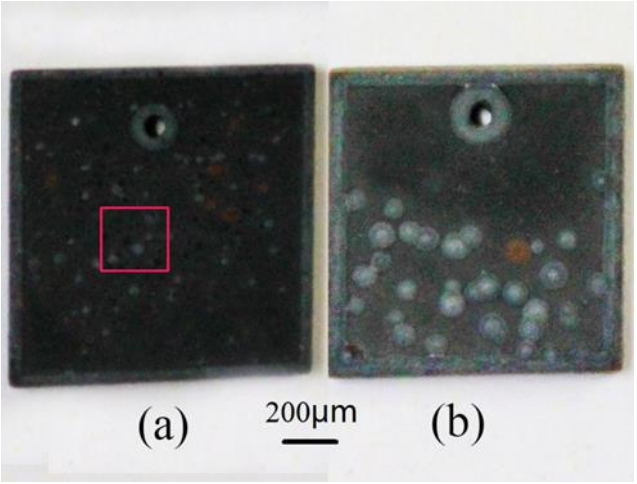

Figure 3.1 Observation macroscopique de l'alliage AISI 430 après 96h d'oxydation à 900°C (a) sous air+2%HA et (b) sous air+5%HA

La formation d'oxyhydroxyde de chrome aboutit au phénomène d'évaporation des espèces chromées. Ainsi, la variation de masse d'un échantillon est la combinaison de la perte de masse due à l'évaporation et la prise de masse pendant l'oxydation.

$$W_{total} = W_{oxydation} + W_{évaporation} \qquad (3\text{-}2)$$

Les courbes de variation de la mass montrent dans la Figure 3.2 sont des superpositions de la prise de masse mesurée par ATG et de la perte de masse calculée due à évaporation après oxydation sous air avec différents humidités absolues à différentes températures. Il est clair que la variation de la masse sous air avec vapeur d'eau après la correction est presque la même que celle sous air sec, qui indique que l'évaporation de $CrO_2(OH)_2$ est la principale raison de la diminue de la masse avec l'introduction de vapeur d'eau par rapport à celle sans vapeur d'eau.

La comparaison de la perte de masse de Cr_2O_3 due à évaporation par le calcul et par la mesure après 96h d'oxydation sous air avec 10% HA à 700°C est montrée dans la Figure 3.3, qui indique l'oxyde de type spinelle permet de retarder significativement la transformation de la chromine en phase volatile.

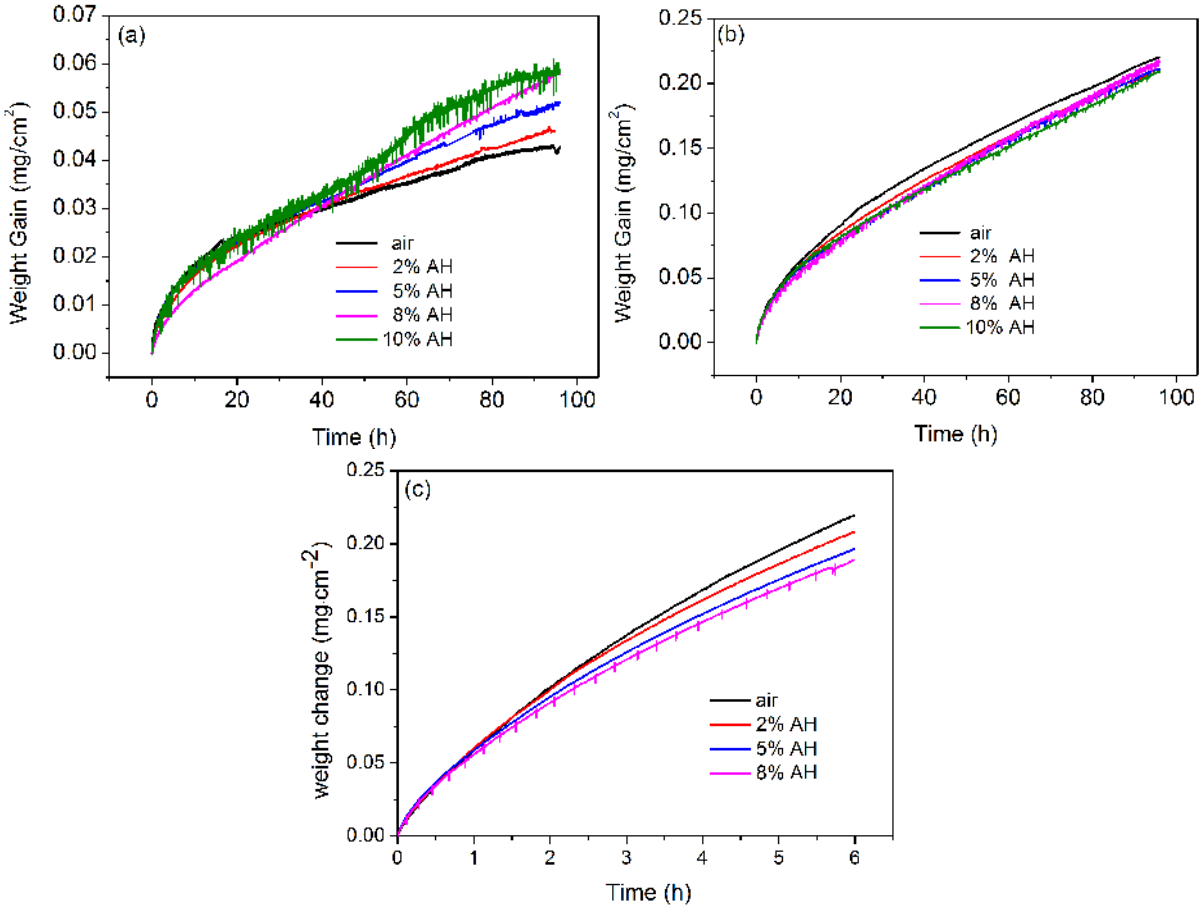

Figure 3.2 Les courbes de variation de la masse après les corrections avec la perte de masse due à évaporation à (a) 700 ℃, (b) 800 ℃ et (c) 900 ℃

Le phénomène de volatilisation d'oxyhydroxyde peut conduire à la dégradation de la couche en présence de plus que 5%HA, car les nodules sont observés près du bord inférieur de l'échantillon (la direction d'écoulement de la vapeur d'eau est du bas vers le haut de l'échantillon). En même temps, les contraintes internes dans la couche d'oxyde peuvent modifier les cinétiques de croissance d'oxyde. Après la relaxation qui se déclenche, le niveau de contraintes résiduelles diminue en fonction de la teneur en vapeur d'eau, qui peut diminuer la vitesse de formation de Cr_2O_3 pendant l'oxydation. Pour cette raison, les contraintes jouent aussi un rôle important sur la dégradation de la couche d'oxyde avec plus de 5% d'humidité absolue.

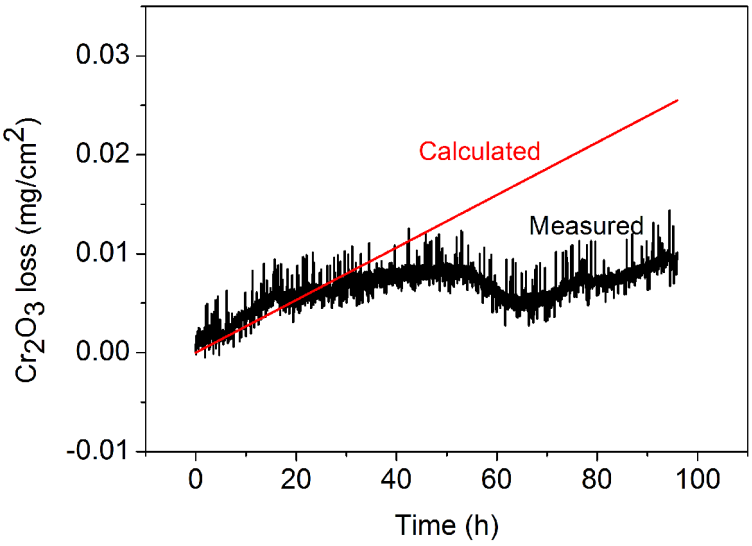

Figure 3.3 Comparaison de la perte de masse de Cr_2O_3 due à l'évaporation par le calcul et par la mesure après 96h d'oxydation sous air avec 10% HA à 700 ℃

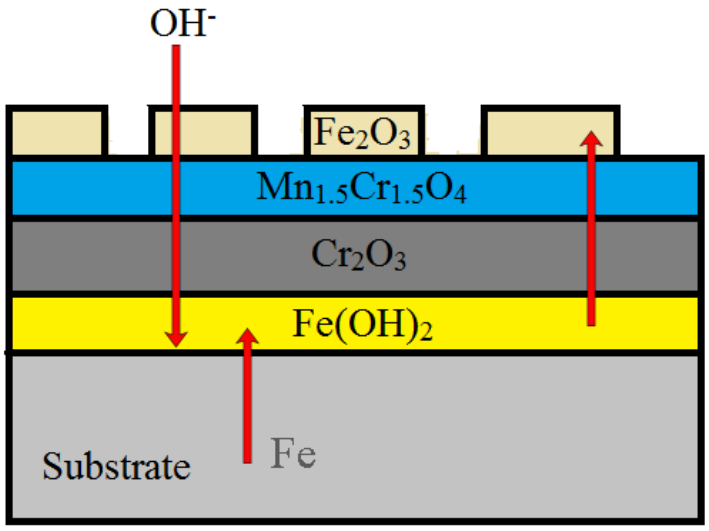

Figure 3.4 Schéma du mécanisme de le dégradation de la couche d'oxyde sous air avec 2%HA

Pourtant sous air avec 2%HA, les nodules sont engendrés au hasard sur la surface, la volatilisation d'oxo-hydroxyde de chrome est négligeable et ne permet pas d'expliquer la dégradation de la couche. La présence de vapeur d'eau augmente la quantité d'hydroxyde qui peut réagir avec des ions de Fe pour générer Fe $(OH)_2$ à l'interface oxyde/ substrat. $Fe(OH)_2$

diffuse à la surface et dépose comme Fe_2O_3 par réaction (3-3). Le schéma de ce mécanisme est présenté dans la Figure 3.4.

$$2Fe(OH)_{2(g)} \rightarrow Fe_2O_3 + H_2O_{(g)} + H_{2(g)} \qquad (3\text{-}3)$$

A partir de nos résultats d'étude, deux mécanismes de la dégradation de la couche d'oxyde ont été proposées dans ce chapitre. Le temps d'incubation pour la dégradation est fonction de la teneur en vapeur d'eau. Sous air avec 2%HA, l'augmentation de la quantité d'hydroxyde et la formation de la phase $Fe(OH)_2$ à interface oxyde/ substrat peuvent conduire à la dégradation de la couche. Avec plus de 5%HA, la dégradation de la couche est principalement due à la volatilisation d'oxyhydroxyde. Les contraintes internes jouent aussi un rôle important sur la dégradation de la couche.

4 Perspectives

En raison de la limitation du temps, de nombreux travaux théoriques et expérimentaux n'ont pas été faits en détail et jusqu'au bout dans cette étude, donc d'autres investigations seront nécessaires à l'avenir.

Il sera très intéressant d'évaluer de contraintes résiduelles en fonction de la profondeur de couche d'oxyde afin de tenir compte de l'effet de gradient chimique.

Des analyses théoriques plus poussées, à l'aide de modélisation numérique, devaient aussi être menées afin d'expliquer le rôle de l'humidité sur l'évolution des contraintes internes.

D'autre part, on peut utiliser H_2O^{18} dans les expériences, avec l'aide de l'analyse des SIMS pour mieux comprendre le rôle de la vapeur d'eau dans le processus d'oxydation à haute température de l'alliage AISI 430.

5 Références bibliographiques

[1]. S.R.J. Saunders, M. Monteiro, F. Rizzo, The oxidation behaviour of metals and alloys at high temperatures in atmospheres containing water vapour: A review, Progress in Materials Science 53 (2008) 775-837.

[2]. A.M. Huntz, Stresses in NiO, Cr_2O_3 and Al_2O_3 oxide scales, Mater. Sci. Eng. A 201 (1995) 211-228.

[3]. J.L. Ruan, Y. Pei, D. Fang, Residual stress analysis in the oxide scale/metal substrate system due to oxidation growth strain and creep deformation, Acta Mechanica 223 (2012) 2597-2607.

[4]. B. Hua, Y. Kong, W. Zhang, J. Pu, B. Chi, L. Jian, The effect of Mn on the oxidation behavior and electrical conductivity of Fe–17Cr alloys in solid oxide fuel cell cathode atmosphere, J. Power Sources 196 (2011) 7627-7638.

[5]. R.K.S. Raman, R.K. Gupta, Oxidation resistance of nanocrystalline vis-à-vis microcrystalline Fe–Cr alloys, Corros. Sci. 51 (2009) 316-321.

[6]. J. Rufner, Oxidation behavior of stainless steel 430 and 441 at 800 ℃ in single (air/air) and dual atmosphere (air/hydrogen) exposures, Int. J. Hydrogen. Energ 33 (2008) 1392-1398.

[7]. J. Xiao, N. Prud'homme, N. Li, V. Ji, Influence of humidity on high temperature oxidation of Inconel 600 alloy: Oxide layers and residual stress study, Appl. Surf. Sci. 284 (2013) 446-452.

[8]. A.M. Huntz, A. Reckmann, C. Haut, C. Sévérac, M. Herbst, F.C.T. Resende, A.C.S. Sabioni, Oxidation of AISI 304 and AISI 439 stainless steels, Mater. Sci. Eng. A 447 (2007) 266-276.

[9]. N. Birks, G.H. Meier, F.S. Pettit, Introduction to the high-temperature oxidation of metals, in, Cambridge University, UK, 2006.

[10]. M. Palcut, L. Mikkelsen, K. Neufeld, M. Chen, R. Knibbe, P.V. Hendriksen, Corrosion stability of ferritic stainless steels for solid oxide electrolyser cell interconnects, Corros. Sci. 52 (2010) 3309-3320.

Titre : Etude du comportement à l'oxydation et des contraintes résiduelles lors de l'oxydation sous air humide de l'alliage AISI 430

Mots clés : Oxydation, Contraintes residuelles, Haute température, Vapeur d'eau

Résumé : Lorsqu'un alliage métallique est mis sous une atmosphère oxydante à haute température, un oxyde est formé en surface de l'alliage. La résistance à l'oxydation à haut température est un critère très important pour le choix des alliages. Il a été observé que le comportement à l'oxydation des alliages sous l'atmosphère avec vapeur d'eau est différente de celle dans l'air sec ou dans l'oxygène. En outre, les contraintes de croissance et les contraintes thermiques sont formées dans la couche d'oxyde. Ces contraintes ont des effets importants sur la durée de vie de l'alliage.
Le présent travail se concentre essentiellement sur l'étude de l'influence de la vapeur d'eau sur le comportement à l'oxydation de l'alliage AISI 430 à haute température, qui est importante pour les applications dans la pile à combustible SOFC (solid oxide fuel cell) comme interconneteurs. Les expériences d'oxydation de l'alliage AISI 430 sous air sec et sous air avec différentes humidités absolues (2%-10%) de 700°C à 900°C sont réalisées à l'aide de l'analyse thermogravimétrique (ATG). Les images MEB des échantillons ont été obtenues avec un MEB-FEG avec un microanalyseur X par dispersion d'énergie (EDX). Les contraintes résiduelles de la couche d'oxyde sont obtenues par la Diffraction des Rayons X (DRX) à la température ambiante, et la méthode de déflexion a été utilisée pour déterminer les contraintes de croissance.
La présence de vapeur d'eau modifie donc le niveau de contraintes résiduelles dans la couche d'oxyde. La degradation de la couche d'oxyde est observée aprés une courte durée d'oxydation à 900 °C et deux mécanismes possibles sont proposés pour expliquer ce phénomène à partir de nos résultats d'étude.

Title : Study the oxidation behavior and residual stresses of AISI 430 alloy in air with water vapor

Keywords : Oxidation, Residual stresses, High temperature, Water vapor

Abstract: When an alloy is placed in an atmosphere containing oxygen at high temperature, the formation of oxide scale may take place. The oxidation resistance of the alloy is a very important criterion for selecting alloys to be used at high temperature. And it has been found that the oxidation behavior of alloys in atmosphere containing water vapor is different from that in dry air or oxygen. Moreover, in the oxide scale systematically accompanied the development of growth stresses and of thermal stresses, which also limit the durability of oxide scale and the lifetime of the alloy.
The purpose of this work is to investigate the influence of water vapor on oxidation behavior of AISI 430 stainless steel at high temperature, which is expected to be used as interconnectors in the planar solid oxide fuel cells (SOFCs). The oxidation experiments have been performed in air with different absolute humidity (2%-10%) at 700 °C, 800 °C and 900 °C by thermal gravimetric analysis (TGA) system. The oxide surface morphology, cross-section microstructure and the chemical composition of the oxide scale were studied after oxidation by FEG-SEM and EDX. The residual stresses distributions in the oxide scale were determined at room temperature by XRD method after oxidation, and the growth stresses were measured by in-situ deflection method during oxidation.
The water vapor can also influence the residual stresses levels in the oxide scale. In the presence of water vapor, breakaway oxidation was observed at 900 °C, and two possible mechanisms were given to explain this.

Université Paris-Saclay
Espace Technologique / Immeuble Discovery
Route de l'Orme aux Merisiers RD 128 / 91190 Saint-Aubin, France